School of Science
Department of Imaging and Applied Physics
Centre for Marine Science and Technology

The Development of a Fast Multipole Boundary Element Method for Coupled Acoustic and Elastic Problems

Daniel Ryan Wilkes

This thesis is presented for the Degree of
Doctor of Philosophy
of
Curtin University

May 2014

Declaration

To the best of my knowledge and belief this thesis contains no material previously published by any other person except where due acknowledgement has been made.

This thesis contains no material which has been accepted for the award of any other degree or diploma in any university.

Signature: _____

Date: _____

Abstract

This thesis presents a numerical model for 3D acoustic coupled fluid–structure interaction (FSI) problems in the frequency domain which involve a single exterior fluid domain and a single interior elastic solid domain, with both media having homogeneous isotropic properties. The fluid and elastic solid domains are respectively modelled via the Helmholtz and elastodynamic boundary integral equations (BIEs) and the fast multipole method (FMM) is used to accelerate the boundary element method (BEM) calculations in both domains. The separate fast multipole boundary element method (FMBEM) models for the two media are coupled together on the common boundary surface defining the interior/exterior domains via the application of boundary conditions between the unknowns of the two BIEs. This coupling procedure thus models the coupled FSI of the acoustic field between the fluid and elastic solid domains, yielding the coupled pressure and displacement solution on the common boundary surface. The use of the FMBEM in both domains allows very large scale coupled FSI problems to be modelled due to the use of the BEM formulations restricting all unknowns to the shared boundary surface (thus minimising the total number of unknowns required to represent the problem), while the use of the FMM accelerates the BEM calculations and reduces the memory requirements in both the fluid and elastic solid domains. Numerical examples are presented for the dual FMBEM model which indicate that substantially faster solution times and smaller memory requirements are achieved over conventional numerical models, while yielding a comparable solution accuracy. The algorithmic complexity of the dual FMBEM is shown to be proportional to $O(N)$ at very low frequencies, and proportional to $O(N^{1.5})$ when using a fixed number of elements per wavelength, which in both cases is in good agreement with the theoretical predictions for the FMM.

To my wife Rochelle, for all of her love and support over the many years it has taken me to finish this thesis.

Acknowledgements

First and foremost, I would like to thank my PhD supervisor, Dr. Alec Duncan: without his mentoring, patience, encyclopaedic knowledge on a broad range of topics, and finally, his unwavering belief that I could complete this thesis work, I could never have achieved such an undertaking. I feel proud to say that under Alec's guidance I have been able to develop the various FMBEM models developed in thesis 'from scratch', with no collaboration from any outside institutions and no prior history in the field from our own institution. Cheers Alec! I couldn't have done it without you.

I would also like to thank Dr. Patrick Macey from PACSYS Limited for his valuable help on running a number of different types of numerical analysis (BEM, modal FEM and coupled FEM–BEM problems) using PACSYS' PAFEC software suite for the various comparative results presented throughout this thesis.

I would also like to thank my thesis co–supervisors, Dr. Darryl McMahon (DSTO), and Prof. Alexander Gavrilov (CMST), for the invaluable feedback and comments they were able to provide (in a very short time frame!) on the final draft of this thesis, which I feel has greatly enhanced the readability and focus of the document as a whole.

Finally, I would to thank both the thesis examiners, who provided their valuable perspectives and constructive criticisms of this thesis, for which I am very grateful.

Contents

List of Figures

LIST OF FIGURES

List of Tables

Glossary

Greek Symbols

α The Burton–Miller coupling parameter used to combine the Helmholtz BIE and the normal derivative of the Helmholtz BIE. Typically set to $\alpha = i/k$ or some fraction of this value, page 49

β Coefficient term involving the shear modulus which appears in the traction fundamental solution. Defined as $\beta = \frac{2\nu}{1-2\nu}$, page 92

δ_{ij} The Kronecker delta function. Defined as $\delta_{ij} = 1$ for $i = j$ and $\delta_{ij} = 0$ for $i \neq j$, page 90

ϵ GMRES convergence tolerance for the outer GMRES loop. Defined as $\epsilon = 10^{-4}$, page 13

ϵ_{pre} GMRES convergence tolerance for the inner preconditioner GMRES loop. Defined as $\epsilon_{\text{pre}} = 0.2$, page 56

λ The acoustic wavelength, page 10

μ Denotes the shear modulus (in GPa), page 90

ν Denotes Poisson's ratio (unitless), page 90

ω The angular frequency. Defined as $\omega = 2\pi f$ for frequency f, page 10

Ω A scaling factor used to reduce the condition number of the coupled coefficient matrix in the dual FMBEM model, page 137

Ψ A scaling factor used to reduce the condition number of the coupled coefficient matrix in the dual FMBEM model, page 137

ρ_f Denotes the density (in kg/m^3) of the fluid, page 134

ρ_s Denotes the density (in kg/m^3) of the elastic solid, page 90

ξ Specified error tolerance in the outer GMRES loop for the accuracy of the Green's function reconstructed from the fast multipole expansions. Defined as $\xi = 10^{-4}$, page 25

$\boldsymbol{\xi}_N$ The N element residual vector arising from the iterative solution of the discretised Helmholtz BIE with N elements. For example $\xi_N = \mathbf{Az} - \mathbf{b}$ for the current iterative solution $\mathbf{z}$, page 60

$\boldsymbol{\xi}_{3N}$ The $3N$ element residual vector arising from the iterative solution of the discretised elastodynamic BIE with N elements, page 104

$\boldsymbol{\xi}_{4N}$ The $4N$ element residual vector arising from the iterative solution of the discretised coupled system of BIEs with N elements, page 139

ξ_{pre} Specified error tolerance in the preconditioner GMRES loop for the accuracy of the Green's function reconstructed from the fast multipole expansions. Defined as $\xi_{\text{pre}} = 0.15$, page 56

Subscripts

$_{ijklmqr}$ Subscripts $_{ij\ldots}$ denote the Cartesian components of a vector field at a point (for example the i^{th} components with $i = 1 : 3$). Particularly $_i$ is always used to denote row indices of vectors (i.e. $u_i(\mathbf{x}), t_i(\mathbf{x})$) and $_j$ for column indices of matrices (i.e. $U_{ij}(\mathbf{x}, \mathbf{y}), T_{ij}(\mathbf{x}, \mathbf{y})$), page 89

$_n$ The integer degree $n = 0, 1, 2, 3, ...$ used in the expansion coefficients of the spherical basis functions S_n^m, R_n^m, page 16

$_{ps}$ Subscripts $_p$ and $_s$ denote the compressional and shear waves respectively for the

wavenumbers, sound speeds, Green's functions, etc., page 90

Superscripts

$^{i\ \text{inc}}$ Superscript ^{i} and $^{\text{inc}}$ denote the incident field component of a variable, for example incident pressure p^i or displacement u_i^{inc}, page 10

^{m} The integer order $m = -n, -n+1, ..., n-1, n$ used in the expansion coefficients of the spherical basis functions S_n^m, R_n^m, page 16

$^{s\ \text{sca}}$ Superscript ^{s} and $^{\text{sca}}$ denote the scattered field component of a variable, for example scattered pressure p^s or displacement u_i^{sca}, page 10

$^{\text{T}}$ Superscript $^{\text{T}}$ denotes the transpose of a matrix. For example $U_{ij}^{\text{T}}(\mathbf{x}, \mathbf{y}) = U_{ji}(\mathbf{x}, \mathbf{y})$, page 89

Symbols

A_N list of N element areas for each element in the mesh, page 56

$A_{\tilde{n}}$ The area of the $\tilde{n}^{th}$ element of the discretised boundary surface, page 31

a_n^m Coefficient involving the degree and order which appear in the partial derivative relations for the multipole expansions, page 50

$\mathbf{Az} = \mathbf{b}$ The generic form of a matrix equation, where $\mathbf{A}$ is a matrix of coefficients, $\mathbf{z}$ is a vector of unknowns and $\mathbf{b}$ is a vector of knowns, page 13

b_n^m Coefficient involving the degree and order which appear in the partial derivative relations for the multipole expansions, page 50

$\mathbf{c}$ The expansion centre used to separate a Green's function into separate series expansions which can be independently calculated, page 14

c_f Denotes the sound speed of compressional waves in the fluid, page 142

E Denotes the Young's modulus of the elastic solid, page 142

$\mathbf{c}_l$ The set of box centres for all occupied boxes on the l^{th} level of the octree, page 57

c_p, c_s Denotes the sound speeds of the compressional c_p and shear c_s waves respectively in the elastic solid, page 90

$\mathbf{c}_{\tilde{m}}$ The centre of the $\tilde{m}^{th}$ octree box on the lowest octree level, page 31

$E_{\tilde{n}}$ The $\tilde{n}^{th}$ triangular element E of a boundary surface mesh consisting of N elements, page 11

$f(\mathbf{x}), g(\mathbf{x})$ Arbitrary known surface functions for defining BCs in the Helmholtz BIE, page 10

$F_n^m(\mathbf{r})$ Notation for representing either type of expansion $F = S, R$ in the partial derivative relations of the multipole expansions, page 50

$G(\mathbf{x}, \mathbf{y})$ The free–space Green's function or fundamental solution to the Helmholtz equation. Defined as $G(\mathbf{x}, \mathbf{y}) = \frac{e^{ikr}}{4\pi r}$ with $r = |\mathbf{x} - \mathbf{y}|$, page 10

$G_p(\mathbf{x}, \mathbf{y})$ $G_s(\mathbf{x}, \mathbf{y})$ The free–space Green's function or fundamental solution to the Helmholtz equation $G(\mathbf{x}, \mathbf{y})$ for the compressional and shear wavenumbers (k_p and k_s) respectively, page 90

$h_n(kr)$ The spherical Hankel function of the first kind of degree n and argument kr, page 16

i The complex number. Defined as $i = \sqrt{-1}$, page 10

$\mathbf{I}_{3N}$ The identity matrix of size $3N \times 3N$ for $3N$ unknowns, page 100

$\mathbf{I}_N$ The identity matrix of size $N \times N$ for N unknowns, page 59

$[\hat{\text{its}}, \hat{\text{its}}_{\text{pre}}]$ The maximum number of iterations for the main and preconditioner GMRES loops. These maxima are proportional to both the wavenumber of the problem and

the complexity of the boundary surface. Typical values $\approx [50 < \hat{\text{its}} < 400, 30 < \hat{\text{its}}_{\text{pre}} < 100]$, page 57

$j_n(kr)$ The spherical Bessel function of the first kind of degree n and argument kr, page 16

k The non–complex wavenumber (units: m^{-1}). Defined as $k = \frac{2\pi}{\lambda}$, page 10

k_p, k_s Denotes the wavenumbers of the compressional k_p and shear k_s waves respectively in the elastic solid, page 90

l Denotes the l^{th} level of the octree structure, page 22

$L(\mathbf{x}, \mathbf{y})$ The surface integral of the Green's function. Defined as $L(\mathbf{x}, \mathbf{y}) = \int_S G(\mathbf{x}, \mathbf{y})\, dS(\mathbf{x})$, page 48

$L'(\mathbf{x}, \mathbf{y})$ The surface integral of the normal derivative of the Green's function at $\mathbf{y}$. Defined as $L'(\mathbf{x}, \mathbf{y}) = \int_S \frac{\partial G(\mathbf{x}, \mathbf{y})}{\partial \mathbf{n}(\mathbf{y})}\, dS(\mathbf{x})$, page 48

$\mathbf{L}_{\text{ff}}$ Denotes the far field part of the $(L(\mathbf{x}, \mathbf{y}) + \alpha L'(\mathbf{x}, \mathbf{y}))h(\mathbf{x})$ surface integrals resulting from the FMM procedure for an arbitrary set of source strengths $h(\mathbf{x})$ defined at the source points $\mathbf{x}$, page 59

$\hat{l}$ Denotes the maximum octree level (i.e. lowest level) l as $\hat{l}$. The set of octree levels then has the range $\hat{l} : 2$, page 57

$(\mathbf{LM})_{\text{pre}}$ The sparse approximate inverse preconditioner constructed from the sparse near field matrices $\mathbf{L}_{\text{nf}}$ and $\mathbf{M}_{\text{nf}}$, page 58

$\mathbf{L}_N$ Defined as $\mathbf{L}_N = \left[L(\mathbf{x}_N, \mathbf{y}_N) + \alpha L'(\mathbf{x}_N, \mathbf{y}_N)\right]$ for the sets of source and receiver points $\mathbf{x}_N$ and $\mathbf{y}_N$ coincident at the centre of each element. Has dimensions of $N \times N$, page 59

$\mathbf{L}_{\text{nf}}$ The sparse near field matrix containing the regular, near–singular and singular integrals of $(L(\mathbf{x}, \mathbf{y}) + \alpha L'(\mathbf{x}, \mathbf{y}))$ for the sets of source elements containing $\mathbf{x}$ which are not well–separated from each of the receiver elements containing $\mathbf{y}$, page 58

$M(\mathbf{x}, \mathbf{y})$ The surface integral of the normal derivative of the Green's function at $\mathbf{x}$. Defined as $M(\mathbf{x}, \mathbf{y}) = \int_S \frac{\partial G(\mathbf{x}, \mathbf{y})}{\partial \mathbf{n}(\mathbf{x})}\, dS(\mathbf{x})$, page 48

$M'(\mathbf{x}, \mathbf{y})$ The surface integral of the normal derivative of the Green's function at both $\mathbf{x}$ and $\mathbf{y}$. Defined as $M'(\mathbf{x}, \mathbf{y}) = \int_S \frac{\partial^2 G(\mathbf{x}, \mathbf{y})}{\partial \mathbf{n}(\mathbf{x}) \partial \mathbf{n}(\mathbf{y})}\, dS(\mathbf{x})$, page 48

$\mathbf{M}_{\text{ff}}$ Denotes the far field part of the $(M(\mathbf{x}, \mathbf{y}) + \alpha M'(\mathbf{x}, \mathbf{y}))h(\mathbf{x})$ surface integrals resulting from the FMM procedure for an arbitrary set of source strengths $h(\mathbf{x})$ defined at the source points $\mathbf{x}$, page 59

$\mathbf{M}_N$ Defined as $\mathbf{M}_N = \left[M(\mathbf{x}_N, \mathbf{y}_N) + \alpha M'(\mathbf{x}_N, \mathbf{y}_N)\right]$ for the sets of source and receiver points $\mathbf{x}_N$ and $\mathbf{y}_N$ coincident at the centre of each element. Has dimensions of $N \times N$, page 59

$\mathbf{M}_{\text{nf}}$ The sparse near field matrix containing the regular, near–singular and singular integrals of $(M(\mathbf{x}, \mathbf{y}) + \alpha M'(\mathbf{x}, \mathbf{y}))$ for the sets of source elements containing $\mathbf{x}$ which are not well–separated from each of the receiver elements containing $\mathbf{y}$, page 58

$\tilde{m}$, $_{\tilde{m}}$ An index counter that denotes the $\tilde{m}^{th}$ octree box of the set of M occupied octree boxes, page 31

$\mathbf{N}$ A list of $N \times 3$ node numbers (the row numbers in $\mathbf{P}$) which specify which of the nodes define each of the N elements in a mesh, page 57

$\mathbf{n}(\mathbf{x})$ The normal vector directed outward from a point $\mathbf{x}$ on a finite enclosed boundary surface. $n_k(\mathbf{x})$ denotes the k^{th} Cartesian component of the normal vector at $\mathbf{x}$, page 10

N The number of elements in the discretised boundary surface mesh, page 11

$\tilde{n}$, $_{\tilde{n}}$ An index counter that denotes the $\tilde{n}^{th}$ element of a boundary element mesh consisting of N elements, page 11

$O(\ )$ Indicates the time or memory complexity of an algorithm, for example $O(N)$ denotes a time/memory complexity proportional to the number of unknowns N, page 4

$\mathbf{P}$ A list of $P \times 3$ Cartesian xyz components for P nodal points that define the elements in a mesh, page 57

$p(\mathbf{x})$ The total acoustic pressure at a point $\mathbf{x}$ (units: N/m^2). Defined as $p(\mathbf{x}) = p^i(\mathbf{x}) + p^s(\mathbf{x})$, page 10

p, p_l The truncation number for a multipole expansion on any level (p) or the l^{th} level p_l of the octree structure. Truncating a multipole expansion at a degree $n = p - 1$ yields p^2 (n, m) coefficients, page 25

$p^i(\mathbf{x})$ The incident acoustic field at a point $\mathbf{x}$ (units: N/m^2), page 10

$\mathbf{p}^i$ Combined incident field for the BM BIE on a discretised boundary surface. Defined as $\mathbf{p}^i = \left[p^i(\mathbf{y}_N) + \alpha q^i(\mathbf{y}_N)\right]$ for the set of receiver points $\mathbf{y}_N$, page 60

$P_n^m(\cos\theta)$ The associated Legendre function, page 16

$p^s(\mathbf{x})$ The scattered acoustic field at a point $\mathbf{x}$ (units: N/m^2), page 10

$q(\mathbf{x})$ The outward–pointing normal derivative of the surface pressure at $\mathbf{x}$. Defined as $q(\mathbf{x}) = \frac{\partial p(\mathbf{x})}{\partial \mathbf{n}(\mathbf{x})}$, page 10

$q^i(\mathbf{x})$ The normal derivative at $\mathbf{x}$ of the incident acoustic field, page 48

r The magnitude of the vector between two points. For example $r = |\mathbf{x} - \mathbf{y}|$, page 10

$R_n^m(\mathbf{r})$ The regular R multipole series expansion, or spherical basis function, for integer degree $n = 0, 1, 2, 3, ...$, order $m = -n, -n+1, ..., n-1, n$ and expansion vector $\mathbf{r}$, page 16

$R|R(\mathbf{t})$ The regular–to–regular translation method, used to translate multipole expansions from parent to children box centres in the downward pass of the FMM algorithm, page 18

$S|R(\mathbf{t})$ The singular–to–regular translation method, used to translate well–separated source expansions to a local receiver group across octree levels in the downward pass of the FMM algorithm, page 18

$S|S(\mathbf{t})$ The singular–to–singular translation method, used to translate multipole expansions from children to parent box centres in the upward pass of the FMM algorithm, page 18

S An arbitrary finite enclosed boundary surface occupying a three–dimensional region of space, page 10

s_{av} Average side length of elements in the boundary mesh, page 54

$S_n^m(\mathbf{r})$ The singular S multipole series expansion, or spherical basis function, for integer degree $n = 0, 1, 2, 3, ...$, order $m = -n, -n+1, ..., n-1, n$ and expansion vector $\mathbf{r}$, page 16

$\mathbf{T}_{\text{ff}}$ Denotes the far field part of the $\int_S T_{ij}^{\text{T}}(\mathbf{x}, \mathbf{y}) h_i(\mathbf{x}) dS(\mathbf{x})$ surface integrals resulting from the FMM procedure where $h_i(\mathbf{x})$ denotes the i^{th} Cartesian components of the set of source strengths defined at the source points $\mathbf{x}$, page 103

$t_i(\mathbf{x})$ The i^{th} Cartesian component of the 3×1 total surface stress vector at $\mathbf{x}$ (units: N/m^2). Defined as $t_i(\mathbf{x}) = t_i^{\text{inc}}(\mathbf{x}) + t_i^{\text{sca}}(\mathbf{x})$, page 89

$t_i^{\text{inc}}(\mathbf{x})$ The i^{th} Cartesian component of the 3×1 incident traction vector at $\mathbf{x}$ (units: N/m^2), page 89

$T_{ij}(\mathbf{x}, \mathbf{y})$ The traction, or surface stress, fundamental solution of the elastodynamic BIE, page 89

$(\mathbf{TM})_{\text{pre}}$ The block diagonal sparse approximate inverse preconditioner for the dual FMBEM

model for acoustic coupled FSI problems. Constructed from the sparse near field matrices $\mathbf{U}_{\text{nf}}$ and $\mathbf{T}_{\text{nf}}$ and the scaling factors Ψ and Ω, page 138

$\mathbf{T}_{3N}$ Defined as $\mathbf{T}_{3N} = \int_S T_{ij}^{\text{T}}(\mathbf{x}_N, \mathbf{y}_N) dS(\mathbf{x}_N)$ for the sets of source and receiver points $\mathbf{x}_N$ and $\mathbf{y}_N$ coincident at the centre of each element. Has dimensions of $3N \times 3N$, page 100

$\mathbf{T}_{\text{nf}}$ The sparse near field matrix containing the regular, near–singular and singular integrals of the form $\int_S T_{ij}^{\text{T}}(\mathbf{x}, \mathbf{y}) h_i(\mathbf{x}) dS(\mathbf{x})$ with source strengths $h_i(\mathbf{x})$ for the sets of source elements containing $\mathbf{x}$ which are not well–separated from each of the receiver elements containing $\mathbf{y}$, page 101

$\mathbf{U}_{\text{ff}}$ Denotes the far field part of the $\int_S U_{ij}^{\text{T}}(\mathbf{x}, \mathbf{y}) h_i(\mathbf{x}) dS(\mathbf{x})$ surface integrals resulting from the FMM procedure where $h_i(\mathbf{x})$ denotes the i^{th} Cartesian components of the set of source strengths defined at the source points $\mathbf{x}$, page 103

$u_i(\mathbf{x})$ The i^{th} Cartesian component of the 3×1 total displacement vector at $\mathbf{x}$ (units: m). Defined as $u_i(\mathbf{x}) = u_i^{\text{inc}}(\mathbf{x}) + u_i^{\text{sca}}(\mathbf{x})$, page 89

$u_i^{\text{inc}}(\mathbf{y})$ The i^{th} Cartesian component of the 3×1 incident displacement vector at $\mathbf{x}$ (units: m), page 89

$U_{ij}(\mathbf{x}, \mathbf{y})$ The displacement fundamental solution of the elastodynamic BIE, page 89

$u_i^{\text{sca}}(\mathbf{x})$ The i^{th} Cartesian component of the 3×1 scattered displacement vector at $\mathbf{x}$ (units: m), page 89

$\mathbf{U}_{3N}$ Defined as $\mathbf{U}_{3N} = \int_S U_{ij}^{\text{T}}(\mathbf{x}_N, \mathbf{y}_N) dS(\mathbf{x}_N)$ for the sets of source and receiver points $\mathbf{x}_N$ and $\mathbf{y}_N$ coincident at the centre of each element. Has dimensions of $3N \times 3N$, page 100

$\mathbf{U}_{\text{nf}}$ The sparse near field matrix containing the regular, near–singular and singular integrals of the form $\int_S U_{ij}^{\text{T}}(\mathbf{x}, \mathbf{y}) h_i(\mathbf{x}) dS(\mathbf{x})$ with source strengths $h_i(\mathbf{x})$ for the sets of source elements containing $\mathbf{x}$ which are not well–separated from each of the receiver elements containing $\mathbf{y}$, page 101

$(\mathbf{UT})_{\text{pre}}$ The sparse approximate inverse preconditioner constructed from the sparse near field matrices $\mathbf{U}_{\text{nf}}$ and $\mathbf{T}_{\text{nf}}$, page 101

$\mathbf{x}$ An arbitrary source location on S. For a discretised surface the value of the unknown field at $\mathbf{x}$ will be used for evaluating the integral over the element containing $\mathbf{x}$, page 10

$\mathbf{x}_{3l}$ The bit–interleaved binary numbers for the source points $\mathbf{x}_N$. Default $l = 21$ (63 bits) for later truncation depending on the number of levels required in the octree structure, page 57

$\mathbf{x}_N$ list of Cartesian xyz components for N source positions (i.e. an $N \times 3$ matrix), one for each of the N elements in the mesh. $\mathbf{x}_N = \mathbf{y}_N$ for the collocation method, page 57

$\mathbf{x}_{\tilde{n}}$ The source point at the centre of the $\tilde{n}^{th}$ element $E_{\tilde{n}}$, page 11

$\mathbf{y}$ An arbitrary receiver location on S at which the unknown field is being evaluated, page 10

$\mathbf{y}_N$ list of Cartesian xyz components for N receiver positions (i.e. an $N \times 3$ matrix), one for each of the N elements in the mesh. $\mathbf{x}_N = \mathbf{y}_N$ for the collocation method, page 57

$Y_n^m(\theta, \phi)$ The spherical harmonic function, page 16

$\mathbf{0}_N$ An N element vector of zeros. Used as the initial guess of the solution to the Helmholtz BIE in the GMRES iterative solution, page 60

$\mathbf{0}_{3N}$ A $3N$ element vector of zeros. Used as the initial guess of the solution to the elastodynamic BIE in the GMRES iterative solution, page 104

$\mathbf{0}_{4N}$ A $4N$ element vector of zeros. Used as the initial guess of the solution to the coupled system of BIEs in the GMRES iterative solution, page 139

Mathematical and Set Operators

$|\ldots|$ Denotes the absolute value of a variable, i.e. $r = |\mathbf{x} - \mathbf{y}| = \sqrt{\sum_{j=1}^{3}(x_j - y_j)^2}$ for points $\mathbf{x} = x_j$ and $\mathbf{y} = y_j$ for $j = 1:3$, or $|a + ib| = \sqrt{a^2 + b^2}$ for complex numbers of the form $a + ib$, page 10

$\{\,\}_{\mathrm{c}}$ Denotes a children search operation of the octree which returns the same data type as the input. For example $\{\mathbf{c}_l\}_c$ returns the set of children boxes on level $l + 1$ of the set of boxes with box centres $\mathbf{c}_l$ on level l, page 58

$\{\,\}_{\mathbf{c}_l}$ Denotes the summations of all multipole expansions on octree level l into sets which share common expansion centres described by $\mathbf{c}_l$, page 59

$\big[\,\big]_{E_{\tilde{n}}}$ Denotes the integral over the $\tilde{n}^{th}$ plane triangle element $E_{\tilde{n}}$. For example $\big[L(\mathbf{x},\mathbf{y})q(\mathbf{x})\big]_{E_{\tilde{n}}} = \Big(\int_{E_{\tilde{n}}} G(\mathbf{x},\mathbf{y})dE_{\tilde{n}}(\mathbf{x})\Big)\, q(\mathbf{x}_{\tilde{n}})$, page 51

$\big[\,\big]_{\mathbf{n}(\mathbf{x})}, \big[\,\big]_{\mathbf{n}(\mathbf{y})}$ Denotes the normal derivative at $\mathbf{x}$ or $\mathbf{y}$ of a multipole expansion. For example $\big[F_n^m(\mathbf{r})\big]_{\mathbf{n}(\mathbf{x})}$, page 51

$\big[\,\big]_{g0}, \big[\,\big]_{0g}$ Denotes the first–order partial derivative of the Green's function with respect to the g^{th} Cartesian component at either $\mathbf{x}$: $\big[G\big]_{g0} = \frac{\partial G(\mathbf{x},\mathbf{y})}{\partial \mathbf{x}_g}$ or $\mathbf{y}$: $\big[G\big]_{0g} = \frac{\partial G(\mathbf{x},\mathbf{y})}{\partial \mathbf{y}_g}$. For the spherical basis functions the first partial derivatives are always applied at the end point of the expansion vector, i.e. $\big[F_n^m(\mathbf{c}-\mathbf{x})\big]_g = \frac{\partial F_n^m(\mathbf{c}-\mathbf{x})}{\partial \mathbf{c}_g}$, page 92

$\big[\,\big]_{ij}$ Denotes the second–order partial derivative of a function with respect to the i^{th} and j^{th} Cartesian components. For the Helmholtz Green's function the i and j partial derivatives are applied at points $\mathbf{x}$ and $\mathbf{y}$ respectively, i.e. $\big[G\big]_{ij} = \frac{\partial^2 G(\mathbf{x},\mathbf{y})}{\partial \mathbf{x}_i \partial \mathbf{y}_j}$, while for spherical basis functions they are applied at the end point of the expansion vector, i.e. $\big[F_n^m(\mathbf{c}-\mathbf{x})\big]_{ij} = \frac{\partial^2 F_n^m(\mathbf{c}-\mathbf{x})}{\partial \mathbf{c}_i \partial \mathbf{c}_j}$, page 91

$\big[\,\big]_{ghi}$ Denotes the third–order partial derivative of the Green's function with respect to the g^{th} and h^{th} Cartesian components at $\mathbf{x}$ and i^{th} component at $\mathbf{y}$: $\big[G\big]_{ghi} = \frac{\partial^3 G(\mathbf{x},\mathbf{y})}{\partial \mathbf{x}_g \partial \mathbf{x}_h \partial \mathbf{y}_i}$, page 92

mean( ) Denotes the mean of the enclosed variable, page 138

$\{\,\}_{\mathrm{n}}$ Denotes a neighbour search operation of the octree which returns the same data type as the input. For example $\{\mathbf{c}_l\}_n$ returns the sets of neighbour box centres for each box in the set of box centres $\mathbf{c}_l$, while $\{\mathbf{x}_n\}_n$ returns the set of source points contained with the neighbouring boxes of the box containing source point $\mathbf{x}_n$, page 58

$\{\,\}_{\mathrm{ns}}$ Denotes the search operation of a set of Green's function integrals to find those which are near–singular integrals i.e. $\mathbf{x}$ and $\mathbf{y}$ in $G(\mathbf{x},\mathbf{y})$ are spatially close but no coincident, page 58

$\overline{}$ An overline denotes the complex conjugate, page 59

$\{\,\}_{\mathrm{p}}$ Denotes a parent search operation of the octree which returns the same data type as the input. For example $\{\mathbf{c}_l\}_p$ returns the set of parent box centres on level $l - 1$ of the set of boxes with box centres $\mathbf{c}_l$ on level l, page 58

$\{\,\}_{\mathrm{r}}$ Denotes the search operation of a set of Green's function integrals to find those which are regular integrals i.e. $\mathbf{x}$ and $\mathbf{y}$ are well–separated in $G(\mathbf{x},\mathbf{y})$, page 58

$\setminus$ Denotes the relative complement between two sets, for example $B \setminus A$ returns the elements of the set B which are not in A, page 58

$\{\,\}_{\mathrm{s}}$ Denotes the search operation of a set of Green's function integrals to find those

which are singular integrals i.e. $\mathbf{x} = \mathbf{y}$ in $G(\mathbf{x}, \mathbf{y})$, page 58

; Denotes vertical concatenation of column vectors in the pseudocode algorithms, for example $[\mathbf{0}_{3N}; \mathbf{0}_N] = \mathbf{0}_{4N}$, page 139

Acronyms and Definitions

3D Three dimensional, page 2

anterpolation Describes the process of resampling a multipole expansion to a smaller set of degree/order coefficients to reduce the length of the truncated multiple expansion. Anterpolation is used in the $R|R$ translations of the downward pass., page 26

BC Boundary condition, page 10

BEM Boundary element method, page 3

BIE Boundary integral equation, page 3

BM Burton–Miller, page 49

FEM Finite element method, page 2

FMBEM Fast multipole boundary element method, page 4

FMM Fast multipole method, page 4

FSI Fluid–structure interaction, page 1

GB Gigabyte, page 73

GFSC Generalised fluid structure coupling, page 151

interpolation Describes the process of resampling a multipole expansion to a larger set of degree/order coefficients to increase the length of the truncated multiple expansion. Interpolation is used in the $S|S$ translations of the upward pass., page 26

MB Megabyte, page 76

RCR Rotation, coaxial translation, rotation, page 4

r.e. norm The relative error norm, which is used here to provide a measure of the error between two solution vectors (i.e. between a FMBEM solution and the analytic solution). For example, the r.e. norm $= \frac{\text{norm}(\mathbf{s}_N - \mathbf{s}_N^{\text{ana}})}{\text{norm}(\mathbf{s}_N^{\text{ana}})}$ for the FMBEM solution $\mathbf{s}_N$ and the analytic solution $\mathbf{s}_N^{\text{ana}}$, page 73

r.r. norm The relative residual norm, which is used here to provide a measure of the residual between the iterative solution vector and the known right–hand side vector in a matrix equation of the form $\mathbf{Az} = \mathbf{b}$. For example, r.r. norm $= \frac{\text{norm}(\mathbf{Az} - \mathbf{b})}{\text{norm}(\mathbf{b})}$, page 13

rhs right hand side, page 13

SAI Sparse approximate inverse, page 56

TS Target Strength, page 81

1

Introduction

1.1 Overview

The focus of this thesis is the frequency domain numerical modelling of underwater acoustic scattering problems involving coupled fluid–structure interactions (FSI). The general problem scenario involves an acoustic field in the fluid medium impinging upon a submerged elastic solid structure and subsequently scattering sound in a coupled interaction between the exterior and interior acoustic fields in the fluid and elastic solid domains respectively (see Fig. 1.1). The numerical evaluation of sound scattering from underwater objects of an arbitrary shape is of interest for a wide range of applications, with many commercial and academic codes developed to model such problems.

A number of numerical techniques have been developed for modelling sound radiation and scattering in both fluid and elastic solid media. Solid elastic structures are typically modelled using the finite element method (FEM), where the appropriate differential equation and boundary conditions for the elastic solid are suitably recast into integral forms over the domain's volume and surface respectively [1]. The volume integral can then be numerically implemented within the three–dimensional (3D) interior of the object by discretising the space into small volume elements whose dimensions are related to the wavelength of the problem. The unknown displacements and stresses at each of the vertices or 'nodes' defining the elements may be constructed into a global matrix equation and solved with the proper application of the boundary conditions [2]. The resulting matrix is sparse, symmetric and real–valued, making it ideal for numerical solution via many of the common iterative solvers available in the

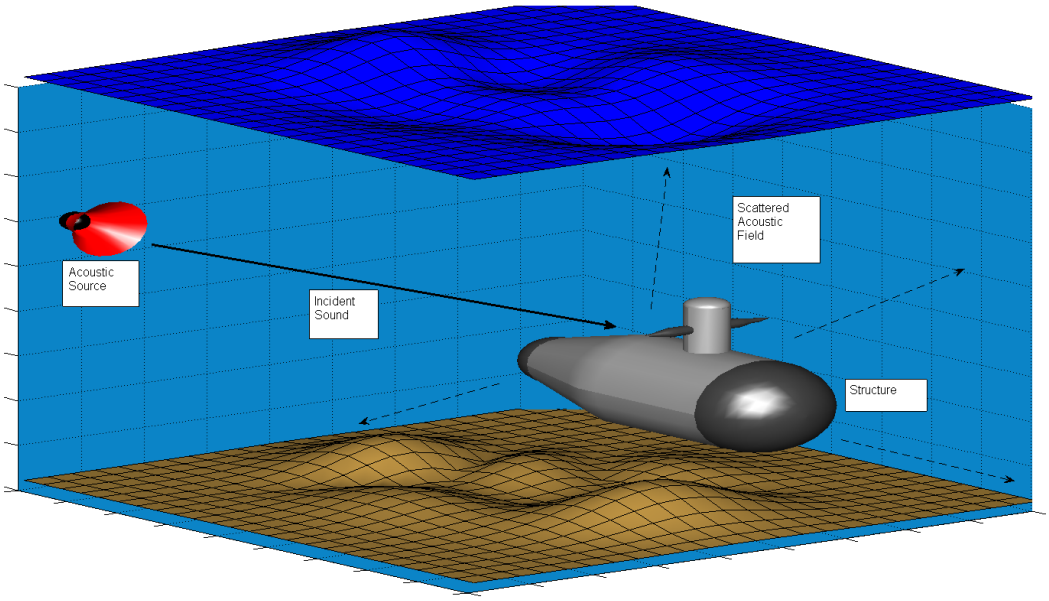

Figure 1.1: Sound scattering from a submerged object.

literature [3]. The discretisation of 3D space imposes a practical upper limit on the problem size that the FEM can feasibly solve as a certain number of elements per wavelength are required to yield an acceptable accuracy in the numerical solution [4], and so the number of finite elements increases as the third power of the frequency for 3D models. A principal advantage of using the FEM to model the interior structure is that the material properties are locally defined for each element, allowing complex internal structures to be modelled [5].

The infinite exterior fluid surrounding an object is typically modelled using the boundary element method (BEM). For acoustic waves propagating in a fluid domain the governing differential equation (the Helmholtz equation) is re–expressed as an integral equation in which all terms are restricted to the domain boundary [6]. This is achieved by choosing trial functions (i.e. fundamental solutions of the differential equation) which automatically satisfy the differential equation everywhere in the domain [7]. The resulting boundary integral equation (BIE) may then be numerically discretised (again proportional to the wavelength [8]) on the domain surface to yield a solvable matrix equation. The coefficients of the BEM matrix equation resulting from the BIE discretisation via the collocation method are non-symmetric, fully populated

and complex valued [9] but far fewer unknowns are involved compared to the volume discretisation of the FEM. The principal advantages of the BEM are that the dimensionality of the problem is reduced by one due to the discretisation being limited to the boundary surface, while infinite exterior domains may be modelled by the BEM with no additional complexity or increase to the problem size [10].

For acoustic coupled FSI problems which involve the interaction of sound between the fluid and solid media, a popular approach is to combine the boundary element and finite element methods to utilise the strengths of both methods i.e. the BEM is used to model the infinite exterior fluid domain and the FEM to model the interior solid domain. In this case the BEM and FEM discretisations share the common boundary surface of the object and coupling boundary conditions may be applied at the interface to model the interaction between the exterior and interior fields [11]. The discretisations for the BEM and FEM meshes may be either conforming, and so the element coupling is applied on a one–to–one basis [12], or non–conforming, where different discretisations are used in the fluid and solid domains which are then related via a coupling matrix (see Ref. [13] and references therein for details on constructing coupling matrices). The use of non–conforming meshes has obvious advantages in reducing the total number of elements when treating media with significantly different sound speeds (i.e. where one mesh may have a coarser discretisation). In any case applying the coupling boundary conditions between the fluid/solid media at the interface will allow the number of unknown quantities at the boundary to be reduced to two — the coupled pressure and displacement — and the system of FEM and BEM equations may be simultaneously solved for both unknowns. Alternatively the coupled system may be reduced to one unknown by substituting either the fluid impedance matrix into the structural FEM, yielding the displacement, or the FEM structural equations into the BEM matrix equation, yielding the pressure [14]. The acoustic coupled FSI between the FEM and BEM models may also be represented via a modal interaction model [15], where the uncoupled rigid modes from the BEM model are analytically coupled to the in–vacuo structural modes [16]. This allows for a substantial reduction in the solution time as the coupled interaction deals with the reduced systems of BEM acoustic transfer vectors and the modal eigenvectors of the structure [17], instead of the full BEM and FEM matrices.

FEM–BEM modelling is still restricted to relatively small problem sizes as both methods require the full coefficient matrices to be built: being a large sparsely popu-

lated matrix in the case of the FEM and a smaller fully populated matrix for the BEM. An iterative solution requires these coefficient matrices to be repeatedly multiplied with the solution vector of unknowns, at a cost of N^2 operations for N surface unknowns in the case of the full BEM matrix [18] and a cost of the order of $O(bM)$ operations for M volume unknowns in a sparse FEM matrix with a matrix 'bandwidth' b [19, 20]. The fast multipole method (FMM), first introduced by Greengard & Rokhlin in 1987 [21], can both reduce the BEM memory requirement and expedite the BEM calculation time by determining the result of the matrix–vector multiplications without needing to explicitly form the full coefficient matrix, and by calculating interactions between groups of elements [22] instead of the pair–wise interactions as with the conventional BEM. The FMM has been successfully applied to both the Helmholtz [23] and elastodynamic [24] BIEs for modelling acoustic and elastic solid domains respectively. Depending on the frequency range of interest and particular implementation used, the FMM can reduce the algorithmic complexity of the BEM matrix–vector product to $O(N\log N)$ operations in both the Helmholtz [25] and elastodynamic [26] BIEs.

1.1.1 Original Contributions of this Thesis

This thesis presents the following contributions to the field of numerical modelling of acoustic coupled FSI problems:

A dual FMBEM for acoustic coupled fluid–structure interactions. A numerical model has been developed for acoustic coupled FSI problems in the frequency domain where both the fluid and elastic solid domains are treated with the fast multipole boundary element method (FMBEM). This dual FMBEM approach restricts all unknowns to the shared boundary surface and allows the fast multipole method to accelerate the BEM calculations in both domains. The FMBEM models developed for both the fluid and elastic solid domains are based on the low frequency multipole expansion of the Helmholtz fundamental solution, and use the rotation, co–axial translation, rotation (RCR) translation method and octree translation stencils to minimise both the cost and the number of multipole translations that must be applied in each FMBEM model. Conforming boundary meshes which employ the same boundary surface discretisations are used for both the fluid and solid domains, and boundary conditions are directly applied between coincident unknowns via a one–to–one element coupling on the shared boundary surface to yield a coupled system of boundary integral equations

(BIEs). This system of BIEs is simultaneously solved for the total surface pressure and displacement via an iterative inner–outer fGMRES solution, where for each outer loop iteration a low accuracy FMBEM is first solved to a coarse residual tolerance in the inner loop and then used as a preconditioned solution for the current outer loop iteration, which is calculated with the full accuracy FMBEM and is solved to fine residual tolerance. Additionally the inner FMBEM is itself preconditioned using a diagonal scaling and sparse approximate inverse preconditioner to reduce the number of inner GMRES iterations required for solution convergence. The dual FMBEM model for acoustic coupled FSI problems has been developed in MATLAB and tested on a number of problems involving the coupling of a single exterior fluid and single interior solid region (i.e. solid objects). Comparisons of the dual FMBEM numerical results with those from a conventional FEM–BEM model indicate that the dual FMBEM model is able to solve acoustic coupled FSI problems to a similar accuracy while having significantly reduced computational and memory requirements. Algorithmic complexity results for the dual FMBEM are also presented and are shown to be in good agreement with the theoretical estimates for the FMM. The dual FMBEM model thus allows very large problem sizes to be treated: numerical models involving 10^5–10^6 unknowns have been solved in several hours on a current generation workstation computer.

Development of an efficient low frequency elastodynamic FMBEM. Ancillary to the principal focus of the thesis (being the development of a dual FMBEM model), the FMBEM models for the both the Helmholtz and elastodynamic BIEs were first developed and tested to ensure their accuracy and performance before utilising them in the coupled FMBEM model. The type of fast multipole expansions used here are stable in the 'low frequency' regime (a relative term referring to the number of wavelengths across the object) but become computationally untenable at higher frequencies, while other types of expansion are available at high frequencies but are unstable in the low frequency range. Thus far only two papers in the published literature for the elastodynamic FMBEM have used the low frequency multipole expansions and translations, with one of those papers using the original forms of the multipole expansions developed in the late 1980s which are known to have a prohibitive computational expense and are now considered obsolete. Superior low frequency translation methods have been developed more recently for the Helmholtz equation and these methods have been incorporated into the elastodynamic FMBEM developed in this thesis work. Additionally,

the use of translation stencils allows the total number of multipole translations which must be applied in the low frequency FMM to be reduced by up to 60%. As such the present low frequency elastodynamic FMBEM appears to be one of only two models in the published literature to use the more advanced low algorithmic complexity FMM translation methods, and the only elastodynamic FMBEM model to incorporate translation stencils. Algorithmic complexity results for the low frequency elastodynamic FMBEM are also presented for what appears to be the first time in the literature.

1.1.2 Comparative Numerical Results

Throughout this thesis various numerical results have been presented from PACSYS' PAFEC FEM/BEM software suite [27] to indicate the expected performance of the equivalent BEM or coupled FEM–BEM models. These results should not be construed to represent the 'best' possible performance from the PAFEC software, as there are many features available in the software (such as utilising planes of symmetry, higher–order finite elements and dissimilar fluid/structural meshes) which will likely increase the solution speeds of the FEM/BEM models by reducing the total number of unknowns in the problem. However utilising these features in the PAFEC models would not allow for a direct comparison of the different numerical models for similar problem sizes and so would detract from the purpose of the numerical comparisons.

1.2 Organisation

The thesis is organised into the following chapters:

- Chapter 2.
  Chapter 2 presents the main details of the FMM implementation used in this thesis for the FMBEM modelling of both the fluid and elastic solid domains. The main mechanisms of the FMM — the multipole expansion and translation methods, octree structure and the fast matrix–vector product calculations via the FMM procedure — among other details are discussed, with the Helmholtz BIE used as an example integral equation to present specifics of the numerical implementation. The main steps of the FMM are the same for both the elastodynamic and Helmholtz BIEs and so only the pertinent details of those FMM implementations are discussed in the later chapters.

- Chapter 3.

  This chapter presents the Helmholtz FMBEM developed for the coupled FSI model. The chapter begins with a literature review of the FMM for the Helmholtz BIE and then presents the particular Helmholtz FMBEM implemented as part of this thesis work, including details of the multipole expansions required to propagate the Burton–Miller integral terms through the FMM and pseudo–algorithms for the set up and iterative fGMRES solution of the problem. The implementation of the translation stencils used to reduce the total number of multipole translations that must be applied in the FMM is also presented here. The chapter is concluded with an analysis of the performance and algorithmic complexity of the developed Helmholtz FMBEM, where numerical examples from the developed code are compared to analytic solutions and/or standard BEM results.

- Chapter 4.

  The elastodynamic FMBEM developed for the dual FMBEM model is presented in Chapter 4. Analogous to Chapter 3, this chapter begins with a literature review of the FMM for the elastodynamic BIE followed by a description of the developed elastodynamic FMBEM, again with a focus on the multipole expansions required to propagate the elastodynamic BIE terms through the FMM and relevant pseudo–algorithms for the set up and iterative solution of the problem. An analysis of the performance and algorithmic complexity of the elastodynamic FMBEM and a comparison of numerical results to both analytic solutions and other elastodynamic BEM/FMBEM models concludes the chapter.

- Chapter 5.

  Chapter 5 presents the dual FMBEM model for acoustic coupled fluid–structure interaction problems developed as the principal focus of this thesis. The chapter begins with a review of the literature on dual BEM models for acoustic coupled FSI problems, as well as a review on the use of FMMs in coupled FSI modelling. Details of the coupling technique applied between the Helmholtz and elastodynamic FMBEM models are then presented, with particular attention paid to the preconditioning strategy employed to improve the iterative solution convergence of the coupled system of discretised BIEs. This is followed by an investigation of the stability of the dual FMBEM model near the eigenfrequencies of the coupled

acoustic FSI problem. Finally the performance and algorithmic complexity of the dual FMBEM model is presented via numerical results from the model which are compared to analytic and coupled FEM–BEM results.

- Chapter 6.
  This final chapter presents the conclusions and recommendations for further work.

2

Background Theory

This chapter presents the main mechanisms of the fast multipole algorithm used in the FMBEM models developed for this thesis. The succeeding chapters on the Helmholtz and elastodynamic FMBEMs focus on the specific implementations of the FMBEM for those BIEs, where the main details of the fast multipole algorithm which allow the fast computation of the BEM matrix–vector products (and corresponding reduction in memory requirements) remain unchanged. This chapter first presents a standard BEM implementation to demonstrate the discretisation and iterative solution of the corresponding matrix equation using a simplified Helmholtz BIE. The main mechanisms of the FMM are then discussed. Finally, the FMBEM implementation used in this thesis is presented for the same example BEM to demonstrate the method.

2.1 The Boundary Element Method

The BEM is a numerical method for discretising a BIE which relates unknown parameters specified over an arbitrary surface via integrals of functions over that surface. The Helmholtz BIE is introduced here to explain the BEM process and the application of the FMM to the BEM. Full details of the implementation of the Helmholtz FMBEM with numerical examples are presented in the next chapter.

The linear wave equation, which describes the propagation of sound in a fluid medium [28], may be represented in the frequency domain by the scalar Helmholtz partial differential equation [11]

$$\nabla^2 p(\mathbf{x}) + k^2 p(\mathbf{x}) = 0 \tag{2.1}$$

where the total acoustic pressure $p(\mathbf{x}) = p^i(\mathbf{x}) + p^s(\mathbf{x})$ is the sum of the incident p^i and scattered p^s field components, $k = \frac{2\pi}{\lambda}$ is the wavenumber and $\mathbf{x}$ is an arbitrary point in the fluid. An integral form of this equation may be derived by substituting the total pressure and the fundamental solution of the Helmholtz equation $G(\mathbf{x}, \mathbf{y})$ into Green's second identity, and then applying a limiting process to restrict all variables to the boundary surface [29]. The resulting Helmholtz BIE for exterior scattering problems is [30]

$$\frac{1}{2}p(\mathbf{y}) = \int_S \left(\frac{\partial G(\mathbf{x}, \mathbf{y})}{\partial \mathbf{n}(\mathbf{x})} p(\mathbf{x}) - G(\mathbf{x}, \mathbf{y}) q(\mathbf{x}) \right) dS(\mathbf{x}) + p^i(\mathbf{y}) \tag{2.2}$$

where p is now the total pressure on the surface, $q(\mathbf{x}) = \frac{\partial p(\mathbf{x})}{\partial \mathbf{n}(\mathbf{x})}$ is the outward–pointing normal derivative of the surface pressure and $\mathbf{x}$ and $\mathbf{y}$ are points on the boundary surface S (which is assumed to be locally smooth at $\mathbf{y}$). The fundamental solution, or Green's function, for the Helmholtz equation takes the form of a point source

$$G(\mathbf{x}, \mathbf{y}) = \frac{e^{ikr}}{4\pi r} \tag{2.3}$$

where r is the magnitude of the vector $\mathbf{r}$ between the location of the the receiver point $\mathbf{y}$ and the source point $\mathbf{x}$, $r = |\mathbf{x} - \mathbf{y}|$, and $i = \sqrt{-1}$ [31]. Throughout the thesis, an $e^{-i\omega t}$ time dependence is assumed. Eq. 2.2 may be directly solved for exterior acoustic scattering problems involving simple boundary conditions (BCs), i.e. of the:

$$\begin{aligned} \text{Dirichlet} \qquad & p(\mathbf{x}) = f(\mathbf{x})\,, \\ \text{Neumann} \qquad & q(\mathbf{x}) = f(\mathbf{x})\,, \text{ or} \\ \text{Robin} \qquad & q(\mathbf{x}) + g(\mathbf{x}) p(\mathbf{x}) = f(\mathbf{x}) \end{aligned}$$

type [32], where f and g are known surface functions and $\mathbf{x}$ is restricted to S. Applying any one of these conditions will reduce the number of unknowns (p, q) in Eq. 2.2 to one, yielding an exactly solvable problem.

2.1.1 BEM Discretisation

In this section the numerical BEM discretisation for the exterior Helmholtz BIE defined on an arbitrary boundary surface S is considered. Assuming a 'sound–soft' Dirichlet B.C. ($\forall \mathbf{x} \in S : p(\mathbf{x}) = 0$), Eq. 2.2 is reduced to a solvable equation with one unknown

$$\int_S G(\mathbf{x}, \mathbf{y}) q(\mathbf{x}) dS(\mathbf{x}) = p^i(\mathbf{y}) \tag{2.4}$$

where $p^i(\mathbf{y})$ remains in the above equation due to the applied B.C. relating to the *total* pressure on S. Eq. 2.4 may be discretised by introducing a test function $\chi(\mathbf{y})$ to satisfy the above equation [33]

$$\int_S \chi(\mathbf{y}) G(\mathbf{x},\mathbf{y}) q(\mathbf{x}) dS(\mathbf{x}) = p^i(\mathbf{y}) \tag{2.5}$$

Here the collocation method is used for the BIE discretisation and so the Dirac delta function is employed as the testing function $\chi(\mathbf{y})$. The resulting BIE thus has the same from as Eq. 2.4, but is now only valid at the collocation point $\mathbf{y}$ [33]. Eq. 2.4 can then be evaluated at a discrete set of collocation points on S. The BEM numerically implements the BIE by approximating the surface as a system of boundary elements, with one or more evaluation points in each of the elements. The continuous integrals in the BIE then become finite sums of the numerically evaluated integrals over the set of elements, and thus for a discrete set of collocation points yields a solvable system of equations.

In this thesis the surface is approximated by plane triangle elements with one evaluation point (made to be coincident with the collocation point) located at the centre of each element and any unknown quantity is assumed to be constant over each element, giving one unknown per element for the discretised form of Eq. 2.4. The integral can then be approximated as

$$\int_S G(\mathbf{x},\mathbf{y}) q(\mathbf{x}) dS(\mathbf{x}) \approx \sum_{\tilde{n}=1}^{N} \left(\int_{E_{\tilde{n}}} G(\mathbf{x},\mathbf{y}) dE_{\tilde{n}}(\mathbf{x}) \right) q(\mathbf{x}_{\tilde{n}}) \tag{2.6}$$

where $\mathbf{x}_{\tilde{n}}$ is the centre of the $\tilde{n}^{th}$ element $E_{\tilde{n}}$ and $\mathbf{y}$ is the centre of the element at which the boundary integral is being evaluated. For each evaluation point, Eq. 2.6 requires a summation of the product of N coefficients $\int_{E_{\tilde{n}}} G(\mathbf{x},\mathbf{y}) dE_{\tilde{n}}(\mathbf{x})$ with the set of N unknowns at the element centres $q(\mathbf{x}_{\tilde{n}})$. When evaluating the integral at the centre of an element, that evaluation point $\mathbf{y}$ is considered the receiver while the centre points $\mathbf{x}_{\tilde{n}}$ of all of the other elements are considered sources. Thus each element centre is considered both a source point $\mathbf{x}_{\tilde{n}}$ when evaluating the field at the centre of another element, and the receiver point $\mathbf{y}$, when the surface integral is evaluated at the centre of that element. Fig. 2.1 shows an example mesh, consisting of 16 elements E_1–E_{16} (with corresponding source points $\mathbf{x}_1$–$\mathbf{x}_{16}$), indicating the numerical integrals over the surface for the evaluation points at the centres of the first two numbered elements. The

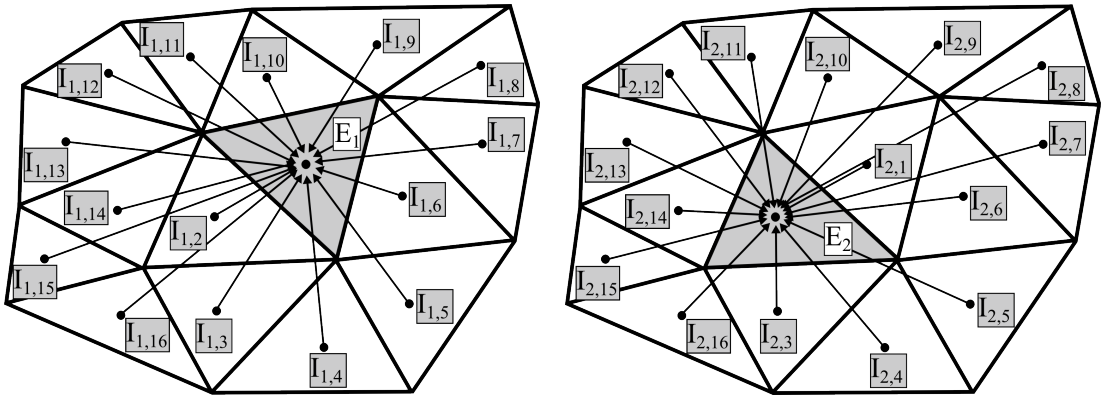

Figure 2.1: Example mesh and numerical integrations for two of the elements. The surface integral in Eq. 2.6 calculated at the evaluation point $\mathbf{y} = \mathbf{x}_1$ in element E_1 (left) is $\sum_{\tilde{n}=1}^{N} \left(\int_{E_{\tilde{n}}} G(\mathbf{x}, \mathbf{x}_1) dE_{\tilde{n}}(\mathbf{x}) \right) q(\mathbf{x}_{\tilde{n}})$, requiring the unique integrals ($\mathrm{I}_{1,1}$–$\mathrm{I}_{1,16}$) to be evaluated. Similarly the evaluation point $\mathbf{y} = \mathbf{x}_2$ in S_2 (right) requires another set of 16 unique integrals ($\mathrm{I}_{2,1}$–$\mathrm{I}_{2,16}$), and so on for each of the evaluation points.

numerical implementation of the boundary integrals in Fig. 2.1 via Eq. 2.6 can be written as a matrix–vector multiplication of the form

$$\begin{bmatrix} I_{1,1} & I_{1,2} & I_{1,3} & \cdots & I_{1,16} \\ I_{2,1} & I_{2,2} & I_{2,3} & \cdots & I_{2,16} \\ \vdots & \vdots & \vdots & \ddots & \vdots \\ I_{16,1} & I_{16,2} & I_{16,3} & \cdots & I_{16,16} \end{bmatrix} \begin{bmatrix} q(\mathbf{x}_1) \\ q(\mathbf{x}_2) \\ \vdots \\ q(\mathbf{x}_{16}) \end{bmatrix} = \begin{bmatrix} p^i(\mathbf{x}_1) \\ p^i(\mathbf{x}_2) \\ \vdots \\ p^i(\mathbf{x}_{16}) \end{bmatrix} \tag{2.7}$$

where the matrix multiplication of each row of the coefficient matrix with the vector of unknowns is equivalent to the operation in Eq. 2.6 for the corresponding evaluation point. The unknown surface quantities and boundary integrals then become N–element vectors and $N \times N$ matrices of coefficients for the Helmholtz BIE. The result of the discretisation process is an exactly solvable system of equations for the evaluation of the unknown quantity at N locations on the boundary surface.

Due to the $\frac{1}{r}$ nature of the Helmholtz Green's function (Eq. 2.3), certain element integrals will exhibit singular behaviour when the source and receiver points are coincident, i.e. when evaluating the $I_{1,1}$ and $I_{2,2}$ integrals along the main diagonal of the coefficient matrix. Similarly when the source and receiver points are very close to one another but not coincident, for example when evaluating integrals between two elements which are on opposite sides of a thin surface whose thickness is much smaller than the typical element dimensions, the integrals will exhibit near–singular behaviour. Full

details of the methods employed to deal with the near–singular and singular integrals for both the Helmholtz and elastodynamic BIEs are later discussed in the corresponding chapters (see Sections 3.2.3 and 4.2.3 respectively). The near–singular/singular integrals involved in the BEM are typically rather difficult to evaluate, while other numerical discretisation techniques such as the FEM do not require the evaluation of singular integrals and so are in general easier to implement than the BEM.

2.1.2 Iterative BEM Solution

Eq. 2.7 has the form of an $\mathbf{Az} = \mathbf{b}$ matrix equation, where $\mathbf{A}$ is a coefficient matrix and the vectors $\mathbf{z}$ and $\mathbf{b}$ represent the unknown and known quantities respectively. Solving for $\mathbf{z}$ via direct inversion $\mathbf{z} = \mathbf{A^{-1}b}$ requires N^3 operations for an $N \times N$ coefficient matrix: a prohibitive cost. Iterative solution methods instead solve the forward problem by initially guessing the solution as $\tilde{\mathbf{z}}_1$, calculating the matrix-vector multiplication $\mathbf{A}\tilde{\mathbf{z}}_1 = \tilde{\mathbf{b}}_1$ and then comparing the result $\tilde{\mathbf{b}}_1$ with the known right hand side (rhs) $\mathbf{b}$. The guess is improved upon using the results of the previous iteration(s), $\mathbf{A}\tilde{\mathbf{z}}$ is recalculated and the residual between the new result and the actual rhs are compared until some tolerance ϵ is reached after $\tilde{\text{its}}$ iterations, i.e. for the relative residual norm (r.r. norm) $\frac{\text{norm}(\mathbf{A}\tilde{\mathbf{z}}_{\tilde{\text{its}}} - \mathbf{b})}{\text{norm}(\mathbf{b})} < \epsilon$. The final iterative solution then approximates the actual solution $\tilde{\mathbf{z}}_{\tilde{\text{its}}} \approx \mathbf{z}$ within the specified tolerance. Each matrix–vector multiplication costs N^2 operations and so the total cost of the iterative solution is of the order of $O(\tilde{\text{its}}(N^2))$ operations. Typically convergence is fast with $\tilde{\text{its}} << N$.

Here the iterative solution of the discretised BIEs is obtained using the GMRES method [34], which has been shown to be a robust solver for acoustic problems [35], with a chosen tolerance of $\epsilon = 10^{-4}$. This tolerance achieves a good trade-off between obtaining accurate results from the FMBEM solution considering the approximation inherent in the method without requiring an excessive number of GMRES iterations. Similar GMRES convergence criteria varying between 10^{-3}–10^{-5} have been used by a number of authors [18, 36, 37, 38, 39, 40] in their FMBEM codes, where further refinement of the convergence tolerance has been observed to not appreciably increase the accuracy in the FMBEM solution (see for example [41]). The main advantage of the GMRES method and other Krylov subspace methods is that they only require the matrix–vector result and so can be used with the FMBEM which does not explicitly form the full coefficient matrix, as will be shown in the next section.

2.2 The FMM

The FMM can substantially reduce the $O(N^2)$ algorithmic cost of the iterative BEM solution by approximately calculating the matrix–vector products to a prescribed accuracy [18], but without explicitly forming nor directly multiplying the coefficient matrix. The advantages of this method are two–fold: as the coefficient matrix is not directly constructed, significantly less memory is required compared to the BEM. Furthermore the matrix–vector multiplication is applied with a lower algorithmic complexity than N^2 operations as it is not computed using standard matrix multiplication.

2.2.1 Green's Function Factorisation

The central idea of the FMM is to 'factorise' the Green's functions such that an intermediate point $\mathbf{c}$ is introduced into the radial distance r between the source and receiver locations in Eq. 2.3 so that $r = |\mathbf{x} - \mathbf{y}|$ can be re–expressed as $r = |(\mathbf{x} - \mathbf{c}) - (\mathbf{y} - \mathbf{c})|$ (see Fig. 2.2).

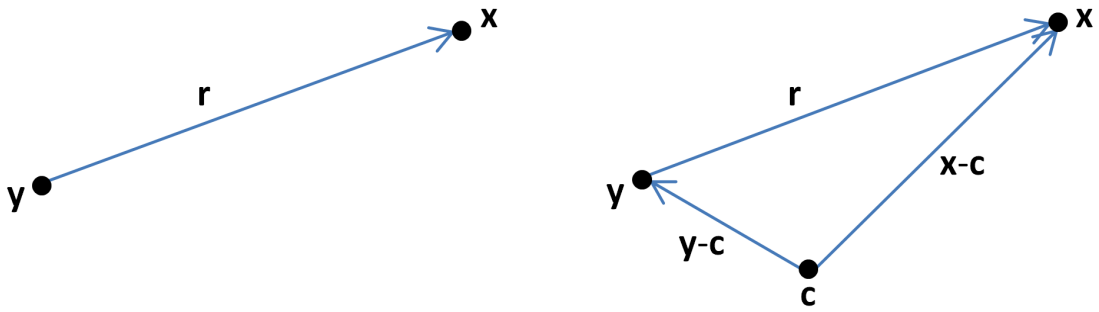

Figure 2.2: Representation of the $\mathbf{r}$ vector of the Green's function. The standard BEM case is shown on the left where the source and receiver points are directly related in the Green's function. The FMBEM case is shown on the right where the $\mathbf{r}$ vector is split into the vectors $(\mathbf{y} - \mathbf{c})$ and $(\mathbf{x} - \mathbf{c})$ which only share the common point $\mathbf{c}$.

This factorisation separates the direct interaction between two boundary elements in the discretised BIE such that only the arbitrary centre point $\mathbf{c}$ is common to both vectors and so the basis functions which are used to represent the factorised components of the Green's function may be independently calculated. These functions take the form of multipole series expansions which describe the Green's function in the 'near' and 'far' field [18] and can be derived by solving the Helmholtz equation in a spherical coordinate system with coordinates r, θ, ϕ and unit normals $\hat{r}$, $\hat{\theta}$, $\hat{\phi}$ as shown in Fig. 2.3.

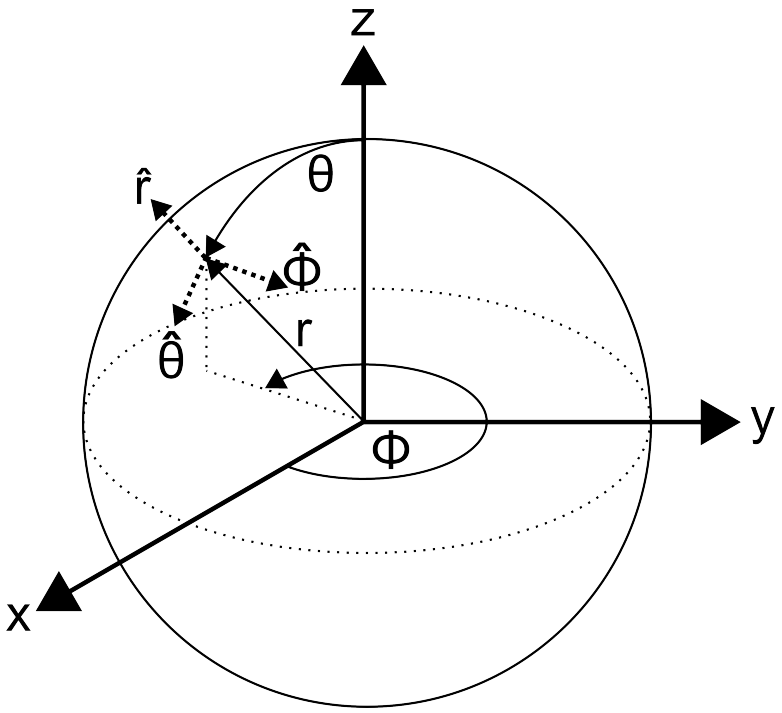

Figure 2.3: Spherical coordinate system for the basis functions. The radial distance $r \geq 0$ from the origin, the polar angle $0 \leq \theta \leq \pi$ is measured from the z–axis and the azimuth angle $0 \leq \phi \leq 2\pi$ is measured in the xy-plane, increasing in the positive x direction.

By applying a separation of variables to the Helmholtz equation expressed in the above spherical coordinate system, the general solutions with respect to the r, θ and ϕ coordinates can be shown to respectively take the form of [42]:

1. spherical Bessel functions of the first and second kinds, of argument kr,
2. Legendre functions of the first kind, of argument $\mu = \cos(\theta)$, and,
3. complex exponentials $e^{im\phi}$ for integer m.

The basis functions can then be constructed from a combination of these linearly independent solutions for each of the spherical coordinates, chosen such that they also satisfy realistic boundary conditions at the limits of the radial coordinate. Specifically, at $r = 0$ the solution should be finite, which reduces the selection of the possible radial solutions to the spherical Bessel functions of the first kind [43]. Conversely, the solution for a radiating field in an infinite 'free space' domain should decay to 0 as $r \to \infty$ and consist only of outgoing waves [44]. This is known as the Sommerfield radiation

condition and only the spherical Hankel functions of the first kind (a combination of the spherical Bessel functions of the first and second kinds) will satisfy this condition [43]. It should be noted that the general solutions for the coordinates in the separated spherical Helmholtz equation are valid for arbitrary complex k and the same radial solutions at the limiting cases are again the only candidates [42]. The multipole series expansions resulting from combining the linearly independent solutions are then:

$$R_n^m(\mathbf{r}) = j_n(kr)Y_n^m(\theta,\phi) \tag{2.8}$$

$$S_n^m(\mathbf{r}) = h_n(kr)Y_n^m(\theta,\phi) \tag{2.9}$$

for integer degree $n = 0, 1, 2, 3, ...$ and order $m = -n, -n+1, ..., n-1, n$, where $j_n(kr)$ and $h_n(kr)$ are respectively the spherical Bessel and spherical Hankel functions of the first kind of degree n and argument kr [45]. The spherical harmonic function $Y_n^m(\theta,\phi)$ contains the fundamental solutions for the angular coordinates

$$Y_n^m(\theta,\phi) = (-1)^m\sqrt{\frac{2n+1}{4\pi}\frac{(n-|m|)!}{(n+|m|)!}}P_n^{|m|}(\cos\theta)e^{im\phi} \tag{2.10}$$

for a similar range of n and m, where $P_n^{|m|}$ is the associated Legendre function and ! denote factorials [46]. The S and R basis functions can be combined to build the Helmholtz Green's function (Eq. 2.3):

$$G((\mathbf{x}-\mathbf{c}),(\mathbf{y}-\mathbf{c})) = ik\sum_{n=0}^{\infty}\sum_{m=-n}^{n} S_n^m(\mathbf{c}-\mathbf{x})R_n^{-m}(\mathbf{c}-\mathbf{y}) \tag{2.11a}$$

$$= ik\sum_{n=0}^{\infty}\sum_{m=-n}^{n} S_n^m(\mathbf{x}-\mathbf{c})R_n^{-m}(\mathbf{y}-\mathbf{c}) \tag{2.11b}$$

where $|\mathbf{y}-\mathbf{c}| < |\mathbf{x}-\mathbf{c}|$ [42] and the sign of the order coefficients m in the two expansions may be interchanged. Eq. 2.11 involves infinite series expansions of the S and R basis functions. In practice these expansions must be suitably truncated after p degree terms, yielding a total of p^2 coefficients with unique combinations of degree n and order m for each expansion. The truncation number is determined by various factors, and a later section of this chapter covers those details. For now, it is just assumed that the multipole series expansions can be truncated after p^2 terms.

Eq. 2.8 involves the spherical Bessel function of the first kind, which is finite or 'regular' (R) at $r = 0$ and Eq. 2.9 involves the spherical Hankel function of the first

kind which is 'singular' (S) at $r = 0$ [40]. The singular basis function is used to represent the radiated field for a 'well–separated' group of source positions centred about the expansion point $\mathbf{c}$ [42] and its domain of validity is *exterior* to a sphere containing those points [47]. Conversely, the regular basis function is used to represent the received field at a group of well–separated receiver positions (i.e. containing only receivers but no sources in the domain) and is valid *interior* to the sphere containing those points. This well–separated criterion is enforced via the domains of validity for the multipole expansion vectors: $|\mathbf{y} - \mathbf{c}| < |\mathbf{x} - \mathbf{c}|$, i.e. the R expansion must lie closer to the expansion centre than the S expansion.

Multipole expansions which have been constructed about the same expansion centre may be combined, allowing local groups of elements to be represented by a single multipole expansion. The FMM accelerates the BEM matrix–vector multiplication by calculating interactions between well–separated groups of elements, instead of the individual Green's functions between each and every pair of elements. The well–separated criterion of Eq. 2.11 means that the grouping of S or R multipoles cannot be made arbitrarily large as the resulting expansion set can only be combined with the opposite expansions for elements which are separated by a distance of a similar size to the spatial region containing the expansions. The intermediate regions of the mesh which are not well–separated for larger groups can instead be treated by multipole expansions for spatially smaller groups of elements. This is the main idea of the so called 'multi–level FMM'. To implement this algorithm requires two mechanisms:

1. The ability to shift or 'translate' the expansion centre for a group of elements to another location, to enable the building of larger sets of multipole expansions by combining pre–existing expansion groups whose expansion centres have been translated to a coincident point. Conversely, the translation operation can shift the expansion centre away from a larger group to the centre of a local group of elements to reduce the spatial range of the multipole expansion set and thus reduce the region around the smaller group which is not well–separated.

2. A system for discretising the 3D space occupied by a boundary element mesh to determine groups of elements which are spatially close for building local multipole expansions, and to determine which other groups of elements of a similar spatial size are well–separated for applying Eq. 2.11. Furthermore, the search procedures

must be computationally very fast to minimise the overall algorithmic complexity of the FMM.

Such mechanisms for the multipole translation and space discretisation required for the FMM are introduced in the next sections.

2.2.2 Multipole Translation Algorithm

Three types of translation operations are required to implement the FMM. They are referred to here as the $R|R$, $S|S$ and $S|R$ translations and their purpose is to translate an established set of coefficients about one expansion centre, $\mathbf{c_1}$ for example, to another expansion centre $\mathbf{c_2}$ by shifting along the translation vector $\mathbf{t} = \mathbf{c_2} - \mathbf{c_1}$ (see Fig. 2.4). The translation operations for the S and R basis functions are defined as:

$$R_n^m(\mathbf{r}+\mathbf{t}) = \sum_{n'=0}^{\infty} \sum_{m'=-n'}^{n'} (R|R)(\mathbf{t}) R_{n'}^{m'}(\mathbf{r}) \tag{2.12}$$

$$S_n^m(\mathbf{r}+\mathbf{t}) = \sum_{n'=0}^{\infty} \sum_{m'=-n'}^{n'} (S|S)(\mathbf{t}) S_{n'}^{m'}(\mathbf{r}) \tag{2.13}$$

$$S_n^m(\mathbf{r}+\mathbf{t}) = \sum_{n'=0}^{\infty} \sum_{m'=-n'}^{n'} (S|R)(\mathbf{t}) R_{n'}^{m'}(\mathbf{r}) \tag{2.14}$$

where Eq. 2.13 and Eq. 2.14 are valid for $|\mathbf{r}| > |\mathbf{t}|$ and $|\mathbf{r}| < |\mathbf{t}|$ respectively [42]. The $S|S$ translations are used to build larger groups of sources by translating local groups to a common expansion centre (see Fig. 2.5), thus allowing the interaction of large distant groups of sources and receivers using a single set of coefficients. Conversely, the $R|R$ translations allow the received field at smaller groups of receivers to be determined by shifting the expansion centre towards a localised group centre (see Fig. 2.5). Finally, the $S|R$ translations are used to translate the radiated field from a distant set of source expansions to a local group of receivers, as shown in Fig. 2.4.

A number of translation algorithms have been published in the literature, with the computational cost of these algorithms strongly influencing the overall algorithmic complexity of the FMBEM. The minimum computational cost to translate a truncated series expansion with p^2 coefficients is to spend one operation per coefficient, giving an $O(p^2)$ translation algorithm. This lower limit is difficult to achieve in practice, with 'slow' translation algorithms which use the Clebsh–Gordan coefficients or Wigner $3-j$

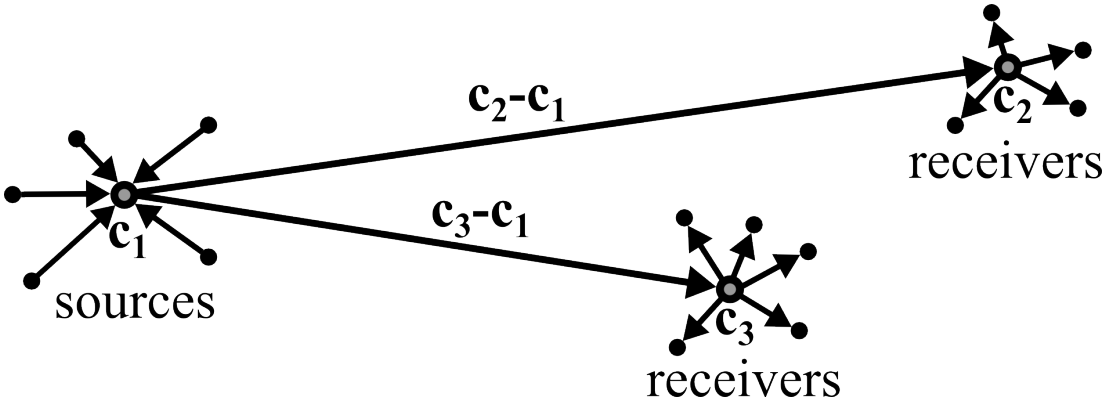

Figure 2.4: Interactions between well–separated groups using multipole expansions. The group of sources may be represented by combining the multipole expansions with $\mathbf{c_1}$ as the expansion centre. The field from these sources can then be evaluated at the distant groups of receivers centred about $\mathbf{c_2}$ and $\mathbf{c_3}$ by applying $S|R$ translations to the $\mathbf{c_1}$ expansion set along the translation vectors $\mathbf{t_1} = \mathbf{c_2} - \mathbf{c_1}$ and $\mathbf{t_2} = \mathbf{c_3} - \mathbf{c_1}$ respectively, i.e. $S_n^m(\mathbf{c_2}) = \sum_{n'=0}^{\infty} \sum_{m'=-n'}^{n'} (S|R)(\mathbf{c_2} - \mathbf{c_1}) R_{n'}^{m'}(\mathbf{c_1})$ and similarly for $S_n^m(\mathbf{c_3})$
.

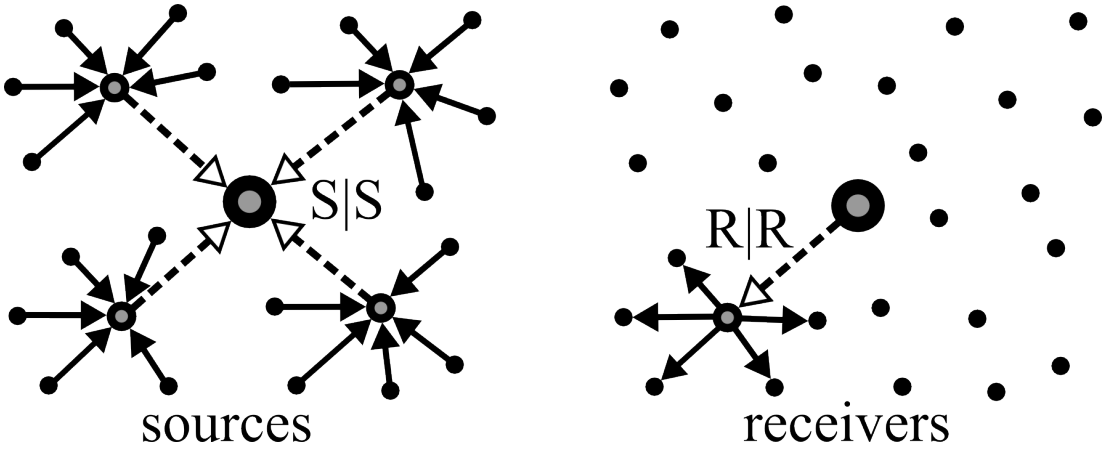

Figure 2.5: $S|S$ (left) and $R|R$ (right) translations. Larger groups of source expansions can be made by $S|S$ translation of local expansion groups to a common expansion centre. The received field for smaller groups can be determined by $R|R$ translating to the spatial centre of a local group of receivers.

symbols arising in quantum mechanics (which are related to integrals of the spherical harmonics [46]) having an $O(p^5)$ algorithmic complexity [48, 49]: a significant cost.

A direct implementation of the translation operations in Eqs. 2.12–2.14, using ef-

ficient recursion relations [43, 50] to obtain the translation coefficients, requires $O(p^4)$ operations with each undashed (n, m) coefficient dependent on all dashed (n', m') coefficients assuming $\max(n) = \max(n')$. Again, the algorithmic cost of such translations become prohibitive with increasing truncation number.

In this thesis the Rotation, Coaxial translation, Rotation (RCR) algorithm [51, 52] is used for all three types of translation operations. This algorithm takes advantage of the fact that all expansion coefficients have the same dependence on the angular coordinate ϕ when applying translations along the z–axis. As a result of the linear independence of the exponential terms in which ϕ appears in Eqs. 2.8 and 2.9, $m' = m$ in the coaxial translation operations. This reduces the algorithmic complexity of co–axially translating p^2 coefficients to $O(p^3)$ operations. Similarly, rotations of the spherical coordinate system defined in Fig. 2.3 do not change the magnitude of the expansion vector r. The linear independence of the spherical Bessel/Hankel functions in which r appears thus yields $n' = n$ in the rotational operations, giving an algorithmic complexity of $O(p^3)$ operations when rotating p^2 coefficients. The RCR algorithm applies translations to the S and R spherical basis functions by first rotating the spherical coordinate system to align the z–axis with the translation vector, co–axially translating along the rotated z–axis, and then reversing the translation back to the original coordinate system, for a total algorithmic complexity of $O(p^3)$ operations (see Fig. 2.6).

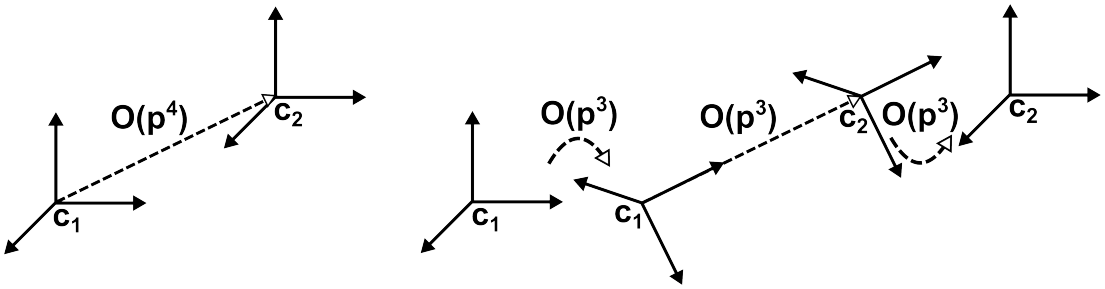

Figure 2.6: Direct (left) and RCR (right) translation procedures for the spherical basis functions. A direct translation via Eqs. 2.12–2.14 of a truncated S or R expansion with p^2 coefficients requires $O(p^4)$ operations. The RCR algorithm can apply the same translation in $O(p^3)$ operations by rotating the coordinate system, co–axially translating along the new z-axis, and then reversing the rotation back to the original coordinate system.

The full derivation of the rotation and coaxial translation coefficients for the RCR algorithm (which are efficiently calculated using symmetry and recursion relations) can

be found in Refs. [43] and [42]. Only a relatively small number of sets of RCR coefficients must be calculated and stored, and so this step only contributes a small component of the overall algorithmic complexity/memory requirements of the FMBEM. The number of 'operations' required to apply the rotations and translations to a truncated series of p^2 coefficients can be calculated using standard summation formulae:

$$\begin{aligned}
\mathrm{Rot(ops)}_{p,p} &= \sum_{n=0}^{p-1}\sum_{m=-n}^{n}\sum_{m'=-n}^{n} 1 = \sum_{n=0}^{p-1}(2n+1)^2 = 4\sum_{n=0}^{p-1}n^2 + 4\sum_{n=0}^{p-1}n + \sum_{n=0}^{p-1}1 \\
&= 4\left(\frac{p(p-1)(2p-1)}{6}\right) + 4\left(\frac{p(p-1)}{2}\right) + p = \frac{1}{3}p(4p^2-1) \qquad (2.15) \\
\mathrm{Trans(ops)}_{p,p} &= \sum_{m=-(p-1)}^{p-1}\sum_{n=|m|}^{p-1}\sum_{n'=|m|}^{p-1} 1 = \sum_{m=-(p-1)}^{p-1}(p-|m|)^2 \\
&= p^2\sum_{m=-(p-1)}^{p-1} 1 - 4p\sum_{m=0}^{p-1} m + 2\sum_{m=0}^{p-1} m^2 \\
&= p^2(2p-1) - 4p\left(\frac{p(p-1)}{2}\right) + 2\left(\frac{p(p-1)(2p-1)}{6}\right) \\
&= \frac{1}{3}p(2p^2+1) \qquad (2.16)
\end{aligned}$$

where one 'operation' is considered the multiplication and addition of two complex double floating point numbers. Comparatively, the BEM matrix–vector product (assuming complex coefficients/unknowns) requires N^2 multiplications and $(N-1)^2$ additions ($\sim N^2$ for large N), giving a total of N^2 multiplication + addition operations.

Finally, it should be noted that the RCR algorithm is only suitable in the 'low frequency' range where there are relatively few wavelengths spanning the dimensions of the object of interest, as the $O(p^3)$ algorithmic cost becomes prohibitive for the larger truncation lengths required at higher frequencies. An alternative $S|R$ translation method is also available in the low frequency range [53] which similarly has a formal algorithmic complexity of $O(p^3)$, but should be faster then the RCR algorithm in practice. However a comparison of these methods for the Laplace equation [54] indicated that the performance of the two methods was comparable, while the RCR method had lower memory requirements. The principal motivation here for using the RCR algorithm was mainly due to the availability of an in–depth description for implementing the method provided in Gumerov & Duraiswami's book [42] and technical paper [43]. Furthermore, the method automatically incorporates interpolation and anterpolation

procedures (see Section 2.2.4) and has been used by Gumerov & Duraiswami in their 'broadband' FMBEM for the Helmholtz equation [18] which appears to be the fastest algorithm in the published literature. The various high and low frequency translation methods currently available are discussed in the literature review in the introduction of the next chapter. An obvious avenue for future work will be to incorporate a high–frequency translation algorithm into this code.

2.2.3 The Octree Structure

The FMBEM requires the 3D region of space occupied by the boundary surface to be systematically discretised (separate to the BEM surface discretisation) to construct multipole expansions of local groups of elements and apply interactions between well–separated groups. An octree structure can be used to discretise the unit cube into subdivided regions, by recursively splitting each cube into eight smaller cubes. The octree is implemented by building a bit-interleaved binary integer from the xyz components of the normalised coordinates of each point in the mesh, in the form [x–bit, y–bit, z–bit, x–bit, y–bit, z–bit, ...] from the most to the least significant bits. The leading three bits then indicate in which of the eight boxes the point resides: for each dimension a 0 bit indicates the box towards the origin (left) and a 1 indicates the box away from the origin (right). Subsequent three–bit groups then recursively indicate which of the eight 'children' boxes the point occupies when the 'parent' cube containing the point is subdivided. Truncating the bit–interleaved numbers after $3l$ bits thus yields l levels in the octree structure with the level number increasing with each subdivision of the domain. An example of the octree structure at the first and second levels of subdivision (8 and 64 boxes respectively) for a normalised point is shown in Fig. 2.7.

Converting the bit–interleaved numbers to decimal integers when truncated after $3l$ bits gives each point a corresponding box number on level l i.e. the box number for the example point on level one is $101 = 5$ in the possible range $0 : 7$, while on level two, $101100 = 44$ in the range $0 : 63$ for the $[4 \times 4 \times 4]$ grid of boxes. The octree structure thus provides an obvious means of grouping elements together for the FMM and has several advantageous features:

- The octree structure is constructed *from* the set of points. Thus empty boxes are never constructed and no search process is required to find which box a point lies

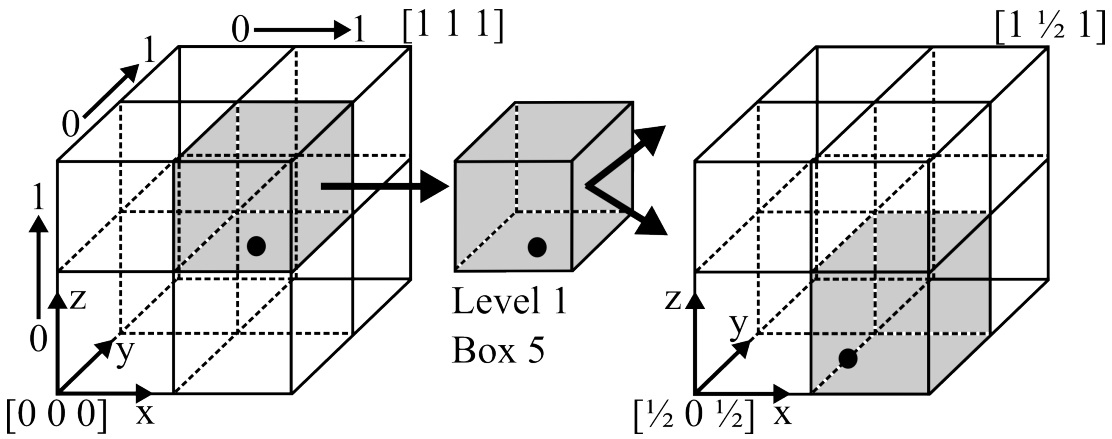

Figure 2.7: Octree for level one (left) and part of level two (right). The example point (the black circle) at [0.78 0.12 0.61] can be bit-interleaved and truncated after 6 bits to give the binary number 101100. The first three bits 101 indicate the point lies within the right x–box, left y–box and right z–box when the unit cube is subdivided into eight children boxes (level one). The next three–bit group 100 indicates in which of the eight children boxes resulting from subdivision of the parent box (level two) that the point resides in.

within: this is directly determined from the bit–interleaved binary numbers.

- The truncated bit–interleaved numbers on any octree level will give the same box number for all points contained within that box, yielding a simple method to find and combine multipole expansions for local groups of elements.

- The domains of validity for the R or S spherical basis functions for a set of box points are, respectively, interior and exterior to the *sphere* containing those points [47]. The spherical domain will overlap with the neighbouring boxes sharing a vertex, edge or side with the box in question, and so only boxes outside of these neighbouring boxes (i.e. separated by at least one box) are considered well–separated for $S|R$ translation. Here, the set of neighbours of a box is defined to be *inclusive* of that box.

- The S expansions of the children boxes on one level may be $S|S$ translated to the centre of the parent box and combined to build larger S expansions groups, while subdivision of the R receiver groups can be achieved by $R|R$ translating from the shared parent expansion centre to each of the children box centres (see Fig. 2.5).

The octree structure yields very fast search procedures due to the bit–interleaved binary numbers: determining the position of a box centre, or the neighbours of a box can be achieved by bit-*de*interleaving, while finding the parent or children boxes entails the use of fast bit–shift operations [42]. Full details of the octree structure can be found in Refs. [47] and [42]. Finally, it should be stated that while the normalised surface mesh is used to construct the bit–interleaved numbers and apply the various search operations between groups of source points in the octree structure, the multipole expansions/translations and FMBEM solution are applied to the full surface mesh.

The choice of the number of octree levels to use for subdividing a particular mesh must also be considered. A trade–off exists between using more levels to reduce the region of the boundary surface which is not well–separated, versus the increasing number of $S|R$ translations required to treat all of the interactions between the more numerous boxes on the finer octree levels. Here, the lowest octree level is determined by limiting the maximum number of source points/elements per box. However this may not be optimal for non–uniformly distributed meshes such as complicated surfaces which need many small elements (i.e. smaller than that dictated by the wavelength discretisation requirements) to adequately represent part of the boundary surface. For these meshes, the coarse parts of the mesh are subdivided to a similar octree level as the refined parts of the mesh, resulting in few sources per box (on average) on the finest octree level and an excessive computational cost for the increased number of translations required. An adaptively refined octree structure [42] instead allows different levels of refinement of the octree depending on the density of points in that region, and so minimises the number of translation operations required. The octree structure implemented here is not adaptive but for many of the numerical examples presented, the refinement of the boundary mesh is either determined by the wavelength or involves a uniform element discretisation, resulting in approximately uniform numbers of elements per octree box.

2.2.4 Truncation and Interpolation/Anterpolation of the Series Expansions

In the preceding sections it has been assumed that the S and R series expansions can be truncated after $n = p - 1$ degree terms giving p^2 (n, m) coefficients in total. The overall error of the approximations introduced by the FMM is dependent upon the truncation number chosen, the translation algorithms employed and the type of the

'well–separated' criterion used. The analysis of the errors introduced by the FMM have been researched by a number of authors (e.g. [55, 56, 57, 58, 59, 60]) for various BIEs and types of expansion/translation. In particular, the errors introduced by both the truncation of the spherical basis functions and the various translation operations are *bounded* [42]. A number of rules have been proposed for determining the truncation number based on empirical or analytic considerations: where p is generally a function of the spatial size of the octree boxes, the wavenumber and a prescribed overall accuracy for the FMBEM. Here the truncation number is determined using the method of Gumerov & Duraiswami [18, 42], which is based on a combination of high and low frequency asymptotes of the theoretical error bounds for the expansions:

$$p_{\text{high}} = ka + \frac{\left(3\ln\left(\frac{1}{\xi}\right)\right)^{\frac{2}{3}}}{2}(ka)^{\frac{1}{3}} \qquad p_{\text{low}} = 1 - \frac{\ln\left[\xi\left(1-\frac{1}{\sigma}\right)^{\frac{3}{2}}\right]}{\ln(\sigma)}$$
$$p = \left(p_{\text{high}}^4 + p_{\text{low}}^4\right)^{\frac{1}{4}} \tag{2.17}$$

where k is the wavenumber, a is the radius of the sphere containing the unnormalised boxes on level l of the octree structure, ξ is a specifiable error tolerance or accuracy for the multipole expansions, usually set to $\xi = 10^{-4}$ to match the GMRES tolerance and $\sigma = 2$ [61]. Some constraints are also imposed on Eq. 2.17 to stop excessively large truncation numbers when using small error tolerances or low wavenumbers.

It can be seen from Eq. 2.17 that the truncation number p is dependent on the subdivision level of the octree structure and so p varies between octree levels. In fact, using multipole octree levels with a variable truncation number reduces the algorithmic complexity of the FMBEM compared to using a constant p across all levels. The $S|R$ translations are applied between well–separated groups of sources and receivers across octree levels, while the $S|S$ and $R|R$ translations are used to combine or separate the expansions of octree boxes *between* octree levels. The expansions of children boxes are combined via $S|S$ translation to build the larger expansion for the parent box, while $R|R$ translation is used to separate an expansion for a parent box to each of the children boxes on the lower octree level. The $S|S$ translations may require 'interpolation' of a preestablished set of expansion coefficients to increase the length of the expansions at the children box centres to the larger truncation number dictated by Eq. 2.17 for the larger parent box. Conversely when applying the $R|R$ translation from the larger expansion domain of a parent box to each of the smaller children boxes, Eq.

2.17 dictates that the truncated expansions may be reduced in length via an anterpolation (adjoint–interpolation) procedure. Interpolation and anterpolation procedures are automatically incorporated into the RCR algorithm and can both be envisioned as applying three matrix multiplications to the truncated expansion as shown in Figs. 2.8 and 2.9, although the actual implementation is more complicated than this.

The interpolation/anterpolation procedures are applied by the coaxial translation step of the RCR algorithm, as indicated by the non–square coaxial translation matrices in Figs. 2.8 and 2.9. The operations count of the coaxial translations when applying interpolation from p^2 to p'^2 coefficients is

$$\text{Trans(ops)}_{p,p'} = \sum_{m=-(p-1)}^{p-1} (p - |m|)(p' - |m|) = \frac{1}{3}p(3pp' - p^2 + 1) \tag{2.18}$$

which differs from the operational cost for coaxial translation when $p = p'$, as described by Eq. 2.16. When applying anterpolation, only the p^2 coefficients which will be retained in the expansion are translated, and so the algorithmic cost of coaxial translation when applying anterpolation from p'^2 to p^2 coefficients is described by Eq. 2.16.

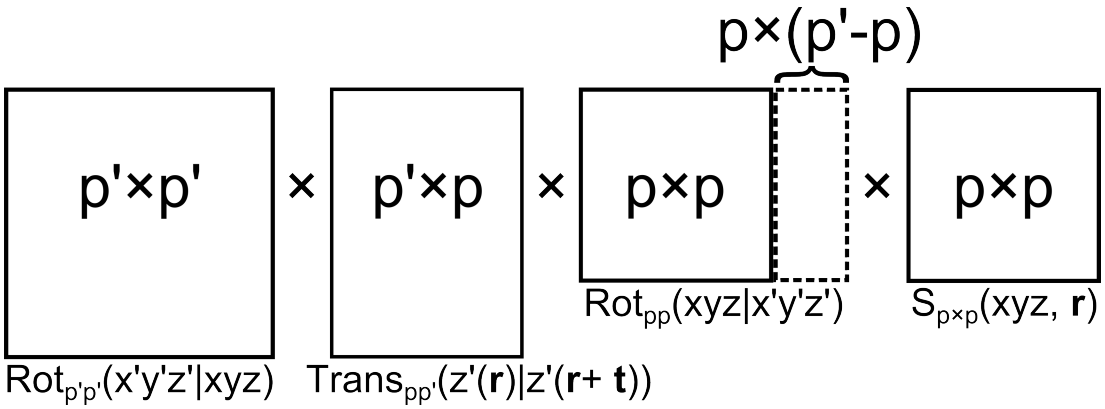

Figure 2.8: The S expansion of vector $\mathbf{r}$ in the Cartesian coordinate system xyz, is interpolated from p^2 to p'^2 coefficients ($p' > p$) while translating the expansion along the vector $\mathbf{t}$ using the RCR algorithm. The square matrix of coefficients $S_{p\times p}(\text{xyz}, \mathbf{r})$ is first multiplied by a p^2 matrix Rot_{pp} to rotate to the new coordinate system x'y'z' (defined such that z' is coaxial with $\mathbf{t}$), and is then padded by $p \times (p' - p)$ zeros (the dashed matrix) to give a $p \times p'$ matrix. The rotated $S_{p\times p'}(\text{x'y'z'}, \mathbf{r})$ coefficients are then multiplied by the rectangular $p' \times p$ coaxial translation matrix $\text{Trans}_{pp'}$, yielding the interpolated $p' \times p'$ matrix of translated coefficients in the rotated x'y'z' coordinate system $S_{p'\times p'}(\text{x'y'z'}, \mathbf{r}+\mathbf{t})$. Finally, multiplication with the p'^2 reverse–rotation matrix $\text{Rot}_{p'p'}$ gives $S_{p'\times p'}(\text{xyz}, \mathbf{r}+\mathbf{t})$.

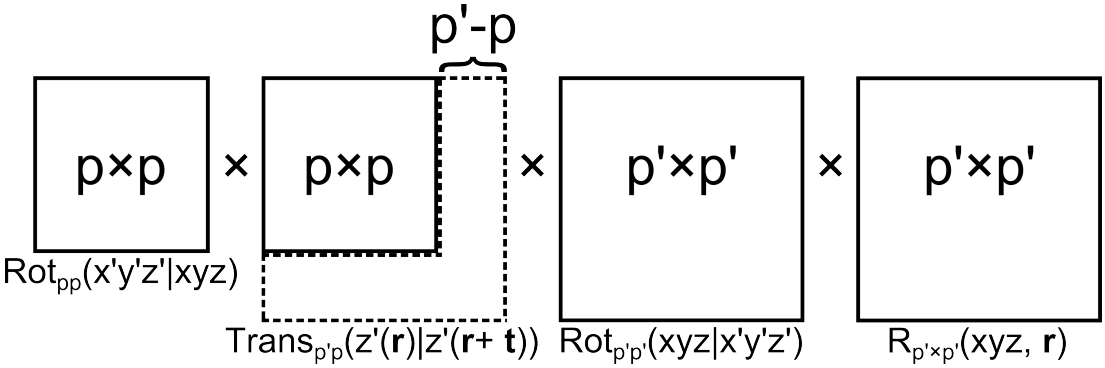

Figure 2.9: The R expansion of vector $\mathbf{r}$ in the Cartesian coordinate system xyz, is anterpolated from p'^2 to p^2 coefficients ($p' > p$) while translating along vector $\mathbf{t}$ using the RCR algorithm. The square matrix of coefficients $R_{p'\times p'}(\text{xyz}, \mathbf{r})$ is first multiplied by a p'^2 matrix, $\text{Rot}_{p'p'}$, to rotate to the x'y'z' system (with z' coaxial to $\mathbf{t}$). The expansion is then anterpolated to p^2 coefficients by multiplying the rotated $R_{p'\times p'}(\text{x'y'z'}, \mathbf{r})$ coefficients with the p'^2 coaxial translation matrix $\text{Trans}_{p'p}$ and then discarding the highest degree terms of the truncated series ($n = p : p', m = -n : n$, denoted by the dashed region), to anterpolate the expansion to p^2 coefficients: $R_{p\times p}(\text{x'y'z'}, \mathbf{r} + \mathbf{t})$. Finally, multiplication with the p^2 reverse–rotation matrix Rot_{pp} gives $R_{p\times p}(\text{xyz}, \mathbf{r} + \mathbf{t})$. In practice the coaxial translations are not applied to coefficients which are to be discarded.

2.3 The FMBEM

The application of the FMM to accelerate the solution of an example BIE (Eq. 2.4) is now presented. The central idea of the FMBEM is to accelerate the matrix–vector products of the iterative BEM solution by calculating the far field part of the boundary integrals for each receiver using the FMM and the near field part (which is not well–separated) via the conventional BEM, as shown in Fig. 2.10. In Fig. 2.10 the distance of the matrix coefficients to the main diagonal represents physical distance between the pair of elements containing $\mathbf{x}$ and $\mathbf{y}$ for the corresponding matrix coefficient. Here the elements are ordered according to their distance from the first element in the mesh, with resulting element ordering yielding a compact diagonal banding in the preconditioner matrix used in the iterative GMRES solution [62] (see Section 3.2.4 for details).

The FMBEM first requires the problem to be set up in a pre–solution stage: analogous to the precalculation of the full coefficient matrix before the iterative BEM solution. The following steps are taken to set up the problem for FMBEM solution:

1. First the bit–interleaved binary numbers for the octree structure are computed

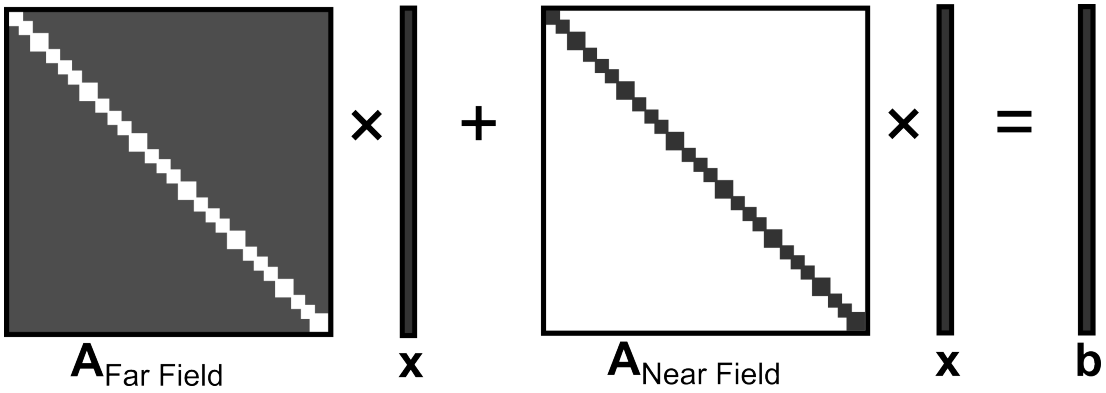

Figure 2.10: Calculation of the BEM $\mathbf{Ax} = \mathbf{b}$ matrix-vector product using the FMM. The far field part of $\mathbf{A}$ is multiplied with $\mathbf{x}$ using the fast multipole algorithm (which does not explicitly build or store this part of the matrix), while the remaining sparse near field component is directly stored and multiplied with $\mathbf{x}$, as per the conventional BEM.

from the normalised source points of the mesh located at the centre of each of the plane triangular elements. The bit–interleaved numbers are initially built to the highest possible precision: for a 64–bit processor, 21 bits from each of the normalised xyz components are combined and the last remaining bit is unused.

2. The lowest (most refined) octree level l is then determined using the bit–interleaved numbers and a user–defined constant which specifies the maximum number of source points per box. The bit–interleaved numbers are truncated to $3l$ bits.

3. The truncation numbers for each octree level are then determined by Eq. 2.17 using the wavenumber for the problem, the radius of the containing sphere for a box on that level and the error tolerance ϵ specified by the user.

4. The octree structure and truncation numbers are then used to precalculate the $S|R$, $S|S$ and $R|R$ translation coefficients for all octree levels.

5. Finally the near field part of the surface integral, consisting of any elements in the same box or neighbouring boxes for each of the source points at the finest octree level, are directly calculated using appropriate numerical integration methods (i.e. dependant upon the regular/singular nature of the fundamental solutions for the particular element being integrated - see Sections 3.2.3 and 4.2.3). These

integrals are stored in a sparse near field matrix which is directly multiplied with the vector of unknowns in the iterative solution.

Once this stage is completed the fast multipole algorithm can be applied to each matrix–vector product of the iterative BEM solution. This involves three main steps, usually referred to as the upward pass, downward pass and final summation.

2.3.1 Upward Pass

The purpose of the upward pass is to build a single multipole expansion for all sets of source points contained in each box on every level of the octree structure. For each box on the lowest octree level the source expansions are built with respect to the centre of the containing box and then combined into a single set of coefficients (see Fig. 2.11 for an example in 2D). One might expect from Eq. 2.11 for the sources and receivers to be represented by the singular S and regular R expansions respectively, but in fact the FMM uses R expansions to represent both sources and receivers. This is because the translations between all source and receiver groups are applied via the $S|R$ translation (Eq. 2.14), due to the expansions vectors $|\mathbf{r}|$ always being smaller than the translation distances $|\mathbf{t}|$ between a box and its nearest well–separated neighbours (see for example Fig. 2.4). Eq. 2.14 acts on R expansions and yields S expansions upon applying the translation and so the R expansions are used in the upward pass such that the $S|R$ translations in the downward pass will yield S expansions.

The combined expansions for each box on the lowest octree level l which share the same parent box on level $l-1$ are $S|S$ translated via Eq. 2.13 to the parent box centre and then combined into a single set of multipole coefficients (see Fig. 2.11). All of the sources contained in each of the larger occupied boxes on octree level $l-1$ are now represented by a single set of expansion coefficients. Any interpolation required to extend the truncation degree p_l on level l to p_{l-1} on level $l-1$ is automatically dealt with via the RCR algorithm. The process of children to parent translation and summation is repeated up until level two of the octree is reached, as this is the highest level at which any box has well–separated boxes for $S|R$ translation (see Fig. 2.12).

At the conclusion of the upward pass on octree level two, a multipole expansion representing the source points contained within each box has been built for every level of the octree structure. The iterative solution of a BIE such as Eq. 2.4 via the FMM

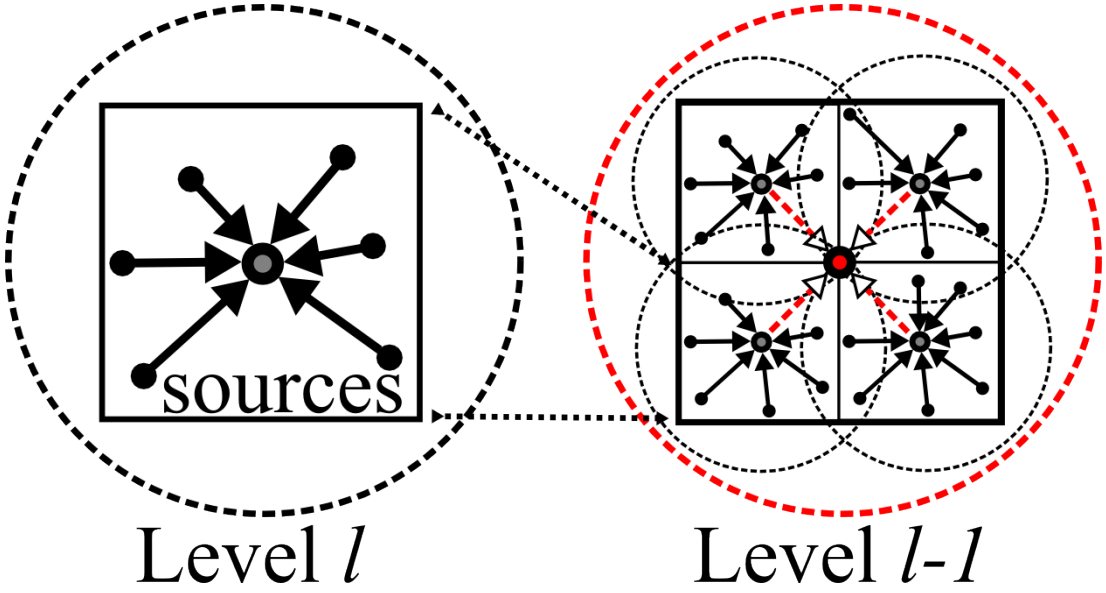

Figure 2.11: Source expansions on the lowest octree level l (black arrows) are built with the vectors directed towards the box centre (left). Each of the combined source expansions on level l with the same parent box on level $l-1$ are $S|S$ translated (red dashed vectors) to parent box centre (red marker, right diagram). The domain of validity for the expansion groups on level l and $l-1$ are indicated by the dashed black and red circles respectively.

(i.e. a FMBEM solution) requires the Green's functions and the current iteration of the solution to be *integrated* over the far field part of the discretised surface. The inverse dependence on the radial distance r of the Green's function (Eq. 2.3) allows the integrals over the set of well–separated elements for each receiver point to be approximated as the product of the area of source element and the Green's function between the source/receiver points of the elements. This approximation assumes that the variation in the Greens functions over the well–separated elements is small compared to the separation distance between the elements. Thus the FMBEM treatment of Eq. 2.4 for the integral over the $\tilde{n}^{th}$ element $E_{\tilde{n}}$ with area $A_{\tilde{n}}$ and unknown quantity $q(\mathbf{x}_{\tilde{n}})$ at the source point $\mathbf{x}_{\tilde{n}}$ at the element's centre is

$$\int_E G(\mathbf{x},\mathbf{y})q(\mathbf{x}_{\tilde{n}})dS(\mathbf{x}) \approx ikA_{\tilde{n}}q(\mathbf{x}_{\tilde{n}})\sum_{n=0}^{p_l}\sum_{m=-n}^{n} S_n^m(\mathbf{c}_{\tilde{m}}-\mathbf{x}_{\tilde{n}})R_n^{-m}(\mathbf{c}_{\tilde{m}}-\mathbf{y}) \qquad (2.19)$$

where $\mathbf{c}_{\tilde{m}}$ is the expansion centre of the $\tilde{m}^{th}$ box containing $\mathbf{x}_{\tilde{n}}$ on the lowest octree level l [1]. Using the R expansions to represent the sources, the expansion for each element

[1] note the direction of the S expansion — see Eq. 2.11a

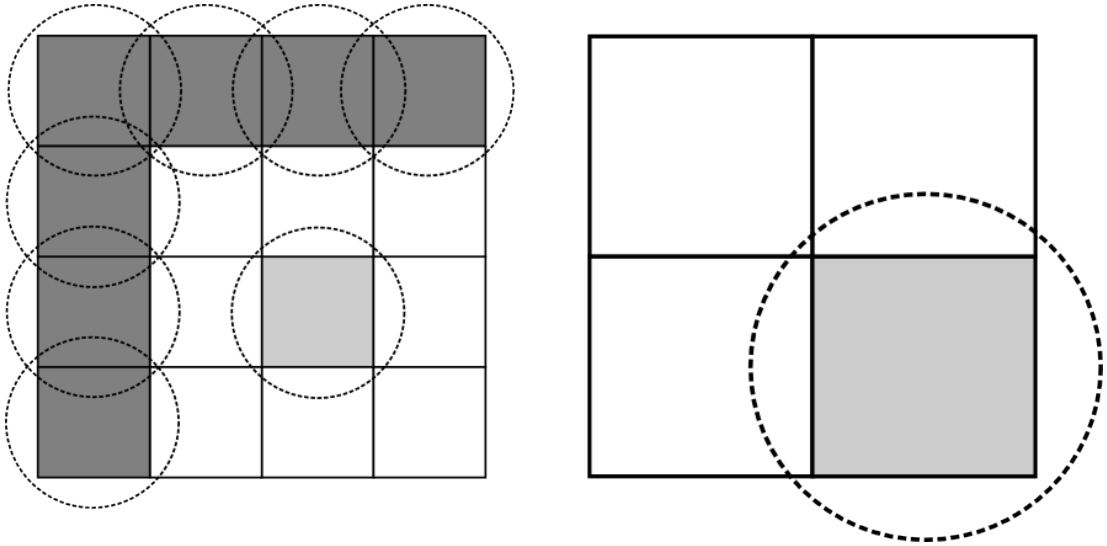

Figure 2.12: On level two of the octree structure (left), the light grey box is well–separated from the dark grey boxes as the domains of validity (the dashed circles) for the box expansions do not overlap, and so $S|R$ translation maybe applied. The neighbours of the light grey box (the white boxes), which connect with the box by a vertex, edge or face, will have overlapping domains and are therefore not well–separated. On octree level one (right) all boxes are neighbours with one another and so no boxes are well–separated for $S|R$ translation. Thus the upward pass is stopped at level two of the octree.

in the far field part of the surface integral in Eq. 2.4 is

$$R_{\tilde{n}} = A_{\tilde{n}} q(\mathbf{x}_{\tilde{n}}) R_{p_l}^m(\mathbf{c}_{\tilde{o}} - \mathbf{x}_{\tilde{n}}) \tag{2.20}$$

where $R_{p_l}^m$ denotes the truncated R expansion with a maximum degree $n = p_l$. Upon incorporation of an $S|R$–type translation, Eq. 2.19 takes the form

$$\int_E G(\mathbf{x}, \mathbf{y}) q(\mathbf{x}_{\tilde{n}}) dS(\mathbf{x}) \approx ik \sum_{n=0}^{p_l} \sum_{m=-n}^{n} R_{\tilde{n}}(S|R)(\mathbf{t}) R_{p_l}^{-m}(\mathbf{c}_{\tilde{m}} - \mathbf{y}) \tag{2.21}$$

where $\mathbf{t} = \mathbf{c}_{\tilde{m}} - \mathbf{c}_{\tilde{o}}$ is the translation vector between the box centres of the $\tilde{m}^{th}$ and $\tilde{o}^{th}$ well–separated octree boxes on level l containing $\mathbf{y}$ and $\mathbf{x}$.

2.3.2 Downward Pass

The downward pass applies the $S|R$ translations via Eq. 2.14 between all well–separated boxes on each successive octree level. Starting with level two, the $S|R$ translations are applied to every box containing receiver points from all well–separated source boxes

(see Fig 2.13). The translated source expansions for each receiver box are then summed into a single S expansion which represents the radiated field from *all* sources in the well–separated boxes. The neighbour boxes to each receiver box are not well–separated and so the source expansions from those boxes cannot be used.

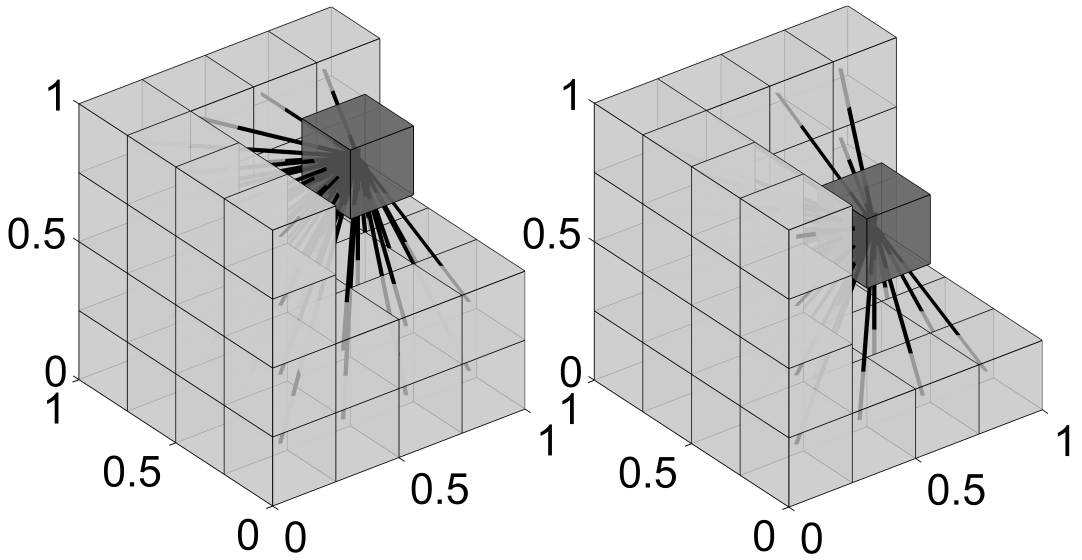

Figure 2.13: $S|R$ translations (black lines) for two boxes on level two of the octree. The source expansions for the well–separated boxes (light grey) are $S|R$ translated to each receiver box (dark grey). The empty space around the dark grey boxes indicates the near field regions (the neighbouring boxes) which are not well–separated.

The far field part of the matrix–vector product (Fig. 2.10) treated by the level two $S|R$ translations can be envisaged as a large off–diagonal region of the coefficient matrix, again assuming the distance to the main diagonal represents physical distance between the pairs of elements. The element integrals yielded from combining the $S|R$ translated sets of far field S expansions for a particular box with the R expansions for the receivers in that box via Eq. 2.11 can be envisaged as a horizontal band of coefficients in the far field matrix. Applying the $S|R$ translations between all level two boxes thus treats a large section of the equivalent full coefficient matrix (see Fig. 2.14).

Figs. 2.13 and 2.14 indicate that significant regions of the far field part of the matrix cannot be treated in the level two $S|R$ translations due to the large domain size of the expansions and the correspondingly large distances between well–separated boxes. To treat these intermediate regions, the combined S expansions for each receiver box are

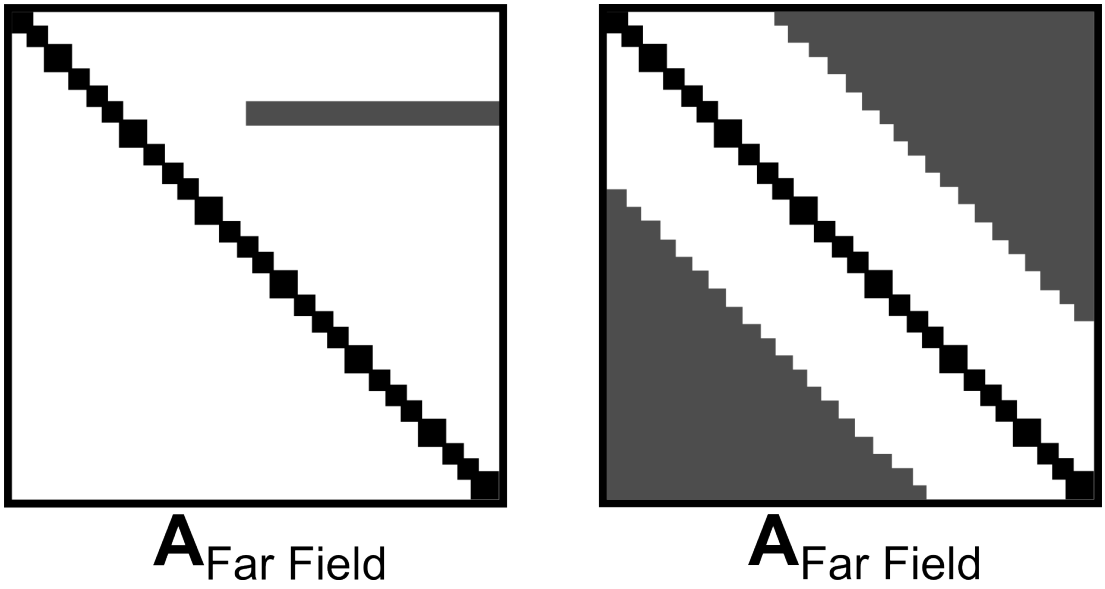

Figure 2.14: The complete set of $S|R$ translations for each level two receiver box is equivalent to a band of coefficients in the far field part of the full coefficient matrix (left). The bands of coefficients resulting from applying the $S|R$ translations between all level two boxes thus treats a large region of the equivalent far field matrix (right).

$R|R$ translated via Eq. 2.12 from the parent box centres on level two, to each of the occupied children box centres on level three (see Fig. 2.5). Thus the S expansions for the well–separated field calculated on level two are now centred about each of the smaller receiver boxes on level three. Any anterpolation required to reduce the expansions from p'^2 coefficients on level two, to p^2 coefficients on level three ($p' > p$), is automatically incorporated into the RCR algorithm. The near field for each box now consists of the smaller level three neighbour boxes and so part of the larger intermediate region which was not well–separated on level two can be treated with the FMM on level three. The $S|R$ translations are thus applied between all level three source and receiver boxes and again combined into a single set of coefficients for each box. The level three $S|R$ expansions are then combined with those $R|R$ translated from level two to give the total well–separated field from both levels (see Fig. 2.15).

The new intermediate region of the octree which become well–separated upon $R|R$ translation to a lower level can be defined as: the parent's neighbour's children boxes of the receiver box (a $[6 \times 6 \times 6]$ box region), minus the neighbours of the receiver box ($[3 \times 3 \times 3]$ boxes, inclusive of the receiver box). Thus the new region consists of

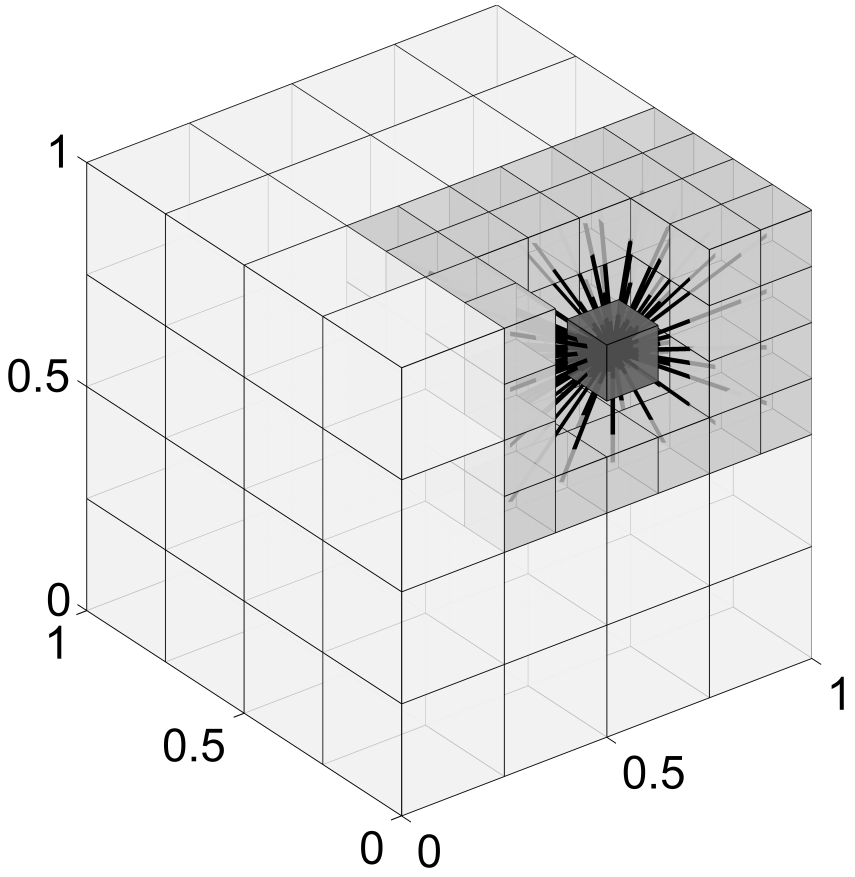

Figure 2.15: The $S|R$ translations (black lines) for a receiver box on level three of the octree. The source expansions for the well–separated level three boxes (light grey) are $S|R$ translated to the receiver box (dark grey). The larger level two boxes have already been treated in the level two $S|R$ translations and so are $R|R$ translated from the parent box centres on level two to the children box centres on level three. The $R|R$ translations from level two are combined with the level three $S|R$ translated sets to give the complete well–separated field from both octree levels at each level three box centre.

a maximum of $6^3 - 3^3 = 189$ occupied boxes, and so up to 189 $S|R$ translations are required for each receiver box per octree level. Fig. 2.16 shows a 2D example of the well–separated region of a receiver box upon $R|R$ translation to level three.

The level three $S|R$ translations can again be envisaged as an off–diagonal region of the full coefficient matrix. The complete set of level three $S|R$ translations for each receiver box corresponds to a thinner horizontal band of coefficients in the far field

matrix. The size of the bands reduces as the number of receivers in the smaller level three boxes is fewer and the well–separated regions treated on level three are spatially smaller. The complete set of level three $S|R$ translations fill a region of the equivalent coefficient matrix which is closer to the main diagonal as the $S|R$ translations are spatially closer to each of the receiver boxes than that for level two (see Fig. 2.17).

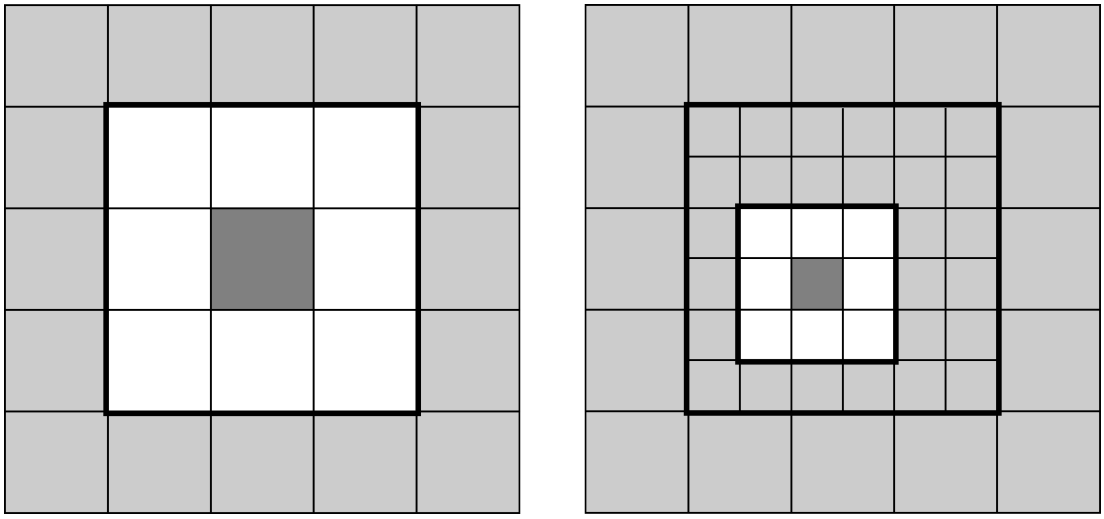

Figure 2.16: Well–separated receiver field from $R|R$ translation to level three. The white boxes denote the near field regions which are not well–separated from the dark grey receiver boxes on level two (left) and three (right). The well–separated light grey boxes outside of the level two neighbours have already been translated in the level two $S|R$ translations (left). The $R|R$ translation to level three reveals a new region which is well–separated from the level three receiver box (right), defined as the region between the two black lines.

The intermediate region which is not well–separated on level three now consists of the neighbours of each level three receiver box (see Fig. 2.16). Again this region can be treated by $R|R$ translating the expansion sets to the receiver boxes on octree level four and the $S|R$ translation process repeated. The $R|R$ translated coefficients for each receiver box will contain the well–separated $S|R$ translations for all of the above octree levels. Each $R|R$ translation to successively lower octree levels will reveal a new well–separated region for $S|R$ translation. These regions represent successively smaller sets of coefficients in the far field matrix which also tend closer to the main diagonal. The downward pass concludes when the lowest octree level is reached via the $R|R$ translations. The complete far field part of the coefficient matrix is then contained

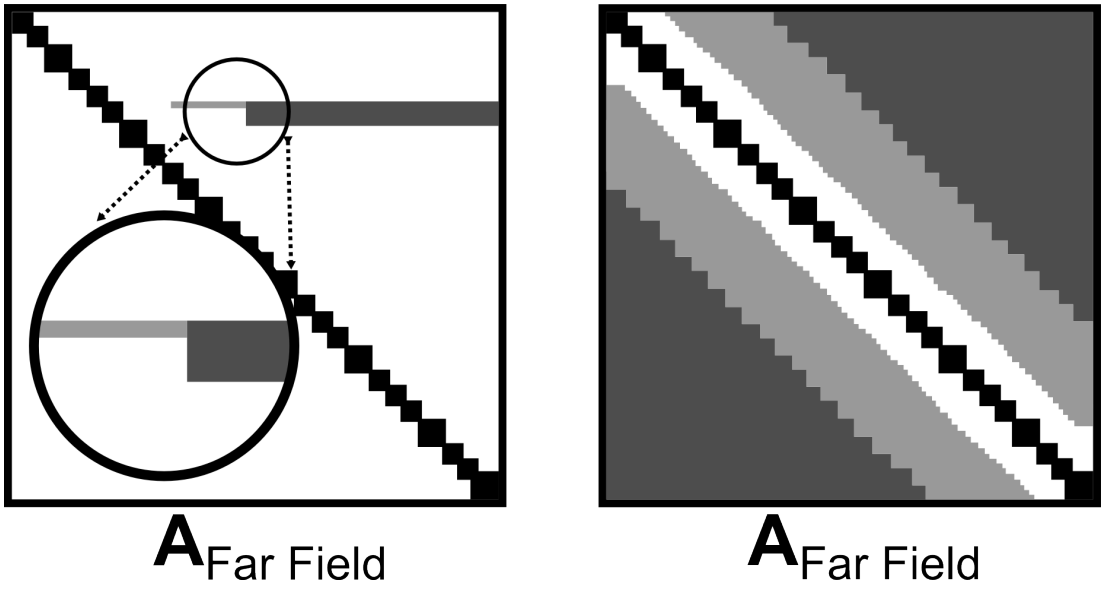

Figure 2.17: The set of $S|R$ translations for each level three box is equivalent to a band of coefficients in the far field part of the full coefficient matrix. The bands of coefficients are smaller than that for level two in both width, as the number of receivers in the level three boxes reduces (i.e. each of the child boxes only contains a portion of the total number of receivers in the parent box), and length, as the well–separated region treated in the level three $S|R$ translations has also reduced (left). After applying all level three translations, an intermediate region of the equivalent far field coefficient matrix is filled (right).

within the final S expansions for each receiver box on the lowest octree level.

2.3.3 Final Summation

The final S expansions from the downward pass represent the radiated field from all well–separated sources on all of the octree levels at the receiver boxes on the lowest octree level. The field at each individual receiver can now be calculated by Eq. 2.11 using the unique R expansions for each receiver point and the S expansion for the box containing the receiver, i.e. all of the receivers contained within the same box have the same far field represented by the final S expansion for that box. The result of applying Eq. 2.11 is the summation of the Helmholtz Green's function for all well–separated points at *every* receiver: equivalent to the dense far field part of the matrix–vector multiplication. For the example BIE (Eq. 2.4), the far field FF integral on the lowest

octree level l for one receiver point at the centre of the $\tilde{n}^{th}$ element, $\mathbf{y}_{\tilde{n}}$, is

$$\int_{FF} G(\mathbf{x}, \mathbf{y}_{\tilde{n}}) q(\mathbf{x}) dS(\mathbf{x}) \approx ik \sum_{n=0}^{p_l} \sum_{m=-n}^{n} R_n^{-m}(\mathbf{c}_{\tilde{m}} - \mathbf{y}_{\tilde{n}}) S_n^m(\mathbf{c}_{\tilde{m}} - \mathbf{x}_{FF}) \tag{2.22}$$

where $S_n^m(\mathbf{c}_{\tilde{m}} - \mathbf{x}_{FF})$ is the final expansion at the lowest octree level l for the $\tilde{m}^{th}$ receiver box containing $\mathbf{y}_{\tilde{n}}$, and $\mathbf{x}_{FF}$ represents the sources of *all* far field elements which are well–separated from the box containing $\mathbf{y}_{\tilde{n}}$. The final expansions $S_n^m(\mathbf{c}_{\tilde{m}} - \mathbf{x}_{FF})$ for the example BIE in Eq. 2.4 result from propagating source expansions of the form of Eq. 2.20 through the FMM procedure (i.e. the propagated source expansions contain the source strengths $q(\mathbf{x})$ and element areas A for the set of far field elements containing $\mathbf{x}_{FF}$), and so the final source expansions approximate the integrals of the Green's function over the far field elements. Note that the R expansion in Eq. 2.22 is directed from the receiver point to the expansion centre of the box $(\mathbf{c}_{\tilde{m}} - \mathbf{y}_{\tilde{n}})$ as the equivalent S expansions for the far field are also directed towards the expansion centre of the receiver box. This is demonstrated in Fig. 2.18, where the expansion for a source point $\mathbf{x}$ (directed towards its local box centre $\mathbf{c}_{\tilde{o}}$) has arbitrary $S|S$, $S|R$ and $R|R$ translations applied to shift the source expansion/box centre $\mathbf{c}_{\tilde{o}}$ to the receiver box centre $\mathbf{c}_{\tilde{m}}$ containing the receiver point $\mathbf{y}_{\tilde{n}}$. The resulting source expansion is thus directed from the source point $\mathbf{x}$ to the receiver box centre $\mathbf{c}_{\tilde{m}}$ and so the reconstruction of the Green's function from the source/receiver expansions is calculated via Eq. 2.11a.

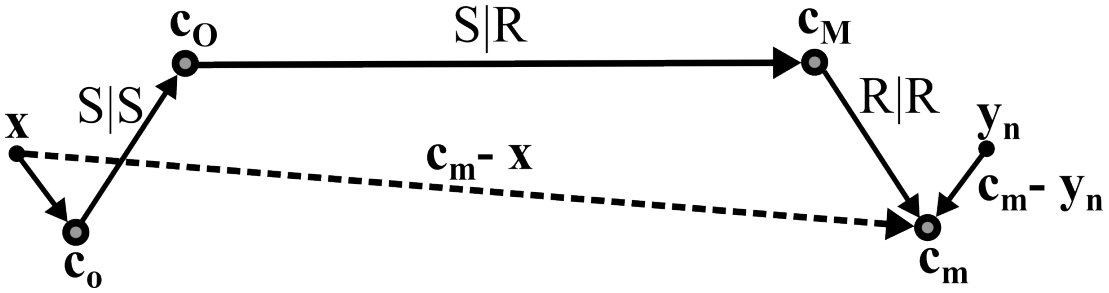

Figure 2.18: Example of S and R expansion vectors in the final summation. The initial R source expansion is towards the box centre $\mathbf{c}_{\tilde{o}}$. After applying arbitrary $S|S$, $S|R$ and $R|R$ translations to shift the source expansion centre to $\mathbf{c}_{\tilde{m}}$, the resulting S expansion is directed from the well–separated source point $\mathbf{x}$ to the expansion centre $\mathbf{c}_{\tilde{m}}$ of the box containing the receiver point $\mathbf{y}_{\tilde{n}}$. Thus the R expansion for the receiver must be of the form $(\mathbf{c}_{\tilde{m}} - \mathbf{y}_{\tilde{n}})$ according to Eq. 2.11a.

The sources in the nearest neighbour boxes on the finest octree level are not well–separated from the receiver boxes and so cannot be treated with the FMM. These interactions correspond to the near field part of the matrix–vector multiplication which are directly calculated and stored (see Fig. 2.10). Combining the FMM treated far field interactions and directly calculated near field NF interactions gives the complete matrix–vector product for the BEM. Thus Eq. 2.22 can be written for the full surface integrals for arbitrary sets of source and receiver points as

$$\int G(\mathbf{x},\mathbf{y})q(\mathbf{x})dS(\mathbf{x}) \approx ik\sum_{n=0}^{p_l}\sum_{m=-n}^{n} R_n^{-m}(\mathbf{c}_{\tilde{m}}-\mathbf{y})S_n^m(\mathbf{c}_{\tilde{m}}-\mathbf{x}_{FF})+\int_{NF} G(\mathbf{x},\mathbf{y})q(\mathbf{x})dS(\mathbf{x})$$

where $\mathbf{c}_{\tilde{m}}$ now represents the expansion centre of the $\tilde{m}^{th}$ receiver box containing an arbitrary receiver point $\mathbf{y}$ and $\mathbf{x}_{FF}$ represents the set of source points which are well–separated from $\mathbf{y}$. The near field integrals are calculated via a matrix–vector product with the precalculated sparse matrix of near field integrals $\mathbf{G}_{NF}$

$$\int G(\mathbf{x},\mathbf{y})q(\mathbf{x})dS(\mathbf{x}) \approx ik\sum_{n=0}^{p_l}\sum_{m=-n}^{n} R_n^{-m}(\mathbf{c}_{\tilde{m}}-\mathbf{y})S_n^m(\mathbf{c}_{\tilde{m}}-\mathbf{x}_{FF}) + \mathbf{G}_{NF}\mathbf{q}$$

Thus the matrix–vector products for the iterative BEM solution can be calculated using the FMBEM without the need to directly build or multiply the full coefficient matrix.

2.4 Chapter Summary

This chapter first presented the background theory of the BEM for numerically solving a BIE on an arbitrary boundary surface, using a simplified Helmholtz BIE for example. The main mechanisms of the FMM relating to the Helmholtz fundamental solution were then presented, including details of the multipole expansion and translation algorithms, octree structure and the interpolation/anterpolation procedures employed in the FMBEMs developed in this thesis. Finally the FMBEM procedure for accelerating the iterative BEM solution was presented, again using the Helmholtz BIE for example.

The theory and implementation of the FMM presented here is referred to in later chapters on the Helmholtz and elastodynamic FMBEMs, where the procedures for accelerating the calculation of the iterative BEM matrix–vector products via the FMM are exactly the same as that presented in this chapter. The more complicated Green's function terms appearing in the full Helmholtz and elastodynamic BIEs are incorporated

by using alternate R expansions (Eq. 2.20) to represent the sources/receivers. However the steps for applying the far field calculation (upward pass, downward pass, final summation) remain unchanged, as do the other technical details for truncating/translating the expansions, use of the octree structure, calculation/storage of the sparse near field, and so on. Thus the later chapters focus on the construction and efficient propagation of the relevant expansions through the FMM procedure and refer back to this chapter for the general details of the FMM procedure.

3

Helmholtz FMBEM

This chapter presents the Helmholtz FMBEM developed to model the fluid part of the coupled FSI model. The chapter begins with a literature review of the FMBEM for the Helmholtz BIE. This is followed by a description of the Helmholtz FMBEM model developed for this thesis work, including pseudo–algorithms for the set up and solution of the Helmholtz BIE using the FMBEM. The next section discusses methods which have been implemented to reduce the algorithmic and memory complexity of the FMBEM. The final section presents numerical results for the FMBEM with comparisons to analytic solutions and/or BEM results from a commercial code. The algorithmic and memory complexity of the Helmholtz FMBEM is also investigated in the results section. A brief summary concludes the chapter.

3.1 Literature Review

The BEM numerical solution of the Helmholtz BIE for acoustic problems is a well established field, with the first applications being in 1963 for both sound radiation [63] and scattering problems [64] into infinite exterior fluid domains, while transient problems were first considered in [65]. Since then a large body of work has been published on the Helmholtz BEM for acoustics, with a number of books wholly or partly devoted to the subject (for example [6, 31, 66, 67, 68]).

The use of the FMM with the BEM for solving acoustic problems is a more recent venture, with the FMM first introduced in 1985 by Rokhlin for solving 2D Laplace BIEs [69] and popularised by Greengard & Rokhlin for solving particle interaction problems

[21, 70]. The FMM was subsequently applied to the Helmholtz fundamental solution in 2D [71] for acoustic scattering problems using the single and double layer potentials and in 3D [23] for electromagnetic scattering. Much of the early development of the FMM for the 3D Helmholtz fundamental solution was related to solving the integral forms of the Maxwell equations for electromagnetic problems (Ref. [72] reviews much of this work), with many of these innovations for the Helmholtz equation being preceded by analogous implementations for the simpler frequency independent Laplace equation. The main foci of the development the FMM have been towards the following:

Translation Methods. The main computational cost of the FMM is the application of multipole translations, particularly of the $S|R$ type, which are typically applied many more times than the $S|S$ and $R|R$ translations. In the worst case when none of the well–separated boxes are empty, 189 $S|R$ translations are required for each receiver box on every octree level [54]. The original translation methods for 3D problems required $O(p^4)$ operations for the multipole expansions of the Laplace fundamental solution [73] and $O(p^5)$ operations (using the Wigner 3–j symbol [46]) for the expansions of the Helmholtz fundamental solution [38, 43, 48]. A reduction in this algorithmic complexity was achieved by 'diagonalising' the coefficient matrices which apply the translations to the vectors of multipole expansion coefficients. This was first introduced for the Laplace solution in both 2D and 3D [74], and then for the Helmholtz solution in 2D [71, 75] and 3D [25, 76]. Diagonalisation reduces the algorithmic complexity of the 3D translations to $O(p^2\log(p))$ for both Laplace/Helmholtz solutions. However it was observed by Coifman et al. [23] and others [46, 77] that Rokhlin's diagonal translations are unstable at low frequencies due to a spherical Hankel function of the form $h_n(kt)$ which appears in the $S|R$ diagonal translations being divergent for $n > kt$, where n is the degree, k is the wavenumber and t is the translation distance [42].

In the low frequency range Chew [50] used efficient recurrence relations to reduce the 3D translation of the Helmholtz multipole expansions from $O(p^5)$ to $O(p^4)$ operations for the $R|R$ translations. Gumerov and Duraiswami derived similar relations and also showed that the $S|R$ translation could be similarly applied with $O(p^4)$ operations [78, 79]. White and Head–Gordon developed an $O(p^3)$ translation method for the Laplace multipole expansions which exploits the fact that both translations coaxial to the z–axis and arbitrary rotations of the spherical coordinate system only require $O(p^3)$ operations [52]. A similar $O(p^3)$ algorithm was developed for the Helmholtz multipole expansions,

with the coefficients derived via efficient recursion relations [41, 43]. Furthermore, symmetries in the rotation coefficients allow a reduction in the stored coefficients for rotations of both the Laplace [80] and Helmholtz [81, 82] series expansions. Gimbutas and Greengard provided an alternate method of calculating the rotation coefficients, which otherwise become unstable above $n \approx 40$ when calculated using the standard recurrence relations [83].

A diagonal $S|R$ translation method which uses exponential plane–wave expansions was developed for the Laplace multipole expansions in 2D [84, 85] and 3D [80, 86], followed by a similar implementation for the Helmholtz multipole expansions in 3D [53]. The conversion of the multipole expansions to and from the exponential expansions requires $O(p^3)$ operations, while the translations (up to 189 per receiver box) of the exponential expansions only require $O(p^2)$ operations [87]. Exploiting symmetries of the exponential translation vectors for the well separated boxes can further reduce the number of translations required from 189 to 40 [53]. Translations using the exponential expansions are stable at all frequencies [88] but are again only implemented in the low frequency range due to their formal $O(p^3)$ algorithmic complexity. Gumerov and Duraiswami showed that for the 3D Laplace equation the $O(p^3)$ low frequency RCR method and exponential expansion method have similar performance for low to moderate accuracy problems [54].

More recently, researchers have been focused towards building 'broadband' FMMs for the Helmholtz equation which utilise different translation algorithms in the low and high frequency domains. Darve and Have used a combination of the multipole expansions and Greengard's exponential expansions [53] to build 'stable plane wave' expansions which are not as costly to implement at high frequencies as the other methods [89]. Jiang and Chew [90] used the original Wigner 3–j translations at low frequencies and the diagonal forms at higher frequencies in their broadband FMM. Cheng et al. used the exponential expansions for the $S|R$ translations and the RCR method for interpolation/anterpolation in the low frequency regime and the diagonal translations at high frequencies [91]. A broadband FMBEM algorithm for solving the Helmholtz BIE was implemented by Gumerov and Duraiswami [18, 61] which employed the RCR algorithm for all $S|S$ and $R|R$ translations, and used the diagonal forms for high frequency $S|R$ translations and the RCR algorithm for low frequency $S|R$ translations. Gumerov and Duraiswami compared high frequency scattering results from their own code to

published results from another (high frequency only) FMBEM code for the Helmholtz BIE [92] where they found their own code was superior. A broadband FMM for the Helmholtz fundamental solution which used a modified version of Darve and Have's stable plane wave expansions in the low frequency regime and diagonal translations in the high frequency regime was developed by Wallen and Sarvas [93, 94] and Dufva and Sarvas [95]. Wolf and Lele have recently implemented a broadband algorithm for solving acoustic scattering problems which uses the RCR algorithm in the low frequency regime and the diagonal translations in the high frequency regime [96].

Multilevel Implementations. Another critical component in the early development of the Laplace/Helmholtz FMM were the use of multiple levels of subdivision — particularly involving interpolation and anterpolation with the various translation methods available. Rokhlin's original publication [69] had all of the hallmarks of a two level FMM but used a binary tree instead of a quadtree (for the 2D case) [88], which was introduced in Rokhlin and Greengard's later paper [21]. In both cases a constant truncation number was used between the two levels. Lu and Chew [97] showed that the algorithmic complexity for 2D Helmholtz problems scales as $O(N^2)$ for N unknowns at high frequencies when Rokhlin's original translations are used. Rokhlin showed that using his Helmholtz diagonal translations with a constant truncation number gives an algorithm that scales as $N^{3/2}$ using two octree levels and $N^{4/3}$ for three levels [76]. The mathematical basis for a 2D multilevel algorithm employing interpolation and anterpolation was proposed by Brandt [98] and implemented for the diagonal translations by Lu and Chew [99, 100], yielding an $O(N\log^2 N)$ algorithm. Dembart and Yip [77] note their use of interpolation/anterpolation in their earlier conference paper [101] (which was unavailable to this author), apparently yielding an $O(N\log^2 N)$ algorithm when multipole octree levels and diagonal translation methods were employed [102]. Song and Chew implemented a 3D multilevel algorithm [103, 104] with interpolation and anterpolation procedures which gave an $O(N\log N)$ algorithmic complexity when combined with the more efficient 'ray–propagation' FMM [105, 106]. A detailed analysis of the interpolation/anterpolation procedures for the diagonal forms of the multipole expansions was given be Gyure and Stalzer [107] and Darve [108]. Current generation fast multipole algorithms (such as the previously mentioned broadband algorithms) implement the interpolation/anterpolation procedures for the 'signature functions' which can be translated with Rokhlin's diagonal methods using the fast Fourier transform

(FFT) [109], or a combination of the FFT and the fast Legendre transform (the later being implemented using a 1D FMM [110, 111]).

In the low frequency regime, the original development of the RCR translation algorithm [52] was applied to a multilevel algorithm [51] but with a constant truncation number between octree levels. It appears that the first RCR methods employing interpolation/anterpolation was by Gumerov and Duraiswami [18, 112], with some of their earlier publications [42, 43] containing the pertinent mathematical details for applying interpolation in the coaxial translation, but no mention of using the RCR for interpolation/anterpolation procedures can be found in those references.

Similarly, the exponential expansion technique for low frequency $S|R$ translations was used in a multilevel algorithm in the original paper [84]. This translation technique is only used in the $S|R$ translations across octree levels and so does not require interpolation and anterpolation techniques. Conversely, Darve and Have's stable plane wave FMBEM [89] was implemented for multilevel octrees and includes specialised interpolation/anterpolation procedures, as do the somewhat related methods of Wallen and Sarvas [93, 94], and Dufva and Sarvas [95].

Finally, it should be noted that the adaptive multilevel FMM mentioned in the previous chapter was an early innovation in the development of the FMM — being first implemented by Carrier et al. in 1988 [113, 114].

Error Analysis. Analysis of the errors introduced by the approximations involved with the FMM was an early area of research in the field, with Rokhlin's original 1985 paper [69] showing that the errors introduced by truncating the series expansions are bounded. Greengard and Rokhlin [21, 73] similarly showed that the errors introduced from translating the expansions (using the original $O(p^5)$ methods) are also bounded. Both of these early works suggested that a desired precision for the FMM approximations could be achieved by truncating the expansions after a number of terms based upon the error bound relations. Petersen et al. used a steepest descent analysis to derive both average and maximum error estimates for the Laplace type multipole expansions in both 2D and 3D [58, 115]. Dembart and Yip provided numerical results for the errors from both the multipole expansions and diagonal signature functions as a function of the truncation number required to achieve a particular accuracy [77]. Rahola [56] and Koc et al. [59] discussed the error analysis for the Helmholtz diagonal translation methods introduced from both the truncation and numerical integration of

the far field signature functions over the unit sphere. Similar error bounds were derived by Amini and Profit when truncating the 2D Helmholtz expansions [55]. Darve improved upon the truncation formulas proposed by both Rahola and Koc et al., which are based on asymptotic forms of the spherical Bessel functions and so are not necessarily valid when the argument of the functions is of a similar magnitude to the degree [57]. A series of papers was published by Ohnuki and Chew [116, 117, 118] providing formulas for predicting the truncation number for the minimum error and the corresponding number of digits of accuracy. Gumerov and Duraiswami discussed the truncation and RCR translation errors for the spherical basis functions in their book [42].

The various errors inherent in the FMM are now well understood, with many of the cited references providing simple rules to select the truncation number of the multipole expansions (or signature functions in the high frequency regime) based on the desired accuracy of the solution, domain size of the problem and wavenumber of interest. Ongoing research is now focusing on the FMM errors resulting from applying the method to more complex BIEs, for example, the vector Green's function for the magnetic field BIE [119], the vortex particle method [120] and visco–elastodynamic problems [121].

The review of the literature on the Helmholtz FMBEM is concluded by citing the article by Nishimura [88] which provides a comprehensive review of the literature published up to 2001, as well as several text books on the subject: including Gumerov and Duraiswami's mathematically rigorous book dedicated to the 3D Helmholtz equation [42], Liu's book [38], which gives an introduction to the FMM for several BIEs including the Laplace and Helmholtz BIEs in both 2D/3D and includes source code for 2D Laplace problems, and two earlier books treating electromagnetics [122] and potential fields [123] which were not available to this author.

Finally, as an addendum to this literature review, it should be noted that the focus here has been on the developments of the fast multipole methods in relation to accelerating the matrix–vector products for the iterative BEM solution of the Helmholtz BIE. The 'other half' of the iterative solution concerns the type of technique used for convergence to the solution, as well as preconditioning methods that can accelerate the convergence. Again a large body of work exists on the subject and reviewing this literature would be outside of the scope of this thesis. As discussed in Chapter 2, the GMRES method is used for the iterative solution as it performs well for acoustic problems. Preconditioning of the FMBEM is still an ongoing area of research and the

published literature is briefly touched upon later in the chapter when introducing the preconditioning strategy used in this work.

3.2 The Helmholtz FMBEM

The Helmholtz BIE was briefly introduced in Chapter 2 and a simplified version of the equation was used to explain the main details of the FMBEM developed for this thesis. As was discussed in the conclusion of that chapter, the main steps of the FMBEM procedure for both the full Helmholtz BIE and elastodynamic BIE are the same. What differs between the BIEs is the forms of the Green's functions that must be integrated over the boundary mesh: either using numerical integration for the near field terms, or the appropriate source and receiver expansions for the FMM algorithm. Details of the numerical solution of the BIE such as the preconditioning and iterative solution of the equation must also be addressed. Finally the BEM and FMBEM for the exterior Helmholtz BIE suffer stability problems at certain frequencies and so the BIE must be modified to provide a stable solution at all frequencies.

3.2.1 The Helmholtz BIE

The Helmholtz BIE for exterior scattering problems was introduced in Chapter 2 as Eq. 2.2

$$\frac{1}{2}p(\mathbf{y}) = \int_S \left(\frac{\partial G(\mathbf{x},\mathbf{y})}{\partial \mathbf{n}(\mathbf{x})} p(\mathbf{x}) - G(\mathbf{x},\mathbf{y}) q(\mathbf{x}) \right) dS(\mathbf{x}) + p^i(\mathbf{y})$$

This equation suffers from a well known 'non–uniqueness' difficulty [28, 31, 32] where the solution is either not unique or does not exist at certain frequencies which correspond to the eigenfrequencies of the adjoint interior problem [124]. This breakdown is a result of trying to represent the problem with a BIE — the eigenfrequencies do not physically exist for the exterior domain and do not occur when using other methods to represent the problem [125]. A number of techniques have been proposed to overcome the non–uniqueness difficulty (see the reviews in, for example, Refs. [32, 126, 127] and the book chapter of Marburg and Wu [128]), with perhaps the two most common methods being the CHIEF method by Schenck [129] and the combined BIE formulation by Burton and Miller [130]. The CHIEF method stabilises the BIE by adding additional solution points located interior to the surface to the system of equations for the discretised boundary. Zero pressure is enforced at the interior points as the total pressure should

be zero everywhere interior to the surface for an exterior problem [131] and only one of the many possible solutions at the characteristic frequencies will simultaneously satisfy these interior constraints [132]. The main disadvantage of the CHIEF method is that the chosen interior points must be placed away from the nodal surfaces of the interior standing waves [132] whose locations are generally not known a priori and so the number of CHIEF points must increase with increasing frequency [6]. Alternatively, Burton and Miller suggested solving a composite BIE consisting of a linear combination of the Helmholtz BIE (Eq. 2.2) and the normal derivative of this equation, which takes the form

$$\frac{1}{2}q(\mathbf{y}) = \int_S \left(\frac{\partial^2 G(\mathbf{x},\mathbf{y})}{\partial \mathbf{n}(\mathbf{x}) \partial \mathbf{n}(\mathbf{y})} p(\mathbf{x}) - \frac{\partial G(\mathbf{x},\mathbf{y})}{\partial \mathbf{n}(\mathbf{y})} q(\mathbf{x}) \right) dS(\mathbf{x}) + q^i(\mathbf{y}) \tag{3.1}$$

where $q^i(\mathbf{x})$ indicates the normal derivative of the incident acoustic field at point $\mathbf{x}$ on the boundary surface. A linear combination of Eqs. 2.2 and 3.1 is thus

$$\begin{aligned} \frac{1}{2}\big(p(\mathbf{y}) + \alpha q(\mathbf{y})\big) =& \big(M(\mathbf{x},\mathbf{y}) + \alpha M'(\mathbf{x},\mathbf{y})\big) p(\mathbf{x}) - \big(L(\mathbf{x},\mathbf{y}) + \alpha L'(\mathbf{x},\mathbf{y})\big) q(\mathbf{x}) \\ &+ \big(p^i(\mathbf{y}) + \alpha q^i(\mathbf{y})\big) \end{aligned} \tag{3.2}$$

where:

$$L(\mathbf{x},\mathbf{y})q(\mathbf{x}) = \int_S G(\mathbf{x},\mathbf{y}) q(\mathbf{x})\, dS(\mathbf{x}) \tag{3.3}$$

$$L'(\mathbf{x},\mathbf{y})q(\mathbf{x}) = \int_S \frac{\partial G(\mathbf{x},\mathbf{y})}{\partial \mathbf{n}(\mathbf{y})} q(\mathbf{x})\, dS(\mathbf{x}) \tag{3.4}$$

$$M(\mathbf{x},\mathbf{y})p(\mathbf{x}) = \int_S \frac{\partial G(\mathbf{x},\mathbf{y})}{\partial \mathbf{n}(\mathbf{x})} p(\mathbf{x})\, dS(\mathbf{x}) \tag{3.5}$$

$$M'(\mathbf{x},\mathbf{y})p(\mathbf{x}) = \int_S \frac{\partial^2 G(\mathbf{x},\mathbf{y})}{\partial \mathbf{n}(\mathbf{x}) \partial \mathbf{n}(\mathbf{y})} p(\mathbf{x})\, dS(\mathbf{x}) \tag{3.6}$$

and α is the coupling coefficient or Burton–Miller (BM) parameter between the two BIEs. Eq. 3.2 yields a unique solution at all frequencies provided α is complex valued [130], with $\alpha = i/k$ being a near optimal choice in terms of the solution accuracy [133].

The Green's functions appearing in the above terms are:

$$G(\mathbf{x},\mathbf{y}) = \frac{e^{ikr}}{4\pi r} \tag{3.7}$$

$$\frac{\partial G(\mathbf{x},\mathbf{y})}{\partial \mathbf{n}(\mathbf{y})} = -\frac{e^{ikr}}{4\pi r^2}(ikr-1)\left(\frac{\mathbf{r}\cdot\mathbf{n}(\mathbf{y})}{r}\right) \tag{3.8}$$

$$\frac{\partial G(\mathbf{x},\mathbf{y})}{\partial \mathbf{n}(\mathbf{x})} = \frac{e^{ikr}}{4\pi r^2}(ikr-1)\left(\frac{\mathbf{r}\cdot\mathbf{n}(\mathbf{x})}{r}\right) \tag{3.9}$$

$$\begin{aligned}\frac{\partial^2 G(\mathbf{x},\mathbf{y})}{\partial \mathbf{n}(\mathbf{x})\partial \mathbf{n}(\mathbf{y})} = & \frac{e^{ikr}}{4\pi r^3}(1-ikr)\left(\mathbf{n}(\mathbf{x})\cdot\mathbf{n}(\mathbf{y})\right) \\ & - \frac{e^{ikr}}{4\pi r^3}\left(3-3ikr-k^2r^2\right)\left(\frac{\mathbf{r}\cdot\mathbf{n}(\mathbf{x})}{r}\right)\left(\frac{\mathbf{r}\cdot\mathbf{n}(\mathbf{y})}{r}\right)\end{aligned} \tag{3.10}$$

where $\cdot$ denotes the dot product between Cartesian vectors, $\mathbf{r} = \mathbf{x}-\mathbf{y}$, $r = |\mathbf{r}|$ and $\mathbf{n}(\mathbf{x})$ and $\mathbf{n}(\mathbf{y})$ are the respective unit normals at the source point $\mathbf{x}$ and receiver point $\mathbf{y}$.

As with the simplified Helmholtz equation (Eq. 2.4 in Chapter 2) the combined Helmholtz BIE can be numerically discretised and solved on an arbitrary boundary surface. Boundary conditions can be similarly employed to reduce the number of unknowns and give an exactly solvable system of equations. The next subsections explain how the FMM is used to treat the well–separated part of the surface integrals in Eq. 3.2, as well as the numerical methods used to calculate the near field integrals of the nearest neighbour elements which are not well–separated from each receiver element.

3.2.2 FMBEM Treatment of the Far Field

The FMBEM procedure presented in Chapter 2 applied the FMM to a simplified Helmholtz BIE (Eq. 2.4) using a multipole expansion of the Helmholtz Green's function (Eq. 2.11), to approximate the far field surface integrals of the form of Eq. 3.3 for each receiver. To apply the FMM to the full Burton–Miller (BM) formulation requires multipole expansions of the normal derivatives of the Green's function and so expressions for the Cartesian first partial derivatives are required, for example

$$\frac{\partial G(\mathbf{x},\mathbf{y})}{\partial \mathbf{n}(\mathbf{x})} = \frac{\partial G(\mathbf{x},\mathbf{y})}{\partial \mathbf{x}}\cdot\mathbf{n}(\mathbf{x})$$

The Cartesian first partial derivatives of the S and R multipole expansions can be expressed in terms of the *same* expansions with 'shifts' to the degree and order of the expansion coefficients. Exact recurrence relations for both S and R multipoles exist for

the following differential operators:

$$\partial_z \equiv \frac{\partial}{\partial z} \tag{3.11}$$

$$\partial_{x+iy} \equiv \frac{\partial}{\partial x} + i\frac{\partial}{\partial y} \tag{3.12}$$

$$\partial_{x-iy} \equiv \frac{\partial}{\partial x} - i\frac{\partial}{\partial y} \tag{3.13}$$

where the x and y partial derivatives can be separated as:

$$\frac{\partial}{\partial x} = \frac{1}{2}\left[\partial_{x+iy} + \partial_{x-iy}\right] \tag{3.14}$$

$$\frac{\partial}{\partial y} = -\frac{i}{2}\left[\partial_{x+iy} - \partial_{x-iy}\right] \tag{3.15}$$

The recurrence relations resulting from applying the above differential operators to the spherical basis functions (with $F = S, R$) are as follows [42, 43, 78]:

$$\partial_z F_n^m(\mathbf{r}) = k\left[a_{n-1}^m F_{n-1}^m(\mathbf{r}) - a_n^m F_{n+1}^m(\mathbf{r})\right] \tag{3.16}$$

$$\partial_{x+iy} F_n^m(\mathbf{r}) = k\left[b_{n+1}^{-m-1} F_{n+1}^{m+1}(\mathbf{r}) - b_n^m F_{n-1}^{m+1}(\mathbf{r})\right] \tag{3.17}$$

$$\partial_{x-iy} F_n^m(\mathbf{r}) = k\left[b_{n+1}^{m-1} F_{n+1}^{m-1}(\mathbf{r}) - b_n^{-m} F_{n-1}^{m-1}(\mathbf{r})\right] \tag{3.18}$$

with the coefficients a_n^m and b_n^m defined as:

$$a_n^m = a_n^{|m|} = \begin{cases} \sqrt{\frac{(n+1+|m|)(n+1-|m|)}{(2n+1)(2n+3)}}, & n \geq |m| \\ 0, & n < |m| \end{cases} \tag{3.19}$$

$$b_n^m = \begin{cases} \sqrt{\frac{(n-m+1)(n-m)}{(2n-1)(2n+1)}}, & m \geq 0 \\ -\sqrt{\frac{(n-m+1)(n-m)}{(2n-1)(2n+1)}}, & m \leq -1 \\ 0, & |m| > n \end{cases} \tag{3.20}$$

Full derivations of the above recurrence relations can be found in Refs. [78] and [42]. The normal derivative of either spherical basis function for a unit normal vector with components $\mathbf{n}(\mathbf{x}) = [n_x, n_y, n_z]$ is then [18]:

$$\begin{aligned} \frac{\partial F_n^m(\mathbf{r})}{\partial \mathbf{n}(\mathbf{x})} =& \frac{1}{2}\left[\partial_{x+iy} + \partial_{x-iy}\right] F_n^m(\mathbf{r}) n_x - \frac{i}{2}\left[\partial_{x+iy} - \partial_{x-iy}\right] F_n^m(\mathbf{r}) n_y + \partial_z F_n^m(\mathbf{r}) n_z \\ =& k\Bigg(\frac{1}{2}(n_x - i n_y)\left[b_{n+1}^{-m-1} F_{n+1}^{m+1}(\mathbf{r}) - b_n^m F_{n-1}^{m+1}(\mathbf{r})\right] \\ &+ \frac{1}{2}(n_x + i n_y)\left[b_{n+1}^{m-1} F_{n+1}^{m-1}(\mathbf{r}) - b_n^{-m} F_{n-1}^{m-1}(\mathbf{r})\right] \\ &+ n_z\left[a_{n-1}^m F_{n-1}^m(\mathbf{r}) - a_n^m F_{n+1}^m(\mathbf{r})\right]\Bigg) \end{aligned} \tag{3.21}$$

Eq. 3.21 can be used to apply normal derivatives to either type of expansion, and these can then be recombined via Eq. 2.11 to give the normal derivative of the Green's function at the source and/or receiver points. Thus applying Eq. 3.21 to R yields L', to S yields M and to both S and R yields M'. For a truncation number p_l on the lowest octree level l, the normal derivatives of the expansion require the degree to be truncated at $p_l + 1$ for the normal derivative coefficients F_{n+1} which are shifted to a higher degree. Denoting the normal derivatives of S and R with respect to the source and receiver points as $\left[S_n^m(\mathbf{r})\right]_{\mathbf{n(x)}}$ and $\left[R_n^m(\mathbf{r})\right]_{\mathbf{n(y)}}$ respectively, the BM integrals (Eqs. 3.3–3.6) can be expressed for the $\tilde{n}^{th}$ plane triangle element $E_{\tilde{n}}$ with area $A_{\tilde{n}}$ and source point $\mathbf{x}_{\tilde{n}}$ at its centre, as:

$$\left[L(\mathbf{x},\mathbf{y})q(\mathbf{x})\right]_{E_{\tilde{n}}} \approx ikA_{\tilde{n}}q(\mathbf{x}_{\tilde{n}})\sum_{n=0}^{\infty}\sum_{m=-n}^{n} S_n^m(\mathbf{c}_{\tilde{m}}-\mathbf{x}_{\tilde{n}})R_n^{-m}(\mathbf{c}_{\tilde{m}}-\mathbf{y}) \tag{3.22}$$

$$\left[L'(\mathbf{x},\mathbf{y})q(\mathbf{x})\right]_{E_{\tilde{n}}} \approx ikA_{\tilde{n}}q(\mathbf{x}_{\tilde{n}})\sum_{n=0}^{\infty}\sum_{m=-n}^{n} -S_n^m(\mathbf{c}_{\tilde{m}}-\mathbf{x}_{\tilde{n}})\left[R_n^{-m}(\mathbf{c}_{\tilde{m}}-\mathbf{y})\right]_{\mathbf{n(y)}} \tag{3.23}$$

$$\left[M(\mathbf{x},\mathbf{y})p(\mathbf{x})\right]_{E_{\tilde{n}}} \approx ikA_{\tilde{n}}p(\mathbf{x}_{\tilde{n}})\sum_{n=0}^{\infty}\sum_{m=-n}^{n} -\left[S_n^m(\mathbf{c}_{\tilde{m}}-\mathbf{x}_{\tilde{n}})\right]_{\mathbf{n}(\mathbf{x}_{\tilde{n}})}R_n^{-m}(\mathbf{c}_{\tilde{m}}-\mathbf{y}) \tag{3.24}$$

$$\left[M'(\mathbf{x},\mathbf{y})p(\mathbf{x})\right]_{E_{\tilde{n}}} \approx ikA_{\tilde{n}}p(\mathbf{x}_{\tilde{n}})\sum_{n=0}^{\infty}\sum_{m=-n}^{n} \left[S_n^m(\mathbf{c}_{\tilde{m}}-\mathbf{x}_{\tilde{n}})\right]_{\mathbf{n}(\mathbf{x}_{\tilde{n}})}\left[R_n^{-m}(\mathbf{c}_{\tilde{m}}-\mathbf{y})\right]_{\mathbf{n(y)}} \tag{3.25}$$

where $\mathbf{c}_{\tilde{m}}$ is the expansion centre of the $\tilde{m}^{th}$ box containing $\mathbf{x}_{\tilde{n}}$. The expansion for L is analogous to Eq. 2.19. The minus signs for L' and M account for the fact that the normal derivatives of the expansions are applied to expansion vectors which are directed *away* from the source and receiver points (see Fig. 2.18) and thus give the negative of the normal derivative at those points when the Green's function is reconstructed. The minus signs from applying the normal derivative to both source/receiver expansions for the M' expansions cancel one another. It can be seen from the above expressions that the four BM terms only require two unique S expansions to be propagated through the FMM procedure, with L, L' and M, M' having the same source expansions. Once propagated through the upward/downward pass of the FMM, the two types of S expansions may be combined with the R expansions in the final summation to give the well–separated surface integrals of the L and M terms, and with the $R_{\mathbf{n(y)}}$ normal derivative expansions to yield the L' and M' terms. Recalling from

Chapter 2 that both sources/receivers are represented with R expansions, the required source expansions for the far field part of the surface integrals in Eq. 3.2 take the form (when truncating the expansions at degree $n = p_l$):

$$A_{\tilde{n}} q(\mathbf{x}_{\tilde{n}}) R_{p_l}^m(\mathbf{c}_{\tilde{m}} - \mathbf{x}_{\tilde{n}}) \tag{3.26}$$

$$A_{\tilde{n}} p(\mathbf{x}_{\tilde{n}}) \left[R_{p_l}^m(\mathbf{c}_{\tilde{m}} - \mathbf{x}_{\tilde{n}})\right]_{\mathbf{n}(\mathbf{x}_{\tilde{n}})} \tag{3.27}$$

for the $\tilde{n}^{th}$ element of the discretised mesh, where the source point $\mathbf{x}_{\tilde{n}}$ of the element is contained within the $\tilde{m}^{th}$ octree box with centre $\mathbf{c}_{\tilde{m}}$ on the lowest octree level l. Note that to build $\left[R_n^m\right]_{\mathbf{n}(\mathbf{x}_{\tilde{n}})}$ with the degree truncated at p_l requires degree terms up to $p_l + 1$ in the truncated series expansion of R_n^m (see Eq. 3.21).

Finally, it should be noted that one of the principal criticisms of the BM formulation is that it doubles the number of surface integrals required compared to the Helmholtz BIE. In the conventional BEM this effectively doubles the set–up time to build all four matrices. In the FMBEM the majority of the work in propagating the expansions through the upward/downward pass of the FMM must already be applied for the Helmholtz BIE for the L and M terms, while the additional integral terms, L' and M', of the BM formulation can be cheaply calculated by 'swapping out' the receiver expansions in the final summation step of the FMM procedure. Thus there is only a small additional computational cost in building the well–separated parts of the two introduced BM integrals and so the calculation of the sparse near field matrices constitutes the main cost in the BM implementation of the FMBEM.

3.2.3 Numerical Treatment of the Near Field

The near field part of the surface integrals for each receiver consist of any elements contained within the same octree box or the nearest neighbour boxes on the lowest octree level which share a vertex, edge or face with the box containing the receiver element (see Fig. 3.1). The elements in this region are integrated using numerical quadrature and combined with the far field FMM contributions to give the complete surface integral at each receiver point. It can be seen from Eqs. 3.7–3.10 that all of the Green's function terms have a $\frac{1}{r}$ type dependence and thus exhibit singular behaviour as $r \to 0$. Different integration methods must be employed depending upon the separation distance r between the source element (to be integrated over) and the receiver element (at which the integral is to be evaluated).

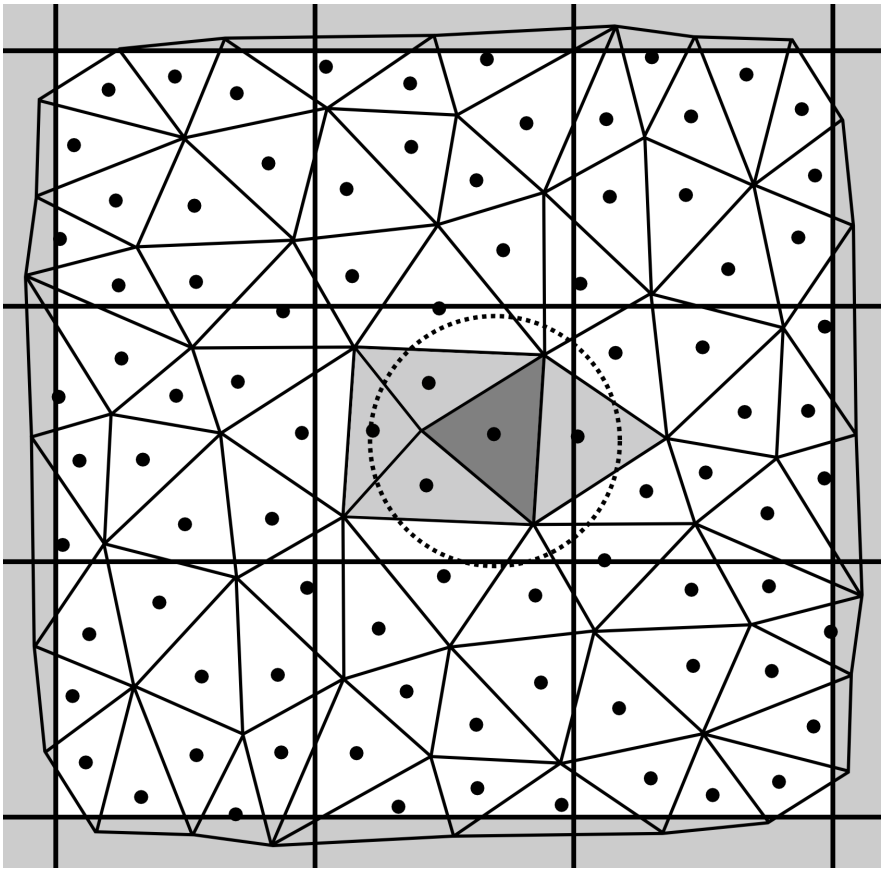

Figure 3.1: The near field elements on the lowest octree level. The sources contained within the white elements are sufficiently separated from the receiver in the dark grey element and can be treated using a standard numerical integration technique. The light grey elements whose sources lie within a certain radius (dashed circle) of the receiver will have a small radial distance between the source/receiver points and this may be sufficiently small for the Green's function to show near–singular behaviour. The integral over the dark grey element from the source at the centre of that element must be evaluated at the *coincident* receiver location in the same element. Thus the radial distance is zero and the integral over the receiver element will be singular.

Regular Integration. The integrals of the near field elements which are separated from the receiver by a sufficient distance do not show near–singular or singular behaviour i.e. r is not small in the various Green's functions (Eqs. 3.7–3.10). Thus the numerical integrations are applied using standard low order Gauss–Legendre quadrature rules, where the triangle is transformed to a (η, ν) square with $-1 \leq (\eta, \nu) \leq 1$

such that the Gauss–Legendre formulae can be directly applied [134].

Near–Singular Integration. For the elements which are very close to the receiver element, for example sharing a vertex or edge with the receiver element, r may be sufficiently small in Eqs. 3.7–3.10 to exhibit near–singular behaviour in the element integrals. Generally these situations occur in the BEM due to the model geometry, for example when dealing with thin shapes or wing/fin edges, or when evaluating the field very close to the boundary surface where r is much smaller than the typical element dimensions. The nearest elements which may show near–singular behaviour are determined by finding the average side length s_{av} of the plane triangles in the boundary mesh and then using a specialised near–singular integration technique [135] for all elements which have $r \lesssim s_{av}$. The near field elements outside of this region can be treated with standard numerical integration techniques.

Singular Integration. Finally the integral over the receiver element from the *coincident* source point collocated at the centre of the same element must be evaluated i.e. at $\mathbf{x} = \mathbf{y}$ in Eqs. 3.3–3.6 for the singular integrals. The orders of singularities for the integral terms appearing in the BM formulation are shown in Table 3.1.

Table 3.1: The order of the singularities involved when integrating the Green's function terms in the BM formulation when $\mathbf{x} = \mathbf{y}$ in Eqs. 3.3–3.6.

BM Integral Term	L	L'	M	M'
Order of Singularity	$O\left(\frac{1}{r}\right)$	$O\left(\frac{1}{r^2}\right)$	$O\left(\frac{1}{r^2}\right)$	$O\left(\frac{1}{r^3}\right)$

The BM formulation for stabilising the Helmholtz BIE introduces the M' term which involves a so called 'hyper–singular' $\frac{1}{r^3}$ integral which are in general very difficult to integrate. Burton and Miller noted the difficulty in integrating the hyper–singular integral in their original paper [130], where they suggested a regularization technique to weaken the singularity at the cost of introducing additional surface integrals. A number of numerical integration methods to weaken or remove the hyper–singular integral have since been developed, with the majority of techniques involving either singularity subtractions, coordinate transformations or the substitution of integral identities: see for example Refs. [136, 137, 138, 139] and references therein for reviews of the literature.

For the plane triangle elements with piece–wise constant unknowns used in this work, and commonly used in many FMM implementations, all of the BM integral terms may be explicitly evaluated using the method of Matsumoto et al. [140, 141]. It can be shown that the $\frac{1}{r^2}$ type singular integrals for L' and M vanish, while the weakly singular and hyper–singular integrals for L and M' may be evaluated as regular contour integrals over the edge of the singular receiver element [140]. These contour integrals may be evaluated using either low order Gauss Legendre quadrature (as is done here), or, as it has recently been shown, evaluated analytically [142].

3.2.4 FMBEM Iterative Solution and Preconditioning

As discussed in Chapter 2, the FMM accelerates the matrix–vector products in the iterative BEM solution of the $\mathbf{Az} = \mathbf{b}$ discretised system of equations and here the GMRES method [34] is used for the iterative solution of acoustic problems [35]. Central to the convergence of the iterative solution is the use of an appropriate preconditioner $\mathbf{A}_{\text{pre}}$, which seeks to improve the condition number of the BEM coefficient matrix and so reduce the number of iterations required for convergence of the system $\mathbf{A}_{\text{pre}}\mathbf{Az} = \mathbf{A}_{\text{pre}}\mathbf{b}$. Particularly, one would like $\mathbf{A}_{\text{pre}} \sim \mathbf{A}^{-1}$ so that $\mathbf{A}_{\text{pre}}\mathbf{A} \sim \mathbf{I}$. A review of various preconditioning methods can be found in Ref. [143].

The use of preconditioners with the FMBEM appears to have been first implemented by Nabors et al. [144, 145], where they calculated the approximate inverse of the near field elements for each receiver box on the lowest octree level using the near field integrals that must be directly calculated for the elements which are not well–separated in the FMM. Similar block–diagonal preconditioners constructed from the sparse diagonal near field matrix were implemented by Song et al. [102] and Sertel and Volakis [146] using LU (lower–upper) and ILU (incomplete lower–upper) decompositions respectively. Gurel and Ergel compared the convergence rates for a number of types of preconditioner [147]. Many of the aforementioned references relate to preconditioning of electromagnetic scattering problems (a review of much of the literature can be found in Ref. [148]). Iterative solution and ILU preconditioning for acoustic problems was treated by Marburg and Schneider [35, 149], while Fischer et al. [150] and Fischer and Gaul [151] applied approximate inverse and Calderon–based preconditioners for acoustic FMBEM problems.

A combination of strategies has been employed here to accelerate the convergence of the iterative solution. Firstly a low accuracy FMBEM is used as a preconditioner for the main FMBEM iterative solution, as was suggested in Ref. [18]. The truncation numbers for the preconditioner FMBEM are similarly calculated via Eq. 2.17 using a large error tolerance of $\epsilon_{\text{pre}} = 0.2$ and the GMRES convergence tolerance for the preconditioner is set to $\xi_{\text{pre}} = 0.15$. It should be noted that the various multipole expansions/translations required for the FMBEM preconditioner do not need to be separately calculated and stored: the same multipole expansions/translations for the main loop can simply be truncated to the required length and used. Similarly, the sparse near field matrix for the FMBEM preconditioner is exactly the same as that for the main loop. Thus the FMBEM preconditioner does not introduce any additional memory requirements and can be applied at the same algorithmic complexity as the main FMBEM (though in practice it is several times faster due to the smaller multipole expansions). The use of the low accuracy FMBEM as a preconditioner to the main FMBEM loop changes the equivalent preconditioning matrix each iteration and so the flexible GMRES (fGMRES) method [152, 153] is used, which allows a different preconditioner each iteration. Additionally the inner GMRES loop is itself preconditioned using a sparse approximate inverse (SAI) preconditioner [62] constructed from the near field part of the surface integrals, as suggested by Carpentieri et al. [154]. It has been observed by some authors [18, 155] that the exclusive use of local preconditioners (based only on the diagonal near field matrix) give poor results at higher frequencies due to the reduced diagonal dominance of the coefficient matrix [156] while the combined method used here provides good convergence over a wide frequency range.

3.2.5 Helmholtz FMBEM Algorithm

This section is concluded by presenting pseudocode algorithms for the iterative FMBEM solution for an arbitrary exterior acoustic scattering problem described by Eq. 3.2. The BIE is discretised with a boundary mesh consisting of N plane triangle elements with corresponding areas A_N, and there is a known incident field of wavenumber k defined at the coincident source/receiver positions at the centres of each of the elements. A Robin type BC is assumed on the surface which relates the total surface pressure $p(\mathbf{x})$ to its normal derivative $q(\mathbf{x})$ by some known function $g(\mathbf{x})$ i.e. $q(\mathbf{x}) = g(\mathbf{x})p(\mathbf{x})$ and so all four BM terms appear in the algorithm. The algorithm is split into two parts: the first part

(Alg. 3.1) sets up the problem by building the octree, multipole expansions/translations and near field integrals while the second part (Alg. 3.3) implements the FMBEM iterative solution to the problem. The algorithm for the FMBEM procedure is presented separately as Alg. 3.2 which is called by both the main and preconditioner GMRES loops in the iterative solution algorithm.

Algorithm 3.1 Helmholtz FMBEM Algorithm: Set up

Define Problem Parameters
$[\epsilon, \epsilon_{\text{pre}}]$ = prescribed accuracy for the FMM and preconditioner FMM expansions: defaults = $[10^{-4}, 0.2]$ respectively
$[\xi, \xi_{\text{pre}}]$ = [main, preconditioner] GMRES convergence tolerance: defaults = $[10^{-4}, 0.15]$ respectively
$[\hat{\text{its}}, \hat{\text{its}}_{\text{pre}}]$ = [main, preconditioner] GMRES maximum number of iterations: typical values $\approx [50 < \hat{\text{its}} < 400, 30 < \hat{\text{its}}_{\text{pre}} < 100]$
$\mathbf{P} = P \times 3$ list of xyz components of P surface mesh points
$\mathbf{N} = N \times 3$ list of node numbers for each of the N triangular elements
s_{av} = average side length of mesh elements
$\mathbf{x}_N, \mathbf{y}_N$ = lists of $N \times 3$ source and receiver points respectively. $\mathbf{x}_N = \mathbf{y}_N$
$\hat{x}$ = maximum number of sources per finest octree box: default $\lesssim 0.1\%$ of N
$\mathbf{x}_{3l}$ = bit–interleaved binary numbers of $\mathbf{x}_N$: default $l = 21$ (63 bits), see Ref. [42]
procedure PRECOMPUTE($\epsilon, \epsilon_{\text{pre}}, s_{\text{av}}, \mathbf{x}_N, \mathbf{y}_N, \hat{x}, \mathbf{x}_{3l}, \alpha, \mathbf{P}, \mathbf{N}$)
    function MAX_OCTREE($\mathbf{x}, \hat{x}$) ▷ determine lowest octree level
        $l = 2$ ▷ initially set max octree level to 2
        while mode($\mathbf{x}_{3l}$) > $\hat{\text{x}}$ **do** ▷ do while most common $\mathbf{x}_{3l}$ exceeds $\hat{x}$
            Calculate $\mathbf{c}_l$ = centres of the boxes containing $\mathbf{x}_N$ on level l
            $l = l + 1$ ▷ increase octree level, increase $\mathbf{x}_{3l}$ by 3 bits, see Ref. [42]
        end while
        return max octree level $\hat{l} = l$, $\mathbf{c}_l$, $\mathbf{x}_{3l}$ truncated to $3l$ leading bits
    end function

    function TRUNC_NOS($\hat{l}, \epsilon, \epsilon_{\text{pre}}$) ▷ set truncation numbers for all levels
        for $l = 2 : \hat{l}$ **do**
            Calculate $p_l, (p_l)_{\text{pre}}$ ▷ via Eq. 2.17
        end for
        return truncation numbers $p_l, (p_l)_{\text{pre}}$ for each octree level
    end function

Algorithm 3.1 Helmholtz FMBEM Algorithm: Set up (Cont.)

function BUILD_EXPTRANS($\mathbf{x}_N, \mathbf{y}_N, \mathbf{c}_l, p_l$) ▷ precompute/store coefficients
  Calculate $R_{\hat{l}}(\mathbf{c}_{\hat{l}} - \mathbf{x}_N) = R^{m=-n:n}_{n=0:(p_{\hat{l}})+1}(\mathbf{c}_{\hat{l}} - \mathbf{x}_N)$ ▷ via Eq. 2.8
  Calculate $[R_{\hat{l}}(\mathbf{c}_{\hat{l}} - \mathbf{x}_N)]_{\mathbf{n}(\mathbf{x}_N)}$ ▷ via Eq. 3.21, truncate $R_{\hat{l}}$ to $n = p_{\hat{l}}$
  for $l = \hat{l} : 3$ **do** ▷ calculate/store $S|S$ and $R|R$ translations
    Calculate $(SS)_l = (S|S)_{p_l \to p_{(l-1)}}(\mathbf{c}_{(l-1)} - \mathbf{c}_l)$ ▷ see Section 2.2.2
    Calculate $(RR)_{(l-1)} = (R|R)_{p_{(l-1)} \to p_l}(\mathbf{c}_l - \mathbf{c}_{(l-1)})$
  end for

  for $l = \hat{l} : 2$ **do** ▷ calculate/store $S|R$ translations
    Calculate $(SR)_l = (S|R)\big(\mathbf{c}_l - \{\{\{\mathbf{c}_l\}_\mathrm{p}\}_\mathrm{n}\}_\mathrm{c} \setminus \{\mathbf{c}_l\}_\mathrm{n}\big)$ ▷ where $\{\,\}_\mathrm{p}$, $\{\,\}_\mathrm{n}$, $\{\,\}_\mathrm{c}$ denote parent, neighbour, children octree searches and $\setminus$ denotes the relative complement of two sets: see Section 2.2.2
  end for
  return $R_{\hat{l}}, [R_{\hat{l}}]_{\mathbf{n}(\mathbf{x}_N)}, (SS)_l, (RR)_l, (SR)_l$
end function

function NEAR_FIELD($N, \mathbf{x}_N, \mathbf{y}_N, s_\mathrm{av}, \mathbf{P}, \mathbf{N}$) ▷ build/store near field matrices
  for $\tilde{n} = 1 : N$ **do** ▷ numerical integrals require $\mathbf{P}, \mathbf{N}$
    if $|\{\mathbf{x}_{\tilde{n}}\}_\mathrm{n} - \mathbf{y}_{\tilde{n}}| > s_\mathrm{av}$ **then** ▷ regular integral set $\{\,\}_\mathrm{r}$, see Fig. 3.1
      Calculate $\big\{L(\{\mathbf{x}_{\tilde{n}}\}_\mathrm{n}, \mathbf{y}_{\tilde{n}}) + \alpha L'(\{\mathbf{x}_{\tilde{n}}\}_\mathrm{n}, \mathbf{y}_{\tilde{n}})\big\}_\mathrm{r}$ ▷ see Ref. [134]
      Calculate $\big\{M(\{\mathbf{x}_{\tilde{n}}\}_\mathrm{n}, \mathbf{y}_{\tilde{n}}) + \alpha M'(\{\mathbf{x}_{\tilde{n}}\}_\mathrm{n}, \mathbf{y}_{\tilde{n}})\big\}_\mathrm{r}$
    end if
    if $|\{\mathbf{x}_{\tilde{n}}\}_\mathrm{n} - \mathbf{y}_{\tilde{n}}| < s_\mathrm{av}$ **&** $\{\mathbf{x}_{\tilde{n}}\}_\mathrm{n} \neq \mathbf{y}_{\tilde{n}}$ **then** ▷ near–singular
      Calculate $\big\{L(\{\mathbf{x}_{\tilde{n}}\}_\mathrm{n}, \mathbf{y}_{\tilde{n}}) + \alpha L'(\{\mathbf{x}_{\tilde{n}}\}_\mathrm{n}, \mathbf{y}_{\tilde{n}})\big\}_\mathrm{ns}$ ▷ integral set $\{\,\}_\mathrm{ns}$
      Calculate $\big\{M(\{\mathbf{x}_{\tilde{n}}\}_\mathrm{n}, \mathbf{y}_{\tilde{n}}) + \alpha M'(\{\mathbf{x}_{\tilde{n}}\}_\mathrm{n}, \mathbf{y}_{\tilde{n}})\big\}_\mathrm{ns}$ ▷ see Ref. [135]
    end if
    if $|\{\mathbf{x}_{\tilde{n}}\}_\mathrm{n} - \mathbf{y}_{\tilde{n}}| < s_\mathrm{av}$ **&** $\{\mathbf{x}_{\tilde{n}}\}_\mathrm{n} = \mathbf{y}_{\tilde{n}}$ **then** ▷ singular integrals $\{\,\}_\mathrm{s}$
      Calculate $\big\{L(\{\mathbf{x}_{\tilde{n}}\}_\mathrm{n}, \mathbf{y}_{\tilde{n}})\big\}_\mathrm{s}, \big\{\alpha M'(\{\mathbf{x}_{\tilde{n}}\}_\mathrm{n}, \mathbf{y}_{\tilde{n}})\big\}_\mathrm{s}$ ▷ see Ref. [140]
    end if
  end for
  Build $\mathbf{L}_\mathrm{nf} = \{L + \alpha L'\}_\mathrm{r} + \{L + \alpha L'\}_\mathrm{ns} + \{L\}_\mathrm{s}$ ▷ sparse near field matrices
  Build $\mathbf{M}_\mathrm{nf} = \{M + \alpha M'\}_\mathrm{r} + \{M + \alpha M'\}_\mathrm{ns} + \{\alpha M'\}_\mathrm{s}$
  Calculate $(\mathbf{LM})_\mathrm{pre}$ ▷ SAI preconditioner from $\mathbf{L}_\mathrm{nf}, \mathbf{M}_\mathrm{nf}$, see Ref. [62]
  return $\mathbf{L}_\mathrm{nf}, \mathbf{M}_\mathrm{nf}, (\mathbf{LM})_\mathrm{pre}$
end function
end procedure

The set up algorithm builds and stores in RAM all required expansions/translations for the FMM, as well as the sparse near field matrices. This data is passed to the iterative solution algorithm to solve the BIE on the boundary surface. Assuming a Robin BC, Eq. 3.2 can be discretised into the form of an $\mathbf{Az} = \mathbf{b}$ matrix equation

$$\left[\Big(\frac{1}{2}\mathbf{I}_N + \mathbf{L}_N\Big)g(\mathbf{x}_N) + \Big(\frac{\alpha}{2}\mathbf{I}_N - \mathbf{M}_N\Big)\right] p(\mathbf{x}_N) = \big(p^i(\mathbf{y}_N) + \alpha q^i(\mathbf{y}_N)\big) \tag{3.28}$$

where $\mathbf{L}_N = \big[L(\mathbf{x}_N, \mathbf{y}_N) + \alpha L'(\mathbf{x}_N, \mathbf{y}_N)\big]$, $\mathbf{M}_N = \big[M_N(\mathbf{x}_N, \mathbf{y}_N) + \alpha M'(\mathbf{x}_N, \mathbf{y}_N)\big]$ and $\mathbf{I}_N$ is the identity matrix of size $N \times N$. Alg. 3.2 presents the FMBEM algorithm for accelerating the calculation of $\mathbf{L}_N$ and $\mathbf{M}_N$. Both the main and preconditioner GMRES loops call Alg. 3.2 each iteration using the truncation numbers $(p_l, (p_l)_{\text{pre}})$.

Algorithm 3.2 Helmholtz FMBEM Algorithm

function HELM_FMBEM($k, p_l, p(\mathbf{x}_N), q(\mathbf{x}_N), \alpha, A_N, R_{\hat{l}}, [R_{\hat{l}}]_{\mathbf{n}(\mathbf{x}_N)}, (SS)_l, (RR)_l, (SR)_l, \mathbf{L}_{\text{nf}}, \mathbf{M}_{\text{nf}}$)
  $[R_{\hat{l}}(\mathbf{c}_{\hat{l}})]_{\mathbf{n}(\mathbf{x}_N)} = \{A_N p(\mathbf{x}_N)[R_{\hat{l}}(\mathbf{c}_{\hat{l}} - \mathbf{x}_N)]_{\mathbf{n}(\mathbf{x}_N)}\}_{\mathbf{c}_l}$ ▷ via Eqs. 3.26 and 3.27
  $R_{\hat{l}}(\mathbf{c}_{\hat{l}}) = \{A_N q(\mathbf{x}_N) R_{\hat{l}}(\mathbf{c}_{\hat{l}} - \mathbf{x}_N)\}_{\mathbf{c}_{\hat{l}}}$ ▷ $\{\,\}_{\mathbf{c}_{\hat{l}}}$ combines R,$[R]_{\mathbf{n}(\mathbf{x}_N)}$ with common $\mathbf{c}$
  for $l = \hat{l} : 3$ **do** ▷ upward pass: see Section 2.3.1
    $R_{l-1}(\mathbf{c}_{l-1}) = \{(SS)_l R_l(\mathbf{c}_l)\}_{\mathbf{c}_{l-1}}$ ▷ apply $S|S$ translations
    $[R_{l-1}(\mathbf{c}_{l-1})]_{\mathbf{n}(\mathbf{x}_N)} = \{(SS)_l [R_l(\mathbf{c}_l)]_{\mathbf{n}(\mathbf{x}_N)}\}_{\mathbf{c}_{l-1}}$ ▷ via Eq. 2.13
  end for
  for $l = 2 : \hat{l}$ **do** ▷ downward pass: see Section 2.3.2
    $S_l(\mathbf{c}_l) = (SR)_l R_l\big(\{\{\{\mathbf{c}_l\}_{\text{p}}\}_{\text{n}}\}_{\text{c}} \setminus \{\mathbf{c}_l\}_{\text{n}}\big)$ ▷ apply $S|R$ translations
    $[S_l(\mathbf{c}_l)]_{\mathbf{n}(\mathbf{x}_N)} = (SR)_l [R_l\big(\{\{\{\mathbf{c}_l\}_{\text{p}}\}_{\text{n}}\}_{\text{c}} \setminus \{\mathbf{c}_l\}_{\text{n}}\big)]_{\mathbf{n}(\mathbf{x}_N)}$ ▷ via Eq. 2.14
    if $l \neq \hat{l}$ **then**
      $S_{l+1}(\mathbf{c}_{l+1}) = \{(RR)_l S_l(\mathbf{c}_l)\}_{\mathbf{c}_{l+1}}$ ▷ apply $R|R$ translations
      $[S_{i+1}(\mathbf{c}_{l+1})]_{\mathbf{n}(\mathbf{x}_N)} = \{(RR)_l [S_l(\mathbf{c}_l)]_{\mathbf{n}(\mathbf{x}_N)}\}_{\mathbf{c}_{l+1}}$ ▷ via Eq. 2.12
    end if
  end for
  ▷ final summation: see Section 2.3.3, where $\overline{\ }$ denotes the complex conjugate
  $\mathbf{L}_{\text{ff}} = ik \sum_{n=0}^{p_{\hat{l}}} \sum_{m=-n}^{n} \Big(S_{\hat{l}}(\mathbf{c}_{\hat{l}}) \overline{R_{\hat{l}}(\mathbf{c}_{\hat{l}} - \mathbf{x}_N)} - \alpha S_{\hat{l}}(\mathbf{c}_{\hat{l}}) \overline{[R_{\hat{l}}(\mathbf{c}_{\hat{l}} - \mathbf{x}_N)]_{\mathbf{n}(\mathbf{x}_N)}}\Big)$
  $\mathbf{M}_{\text{ff}} = ik \sum_{n=0}^{p_{\hat{l}}} \sum_{m=-n}^{n} \Big(\alpha [S_{\hat{l}}(\mathbf{c}_{\hat{l}})]_{\mathbf{n}(\mathbf{x}_N)} \overline{[R_{\hat{l}}(\mathbf{c}_{\hat{l}} - \mathbf{x}_N)]_{\mathbf{n}(\mathbf{x}_N)}} - [S_{\hat{l}}(\mathbf{c}_{\hat{l}})]_{\mathbf{n}(\mathbf{x}_N)} \overline{R_{\hat{l}}(\mathbf{c}_{\hat{l}} - \mathbf{x}_N)}\Big)$
  return $\big(\mathbf{L}_N\big)q(\mathbf{x}_N) = \mathbf{L}_{\text{ff}} + \big(\mathbf{L}_{\text{nf}}\big)q(\mathbf{x}_N)$, $\big(\mathbf{M}_N\big)p(\mathbf{x}_N) = \mathbf{M}_{\text{ff}} + \big(\mathbf{M}_{\text{nf}}\big)p(\mathbf{x}_N)$
end function

In the final summation procedure the receiver expansions are constructed from the complex conjugates of the source expansions (for coincident source/receiver points) using the relation $\overline{R_n^m(\mathbf{r})} = R_n^{-m}(\mathbf{r})$ [42]. Alg. 3.3 presents the iterative FMBEM solution of Eq. 3.28 using the nested fGMRES loop and SAI preconditioner.

Algorithm 3.3 Helmholtz FMBEM Algorithm: Iterative Solution

function IT_SOLVE($p^i(\mathbf{y}_N), q^i(\mathbf{y}_N), \alpha,$ HELM_FMBEM$(\ldots), \xi, \xi_{\text{pre}}, \hat{\text{its}}, \hat{\text{its}}_{\text{pre}}$)
  $p(\mathbf{x}_N) = \mathbf{0}_N$ ▷ set initial guess as vector of zeros
  $\mathbf{p}^i = \big[p^i(\mathbf{y}_N) + \alpha q^i(\mathbf{y}_N)\big], \quad \mathbf{g}_N = \frac{1}{2}\big[1+\alpha\big]\mathbf{I}_N g(\mathbf{x}_N)$ ▷ simplify notation
  $\big[\big(\mathbf{L}_N\big)[g(\mathbf{x}_N)p(\mathbf{x}_N)], \big(\mathbf{M}_N\big)p(\mathbf{x}_N)\big]$ = HELM_FMBEM$\big(k, p_l, p(\mathbf{x}_N),$ $[g(\mathbf{x}_N)p(\mathbf{x}_N)], \ldots\big)$
  $\boldsymbol{\xi}_N = \mathbf{g}_N p(\mathbf{x}_N) + \big(\mathbf{L}_N\big)[g(\mathbf{x}_N)p(\mathbf{x}_N)] - \big(\mathbf{M}_N\big)p(\mathbf{x}_N) - \mathbf{p}^i, \quad \tilde{\text{its}} = 0$ ▷ calculate initial residual and set loop counter

  while norm$(\boldsymbol{\xi}_N) > \xi$ **and** $\tilde{\text{its}} < \hat{\text{its}}$ **do** ▷ main GMRES loop
    $p(\mathbf{x}_N)_{\text{pre}} = \mathbf{0}_N, \quad (\boldsymbol{\xi}_N)_{\text{pre}} = \infty, \quad \tilde{\text{its}}_{\text{pre}} = 0$ ▷ preconditioner initial values
    while norm$((\boldsymbol{\xi}_N)_{\text{pre}}) > \xi_{\text{pre}}$ **and** $\tilde{\text{its}}_{\text{pre}} < \hat{\text{its}}_{\text{pre}}$ **do** ▷ preconditioner
      $\big[(\mathbf{L}_N)_{\text{pre}}[g(\mathbf{x}_N)p(\mathbf{x}_N)], (\mathbf{M}_N)_{\text{pre}}p(\mathbf{x}_N)\big]$ = HELM_FMBEM$\big(k, (p_l)_{\text{pre}},$ $p(\mathbf{x}_N)_{\text{pre}}, [g(\mathbf{x}_N)p(\mathbf{x}_N)_{\text{pre}}], \ldots\big)$
      $(\boldsymbol{\xi}_N)_{\text{pre}} = (\mathbf{LM})_{\text{pre}}\big[\mathbf{g}_N p(\mathbf{x}_N)_{\text{pre}} + (\mathbf{L}_N)_{\text{pre}}[g(\mathbf{x}_N)p(\mathbf{x}_N)_{\text{pre}}] - (\mathbf{M}_N)_{\text{pre}} \times$ $p(\mathbf{x}_N)_{\text{pre}}\big] - (\mathbf{LM})_{\text{pre}}\left(\frac{(\boldsymbol{\xi}_N)}{\text{norm}(\boldsymbol{\xi}_N)}\right)$ ▷ residual of $\mathbf{A}_{\text{inv}}\mathbf{A}\mathbf{x} - \mathbf{A}_{\text{inv}}\mathbf{b}$ with $\mathbf{b} = \left(\frac{(\boldsymbol{\xi}_N)}{\text{norm}(\boldsymbol{\xi}_N)}\right)$ from the main GMRES loop and $\mathbf{A}_{\text{inv}} = (\mathbf{LM})_{\text{pre}}$
      $p(\mathbf{x}_N)_{\text{pre}} = \text{GMRES}((\boldsymbol{\xi}_N)_{\text{pre}}), \quad \tilde{\text{its}}_{\text{pre}} = \tilde{\text{its}}_{\text{pre}} + 1$ ▷ update preconditioner solution using GMRES (see Ref. [152]) and update inner counter
    end while

    $\big[\big(\mathbf{L}_N\big)[g(\mathbf{x}_N)p(\mathbf{x}_N)_{\text{pre}}], \big(\mathbf{M}_N\big)p(\mathbf{x}_N)_{\text{pre}}\big]$ = HELM_FMBEM$\big(k, p_l, p(\mathbf{x}_N)_{\text{pre}},$ $[g(\mathbf{x}_N)p(\mathbf{x}_N)_{\text{pre}}], \ldots\big)$ ▷ use inner GMRES solution in main FMBEM
    $\boldsymbol{\xi}_N = \mathbf{g}_N p(\mathbf{x}_N)_{\text{pre}} + \big(\mathbf{L}_N\big)[g(\mathbf{x}_N)p(\mathbf{x}_N)_{\text{pre}}] - \big(\mathbf{M}_N\big)p(\mathbf{x}_N)_{\text{pre}} - \mathbf{p}^i$ ▷ residual from main GMRES iteration
    $p(\mathbf{x}_N) = \text{fGMRES}(\boldsymbol{\xi}_N) \quad \tilde{\text{its}} = \tilde{\text{its}} + 1$ ▷ update solution using fGMRES (see Ref. [152]) and update outer counter
  end while
end function

Thus applying Alg. 3.3 allows the total surface pressure $p(\mathbf{y}_N)$ in Eq. 3.28 to be solved using the FMBEM. The above algorithms have been presented for Eq. 3.2 assuming a Robin BC of the form $q(\mathbf{x}) = g(\mathbf{x})p(\mathbf{x})$. The algorithms can be suitably modified for the other common BCs: if the total surface pressure is described by a known function $p(\mathbf{x}_N) = g(\mathbf{x}_N)$ on the discretised boundary surface (Dirichlet BC), Eq. 3.2 becomes:

$$\Big(\frac{\alpha}{2}\mathbf{I}_N + \mathbf{L}_N\Big)q(\mathbf{x}_N) = \big(p^i(\mathbf{y}_N) + \alpha q^i(\mathbf{y}_N)\big) - \Big(\frac{1}{2}\mathbf{I}_N - \mathbf{M}_N\Big)g(\mathbf{x}_N) \tag{3.29}$$

in the form $\mathbf{Az} = \mathbf{b}$. Alg. 3.2 is called once to precompute $\left(\frac{1}{2}\mathbf{I}_N - \mathbf{M}_N\right) g(\mathbf{x}_N)$ and this is added to the known incident field $\mathbf{p}^i$ to construct $\mathbf{b}$ in the matrix equation. Alg. 3.3 is then used to solve Eq. 3.29 with $p(\mathbf{x}) = \mathbf{0}_N$ (in practice the $\mathbf{M}_N$ terms are not calculated at all in the iterative solution). Conversely if the normal derivative of the total surface pressure is known on the surface $q(\mathbf{x}_N) = g(\mathbf{x}_N)$ (Neumann BC), Eq. 3.2 can be written as a matrix equation of the form

$$\Big(\frac{1}{2}\mathbf{I}_N - \mathbf{M}_N\Big)p(\mathbf{x}_N) = \big(p^i(\mathbf{y}_N) + \alpha q^i(\mathbf{y}_N)\big) - \Big(\frac{\alpha}{2}\mathbf{I}_N + \mathbf{L}_N\Big)g(\mathbf{x}_N) \tag{3.30}$$

Eq. 3.30 can be similarly solved by precomputing $\left(\frac{\alpha}{2}\mathbf{I}_N + \mathbf{L}_N\right) g(\mathbf{x}_N)$ for the known $\mathbf{b}$ vector and then applying Alg. 3.3 with $q(\mathbf{x}_N) = \mathbf{0}_N$ (i.e. ignoring the $\mathbf{L}$ terms).

3.3 Reduction of the Number of RCR Translations

This section presents two techniques implemented in the FMBEM code which respectively reduce the number of translation coefficients which must be precomputed in the set up stage of the FMBEM, and the number of translations which must be applied in the FMM procedure. Both techniques have been implemented in the Helmholtz FMBEM to further reduce the algorithmic and memory complexity of the FMBEM.

3.3.1 Reduction of the Number of Stored Translation Coefficients

It can be seen from Eqs. 2.12–2.14 that the multipole translations are only dependent on the translation vector $\mathbf{t}$ and are independent of the actual S or R expansion vector being translated. Thus the number of RCR translations that must be calculated and stored in the set up stage of the FMBEM can be drastically reduced by noting that for each octree level, only a single set of $S|R$ translations must be stored between the

sets of well–separated source boxes and an arbitrary local group of receivers which share a common parent box. The $S|R$ translations for other local receiver groups will require exactly the same set of translation vectors defined by $\mathbf{t}$ as the relative distance between the source and receiver boxes will be the same. Thus the total number of $S|R$ translation vectors that must be stored per octree level will be $6^3 - 3^3 = 189$ for each of the eight possible receiver locations in the local receiver group, totalling 1512 $S|R$ translations per octree level.

Furthermore, only a fraction of the full set of 1512 $S|R$ translations will possess unique expansion vectors. For example the complete set of possible $S|R$ expansions in 2D is shown in Fig. 3.2. Each of the four possible receiver boxes in the local group have $6^2 - 3^2 = 27$ RCR translations. However it can be seen that only 40 of the 108 vectors in Fig. 3.2 are unique (i.e. $7^2 - 3^2$ translations). A similar analysis of the 3D case shows that only $7^3 - 3^3 = 316$ of the 1512 possible $S|R$ translation vectors are unique. The Helmholtz FMBEM algorithm thus precomputes and stores at most 316 $S|R$ translation vectors per octree level, or fewer in the case that not all possible well–separated translations are required on a particular octree level due to some boxes being empty. In the case of the $S|S$ and $R|R$ translations there are only eight unique translation vectors from the children box centres to the parent box centre (or vice versa) on each octree level.

3.3.2 Reduction of the Number of Applied Translations

As previously discussed, up to 189 $S|R$ translations must be applied per receiver box on each octree level. The total number of applied $S|R$ translations can be reduced by noting that many of the well–separated source boxes are common to more than one of the receiver boxes in the local receiver group of eight boxes which share the same parent box. Instead of translating to the centre of each individual receiver box, the $S|R$ translations for well–separated source boxes which are common to the receiver group can instead be applied to a point at the centre of the group. The translated expansions can then be $R|R$ translated to shift the expansion centre from the local group centre to each of the individual receiver boxes which shared the common set of source boxes.

This method for reducing the number of applied $S|R$ translations using the RCR translation method was first implemented by Gumerov and Duraiswami [157] for the Laplace fundamental solution. They implemented a so–called 'translation stencil' for a

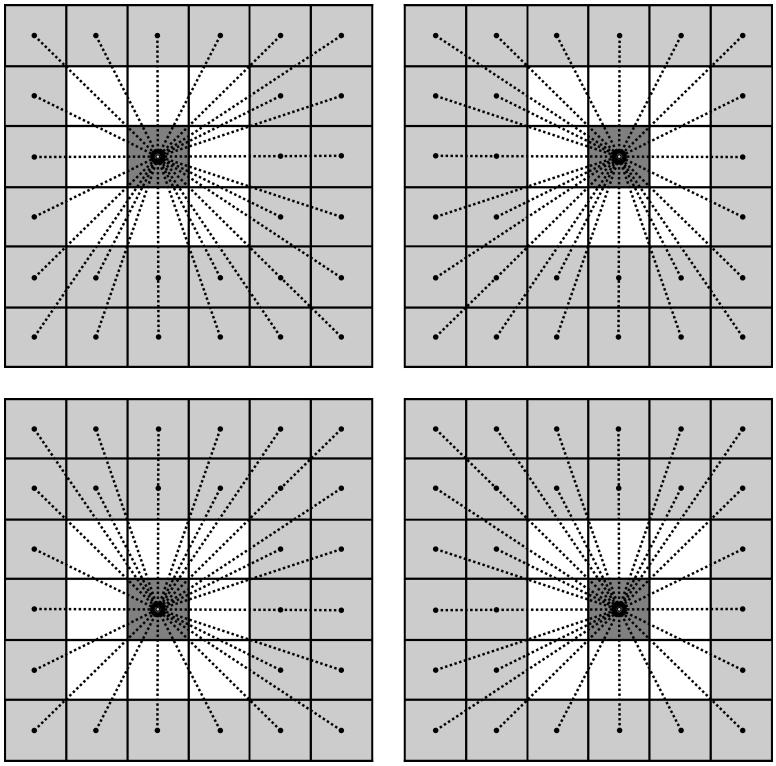

Figure 3.2: The complete set of possible $S|R$ expansions in 2D. Each of the four possible receiver boxes has at most $6^2 - 3^2 = 27$ RCR translations. Only 40 of the 108 $S|R$ possible translations are unique.

set of the well–separated source boxes which are common to all eight of the receivers in the local receiver group, by applying the $S|R$ translations to the centre of the parent box containing the receivers. The well–separated criterion that must be enforced for $S|R$ translation between two expansions can be described by the parameter

$$\eta = \frac{\max(r_1, r_2)}{D - \min(r_1, r_2)} \tag{3.31}$$

where r_1 and r_2 are the magnitudes of the expansion vectors of the two expansions (one of which is being $S|R$ translated to the expansion centre of the other) and D represents the magnitude of the translation vector $\mathbf{t}$ [157]. Assigning a unit distance to the box length, in the worst case the largest expansion vectors that can be contained within an octree box will be from the box centre to any of the box corners, giving an expansion vector length of $\frac{3^{1/2}}{2}$. Similarly the smallest translation vector between a receiver box

and its nearest well–separated source boxes will be $D = 2$. Thus in the worst case $\eta \approx 0.7637$ and Eq. 3.31 can be rearranged in terms of the separation distance as

$$D \approx \min(r_1, r_2) + \frac{\max(r_1, r_2)}{0.7637} \tag{3.32}$$

For the translation stencil presented in Ref. [157] the set of 80 well–separated source boxes shown in Fig. 3.3 are common to all eight receiver boxes and so the $S|R$ translations can be applied to the centre of the parent box. This set of source boxes has translation vectors which, in the worst case when the source/receiver expansions are largest, still satisfy Eq. 3.32: where $\max(r) = \frac{3^{1/2}}{2}$ for the source boxes and $\max(r) = \sqrt{3}$ for the parent box of the receiver group. Thus the $S|R$ translations for this set of boxes can be applied between the source box centres and the centre of the parent box of the group of receivers. The translated field can then be $R|R$ translated from the parent box centre to each of the children box centres.

It should be noted that the process of parent to children $R|R$ translations that is required to shift the stencil translations to the individual receivers is already applied in the downward pass of the FMM. The stencil translations can be applied on the parent octree level and then added to the consolidated $S|R$ translated field on the parent level. The required $R|R$ translations for the stencil will then be automatically applied in this process of downward $R|R$ translation to the children boxes in the lower level. The translation stencil reduces the number of $S|R$ translations for each receiver box by 80, at a cost of 80 $S|R$ translations applied directly to the parent box. Thus the complete set of $S|R$ translations is reduced from 1512 to $1512 - 8 \times 80 + 80 = 952$, which is equivalent to 119 $S|R$ translations per octree box: a $\sim 37\%$ reduction in the number of translations. The numbers presented here assume the optimal case where all children boxes are occupied. If, for example, only four children boxes are occupied the $S|R$ translations are only reduced to 159 per box, representing only a $\sim 16\%$ reduction.

The aforementioned translation stencil exploited the fact that a set of the source boxes was common to all eight of the receiver boxes and that those source boxes were well–separated from the parent of the receiver box. This idea can be extended further by applying translation stencils for source boxes which are common to *subsets* of the local receiver group. Again, this is provided that the maximum expansion vectors of both the source boxes and the combined group of receiver boxes satisfies Eq. 3.32 and so are considered well–separated for the $S|R$ translations. Translation stencils can be

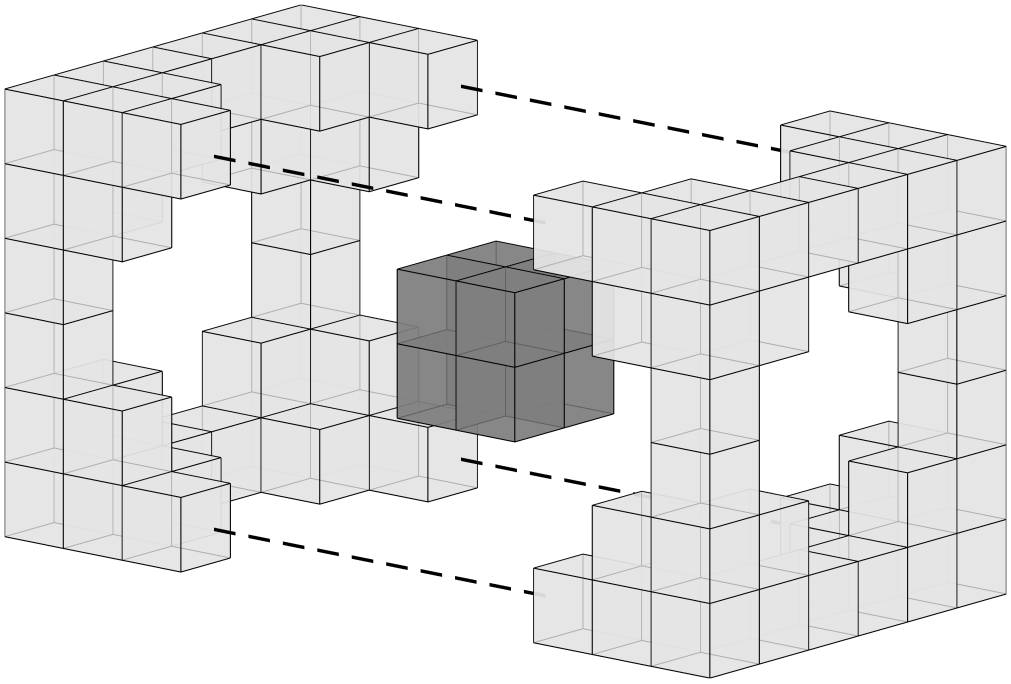

Figure 3.3: Translation stencil boxes for all eight receivers. The set of 80 light grey source boxes are considered well–separated from the parent box containing the local group of eight receivers (dark grey), and so the set of source boxes in the stencil can be translated to the parent box centre. The translated expansions at the parent box centre can then be combined and $R|R$ translated to each of the children box centres. For clarity, in the diagram the translation stencil has been split into two halves which connect via the dashed lines: the receiver group is the central $[2 \times 2 \times 2]$ set of boxes in the $[6 \times 6 \times 6]$ region.

constructed for groups of four receiver boxes which are in planes in the lower/upper xyz directions. The upper and lower translation stencils for the receiver box groups aligned along the z–axis are shown in Fig. 3.4. Each of the sets contains 40 source boxes. Similar sets can be made for groups of receiver boxes aligned along the other axis directions. It can be seen from Fig. 3.4 that 16 of the source boxes are common to both stencil sets but these are evaluated at different receiver groups (lower and upper groups of four receiver boxes). However for the groups of 4 receivers aligned along the x and y axes, each will consist of two boxes from the lower and upper z–planes of receivers. Thus to avoid overlaps, the sets of source boxes for the x/y groups of receivers must only include the source boxes which do not already appear in the z groups.

Removal of the overlapping source boxes between the upper/lower z–plane receiver

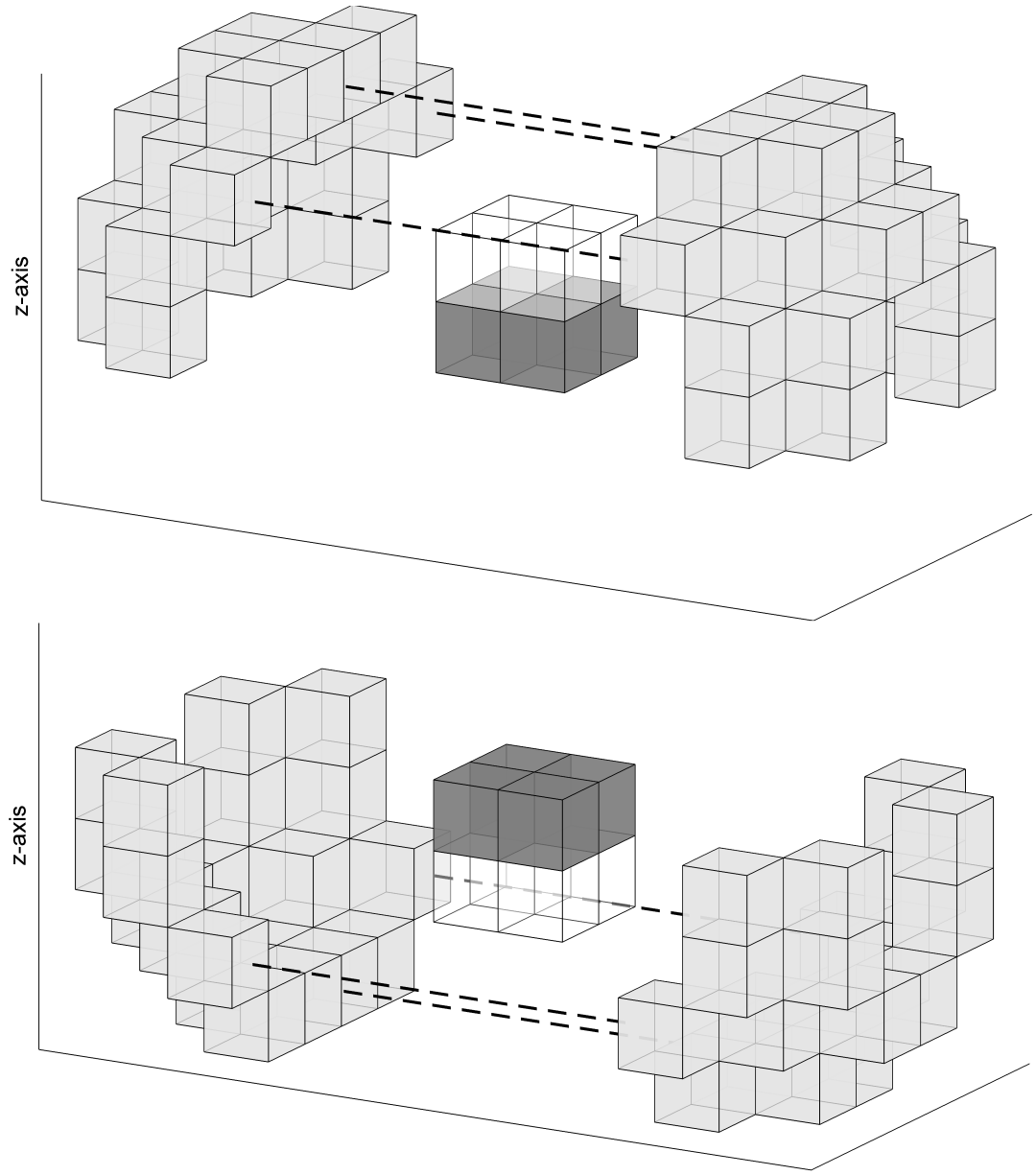

Figure 3.4: Translation stencil boxes for lower/upper groups of four receiver boxes for the z–axis. The top diagram shows the set of 40 source boxes which are well–separated from the group of 4 receivers which lie in the lower z–plane. The bottom diagram shows the corresponding set for the group of 4 receivers in the upper z–plane. In both diagrams the other 4 receiver boxes in the local receiver group are indicated by the clear boxes. Again the translation stencils have been separated into two halves for clarity.

groups and those for the analogous x/y groups reduces the x/y source box sets to only four boxes for each upper/lower group. Each receiver box will be a member of either the upper or lower receiver group for all three axis directions. An example of the source box sets treated by applying the $S|R$ translations to groups of four receiver boxes is shown in Fig 3.5 for two of the receivers in the local group. It can be seen from Fig 3.5 that for each receiver the $S|R$ translations from up to 48 source boxes can be treated by applying translations to groups of four receiver boxes. For each of the upper/lower z–plane source sets $4 \times 40 = 160$ $S|R$ translations are reduced to 40 $S|R$ translations plus four $R|R$ translations to shift the combined $S|R$ expansions from the group centre to the box centres of the four individual receivers in the group. For each of the upper/lower x/y–plane source sets $4 \times 4 = 16$ $S|R$ translations are reduced to four $S|R$ translations plus four $R|R$ translations. Thus the total number of $S|R$ translations for the local receiver group is further reduced to $952 - 320 + 80 - 32 + 8 - 32 + 8 = 664$ $S|R$ translations plus 24 $R|R$ translations, which is equivalent to 83 $S|R$ translations per octree box. Finally it should be noted that there is no advantage in preferentially applying the translation stencil to the z–plane receiver groups as was done in the above analysis: the receiver groups for the x/y directions could just as easily be chosen to treat the majority of the source boxes and this would reduce the source sets for the remaining axis directions. In fact in the general case all eight receiver boxes are seldom occupied in one receiver group and it is advantageous to choose the first axis to apply the translation stencil to maximise the reduction in the number of translations.

Finally, translation stencils can also be constructed for pairs of receiver boxes which are aligned along the xyz axis directions in the local receiver group. Each receiver will be a member of three of the groups of two receivers, one for each of the axis directions, as was the case for the groups of four receivers. Fig. 3.6 shows the sets of source boxes for three of the pairs of receivers aligned along the x, y and z directions. The source box sets for the receiver pairs aligned along the x and y axes each contain 24 source boxes while that for the z–axis receiver group only contains ten source boxes. This is because the $S|R$ translations for the groups of four receivers were first applied along the z–axis direction and so many of the well–separated source boxes for the two receivers aligned along the z–axis have already been treated in those translations. The source boxes for the groups of four receiver boxes aligned along the x and y axes were much smaller and so more of the source boxes still remain for $S|R$ translation to the groups

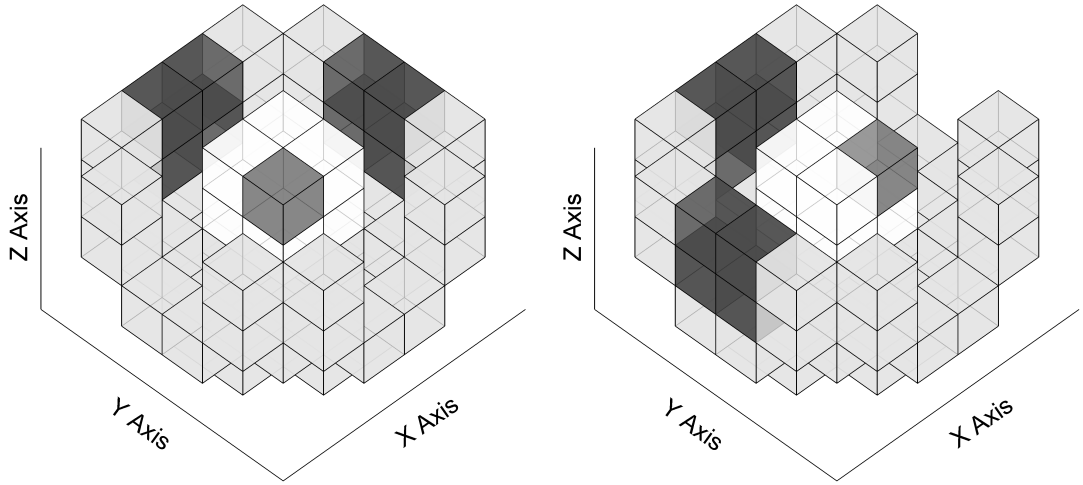

Figure 3.5: Translation stencil boxes for groups of four receiver boxes shown for two receivers in the local receiver group. The two receivers shown lie in the upper z–plane, lower y–plane and the lower (left) and upper (right) x–planes. The groups of four dark grey boxes are the remaining source boxes in the x/y sets which do not overlap with that for the upper/lower z sets. In both diagrams the clear boxes again indicate the other boxes in the local receiver group.

of two receiver boxes. A similar situation occurs if the $S|R$ translations for the groups of four receiver boxes are first applied to one of the other axis directions: the source box sets for the pairs of receivers aligned along that axis direction will only contain ten boxes while the other two axis direction will contain 24 boxes per set.

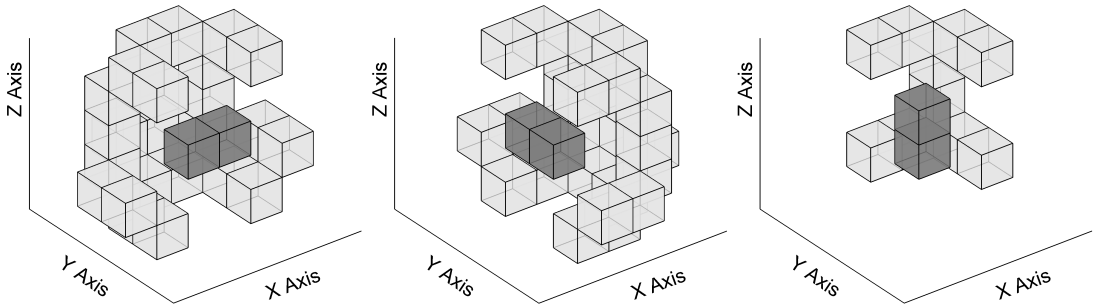

Figure 3.6: Translation stencil boxes for groups of two receiver boxes aligned along each axis direction. The source box sets for the receivers aligned along the x–axis (left) and y–axis (middle) each contain 24 boxes while that for the z–axis (right) only contains 10 source boxes as the groups of four receivers were first treated for the z–axis groups.

The source box sets for the four possible pairs of receivers aligned along the x and y axes exactly overlap, while those for the z–axis are a subset of the x/y axis sets. Hence the translations must only be applied to pairs of receiver boxes aligned along one of the axes to treat the remainder of the source boxes which are considered well–separated from the local group of receivers. The source box sets for the receiver pairs aligned along the other axes will become empty once the overlapping boxes already treated by the first receiver pairs have been removed from the sets. Choosing the z–axis for applying the $S|R$ translations to the pairs of receivers will be disadvantageous for the above example as the x and y axes have larger box sets and so greater savings in the number of $S|R$ translations can be achieved. Applying the $S|R$ translations to the four pairs of receivers aligned along the x or y axes in this case will reduce $8 \times 24 = 192$ $S|R$ translations to $4 \times 24 = 96$ $S|R$ translations plus eight $R|R$ translations to shift the combined $S|R$ expansions from the centre of each pair of receiver boxes to the eight individual receivers in the local group. Again in the general case where not all source and receiver boxes are occupied it may be advantageous to use a combination of four non–overlapping pairs of receivers which may be aligned along different axis directions to give the best reduction in the total number of translations. Upon applying the $S|R$ translations to the pairs of receivers there remains 37 source boxes per receiver which are too close to satisfy Eq. 3.32 with any kind of receiver grouping and so these translations must be applied directly to each individual receiver box.

Thus the total number of translations is finally reduced to $664 - 192 + 96 = 568$ $S|R$ translations plus 32 $R|R$ translations, which is equivalent to 71 $S|R$ translations plus four $R|R$ translations per receiver box. Gumerov and Duraiswami note that their implementation of the RCR method utilising $S|R$ translations to groups of four and two receivers only requires 61 $S|R$ translations per receiver box [157] but they do not provide details of this implementation. Presumably a more complex implementation than that presented here is used to achieve the additional reduction in the number of translations. Nonetheless, the method discussed here can reduce the number of $S|R$ translations from 189 per box to 71 per box when all eight receivers in the local group are occupied: a $\sim 62\%$ reduction in the number of translations. Fig 3.7 shows the complete process of applying the translation stencils for groups of eight, four and two receivers for one of the receivers in a local group.

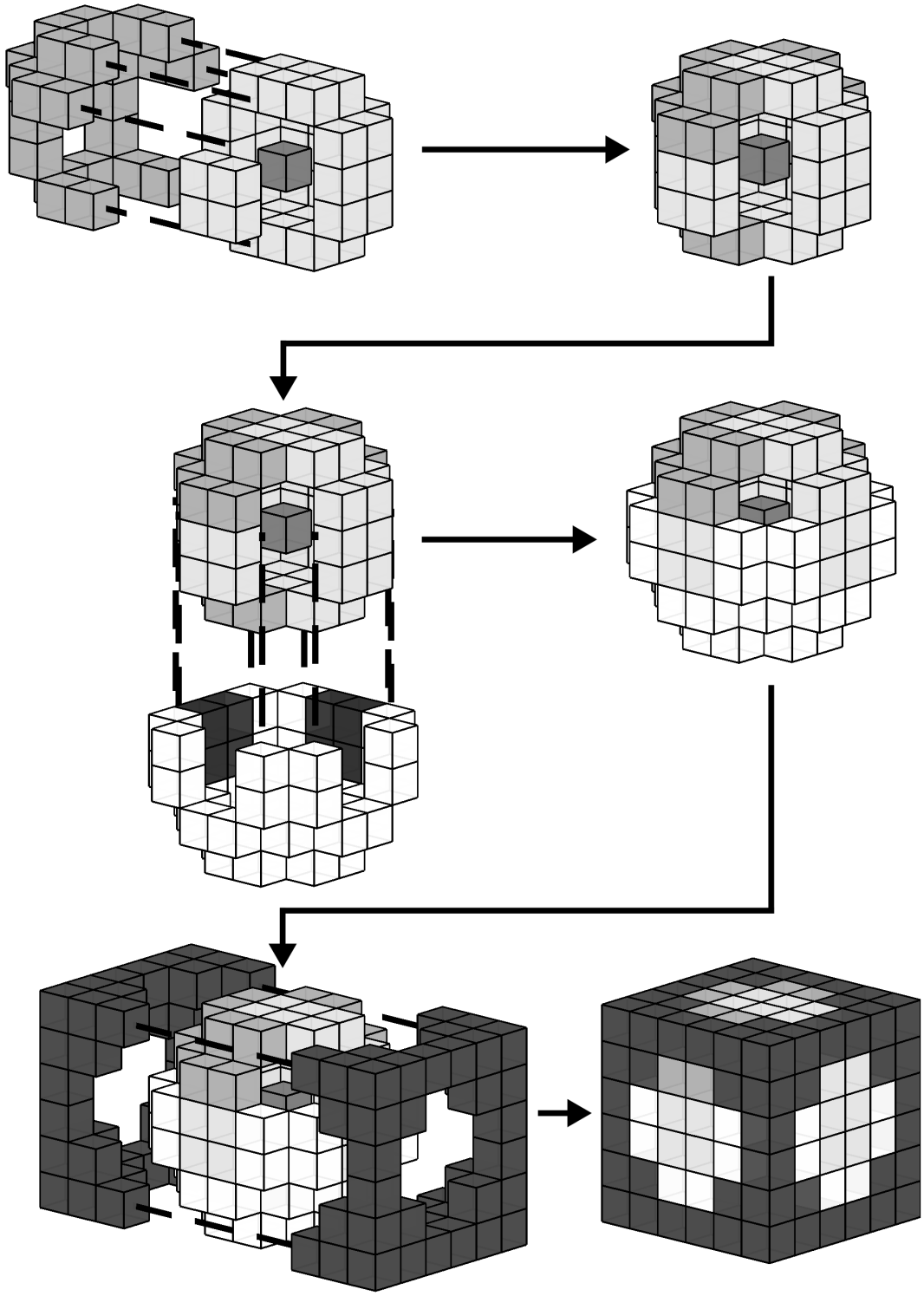

Figure 3.7: Complete set of translation stencils for one receiver. The top, middle and bottom rows show the sets of source boxes which are treated via $S|R$ translations to groups of two, four and eight receivers for one of the receivers in the local group. The top left image also shows the set of 37 source boxes which are directly $S|R$ translated to the receiver.

Finally, it should be noted that the use of the translation stencils increases the number of unique $S|R$ translations that must be precomputed and stored in the FMBEM. The centres of the groups of receiver boxes will lie on the box edges for the groups of four receivers and on the box faces for the groups of two receivers and so will introduce additional sets of unique translation vectors. In total up to twelve sets of $S|R$ translations will be required: six sets for the groups of four receivers, four sets for the pairs of receivers, one set for the translations to the group of all eight receivers and one set for the remaining source boxes which must be directly translated to individual receivers. However the total number of unique $S|R$ translation coefficients that must be stored does not increase by a factor of twelve as each of the stencils is only a subset of the complete set of $S|R$ translations. For example, to solve a sphere scattering problem with a Robin BC on a mesh containing 19776 elements, using the translation stencils reduced the solution time by 36% while the total storage requirements only increased by about 6%. The method using the translation stencils stored 576 sets of $S|R$ translation coefficients on the lowest octree level while the direct method stored 260 sets.

3.4 Numerical Results

This section explores the performance of the Helmholtz FMBEM model in terms of both its accuracy, and the algorithmic complexity and memory requirements of the model. The Helmholtz FMBEM model has been written in MATLAB, implemented using double–precision floating point numbers and the code has not been explicitly compiled/multithreaded, however MATLAB may do this internally to parts of the code during execution. Numerical examples are presented for exterior acoustic scattering from a sphere under various boundary conditions and compared to the analytic solution [42]. An 'application example' of the Helmholtz FMBEM code is also presented in the form of monostatic target strength (TS) results for the improved BASIS model of the BeTSSi submarine [158]. The Burton–Miller coupling parameter is set to $\alpha = 0.05i/k$ unless otherwise stated. Numerical results are compared where possible to those obtained from a commercially available code called PAFEC, developed by PACSYS [27].

All numerical results from both the FMBEM code and the commercial PAFEC code have been calculated on a workstation computer equipped with an i7–3930K hexacore processor running at 3.2GHz, and 32GB of RAM.

3.4.1 Plane Wave Scattering from a Sphere

Fig. 3.8 shows a comparison between the total surface pressure on a unit radius $a = 1$ sphere for $ka = 30$ and the analytic solution. A Robin BC has been applied which relates p and q as: $q(\mathbf{x}) = -5ip(\mathbf{x})$ i.e. $g(\mathbf{x}) = -5i$ in Eq. 3.28. The incident acoustic field is a unit strength plane wave propagating in the direction [1 0 0]. Fig. 3.9 shows a comparison of the real/imaginary components of the total surface pressure as a function of angle away from the direction of the incident field such that 0° corresponds to the back–scatter direction.

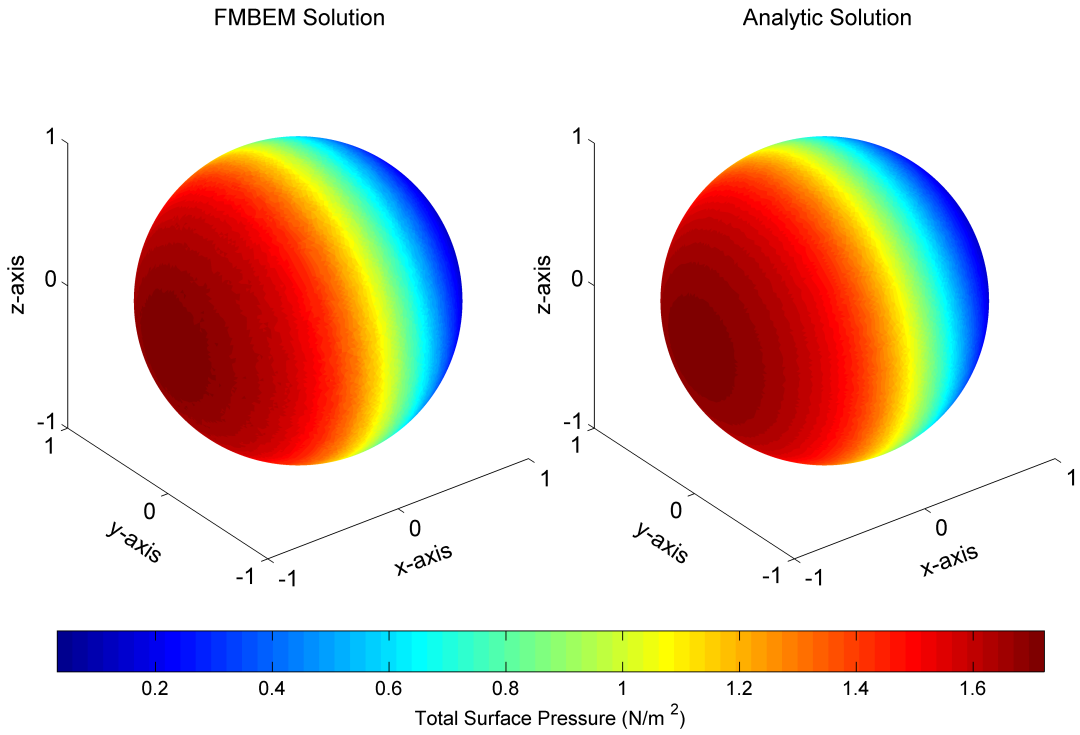

Figure 3.8: Helmholtz FMBEM total surface pressure (left) versus the analytic solution (right) for plane wave scattering from a sphere at $ka = 30$ under a Robin BC.

The relative error norm (r.e. norm) $\frac{\text{norm}(\mathbf{s}_N - \mathbf{s}_N^{\text{ana}})}{\text{norm}(\mathbf{s}_N^{\text{ana}})}$ between the N–element vectors from the FMBEM ($\mathbf{s}_N$) and analytic ($\mathbf{s}_N^{\text{ana}}$) solutions was 0.62%. For this example the boundary element mesh contained 40096 elements giving approximetaly 15 elements per wavelength at the specified wavenumber. The FMBEM took approximately 48 minutes

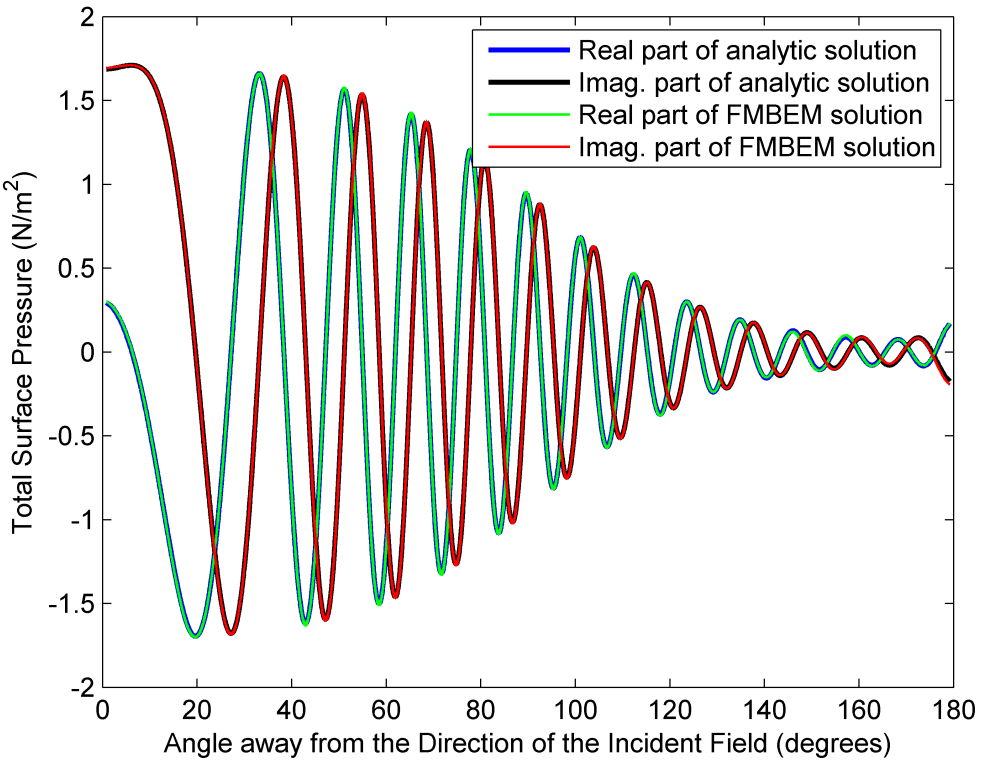

Figure 3.9: Helmholtz FMBEM real/imaginary components of the total surface pressure versus the analytic solution for plane wave scattering from a sphere at $ka = 30$ under a Robin BC.

to set–up and solve the problem and required 1.08GB of storage space. Comparitively, the full complex 40096×40096 $\mathbf{L}_N$ and $\mathbf{M}_N$ coefficient matrices in Eq. 3.28 would each require 25.7GB of space to store. It can be seen from Figs. 3.8 and 3.9 that the Helmholtz FMBEM is in close agreement with the analytic solution. This example is somewhat oversampled compared to the commonly quoted '6–10 elements/wavelength' rule of thumb [8]. Analogous results to those shown in Fig. 3.9 are presented in Fig. 3.10 for the same problem at a higher wavenumber of $ka = 45$ which corresponds to 10 elements per wavelength. In this case the r.e. norm between the FMBEM and analytic solution was 2.2% and both the solution time and memory requirements increased (to 129 minutes and 1.57GB respectively) compared to the $ka = 30$ case. This is due to the expansion lengths determined by Eq. 2.17, and so the number of operations required in the FMBEM, being dependent on the wavenumber.

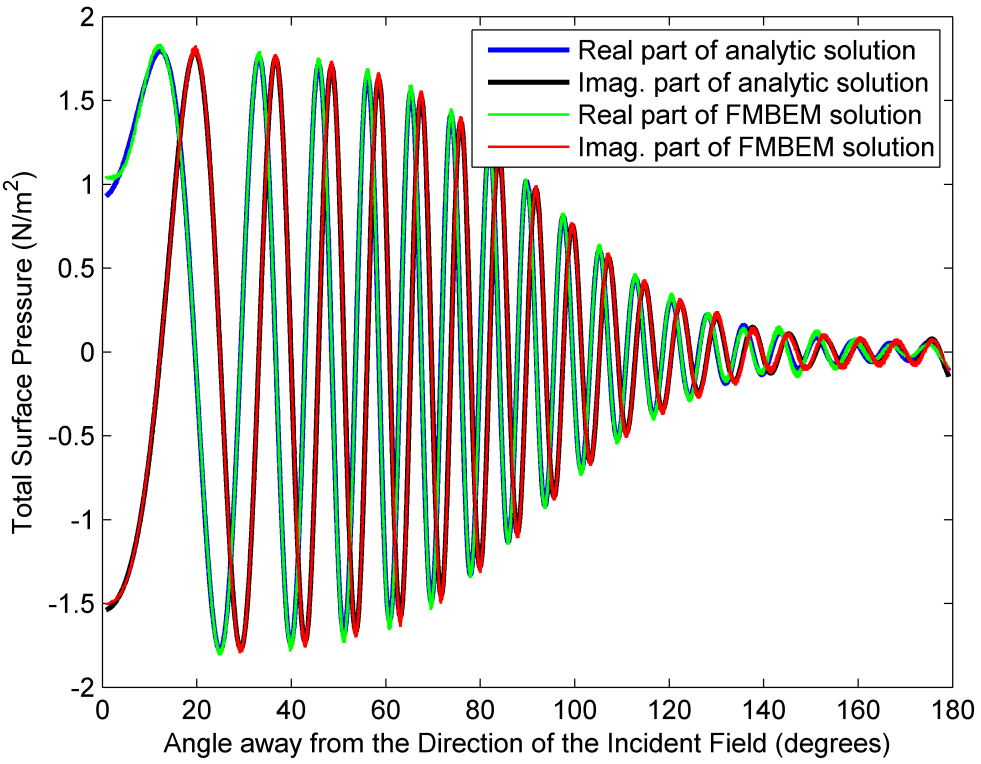

Figure 3.10: Helmholtz FMBEM real/imaginary components of the total surface pressure versus the analytic solution for plane wave scattering from a sphere at $ka = 45$ under a Robin BC.

Finally, Fig. 3.11 shows the FMBEM results with and without a Burton–Miller coupling parameter as well as the analytic solution for plane wave scattering from a sphere under a Neumann BC for $ka \approx 3\pi$. This wavenumber corresponds to the third eigenfrequency of the equivalent interior problem. It can be seen from Fig. 3.11 that the FMBEM agrees with the analytic solution when $\mathrm{Im}(\alpha) \neq 0$ while the solution breaks down at the eigenfrequency when $\mathrm{Im}(\alpha) = 0$, as expected.

3.4.2 Helmholtz FMBEM Algorithmic Performance

This section presents results for the Helmholtz FMBEM algorithm which indicate the performance of the algorithm in terms of its algorithmic complexity and memory requirements. Comparisons of the algorithmic complexity, computational accuracy and

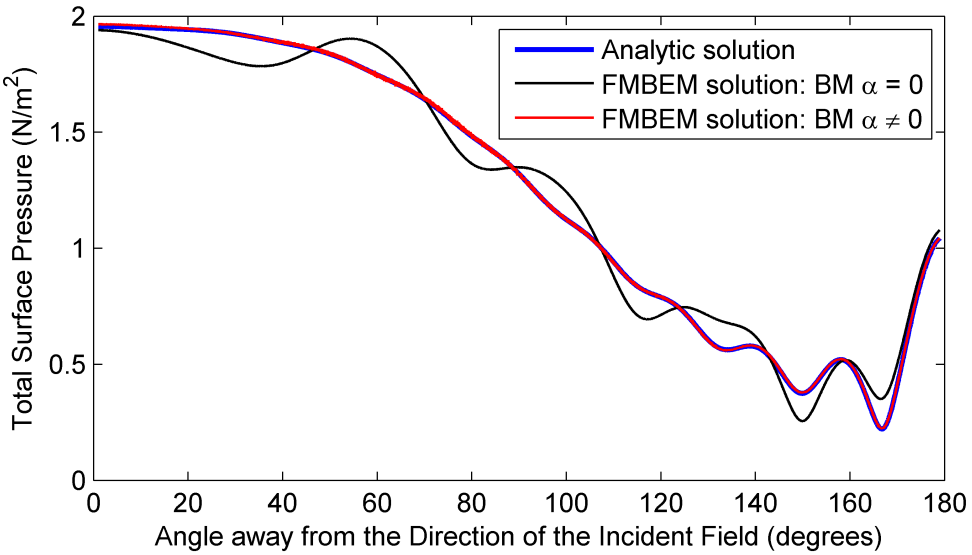

Figure 3.11: Helmholtz FMBEM solution of the total surface pressure with and without a Burton–Miller coupling parameter versus the analytic solution for plane wave scattering from a sphere at $ka \approx 3\pi$ under a Neumann BC.

memory requirements of the Helmholtz FMBEM code are presented for the problem of sphere scattering under a Neumann BC and compared to analytic solution and numerical BEM results from PAFEC. Two scenarios are presented: the first investigates how the algorithm scales as a function of the number of unknowns with a fixed wavenumber and the second case shows the maximum wavenumber for each mesh size as a function of the number of unknowns.

Plots of the solution time, memory usage and solution error versus the number of unknowns for a fixed wavenumber of $ka = 13$ are shown in Figs. 3.12, 3.13 and 3.14 respectively. Numerical results for the solution time and solution error from PAFEC's standard BEM model are also presented in the relevant figures. It can be seen from Fig. 3.12 that the least squares fit of the total solution time for the FMBEM is approximately proportional to N while that for the BEM code is greater than N^2. The standard deviations in the least–squares data fits for the algorithmic N–scaling, calculated from the covariance matrix of the polynomial coefficients used in the data fit, are also shown in Fig. 3.12 (and in similar plots throughout the thesis) as a measure of the uncertainty in the data fits. However it should be noted that the residual errors should not be considered as randomly distributed due to the strong correlation of the octree structure

on the total solution time and memory usage (discussed next) and so will likely not follow a normal probability distribution. Thus the standard deviations presented for the algorithmic N–scaling should only be considered as very rough measure of the uncertainty in the data fit.

Fig. 3.12 also shows that at the larger mesh sizes distinct 'steps' in the increase of the solution time can be seen. These steps correspond to increases in the boundary element mesh which require a new level to be added to the octree structure and so the total number of applied $S|R$ translations sharply increases. Once the new octree level is included the number of unknowns in the mesh can be made several times larger before another octree level is required. The total storage requirements in MB of the FMBEM are shown in Fig. 3.13 where a dependence proportional to less than N is observed. A line showing the gradient proportional to N^2 memory usage is also shown for reference. A comparison of Figs. 3.12 and 3.13 shows that the upward steps in the solution times correspond to downward steps in the memory requirements. The introduction of the new octree level reduces the number of integrals that must be stored in the sparse near field matrix, at the cost of an increased number of $S|R$ translations on the new octree level. The results in these two figures exemplify the typical trade off between speed and memory inherent in the FMBEM. Finally, the relative error norm between the analytic and FMBEM solution is shown in Fig. 3.14, as well as similar results for the PAFEC BEM code. The error reduces as the number of elements per wavelength increases, as expected. Here the stepped increases in the error result from the separation distances for the multipole expansions being halved on each new octree level. Initially the sizes of the elements on each new level are relatively large compared to the separation distance and so the error introduced by the piecewise constant elements is initially larger but then reduces as the element size is reduced.

Plots of the solution time, memory usage and solution error versus the number of unknowns for the second scenario using the maximum wavenumber for each boundary element mesh are shown in Figs. 3.15, 3.16 and 3.17 respectively. Each of the selected wavenumbers gives approximately 8–10 elements per wavelength on the corresponding mesh (measured at the equator of the sphere). It can be seen from Fig. 3.15 that the least squares fit of the total solution time for the FMBEM in this scenario is approximately proportional to $N^{1.5}$ while that for the BEM code remains effectively unchanged.

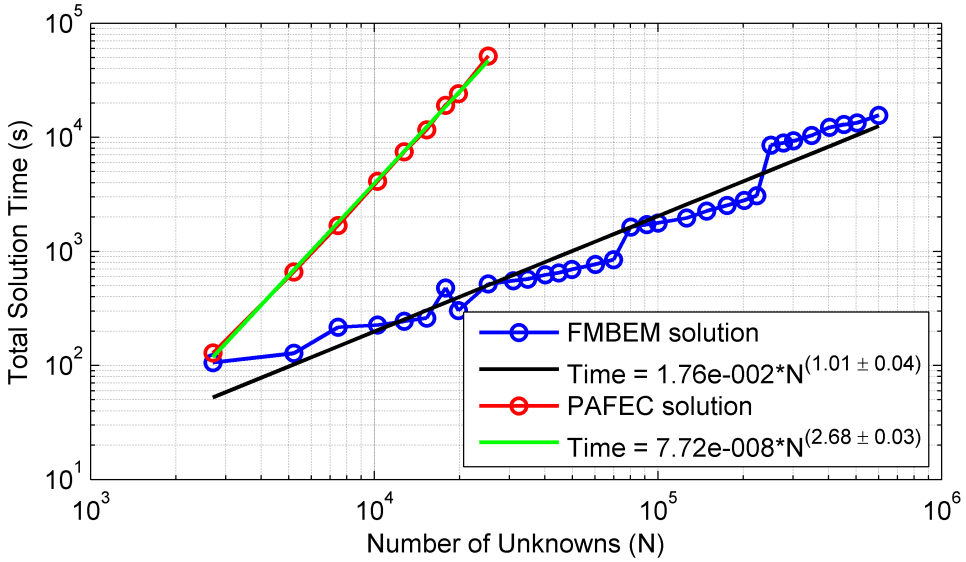

Figure 3.12: Solution time versus the number of unknowns for the Helmholtz FMBEM with a fixed wavenumber. The FMBEM total solution time is approximately proportional to N.

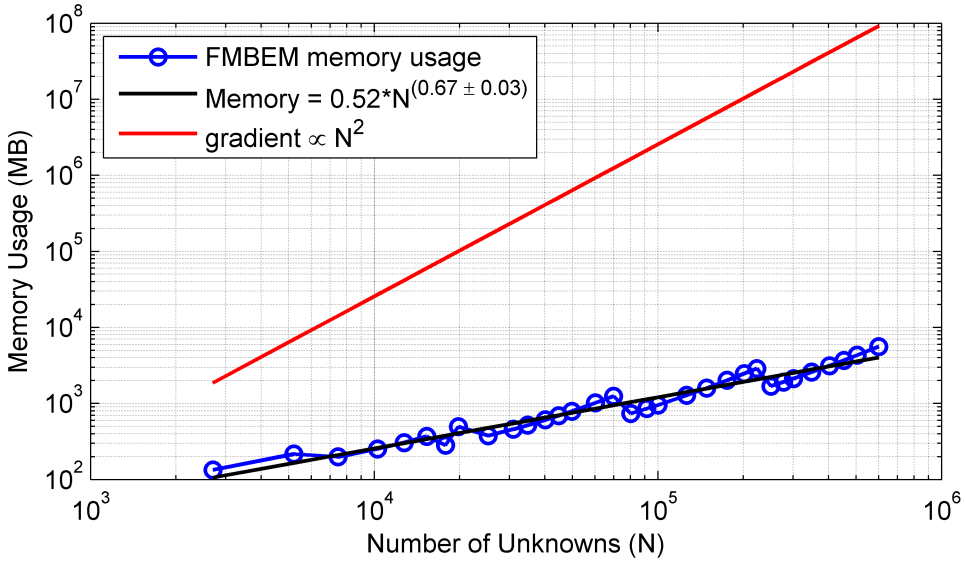

Figure 3.13: Memory usage versus the number of unknowns for the Helmholtz FMBEM with a fixed wavenumber. The storage requirements in MB of memory shows a proportionality which is less than N.

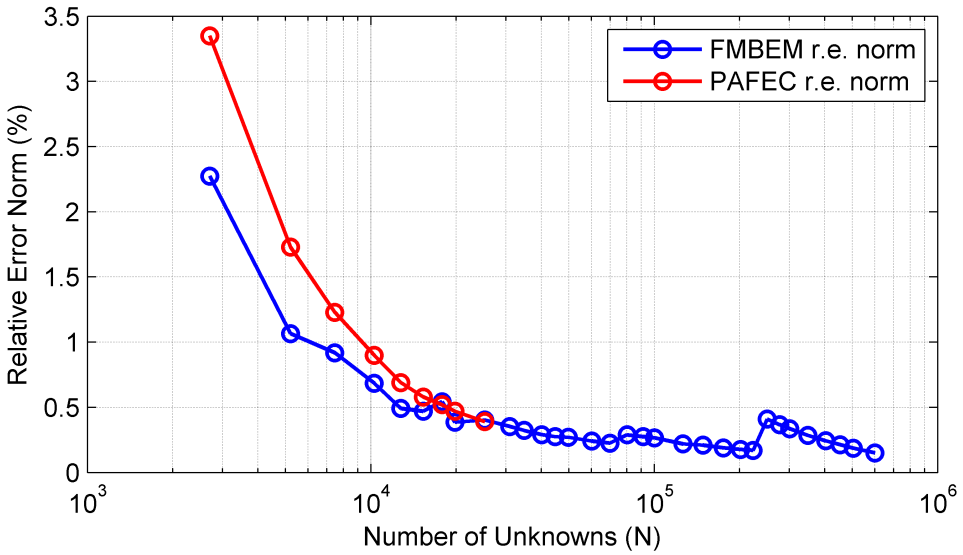

Figure 3.14: Solution error versus the number of unknowns for the Helmholtz FMBEM with a fixed wavenumber. The r.e. norm generally decreases as the number of elements per wavelength increases.

This is because the cost per matrix–vector product for the conventional BEM is independent of the wavenumber of the problem while that for the FMBEM is strongly dependent upon the wavenumber. Fig. 3.16 shows that memory usage also increases for this scenario as the truncation numbers for the expansions and RCR translation coefficients are proportional to the wavenumber. Finally, Fig. 3.17 shows that the relative error norm between the analytic and FMBEM solutions remains approximately constant at $\sim 2\%$ for a roughly constant number of elements per wavelength.

Comparative studies on the numerical error for acoustic BEM problems performed by Marburg [8, 159] for different types of elements (constant, continuous, discontinuous) indicated that a discretisation of 6–10 constant elements per wavelength would achieve an error of about 10% in the L^2–norm of the pressure magnitude for the numerical example of a plane wave travelling in a long duct. Certainly one would expect the spherical scatterer results presented here to be a more favourable numerical example than the long duct due to the simpler geometry and boundary conditions. Osetrov and Ochmann [160] observed discretisation errors of about 3–4% from their high frequency FMBEM when using 10 constant elements per wavelength, while the average pressure and normal velocity errors for the 'Cats–eye' structure [161] were approximately 6–

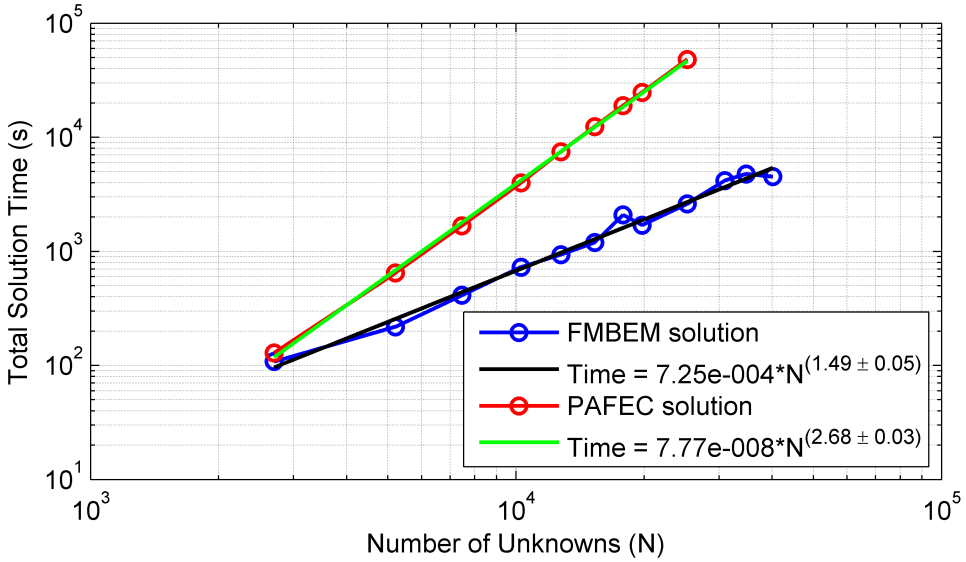

Figure 3.15: Solution time versus the number of unknowns for the Helmholtz FMBEM using the maximum allowed wavenumber on each mesh. The FMBEM total solution time is approximately proportional to $N^{1.5}$.

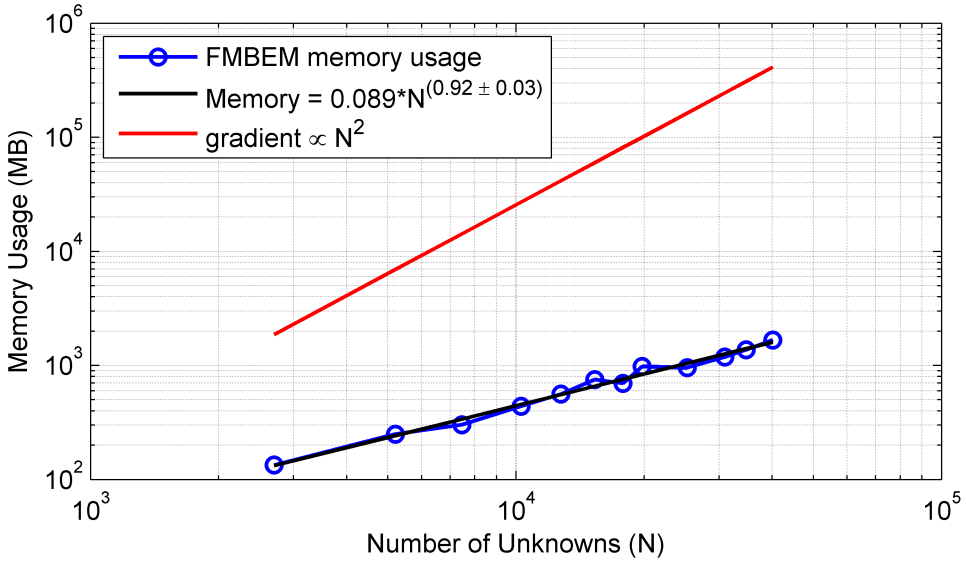

Figure 3.16: Memory usage versus the number of unknowns for the Helmholtz FMBEM using the maximum allowed wavenumber on each mesh. The storage requirements in MB of memory is approximately proportional to N.

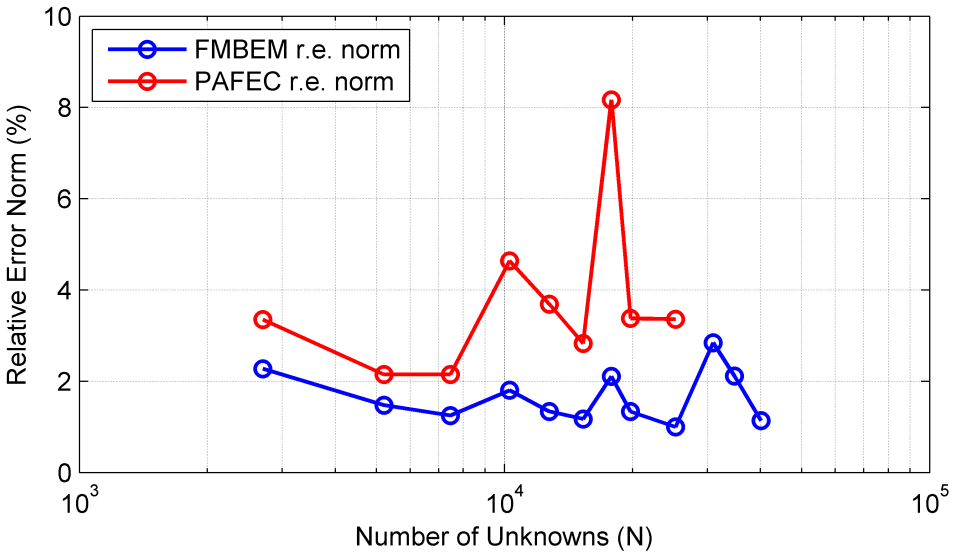

Figure 3.17: Solution error versus the number of unknowns for the Helmholtz FMBEM using the maximum allowed wavenumber on each mesh. The r.e. norm remains approximately constant for a roughly similar number of elements per wavelength.

12% and 11–17% respectively when using between 3.4 and 8.5 constant elements per wavelength. Fischer and Gaul [162] observed an L^2–norm of about 5% in the surface pressure results for an L–shaped structure when using 9 linear elements per wavelength in their high frequency FMBEM. It should also be noted that for a fixed element mesh, the solution error in the FMBEM can be varied by several percent depending on the chosen truncation number of the multipole expansions (Eq. 2.17), as evinced by Schneider [163] and Yasuda et al. [41].

The second scenario effectively shows the worst case performance of the FMBEM, particularly at the higher wavenumbers where the number of operations required to apply the RCR translations becomes substantial. For example at the highest wavenumber tested ($ka = 40$, 25230 elements) the truncation numbers on the highest two octree levels were 27 and 44 respectively. Thus according to Eqs. 2.15, 2.16 and 2.18 the $S|S$ and $R|R$ translation to and from the highest octree level require 1.79×10^5 operations per translation while $S|R$ translations across level two require 3.04×10^5 operations per translation. In this example 2504 $S|R$ translations were required on the highest octree level, totalling 7.60×10^5 operations which is actually larger than the N^2 operations for a direct matrix–vector product. Including all of the translations for all octree lev-

els gives an estimate of the total number of translations which is substantially larger than N^2. Despite this, the FMBEM still solves the problem about 15 times faster than the conventional BEM and this is likely due in part to the fact the conventional BEM code being compared to here scales as greater than N^2 algorithmic complexity. The operation counts provided by Eqs. 2.15, 2.16 and 2.18 must only be indirectly related to the actual calculation times required by the computer hardware. The differing programming languages used between the FMBEM (MATLAB code) and commercial BEM code (compiled Fortran) would also play a role in the observed execution times but it is difficult to quantify what impact this would have.

Finally it should be noted that the $N^{1.5}$ algorithmic complexity observed when using the maximum allowed wavenumber for each mesh is in good agreement with the $O(N^{1.5})$ simplified theoretical estimate of the algorithmic complexity derived by Gumerov and Duraiswami [42] for the BEM when using $O(p^3)$ translation methods. Similarly the order N algorithmic complexity observed in the low frequency scenario, where the number of unknowns was increased independently of the wavenumber, appears to agree with the $O(N)$ theoretical algorithmic complexity derived by Gumerov and Duraiswami [42] for surface distributions of sources and receivers of so–called 'simple objects' when using translation methods which have a greater than $O(p^2)$ algorithmic complexity.

3.4.3 Monostatic Target Strength Scattering for the BeTSSi Submarine Model

As an example of the application of the Helmholtz FMBEM model, monostatic target strength (TS) results are presented for the benchmark BeTSSi submarine model which was developed for predicting TS results for frequencies up to 8kHz. A schematic for an improved BASIS model of the BeTSSi submarine is presented in Ref. [158]. The BASIS model approximates the submarine hull as a series of simple geometric shapes and the monostatic TS for each shape can be independently calculated and combined to form the complete hull. The schematic of the improved BASIS model was used to build a 3D surface mesh of the BeTSSi submarine, consisting of 14640 elements. A comparison of the total surface pressure for the improved BASIS model as calculated by the FMBEM and PAFEC BEM codes for a 200Hz plane wave at broadside incidence is shown in Fig. 3.18. The total solution time of the FMBEM code for this problem was 290 seconds and required 740MB of storage space while the PAFEC BEM code took

3.08 hours and required 13.6GB of storage space. Thus for this particular example the FMBEM model solved the problem approximately 38 times faster and used 18 times less memory compared to the BEM model.

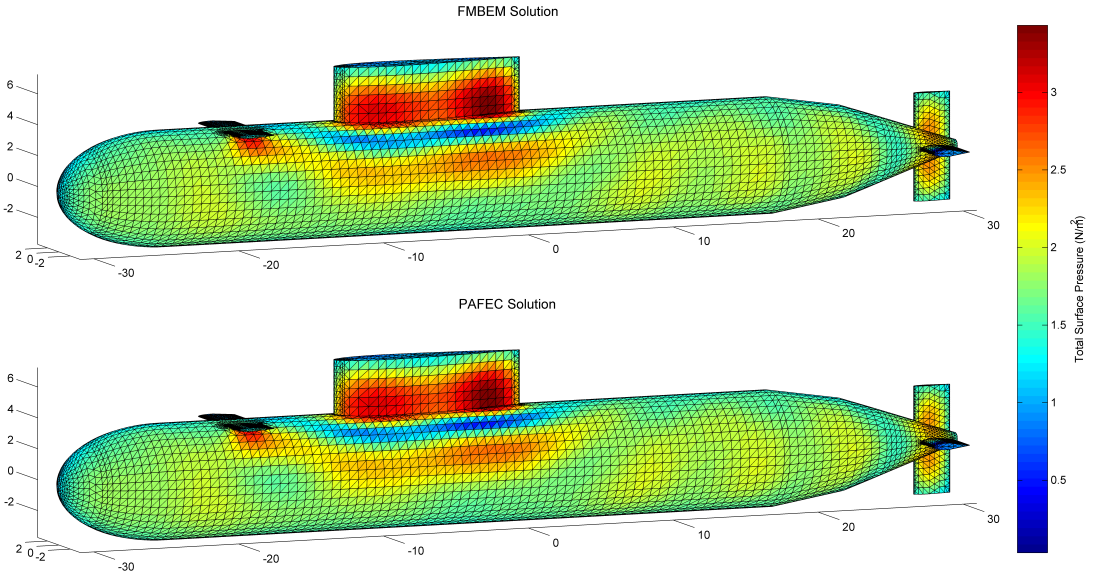

Figure 3.18: Total surface pressure for a 200Hz plane wave at broadside incidence for the improved BASIS model of the BeTSSi submarine. The Helmholtz FMBEM (top) and PAFEC BEM (bottom) results are in good agreement except at the fin edges.

The r.e. norm between the FMBEM and PAFEC solution is 11.7% despite what appears to be good agreement in Fig. 3.18. The discrepancies between the FMBEM and PAFEC results appears to be localised to the edges of the stabiliser and tail fins where the two sides of the mesh converge to a single edge. Fig. 3.19 shows a close up of the total surface pressue on the vertical tail fins for both models, where it can be seen that there is sharp variations in the total surface pressure of the edge elements in the PAFEC model. Similar sharp variations in the total surface pressure on the edge elements can also be observed in the FMBEM results if the near–singular integration method is not used when calculating the sparse near field matrix, suggesting that the discrepancy may be due to the treatment of the near–singular integrals in PAFEC. Ignoring the 50 elements with the largest difference in calculated pressures on the fin edges reduces the r.e. norm between the FMBEM/PAFEC results to 5.2%, indicating that over half of the observed 11.7% r.e. norm between the FMBEM/PAFEC solutions

over the full BEM surface are due to the discrepancies on the fin edges, while agreement between the two solutions over the remainder of the BEM surface is quite good.

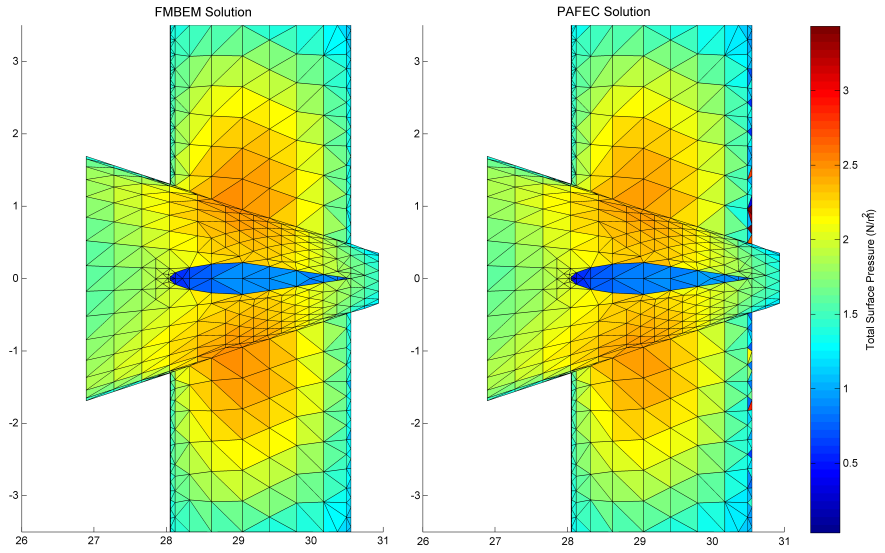

Figure 3.19: Total surface pressure for a 200Hz plane wave at broadside incidence for the improved BASIS model of the BeTSSi submarine: close up view of the vertical tail fins. The Helmholtz FMBEM (left) and PAFEC BEM (right) results show significant differences along the edges of the fins.

Fig. 3.20 shows the monostatic TS as a function of angle in the horizontal plane for the improved BASIS model of the BeTSSi submarine as calculated by the FMBEM code at 1° angular increments and the PAFEC BEM code at 10° angular increments. Also shown in the figure are the numerical results presented in Ref. [158] for the monostatic TS calculated from another BEM code called AVAST. The AVAST results are for the original BeTSSi submarine hull as opposed to the improved BASIS model used for the FMBEM/PAFEC results. The main differences between the two models are that the original BeTSSi hull incorporates a flat top section to simulate a deck and that the tail section varies smoothly from the main pressure hull while the BASIS implementation models the tail as two connected conical sections which have a sharp change in angle between the edges of each section. It can be seen from Fig. 3.20 that the overall agreement between the various data sets is good, particularly between the FMBEM/PAFEC results for the improved BASIS model.

The number of elements in the model may be significantly increased for the FMBEM

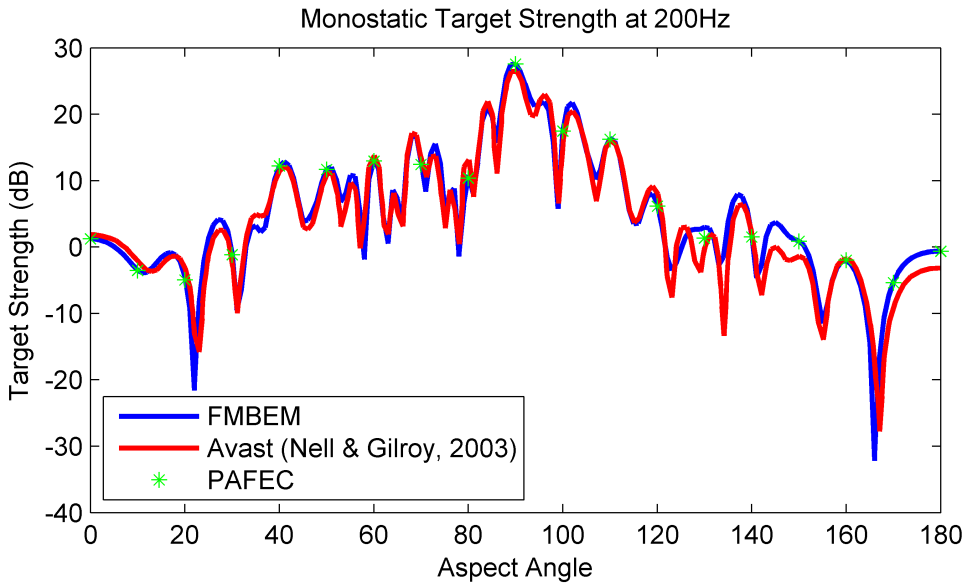

Figure 3.20: Monostatic TS as a function of angle for the BeTSSi submarine hull for 200Hz plane wave incident field. The FMBEM and PAFEC BEM results are both for the improved BASIS model of the BeTSSi submarine and are in good agreement. The reference BEM results from AVAST are for the original BeTSSi submarine hull and show some differences to the FMBEM/PAFEC results due to the differences in the two models. Overall agreement between the two models is good.

code. Fig. 3.21 shows the FMBEM results for the same scenario presented in Fig. 3.18 for a larger mesh containing 96866 elements. The total solution time was 29 minutes and the problem required 1.6GB of storage space. A high resolution model of the BeTSSi submarine containing 331 039 elements was solved for the same 200Hz incident field in 1.60 hours, requiring 3.44GB of storage space.

3.5 Chapter Summary

This chapter has presented the Helmholtz FMBEM model developed for the coupled fluid–structure interaction model. The chapter contains a literature review of the FMM for the Helmholtz BIE, a description of the implementation of the Helmholtz FMBEM including pseudocode algorithms for the setup and iterative solution of the Helmholtz BIE using the FMM, a discussion of the methods implemented to reduce the number of multipole translations that must be both applied and stored in memory, and finally, numerical results which demonstrate the performance of the Helmholtz FMBEM model.

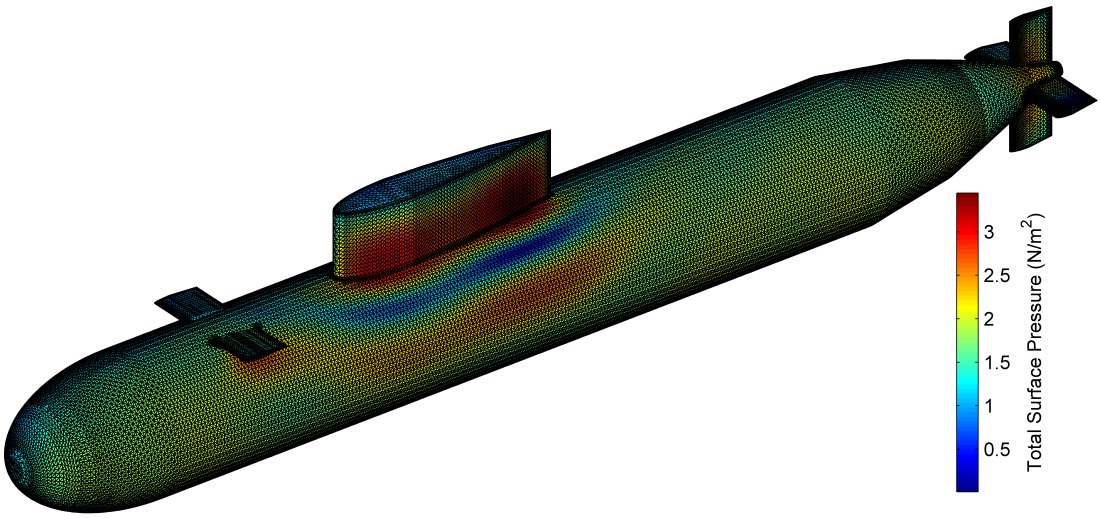

Figure 3.21: Total surface pressure for a 200Hz plane wave at broadside incidence for the improved BASIS model of the BeTSSi submarine for a 96866 element mesh calculated using the FMBEM.

The solution time of the Helmholtz FMBEM model was shown to scale between N in the low frequency range and $N^{1.5}$ in the high frequency limit of the low frequency FMBEM, with both estimates being in good agreement with the theoretical algorithmic complexities, while the storage requirements were equal to or less than N. As expected the FMBEM provides a substantial performance improvement over the conventional BEM, yielding faster solution times and smaller memory requirements.

4

Elastodynamic FMBEM

This chapter presents the elastodynamic FMBEM developed to model the elastic solid part of the coupled FSI model. The chapter sections mirror those of the Helmholtz FMBEM presented in Chapter 3. First a literature review for the elastodynamic FMBEM is presented. This is followed by a description of the developed elastodynamic FMBEM model, including pseudo–algorithms for the set up and solution of the elastodynamic BIE using the FMBEM. The final section presents numerical results for the FMBEM with comparisons to analytic solutions and/or published FMBEM results. The algorithmic and memory complexity of the elastodynamic FMBEM is also investigated in the results section. The chapter is concluded with a brief summary.

4.1 Literature Review

The elastodynamic BEM for frequency domain problems was first researched by Kupradze in the 1930s/1940s [164], and by Cruse and Rizzo in 1968 [165, 166]. The elastodynamic BEM is considered a mature field with a number of review articles [167, 168, 169] and books [170, 171, 172, 173, 174] available on the subject.

The FMM was first applied to the elastodynamic BEM for 2D frequency–domain problems in 1997 by Chen et al. [175] using Rokhlin's diagonal translation method. Elastodynamic 2D scattering problems using the low frequency FMM were treated by Fukui and Inoue [176] and Fujiwara [177]. The elastodynamic FMBEM for 3D frequency–domain problems was implemented by Fujiwara [24] in 2000 using the high frequency diagonal translation method and multiple octree levels but with a level–

independent truncation number. Yoshida et al. [178, 179] implemented a low–frequency elastodynamic FMBEM in 3D using the Wigner 3–j symbols for the translations, making them $O(p^5)$ operations, as well as a high–frequency elastodynamic FMBEM using diagonal translations [180]. In both cases the authors were interested in modelling the scattering of elastic waves by cracks. Isakari et al. applied the low frequency elastodynamic FMBEM to periodic inclusion problems using the $O(p^3)$ RCR translation method [181, 182]. Chaillat et al. improved upon the high–frequency implementation of the 3D elastodynamic FMBEM by using a level–dependent truncation number to reduce the algorithmic complexity to $O(N\log^2 N)$ [37, 183]. Sanz et al. implemented a high frequency elastodynamic FMBEM which utilised a sparse approximate inverse preconditioner [184] while Chaillat [185] used a nested inner–outer GMRES loop for preconditioning (analogous to Gumerov and Duraiswami for the Helmholtz FMBEM [18]). Elastodynamic problems involving FMBEM–FMBEM coupling between multiple piecewise–homogeneous domains were treated by Chaillat et al. [186]. Tong and Chew showed that the number of multipole expansions that must be translated in the FMM can be reduced by treating the relevant Green's function expansions in a spherical coordinate system [187]. Preconditioning strategies for periodic structures using the low frequency elastodynamic FMBEM were treated by Isakari et al. [182, 188]. Visco–elastodynamic problems have been treated by Grasso et al. [121]. Finally, Takahashi has recently developed a broadband 2D elastodynamic FMBEM [189]. Reviews of the literature for the elastodynamic FMBEM can be found in Refs. [164] and [190].

4.2 The Elastodynamic FMBEM

In this section the elastodynamic BIE for solving frequency–domain problems in solid elastic structures is introduced. The implementation of the elastodynamic FMBEM is presented in subsections which respectively focus on the FMBEM treatment of the far field and the direct BEM integration of the near field. Preconditioning and iterative solution strategies for the elastodynamic FMBEM which mirror those for the Helmholtz FMBEM are also discussed. The salient features of this section should be recognised as the low frequency FMBEM treatment of the elastodynamic BIE, particularly the construction of the spherical basis expansions which are input into the FMM algorithm. Again it is stressed that once the relevant expansions are passed into the

FMM algorithm, the procedural steps (upward pass, downward pass, final summation) as discussed in Chapter 2 are exactly the same as those for the Helmholtz FMBEM.

The elastodynamic FMBEM presented in this section is the first such model to utilise both low algorithmic complexity $O(p^3)$ translation methods and $S|R$ translation stencils to minimise the computation cost of the FMM in the low frequency domain. Prior low frequency implementations in the published literature have either used the original $O(p^5)$ FMM translation methods based on the Wigner 3–j symbols [178], or the $O(p^3)$ RCR translation methods [181, 182], but have required the application of the full set of up to 189 $S|R$ translations per octree box.

4.2.1 The Elastodynamic BIE

The three equations which describe linear elasticity in a homogeneous elastic solid are the linear–elastic constitutive relation, the compatibility relation, and Cauchy's first law of motion [191]. Assuming a time–harmonic motion of the form $e^{-i\omega t}$, Cauchy's first law takes the form

$$\nabla \cdot \boldsymbol{\sigma} + \rho\omega^2 \mathbf{u} + \rho \mathbf{F} = 0 \tag{4.1}$$

where the total displacement $\mathbf{u}$ and body force distribution $\mathbf{F}$ are vector quantities and $\boldsymbol{\sigma}$ is the Cauchy stress tensor. The elastodynamic BIE may be derived by relating two distinct elastodynamic states described by Eq. 4.1 via the reciprocity theorem and then integrating the resulting equation over the elastic domain [191]. Assuming that no body forces are present, the elastodynamic BIE for an infinite exterior elastic domain may be derived by limiting all variables to the boundary surface [37], giving

$$\frac{1}{2} u_i(\mathbf{y}) = \int_S \Big(U_{ij}^{\mathrm{T}}(\mathbf{x},\mathbf{y}) t_i(\mathbf{x}) - T_{ij}^{\mathrm{T}}(\mathbf{x},\mathbf{y}) u_i(\mathbf{x}) \Big) dS(\mathbf{x}) + u_i^{\mathrm{inc}}(\mathbf{y}) \tag{4.2}$$

where u_i and t_i are the i^{th} Cartesian components of the total displacement and surface stress (or traction) on the boundary surface S, $\mathbf{x}$ & $\mathbf{y}$ are points on the surface, again assumed to be locally smooth at $\mathbf{y}$, and the superscript $^{\mathrm{T}}$ denotes the transpose of the 3×3 coefficient matrices of the fundamental displacement U_{ij} and traction T_{ij} solutions [192]. The total displacement $u_i(\mathbf{x}) = u_i^{\mathrm{inc}}(\mathbf{x}) + u_i^{\mathrm{sca}}(\mathbf{x})$ is the sum of the incident $u_i^{\mathrm{inc}}(\mathbf{x})$ and scattered $u_i^{\mathrm{sca}}(\mathbf{x})$ field components and similarly for the total surface stress. The

elastodynamic fundamental solutions may be expressed as [178]:

$$U_{ij}(\mathbf{x},\mathbf{y}) = \frac{1}{k_s^2\mu}\left[(\delta_{qr}\delta_{ij} - \delta_{qj}\delta_{ir})\frac{\partial}{\partial x_q}\frac{\partial}{\partial y_r}G_s(\mathbf{x},\mathbf{y}) + \frac{\partial}{\partial x_i}\frac{\partial}{\partial y_j}G_p(\mathbf{x},\mathbf{y})\right] \tag{4.3}$$

$$T_{ij}(\mathbf{x},\mathbf{y}) = \mu\left[\frac{2\nu}{1-2\nu}\delta_{ik}\delta_{lm} + \delta_{il}\delta_{km} + \delta_{kl}\delta_{im}\right]\frac{\partial}{\partial x_m}U_{lj}(\mathbf{x},\mathbf{y})n_k(\mathbf{x}) \tag{4.4}$$

where the subscript indices $i, j, k, l, m, q, r = 1\!:\!3$ (repeated subscript indices in products imply summation over all indices), $G_p(\mathbf{x},\mathbf{y})$ and $G_s(\mathbf{x},\mathbf{y})$ are the Helmholtz Green's functions (Eq. 2.3) for the compressional (primary) k_p and shear (secondary) k_s wavenumbers in the elastic solid, $n_k(\mathbf{x})$ is the k^{th} component of the outward pointing surface normal at $\mathbf{x}$ and δ_{ij} is the Kronecker delta function [183]. The compressional and shear waves have the following sound speeds and wavenumbers:

$$c_p = \sqrt{\frac{2(1-\nu)}{1-2\nu}}c_s \qquad k_p = \sqrt{\frac{1-2\nu}{2(1-\nu)}}k_s$$

$$c_s = \sqrt{\frac{\mu}{\rho_s}} \qquad k_s = \sqrt{\frac{\rho_s\omega^2}{\mu}}$$

where ρ_s, μ and ν are respectively the density, shear modulus and Poisson's ratio of the elastic solid. Eq. 4.3 contains second–order partial derivatives of $G(\mathbf{x},\mathbf{y})$ with respect to the Cartesian coordinates, while Eq. 4.4 can be seen to contain third–order partial derivatives upon substituting for U_{ij} via Eq. 4.3. The second partial derivatives with respect to mixed and non-mixed Cartesian components are:

$$\frac{\partial^2 G(\mathbf{x},\mathbf{y})}{\partial \mathbf{x}_i \partial \mathbf{y}_j} = -\frac{e^{ikr}}{4\pi r^3}\left(3 - 3ikr - k^2r^2\right)\left(\frac{r_i}{r}\right)\left(\frac{r_j}{r}\right) \tag{4.5}$$

$$\frac{\partial^2 G(\mathbf{x},\mathbf{y})}{\partial \mathbf{x}_i \partial \mathbf{y}_i} = \frac{e^{ikr}}{4\pi r^3}\left(1 - ikr\right) - \frac{e^{ikr}}{4\pi r^3}\left(3 - 3ikr - k^2r^2\right)\left(\frac{2r_i}{r}\right) \tag{4.6}$$

while the third partial derivatives with respect to mixed, partially mixed and non–mixed Cartesian components are:

$$\frac{\partial^3 G(\mathbf{x},\mathbf{y})}{\partial \mathbf{x}_i \partial \mathbf{x}_j \partial \mathbf{y}_k} = \frac{e^{ikr}}{4\pi r^4}\left(15 - 15ikr - 6k^2r^2 + ik^3r^3\right)\left(\frac{r_i}{r}\right)\left(\frac{r_j}{r}\right)\left(\frac{r_k}{r}\right) \tag{4.7}$$

$$\frac{\partial^3 G(\mathbf{x},\mathbf{y})}{\partial \mathbf{x}_i \partial \mathbf{x}_i \partial \mathbf{y}_j} = -\frac{e^{ikr}}{4\pi r^4}\left(3 - 3ikr - k^2r^2\right)\left(\frac{r_j}{r}\right) + \frac{e^{ikr}}{4\pi r^4}\left(15 - 15ikr - 6k^2r^2 + ik^3r^3\right)\left(\frac{2r_i}{r}\right)\left(\frac{r_j}{r}\right) \tag{4.8}$$

$$\frac{\partial^3 G(\mathbf{x},\mathbf{y})}{\partial \mathbf{x}_i \partial \mathbf{x}_i \partial \mathbf{y}_i} = -\frac{e^{ikr}}{4\pi r^4}\left(3 - 3ikr - k^2r^2\right)\left(\frac{3r_i}{r}\right) + \frac{e^{ikr}}{4\pi r^4}\left(15 - 15ikr - 6k^2r^2 + ik^3r^3\right)\left(\frac{3r_i}{r}\right) \tag{4.9}$$

where $r = |\mathbf{x} - \mathbf{y}|$ and $r_i = \mathbf{x}_i - \mathbf{y}_i$. Denoting the double partial derivatives $\frac{\partial^2 G(\mathbf{x},\mathbf{y})}{\partial \mathbf{x}_i \partial \mathbf{y}_j}$ as $[G_s]_{ij}$ or $[G_p]_{ij}$ for the shear/compressional waves and dropping the $(\mathbf{x},\mathbf{y})$ dependence in the notation, the main diagonal terms of the displacement fundamental solution may be expressed in terms of the Green's functions as

$$U_{ii} = \frac{1}{k_s^2 \mu}\Big(k_s^2 G_s - \big[G_s\big]_{ii} + \big[G_p\big]_{ii}\Big) \tag{4.10}$$

with the above equation simplified using the substitution [178]

$$(\nabla^2 + k^2)G(\mathbf{x},\mathbf{y}) = 0, \quad \mathbf{y} \neq \mathbf{x} \tag{4.11}$$

while the off-diagonal terms ($i \neq j$) can be expressed as

$$U_{ij} = U_{ji} = \frac{1}{k_s^2 \mu}\Big(\big[G_p\big]_{ij} - \big[G_s\big]_{ji}\Big) \tag{4.12}$$

The Green's function is invariant to the order of the double partial differentiation with respect to the Cartesian coordinates and so U_{ij} is symmetric. Each row of the 3×3 traction fundamental solution may be expressed in terms of the displacement fundamental solution as follows:

$$\begin{aligned} T_{1j} =& \mu\left[\left(\frac{2\nu}{1-2\nu}\right)\frac{\partial}{\partial \mathbf{x}_g}U_{hj}\delta_{gh} + 2\frac{\partial}{\partial \mathbf{x}_1}U_{1j}\right]n_1(\mathbf{x}) \\ &+\mu\left[\frac{\partial}{\partial \mathbf{x}_1}U_{2j} + \frac{\partial}{\partial \mathbf{x}_2}U_{1j}\right]n_2(\mathbf{x}) \\ &+\mu\left[\frac{\partial}{\partial \mathbf{x}_1}U_{3j} + \frac{\partial}{\partial \mathbf{x}_3}U_{1j}\right]n_3(\mathbf{x}) \end{aligned} \tag{4.13}$$

$$
\begin{aligned}
T_{2j} =& \mu \left[\frac{\partial}{\partial \mathbf{x}_1} U_{2j} + \frac{\partial}{\partial \mathbf{x}_2} U_{1j} \right] n_1(\mathbf{x}) \\
&+ \mu \left[\left(\frac{2\nu}{1-2\nu} \right) \frac{\partial}{\partial \mathbf{x}_g} U_{hj} \delta_{gh} + 2 \frac{\partial}{\partial \mathbf{x}_2} U_{2j} \right] n_2(\mathbf{x}) \\
&+ \mu \left[\frac{\partial}{\partial \mathbf{x}_2} U_{3j} + \frac{\partial}{\partial \mathbf{x}_3} U_{2j} \right] n_3(\mathbf{x}) \qquad (4.14) \\
T_{3j} =& \mu \left[\frac{\partial}{\partial \mathbf{x}_1} U_{3j} + \frac{\partial}{\partial \mathbf{x}_3} U_{1j} \right] n_1(\mathbf{x}) \\
&+ \mu \left[\frac{\partial}{\partial \mathbf{x}_2} U_{3j} + \frac{\partial}{\partial \mathbf{x}_3} U_{2j} \right] n_2(\mathbf{x}) \\
&+ \mu \left[\left(\frac{2\nu}{1-2\nu} \right) \frac{\partial}{\partial \mathbf{x}_g} U_{hj} \delta_{gh} + 2 \frac{\partial}{\partial \mathbf{x}_3} U_{3j} \right] n_3(\mathbf{x}) \qquad (4.15)
\end{aligned}
$$

where $g, h, j = 1:3$. Substituting the diagonal and off-diagonal relations for U_{ij} (Eqs. 4.10 and 4.12) and using Eq. 4.11 in the form

$$
\left(\frac{\partial}{\partial x_1} \frac{\partial}{\partial y_1} + \frac{\partial}{\partial x_2} \frac{\partial}{\partial y_2} + \frac{\partial}{\partial x_3} \frac{\partial}{\partial y_3} \right) G(\mathbf{x}, \mathbf{y}) = k^2 G(\mathbf{x}, \mathbf{y})
$$

allows the T_{ij} terms to be expressed explicitly in terms of G as:

$$
\begin{aligned}
T_{1j} = \frac{1}{k_s^2} \Big[& \Big(\beta k_p^2 \big[G_p\big]_{j0} + 2k_s^2 \big[G_s\big]_{10} \delta_{1j} + 2\big(\big[G_p\big]_{j11} - \big[G_s\big]_{j11} \big) \Big) n_1(\mathbf{x}) \\
& + \Big(k_s^2 \big[G_s\big]_{20} \delta_{1j} + k_s^2 \big[G_s\big]_{10} \delta_{2j} + 2\big(\big[G_p\big]_{j12} - \big[G_s\big]_{j12} \big) \Big) n_2(\mathbf{x}) \\
& + \Big(k_s^2 \big[G_s\big]_{30} \delta_{1j} + k_s^2 \big[G_s\big]_{10} \delta_{3j} + 2\big(\big[G_p\big]_{j13} - \big[G_s\big]_{j13} \big) \Big) n_3(\mathbf{x}) \Big] \qquad (4.16) \\
T_{2j} = \frac{1}{k_s^2} \Big[& \Big(k_s^2 \big[G_s\big]_{10} \delta_{2j} + k_s^2 \big[G_s\big]_{20} \delta_{1j} + 2\big(\big[G_p\big]_{j21} - \big[G_s\big]_{j21} \big) \Big) n_1(\mathbf{x}) \\
& + \Big(\beta k_p^2 \big[G_p\big]_{j0} + 2k_s^2 \big[G_s\big]_{20} \delta_{2j} + 2\big(\big[G_p\big]_{j22} - \big[G_s\big]_{j22} \big) \Big) n_2(\mathbf{x}) \\
& + \Big(k_s^2 \big[G_s\big]_{30} \delta_{2j} + k_s^2 \big[G_s\big]_{20} \delta_{3j} + 2\big(\big[G_p\big]_{j23} - \big[G_s\big]_{j23} \big) \Big) n_3(\mathbf{x}) \Big] \qquad (4.17) \\
T_{3j} = \frac{1}{k_s^2} \Big[& \Big(k_s^2 \big[G_s\big]_{10} \delta_{3j} + k_s^2 \big[G_s\big]_{30} \delta_{1j} + 2\big(\big[G_p\big]_{j31} - \big[G_s\big]_{j31} \big) \Big) n_1(\mathbf{x}) \\
& + \Big(k_s^2 \big[G_s\big]_{20} \delta_{3j} + k_s^2 \big[G_s\big]_{30} \delta_{2j} + 2\big(\big[G_p\big]_{j32} - \big[G_s\big]_{j32} \big) \Big) n_2(\mathbf{x}) \\
& + \Big(\beta k_p^2 \big[G_p\big]_{j0} + 2k_s^2 \big[G_s\big]_{30} \delta_{3j} + 2\big(\big[G_p\big]_{j33} - \big[G_s\big]_{j33} \big) \Big) n_3(\mathbf{x}) \Big] \qquad (4.18)
\end{aligned}
$$

where $\beta = \frac{2\nu}{1-2\nu}$ and the notation $\big[G\big]_{g0}$ denotes the first partial derivative of $G(\mathbf{x}, \mathbf{y})$ with respect to the g^{th} Cartesian component of $\mathbf{x}$: $\big[G\big]_{g0} = \frac{\partial G(\mathbf{x}, \mathbf{y})}{\partial \mathbf{x}_g}$. Conversely, $\big[G\big]_{0g}$ is later used to denote the first partial derivative of $G(\mathbf{x}, \mathbf{y})$ with respect to the g^{th} component of $\mathbf{y}$. The third–order partial derivatives of $G(\mathbf{x}, \mathbf{y})$ are denoted as $\big[G\big]_{ghi} = \frac{\partial^3 G(\mathbf{x}, \mathbf{y})}{\partial \mathbf{x}_g \partial \mathbf{x}_h \partial \mathbf{y}_i}$ where g and h are applied at $\mathbf{x}$ and i is applied at y.

As with the Helmholtz BIE, Eq. 4.2 may be numerically discretised and solved on an arbitrary boundary surface. Boundary conditions can be similarly employed to eliminate one of the unknowns (u_i, t_i) on S to yield an exactly solvable system of equations. If plane triangular elements with piece–wise constant unknowns are used for the discretisation then a surface mesh containing N elements will have $3N$ unknowns for the Cartesian components of the displacement/traction at the centre of each element. The full BEM coefficients matrices of the fundamental solutions U_{ij} and T_{ij} will similarly be of size $3N \times 3N$ for an N–element mesh. The following subsections explain how the FMBEM and direct numerical integration techniques are employed to respectively treat the well–separated and near field parts of the surface integrals in Eq. 4.2.

4.2.2 FMBEM Treatment of the Far Field

In the previous chapter recursion relations were presented for differential operators involving the first–order partial derivatives of the spherical basis functions with respect to the Cartesian coordinates (Eqs. 3.16–3.18) and these were used for building the integral terms in the Burton–Miller formulation (Eqs. 3.22–3.25). Here an analogous process must be applied to the displacement and traction fundamental solutions of the elastodynamic BIE (Eqs. 4.3 and 4.4) which involve up to third–order partial derivatives of the Helmholtz Green's function. However in practice only second–order partial derivatives of the spherical basis functions are required for the multipole expansion of the U_{ij} and T_{ij} terms as the partial derivative relations may be applied to both the source and receiver multipole expansions. Recurrence relations for the second–order differential operators can be derived by substituting the first–order relations back into those same relations. The following operators are defined:

$$\partial_{z^2} \equiv \frac{\partial^2}{\partial z^2} \tag{4.19}$$

$$\partial_{zx+izy} \equiv \frac{\partial}{\partial z}\frac{\partial}{\partial x} + i\frac{\partial}{\partial z}\frac{\partial}{\partial y} \tag{4.20}$$

$$\partial_{zx-izy} \equiv \frac{\partial}{\partial z}\frac{\partial}{\partial x} - i\frac{\partial}{\partial z}\frac{\partial}{\partial y} \tag{4.21}$$

$$\partial_{(x+iy)^2} \equiv \frac{\partial^2}{\partial x^2} + 2i\frac{\partial}{\partial x}\frac{\partial}{\partial y} - \frac{\partial^2}{\partial y^2} \tag{4.22}$$

$$\partial_{(x-iy)^2} \equiv \frac{\partial^2}{\partial x^2} - 2i\frac{\partial}{\partial x}\frac{\partial}{\partial y} - \frac{\partial^2}{\partial y^2} \tag{4.23}$$

$$\partial_{(x+iy)(x-iy)} \equiv \frac{\partial^2}{\partial x^2} + \frac{\partial^2}{\partial y^2} \tag{4.24}$$

where the unique second–order partial derivatives may be separated as:

$$\frac{\partial}{\partial z}\frac{\partial}{\partial x} = \frac{1}{2}\left[\partial_{zx+izy} + \partial_{zx-izy}\right] \tag{4.25}$$

$$\frac{\partial}{\partial z}\frac{\partial}{\partial y} = -\frac{i}{2}\left[\partial_{zx+izy} - \partial_{zx-izy}\right] \tag{4.26}$$

$$\frac{\partial^2}{\partial x^2} = \frac{1}{4}\left[\partial_{(x+iy)^2} + \partial_{(x-iy)^2} + 2\partial_{(x+iy)(x-iy)}\right] \tag{4.27}$$

$$\frac{\partial^2}{\partial y^2} = -\frac{1}{4}\left[\partial_{(x+iy)^2} + \partial_{(x-iy)^2} - 2\partial_{(x+iy)(x-iy)}\right] \tag{4.28}$$

$$\frac{\partial}{\partial x}\frac{\partial}{\partial y} = -\frac{i}{4}\left[\partial_{(x+iy)^2} - \partial_{(x-iy)^2}\right] \tag{4.29}$$

The recurrence relations for the second–order differential operators (Eqs. 4.19–4.24) for either of the spherical basis functions ($F = S, R$) can be expressed as follows:

$$\begin{aligned}\partial_{z^2} F_n^m(\mathbf{r}) = k^2 \big[&a_{n-1}^m a_{n-2}^m F_{n-2}^m(\mathbf{r}) - (a_{n-1}^m)^2 F_n^m(\mathbf{r}) \\ &- (a_n^m)^2 F_n^m(\mathbf{r}) + a_n^m a_{n+1}^m F_{n+2}^m(\mathbf{r})\big]\end{aligned} \tag{4.30}$$

$$\begin{aligned}\partial_{zx+izy} F_n^m(\mathbf{r}) = k^2 \big[&-a_{n-1}^m b_{n-1}^m F_{n-2}^{m+1}(\mathbf{r}) + a_{n-1}^m b_n^{-m-1} F_n^{m+1}(\mathbf{r}) \\ &+ a_n^m b_{n+1}^m F_n^{m+1}(\mathbf{r}) - a_n^m b_{n+2}^{-m-1} F_{n+2}^{m+1}(\mathbf{r})\big]\end{aligned} \tag{4.31}$$

$$\begin{aligned}\partial_{zx-izy} F_n^m(\mathbf{r}) = k^2 \big[&-a_{n-1}^m b_{n-1}^{-m} F_{n-2}^{m-1}(\mathbf{r}) + a_{n-1}^m b_n^{m-1} F_n^{m-1}(\mathbf{r}) \\ &+ a_n^m b_{n+1}^{-m} F_n^{m-1}(\mathbf{r}) - a_n^m b_{n+2}^{m-1} F_{n+2}^{m-1}(\mathbf{r})\big]\end{aligned} \tag{4.32}$$

$$\begin{aligned}\partial_{(x+iy)^2} F_n^m(\mathbf{r}) = k^2 \big[&b_n^m b_{n-1}^{m+1} F_{n-2}^{m+2}(\mathbf{r}) - b_n^m b_n^{-m-2} F_n^{m+2}(\mathbf{r}) \\ &- b_{n+1}^{-m-1} b_{n+1}^{m+1} F_n^{m+2}(\mathbf{r}) + b_{n+1}^{-m-1} b_{n+2}^{-m-2} F_{n+2}^{m+2}(\mathbf{r})\big]\end{aligned} \tag{4.33}$$

$$\begin{aligned}\partial_{(x-iy)^2} F_n^m(\mathbf{r}) = k^2 \big[&b_n^{-m} b_{n-1}^{-m+1} F_{n-2}^{m-2}(\mathbf{r}) - b_n^{-m} b_{n-1}^{m-2} F_n^{m-2}(\mathbf{r}) \\ &- b_{n+1}^{m-1} b_{n+1}^{-m+1} F_n^{m-2}(\mathbf{r}) + b_{n+1}^{m-1} b_{n+2}^{m-2} F_{n+2}^{m-2}(\mathbf{r})\big]\end{aligned} \tag{4.34}$$

$$\begin{aligned}\partial_{(x+iy)(x-iy)} F_n^m(\mathbf{r}) = k^2 \big[&b_n^m b_{n-1}^{-m-1} F_{n-2}^m(\mathbf{r}) - (b_n^m)^2 F_n^m(\mathbf{r}) \\ &- (b_{n+1}^{-m-1})^2 F_n^m(\mathbf{r}) + b_{n+1}^{-m-1} b_{n+2}^m F_{n+2}^m(\mathbf{r})\big]\end{aligned} \tag{4.35}$$

where k is the relevant wavenumber and a_n^m and b_n^m have been previously defined in Eq. 3.19 and Eq. 3.20 respectively. For a truncation number of p_l on the lowest octree level l, the second–order partial derivatives of the expansions require the degree to be truncated at $p_l + 2$ for the F_{n+2} coefficients. For the multipole expansion of $T_{ij}(\mathbf{x}, \mathbf{y})$, the above expressions for the second–order partial derivatives may be applied to the

source expansions, propagated through the FMM procedure (upward pass, downward pass) and then combined with the first–order partial derivatives of the receiver expansions (Eqs. 3.11, 3.14 and 3.15) in the final summation to build the third–order partial derivatives in $T_{ij}(\mathbf{x},\mathbf{y})$. The first–order relations are sufficient for the multipole expansion of $U_{ij}(\mathbf{x},\mathbf{y})$ when applied to both source and receiver expansions to give the second–order partial derivatives appearing in that solution. Obviously the application of Eqs. 4.32–4.35 to both the source and receiver multipole expansions will allow up to fourth–order partial derivatives of the Helmholtz Green's function to be expressed in terms of the R and S spherical basis functions.

It can be seen from Eqs. 4.3 and 4.4 that each of the fundamental solutions have nine components and each of these involve both the shear and compressional wave speeds, totalling thirty–six terms which must be propagated through the FMM algorithm. In practice this number can be substantially reduced by finding common Green's function terms in the components of the fundamental solutions and then only propagating these common terms through the FMM procedure.

Applying the $U_{ij}^{\mathrm{T}}t_i$ matrix–vector product and substituting Eqs. 4.10 and 4.12, the following common terms are observed:

$$\begin{aligned} k_s^2 G_s t_j - \left[G_s\right]_{gj} t_h \delta_{gh} & \\ &= k_s^2 G_s t_j - \left(\left[G_s\right]_{1j} t_1 + \left[G_s\right]_{2j} t_2 + \left[G_s\right]_{3j} t_3\right) \\ &= ik_s \sum_{n=0}^{\infty}\sum_{m=-n}^{n} \left(k_s^2 S_n^m(k_s) t_j + \left[S_n^m(k_s)\right]_{1j} t_1 + \left[S_n^m(k_s)\right]_{2j} t_2 + \left[S_n^m(k_s)\right]_{3j} t_3\right) \\ &\qquad \times \left(R_n^{-m}(k_s)\right) \end{aligned} \tag{4.36}$$

$$\left[G_p\right]_{gj} t_h \delta_{gh} = ik_p \sum_{n=0}^{\infty}\sum_{m=-n}^{n} \left(\left[S_n^m(k_p)\right]_1 t_1 + \left[S_n^m(k_p)\right]_2 t_2 + \left[S_n^m(k_p)\right]_3 t_3\right)\left(\left[R_n^{-m}(k_p)\right]_j\right) \tag{4.37}$$

where $g,h,j = 1:3$ and $F_n^m(k_f)$ denotes the spherical basis functions $F = S,R$ with compressional/shear wavenumbers k_f $(f = p,s)$. Additionally the subscripts of the multipole expansions denote the first partial derivatives $[F_n^m(k_f)]_j = \partial_j F_n^m(k_f)$. Note that the sign of the S expansions in Eq. 4.36 for the $\left[G_s\right]_{gj}$ terms has been changed to account for the fact that both partial derivatives have been applied at the source location i.e. $\frac{\partial^2 G(\mathbf{x},\mathbf{y})}{\partial \mathbf{x}_i \partial \mathbf{y}_j} = -\frac{\partial^2 G(\mathbf{x},\mathbf{y})}{\partial \mathbf{x}_i \partial \mathbf{x}_j}$ The integral of $U_{ij}^{\mathrm{T}}t_i$ over the $\tilde{n}^{th}$ plane triangular

element $E_{\tilde{n}}$ with area $A_{\tilde{n}}$ and source point $\mathbf{x}_{\tilde{n}}$ at its centre may then be approximated with the S and R spherical basis functions using Eqs. 4.36 and 4.37 as

$$\left[U_{ij}^{\mathrm{T}} t_i\right]_{E_{\tilde{n}}} \approx \frac{A_{\tilde{n}}}{k_s^2 \mu} \begin{bmatrix} k_s^2 G_s t_1 + \Big(\left[G_p\right]_{g1} - \left[G_s\right]_{g1}\Big) t_h \delta_{gh} \\ k_s^2 G_s t_2 + \Big(\left[G_p\right]_{g2} - \left[G_s\right]_{g2}\Big) t_h \delta_{gh} \\ k_s^2 G_s t_3 + \Big(\left[G_p\right]_{g3} - \left[G_s\right]_{g3}\Big) t_h \delta_{gh} \end{bmatrix} \tag{4.38}$$

Thus the treatment of the far field integrals of $U_{ij}^{\mathrm{T}} t_i$ requires the propagation of four sets of S expansions: three for Eq. 4.36 with $j = 1:3$ and one for Eq. 4.37. A similar process may be applied to the $T_{ij}^{\mathrm{T}} u_i$ matrix–vector product: the following common terms are observed when Eqs. 4.16–4.18 are multiplied with u_i:

$$\begin{aligned} &\Big(2\left[G_p\right]_{gjh} + \beta k_{p^2} \left[G_p\right]_{h0} \delta_{gj}\Big) n_g u_j \\ &\qquad = \Big(2\left[G_p\right]_{gjh} - \beta k_{p^2} \left[G_p\right]_{0h} \delta_{gj}\Big) n_g u_j \\ &\qquad = i k_p \sum_{n=0}^{\infty} \sum_{m=-n}^{n} \Big(\Big(\beta k_p^2 S_n^m(k_p) \delta_{gj} - 2\left[S_n^m(k_p)\right]_{gj}\Big) n_g u_j\Big)\Big(\left[R_n^{-m}(k_p)\right]_h\Big) \end{aligned} \tag{4.39}$$

$$2\left[G_s\right]_{gjh} n_g u_j = -i k_s \sum_{n=0}^{\infty} \sum_{m=-n}^{n} \Big(2\left[S_n^m(k_s)\right]_{gj} n_g u_j\Big)\Big(\left[R_n^{-m}(k_s)\right]_h\Big) \tag{4.40}$$

$$\begin{aligned} &k_{s^2} \left[G_s\right]_{g0} \big(n_g u_j + n_j u_g\big) \\ &\qquad = -i k_s^3 \sum_{n=0}^{\infty} \sum_{m=-n}^{n} \Big(\left[S_n^m(k_s)\right]_g \big(n_g u_j + n_j u_g\big)\Big)\Big(R_n^{-m}(k_s)\Big) \end{aligned} \tag{4.41}$$

where $g, h, j = 1:3$ and the second–order partial derivatives of the multipole expansions $\partial_i \partial_j F_n^m(k_f)$ are denoted as $[F_n^m(k_f)]_{ij}$. The integral of $T_{ij}^{\mathrm{T}} u_i$ over the $\tilde{n}^{th}$ plane triangular element $E_{\tilde{n}}$ with area $A_{\tilde{n}}$ and source point $\mathbf{x}_{\tilde{n}}$ at its centre may then be approximated with the S and R spherical basis functions using Eqs. 4.39–4.41 as

$$\begin{aligned} &\left[T_{ij}^{\mathrm{T}} u_i\right]_{E_{\tilde{n}}} \approx A_{\tilde{n}} \times \\ &\begin{bmatrix} \Big(2\Big(\left[G_p\right]_{gj1} - \left[G_s\right]_{gj1}\Big) - \beta k_{p^2} \left[G_p\right]_{01} \delta_{gj}\Big) n_g u_j + k_{s^2} \left[G_s\right]_{g0} \Big(n_g u_1 + n_1 u_g\Big) \\ \Big(2\Big(\left[G_p\right]_{gj2} - \left[G_s\right]_{gj2}\Big) - \beta k_{p^2} \left[G_p\right]_{02} \delta_{gj}\Big) n_g u_j + k_{s^2} \left[G_s\right]_{g0} \Big(n_g u_2 + n_2 u_g\Big) \\ \Big(2\Big(\left[G_p\right]_{gj3} - \left[G_s\right]_{gj3}\Big) - \beta k_{p^2} \left[G_p\right]_{03} \delta_{gj}\Big) n_g u_j + k_{s^2} \left[G_s\right]_{g0} \Big(n_g u_3 + n_3 u_g\Big) \end{bmatrix} \end{aligned} \tag{4.42}$$

which only requires the propagation of five sets of expansions through the FMM: one each for Eqs. 4.39 and Eq. 4.40 and three for Eq. 4.41 with $j = 1:3$. Thus the far field part of both integral terms in Eq. 4.2 can be treated by propagating nine sets of source expansions through the FMM algorithm and this may be reduced to four/five sets when using BCs which remove one of the unknowns from the BIE.

As a point of comparison, both the low–frequency elastodynamic FMBEM implemented by Yoshida [178] and the high–frequency one implemented by Chaillat [191] require four expansions each for both the U_{ij} and T_{ij} terms. The additional expansion required for T_{ij} in this implementation arises from the fact that Eq. 4.41 cannot be combined with Eq. 4.40, as was done by Chaillat [37], without directly evaluating the triple partial derivatives in Eq. 4.40 with respect to the source expansion (i.e. $\left[S_n^m(k_s)\right]_{gjh}$). The high–frequency multipole expansions used by Chaillat have the form of e^{ikr} terms and so the partial derivatives manifest as simple ik factors in the source expansions which pose no difficulty when calculating higher order partial derivatives. Conversely the low–frequency spherical basis functions used in this work, as well as similar forms used by Yoshida, directly incorporate spherical Bessel and associated Legendre functions and so the corresponding partial derivatives are more complex. Yoshida similarly has three shear and one compressional multipole expansion for T_{ij} but does not appear to elaborate on how the second–order partial derivatives are calculated, while formulae similar to those of Gumerov and Duraiswami [42] are presented for the first–order partial derivatives. In the implementation presented here, third–order partial derivatives could feasibly be derived from appropriate third–order differential operators but one would expect a corresponding increase in both the number of unique terms (18 terms) and the complexity of the expansions (eight F_n^m terms per expansion). A direction for future work will be to derive more compact recursions for the partial derivative relations which are amenable to deriving higher order derivatives.

Appropriate source expansions analogous to Eqs. 3.26–3.27 for the Helmholtz BIE can be constructed from the S expansions in the elastodynamic common factor equations, again recalling from Chapter 2 that both sources/receivers are represented with R expansions when using the $S|R$ translations (see Eq. 2.14). For U_{ij} the four sets of

source expansions (truncated at degree $n = p_l$) are:

$$ik_s \frac{A_{\tilde{n}}}{k_s^2 \mu} \Big(k_s^2 R_{p_l}^m(\mathbf{c}_{\tilde{m}} - \mathbf{x}_{\tilde{n}}, k_s) t_j(\mathbf{x}_{\tilde{n}}) + \big[R_{p_l}^m(\mathbf{c}_{\tilde{m}} - \mathbf{x}_{\tilde{n}}, k_s) \big]_{gj} t_g(\mathbf{x}_{\tilde{n}}) \Big) \tag{4.43}$$

$$ik_p \frac{A_{\tilde{n}}}{k_s^2 \mu} \big[R_{p_l}^m(\mathbf{c}_{\tilde{m}} - \mathbf{x}_{\tilde{n}}, k_p) \big]_g t_g(\mathbf{x}_{\tilde{n}}) \tag{4.44}$$

where $g, j = 1 : 3$. Also the notation $R_n^m(\mathbf{r}, k_f)$ has been used here to denote the relevant wavenumber ($k_f = k_p, k_s$) for the regular spherical basis functions with expansion vector $\mathbf{r}$. Similarly for T_{ij} the five sets of source expansions are:

$$ik_p A_{\tilde{n}} \Big(\beta k_p^2 R_{p_l}^m(\mathbf{c}_{\tilde{m}} - \mathbf{x}_{\tilde{n}}, k_p) \delta_{gj} - 2 \big[R_{p_l}^m(\mathbf{c}_{\tilde{m}} - \mathbf{x}_{\tilde{n}}, k_p) \big]_{gj} \Big) n_g(\mathbf{x}_{\tilde{n}}) u_j(\mathbf{x}_{\tilde{n}}) \tag{4.45}$$

$$-ik_s A_{\tilde{n}} \Big(2 \big[R_{p_l}^m(\mathbf{c}_{\tilde{m}} - \mathbf{x}_{\tilde{n}}, k_s) \big]_{gj} n_g(\mathbf{x}_{\tilde{n}}) u_j(\mathbf{x}_{\tilde{n}}) \Big) \tag{4.46}$$

$$-ik_s^3 A_{\tilde{n}} \big[R_{p_l}^m(\mathbf{c}_{\tilde{m}} - \mathbf{x}_{\tilde{n}}, k_s) \big]_g \big(n_g(\mathbf{x}_{\tilde{n}}) u_j(\mathbf{x}_{\tilde{n}}) + n_j(\mathbf{x}_{\tilde{n}}) u_g(\mathbf{x}_{\tilde{n}}) \big) \tag{4.47}$$

Finally it should be noted that the truncated source expansions in Eqs. 4.43 and 4.47 with maximum degree p_l require expansions truncated at $p_l + 1$ for the recursion relations of the first–order partial derivatives while Eq. 4.46 requires terms up to degree $p_l + 2$ for the second–order partial derivative recursion relations. Similarly the receiver expansions which are combined with Eqs. 4.43, 4.45 and 4.46 in the final stage of the downward pass require the expansions to be truncated at $p_l + 1$ to construct the first–order partial derivatives applied at the receiver locations.

4.2.3 Numerical Treatment of the Near Field

The near field part of the surface integrals defined by the boxes on the lowest level of the octree structure, as well as the definitions of the regular, near–singular and singular integrals for the elastodynamic BIE are essentially the same as that for the Helmholtz FMBEM presented in Section 3.2.3 of Chapter 3. The only difference here is the form of the fundamental solutions that must be integrated. Upon inspection of the relevant Green's function partial derivatives (Eqs. 4.5–4.9), the displacement and traction fundamental solutions appear to involve singularities of the order $\frac{1}{r^3}$ and $\frac{1}{r^4}$ respectively. However it has been shown that by applying a series expansion to the exponential terms appearing in the fundamental solutions, the order of the singularities of U_{ij} and T_{ij} reduce to $\frac{1}{r}$ and $\frac{1}{r^2}$ respectively [172]. Thus the three types of surface integral in the elastodynamic FMBEM are treated as follows:

Regular Integration. The numerical integration of the regular integrals are applied directly to the original U_{ij} and T_{ij} terms using standard low order Gauss–Legendre quadrature adapted for plane triangular elements [134].

Near–Singular Integration. The element integrals which may exhibit near–singular behaviour are treated using a specialised near–singular integration technique [135] and are applied to the fundamental solutions which have had the singularities weakened using the series expansion of the exponential terms.

Singular Integration. The singular integrals of the U_{ij} and T_{ij} terms are again weakened using the series expansions of the exponential terms. The $\frac{1}{r}$ singularity of U_{ij} is then treated using a radial coordinate transformation [29] while the $\frac{1}{r^2}$ singularity of T_{ij} is approximated by using a limiting case of the near–singular integration technique, where the source point is placed arbitrarily close to the surface of the singular element. The source point for the singular integration of each element is displaced in the direction normal to the element surface (directly above the element centre/corresponding receiver point) by a static value of 10^{-10}m. The accuracy of the approximation of the T_{ij} singular integration was compared to an analytic integration technique for T_{ij} [191]. This analytic method was unable to be fully implemented in the model to simply replace the approximation to the singular integrals due to time constraints. However the analytic technique was successfully implemented for the diagonal T_{ii} terms where it was observed that the singular integrals calculated by the approximate method agreed with the analytic integral results to three–four significant figures when using a 30 point Gauss–Legendre quadrature rule. This level of accuracy is sufficient for the piece–wise constant triangular elements and is consistent with the errors inherent in the FMM. An obvious avenue for future work will be to implement a proper singular integration technique for the T_{ij} terms or implement a suitable regularisation technique to the elastodynamic BIE (for example [193]) to reduce the order of the singularities appearing in the integral terms.

4.2.4 FMBEM Iterative Solution and Preconditioning

The elastodynamic FMBEM uses the same iterative solution and preconditioning techniques as the Helmholtz FMBEM, as previously discussed in Section 3.2.4 of Chapter 3. The iterative solution is implemented using a nested inner–outer fGMRES loop which

allows for a different preconditioner each iteration [152, 153]. The inner loop is a low accuracy FMBEM which is used as a preconditioner for the outer loop, where the FMBEM is calculated at full accuracy. The FMBEM in the inner GMRES loop is itself preconditioned using a sparse approximate inverse (SAI) preconditioner [62] constructed from the near field part of the surface integrals. Similar values are used in the elastodynamic FMBEM for the inner/outer GMRES convergence tolerances ($\xi = 10^{-4}$,$\xi_{\text{pre}} = 0.15$) and the specified accuracies for the main/preconditioner multipole expansions of the Green's functions ($\epsilon = 10^{-4}$,$\epsilon_{\text{pre}} = 0.2$).

4.2.5 Elastodynamic FMBEM Algorithm

This section is concluded by presenting pseudocode algorithms for the iterative FMBEM solution for an exterior elastodynamic scattering problem involving an incident displacement field impinging upon an arbitrary enclosed surface in an infinite elastic solid. The surface is discretised with a boundary mesh consisting of N plane triangle elements with corresponding areas listed in A_N and source/receiver points at the element centres listed in $\mathbf{x}_N$ and $\mathbf{y}_N$ (with $\mathbf{x}_N = \mathbf{y}_N$ for the collocation method). Assuming an impedance type BC which relates the total surface stress $t_i(\mathbf{x})$ to the total displacement $u_i(\mathbf{x})$ by some known function $g(\mathbf{x})$ i.e. $t_i(\mathbf{x}) = g(\mathbf{x})u_i(\mathbf{x})$, then the discretised elastodynamic BIE can be written in the form of an $\mathbf{Az} = \mathbf{b}$ matrix equation

$$\left(\frac{1}{2}\mathbf{I}_{3N} - \big(\mathbf{U}_{3N}\big)g(\mathbf{x}_N) + \mathbf{T}_{3N}\right) u_i(\mathbf{x}_N) = u_i^{\text{inc}}(\mathbf{y}_N) \tag{4.48}$$

where $\mathbf{U}_{3N} = \int_S U_{ij}^{\text{T}}(\mathbf{x}_N, \mathbf{y}_N)dS(\mathbf{x}_N)$, $\mathbf{T}_{3N} = \int_S T_{ij}^{\text{T}}(\mathbf{x}_N, \mathbf{y}_N)dS(\mathbf{x}_N)$ (the transpose operations are applied individually to each of the 3×3 submatrices) and $\mathbf{I}_{3N}$ is the identity matrix, all being of size $3N \times 3N$. The set up algorithm for the elastodynamic FMBEM performs essentially the same tasks as Alg. 3.1 for the Helmholtz FMBEM and so an equivalent algorithm is not presented here. The principal modifications to the set up algorithm for the elastodynamic FMBEM are as follows:

1. The octree truncation numbers, source/receiver expansions and various translations ($S|S$, $R|R$, $S|R$) are constructed for two wavenumbers: k_p and k_s.

2. Function BUILD_EXPTRANS builds the set of source expansions and the corresponding sets of first/second–order partial derivatives: $R_{\hat{l}}(\mathbf{c}_{\hat{l}} - \mathbf{x}_N)$, $\big[R_{\hat{l}}(\mathbf{c}_{\hat{l}} - \mathbf{x}_N)\big]_i$ and $\big[R_{\hat{l}}(\mathbf{c}_{\hat{l}} - \mathbf{x}_N)\big]_{ij}$ required for the displacement/traction fundamental solutions.

3. Function NEAR_FIELD builds the analogous sparse near field and SAI preconditioner matrices $\mathbf{U}_{\text{nf}}$, $\mathbf{T}_{\text{nf}}$ and $(\mathbf{UT})_{\text{pre}}$ for the elastodynamic BIE.

The other stages of setting up the octree levels, truncation numbers and multipole translations for the elastodynamic BIE remain unchanged.

The FMBEM algorithm for the elastodynamic BIE is presented in Alg. 4.1. The main steps of the algorithm (upward pass, downward pass, final summation) are the same as that in Alg. 3.2 for the Helmholtz FMBEM but are complicated by the fact that multiple sets of expansions are propagated through the FMM for the more complicated displacement/traction fundamental solutions.

Alg. 4.1 similarly utilises the relation $\overline{R_n^m(\mathbf{r})} = R_n^{-m}(\mathbf{r})$ in the final summation to reconstruct the $U_{ij}^{\text{T}} t_i$ and $T_{ij}^{\text{T}} u_i$ terms, as was done in Alg. 3.2 to reconstruct the BM terms. Furthermore the partial derivatives of the spherical basis functions are applied along the expansion vectors which are directed away from the source/receiver points (i.e. towards the local expansion centres: see Eq. 2.11a and Fig. 2.18) and so give the negative of the Green's function for odd–number partial derivatives. The source expansions for the common factors in the traction fundamental solution have been multiplied by -1 to account for this sign change (see Eqs. 4.39–4.41) and hence give the correct sign of the Green's function terms when reconstructing $T_{ij}^{\text{T}} u_i$ in the final summation. The displacement fundamental solution only involves even–number partial derivatives applied at the source and receiver positions and so the pairs of -1 factors cancel one another without intervention.

Algorithm 4.1 Elastodynamic FMBEM Algorithm

function ELASTO_FMBEM($k_p, k_s, p_l, u_i(\mathbf{x}_N), t_i(\mathbf{x}_N), \beta, \mu, A_N, R_{\hat{l}}, [R_{\hat{l}}]_i, [R_{\hat{l}}]_{ij}$, $(SS)_l, (RR)_l, (SR)_l, \mathbf{U}_{\mathrm{nf}}, \mathbf{T}_{\mathrm{nf}}$)

▷ Build the 4 sets of source expansions for $U_{ij}^{\mathrm{T}} t_i$ as $R_{\hat{l}}^{[U(1)]}(\mathbf{c}_{\hat{l}})$:$R_{\hat{l}}^{[U(4)]}(\mathbf{c}_{\hat{l}})$

$R_{\hat{l}}^{[U(1)]}(\mathbf{c}_{\hat{l}}) = \Big\{ ik_s \frac{A_N}{k_s^2 \mu} \Big(k_s^2 R_{\hat{l}}(\mathbf{c}_{\hat{l}} - \mathbf{x}_N, k_s) t_1(\mathbf{x}_N) + [R_{\hat{l}}(\mathbf{c}_{\hat{l}} - \mathbf{x}_N, k_s)]_{g1} t_g(\mathbf{x}_N) \Big) \Big\}_{\mathbf{c}_l}$

$R_{\hat{l}}^{[U(2)]}(\mathbf{c}_{\hat{l}}) = \Big\{ ik_s \frac{A_N}{k_s^2 \mu} \Big(k_s^2 R_{\hat{l}}(\mathbf{c}_{\hat{l}} - \mathbf{x}_N, k_s) t_2(\mathbf{x}_N) + [R_{\hat{l}}(\mathbf{c}_{\hat{l}} - \mathbf{x}_N, k_s)]_{g2} t_g(\mathbf{x}_N) \Big) \Big\}_{\mathbf{c}_l}$

$R_{\hat{l}}^{[U(3)]}(\mathbf{c}_{\hat{l}}) = \Big\{ ik_s \frac{A_N}{k_s^2 \mu} \Big(k_s^2 R_{\hat{l}}(\mathbf{c}_{\hat{l}} - \mathbf{x}_N, k_s) t_3(\mathbf{x}_N) + [R_{\hat{l}}(\mathbf{c}_{\hat{l}} - \mathbf{x}_N, k_s)]_{g3} t_g(\mathbf{x}_N) \Big) \Big\}_{\mathbf{c}_l}$ ▷ via Eq. 4.43

$R_{\hat{l}}^{[U(4)]}(\mathbf{c}_{\hat{l}}) = \big\{ ik_p \frac{A_N}{k_s^2 \mu} [R_{\hat{l}}(\mathbf{c}_{\hat{l}} - \mathbf{x}_N, k_p)]_g t_g(\mathbf{x}_N) \big\}_{\mathbf{c}_l}$ ▷ via Eq. 4.44

▷ Build the 5 sets of source expansions for $T_{ij}^{\mathrm{T}} u_i$ as $R_{\hat{l}}^{[T(1)]}(\mathbf{c}_{\hat{l}})$:$R_{\hat{l}}^{[T(5)]}(\mathbf{c}_{\hat{l}})$

$R_{\hat{l}}^{[T(1)]}(\mathbf{c}_{\hat{l}}) = \Big\{ ik_p A_N \Big(k_p^2 R_{\hat{l}}(\mathbf{c}_{\hat{l}} - \mathbf{x}_N, k_p) \delta_{gj}$

$- 2 \big[R_{\hat{l}}(\mathbf{c}_{\hat{l}} - \mathbf{x}_N, k_p) \big]_{gj} \Big) n_g(\mathbf{x}_N) u_j(\mathbf{x}_N) \Big\}_{\mathbf{c}_l}$ ▷ via Eq. 4.45

$R_{\hat{l}}^{[T(2)]}(\mathbf{c}_{\hat{l}}) = \Big\{ - ik_s A_N \Big(2 \big[R_{\hat{l}}(\mathbf{c}_{\hat{l}} - \mathbf{x}_N, k_s) \big]_{gj} n_g(\mathbf{x}_N) u_j(\mathbf{x}_N) \Big) \Big\}_{\mathbf{c}_l}$ ▷ via Eq. 4.46

$R_{\hat{l}}^{[T(3)]}(\mathbf{c}_{\hat{l}}) = \big\{ - ik_s^3 A_N \big[R_{\hat{l}}(\mathbf{c}_{\hat{l}} - \mathbf{x}_N, k_s) \big]_g \big(n_g(\mathbf{x}_N) u_1(\mathbf{x}_N) + n_1(\mathbf{x}_N) u_g(\mathbf{x}_N) \big) \big\}_{\mathbf{c}_l}$

$R_{\hat{l}}^{[T(4)]}(\mathbf{c}_{\hat{l}}) = \big\{ - ik_s^3 A_N \big[R_{\hat{l}}(\mathbf{c}_{\hat{l}} - \mathbf{x}_N, k_s) \big]_g \big(n_g(\mathbf{x}_N) u_2(\mathbf{x}_N) + n_2(\mathbf{x}_N) u_g(\mathbf{x}_N) \big) \big\}_{\mathbf{c}_l}$

$R_{\hat{l}}^{[T(5)]}(\mathbf{c}_{\hat{l}}) = \big\{ - ik_s^3 A_N \big[R_{\hat{l}}(\mathbf{c}_{\hat{l}} - \mathbf{x}_N, k_s) \big]_g \big(n_g(\mathbf{x}_N) u_3(\mathbf{x}_N) + n_3(\mathbf{x}_N) u_g(\mathbf{x}_N) \big) \big\}_{\mathbf{c}_l}$ ▷ via Eq. 4.47

for $l = \hat{l} : 3$ **do** ▷ upward pass: see Section 2.3.1

  for $i = 1 : 4$ **do** ▷ apply $S|S$ translations

    $R_{l-1}^{[U(i)]}(\mathbf{c}_{l-1}) = \{ (SS)_l R_{l-1}^{[U(i)]}(\mathbf{c}_l) \}_{\mathbf{c}_{l-1}}$ ▷ via Eq. 2.13

  end for

  for $i = 1 : 5$ **do** ▷ apply $S|S$ translations

    $R_{l-1}^{[T(i)]}(\mathbf{c}_{l-1}) = \{ (SS)_l R_{l-1}^{[T(i)]}(\mathbf{c}_l) \}_{\mathbf{c}_{l-1}}$ ▷ via Eq. 2.13

  end for

end for

for $l = 2 : \hat{l}$ **do** ▷ downward pass: see Section 2.3.2

  for $i = 1 : 4$ **do** ▷ apply $S|R$ translations

    $S_l^{[U(i)]}(\mathbf{c}_l) = (SR)_l R_l^{[U(i)]}\big(\{\{\{\mathbf{c}_l\}_{\mathrm{p}}\}_{\mathrm{n}}\}_{\mathrm{c}} \setminus \{\mathbf{c}_l\}_{\mathrm{n}} \big)$ ▷ via Eq. 2.14

  end for

  for $i = 1 : 5$ **do** ▷ apply $S|R$ translations

    $S_l^{[T(i)]}(\mathbf{c}_l) = (SR)_l R_l^{[T(i)]}\big(\{\{\{\mathbf{c}_l\}_{\mathrm{p}}\}_{\mathrm{n}}\}_{\mathrm{c}} \setminus \{\mathbf{c}_l\}_{\mathrm{n}} \big)$ ▷ via Eq. 2.14

  end for

Algorithm 4.1 Elastodynamic FMBEM Algorithm (Cont.)

if $l \neq \hat{l}$ **then**
  for $i = 1 : 4$ **do** ▷ apply $R|R$ translations
    $S_{l+1}^{[U(i)]}(\mathbf{c}_{l+1}) = \{(RR)_l S_l^{[U(i)]}(\mathbf{c}_l)\}_{\mathbf{c}_{l+1}}$ ▷ via Eq. 2.12
  end for
  for $i = 1 : 5$ **do** ▷ apply $R|R$ translations
    $S_{i+1}^{[T(i)]}(\mathbf{c}_{l+1}) = \{(RR)_l S_l^{[T(i)]}(\mathbf{c}_l)\}_{\mathbf{c}_{l+1}}$ ▷ via Eq. 2.12
  end for
end if
end for
▷ final summation: see Section 2.3.3 and Eqs. 4.38 and 4.42

$$\mathbf{U}_{\text{ff}} = \begin{bmatrix} \sum_{n=0}^{p_{\hat{l}}} \sum_{m=-n}^{n} \left(S_{\hat{l}}^{[U(1)]}(\mathbf{c}_{\hat{l}}) \overline{R_{\hat{l}}(\mathbf{c}_{\hat{l}} - \mathbf{x}_N, k_s)} + S_{\hat{l}}^{[U(4)]}(\mathbf{c}_{\hat{l}}) \overline{\left[R_{\hat{l}}(\mathbf{c}_{\hat{l}} - \mathbf{x}_N, k_p)\right]_1} \right) \\ \sum_{n=0}^{p_{\hat{l}}} \sum_{m=-n}^{n} \left(S_{\hat{l}}^{[U(2)]}(\mathbf{c}_{\hat{l}}) \overline{R_{\hat{l}}(\mathbf{c}_{\hat{l}} - \mathbf{x}_N, k_s)} + S_{\hat{l}}^{[U(4)]}(\mathbf{c}_{\hat{l}}) \overline{\left[R_{\hat{l}}(\mathbf{c}_{\hat{l}} - \mathbf{x}_N, k_p)\right]_2} \right) \\ \sum_{n=0}^{p_{\hat{l}}} \sum_{m=-n}^{n} \left(S_{\hat{l}}^{[U(3)]}(\mathbf{c}_{\hat{l}}) \overline{R_{\hat{l}}(\mathbf{c}_{\hat{l}} - \mathbf{x}_N, k_s)} + S_{\hat{l}}^{[U(4)]}(\mathbf{c}_{\hat{l}}) \overline{\left[R_{\hat{l}}(\mathbf{c}_{\hat{l}} - \mathbf{x}_N, k_p)\right]_3} \right) \end{bmatrix}$$

$$\mathbf{T}_{\text{ff}} = \begin{bmatrix} \sum_{n=0}^{p_{\hat{l}}} \sum_{m=-n}^{n} \left(S_{\hat{l}}^{[T(1)]}(\mathbf{c}_{\hat{l}}) \overline{\left[R_{\hat{l}}(\mathbf{c}_{\hat{l}} - \mathbf{x}_N, k_p)\right]_1} - S_{\hat{l}}^{[T(2)]}(\mathbf{c}_{\hat{l}}) \overline{\left[R_{\hat{l}}(\mathbf{c}_{\hat{l}} - \mathbf{x}_N, k_s)\right]_1} \right. \\ \left. \quad + S_{\hat{l}}^{[T(3)]}(\mathbf{c}_{\hat{l}}) \overline{R_{\hat{l}}(\mathbf{c}_{\hat{l}} - \mathbf{x}_N, k_s)} \right) \\ \sum_{n=0}^{p_{\hat{l}}} \sum_{m=-n}^{n} \left(S_{\hat{l}}^{[T(1)]}(\mathbf{c}_{\hat{l}}) \overline{\left[R_{\hat{l}}(\mathbf{c}_{\hat{l}} - \mathbf{x}_N, k_p)\right]_2} - S_{\hat{l}}^{[T(2)]}(\mathbf{c}_{\hat{l}}) \overline{\left[R_{\hat{l}}(\mathbf{c}_{\hat{l}} - \mathbf{x}_N, k_s)\right]_2} \right. \\ \left. \quad + S_{\hat{l}}^{[T(4)]}(\mathbf{c}_{\hat{l}}) \overline{R_{\hat{l}}(\mathbf{c}_{\hat{l}} - \mathbf{x}_N, k_s)} \right) \\ \sum_{n=0}^{p_{\hat{l}}} \sum_{m=-n}^{n} \left(S_{\hat{l}}^{[T(1)]}(\mathbf{c}_{\hat{l}}) \overline{\left[R_{\hat{l}}(\mathbf{c}_{\hat{l}} - \mathbf{x}_N, k_p)\right]_3} - S_{\hat{l}}^{[T(2)]}(\mathbf{c}_{\hat{l}}) \overline{\left[R_{\hat{l}}(\mathbf{c}_{\hat{l}} - \mathbf{x}_N, k_s)\right]_3} \right. \\ \left. \quad + S_{\hat{l}}^{[T(5)]}(\mathbf{c}_{\hat{l}}) \overline{R_{\hat{l}}(\mathbf{c}_{\hat{l}} - \mathbf{x}_N, k_s)} \right) \end{bmatrix}$$

return $\big(\mathbf{U}_{3N}\big)t_i(\mathbf{x}_N) = \mathbf{U}_{\text{ff}} + \big(\mathbf{U}_{\text{nf}}\big)t_i(\mathbf{x}_N)$, $\big(\mathbf{T}_{3N}\big)u_i(\mathbf{x}_N) = \mathbf{T}_{\text{ff}} + \big(\mathbf{T}_{\text{nf}}\big)u_i(\mathbf{x}_N)$
end function

The iterative solution for the elastodynamic FMBEM using the inner–outer fGMRES loop and SAI preconditioner is presented in Alg. 4.2. The main steps of the algorithm parallel those of Alg. 3.3 for the iterative solution of the Helmholtz equation.

Algorithm 4.2 Elastodynamic FMBEM Algorithm: Iterative Solution

function IT_SOLVE($u_i(\mathbf{y}_N)^{\text{inc}}$, ELASTO_FMBEM$(\ldots)$, ξ, ξ_{pre}, $\hat{\text{its}}$, $\hat{\text{its}}_{\text{pre}}$)
  $u_i(\mathbf{x}_N) = \mathbf{0}_{3N}$ ▷ set initial guess as vector of zeros
  $\big[\big(\mathbf{U}_{3N}\big)[g(\mathbf{x}_N)u_i(\mathbf{x}_N)], \big(\mathbf{T}_{3N}\big)u_i(\mathbf{x}_N)\big]$ = ELASTO_FMBEM$\big(k_p, k_s, p_l, u_i(\mathbf{x}_N),$ $[g(\mathbf{x}_N)u_i(\mathbf{x}_N)], \ldots\big)$
  $\boldsymbol{\xi}_{3N} = \big(\frac{1}{2}\mathbf{I}_{3N} + \big(\mathbf{T}_{3N}\big)\big)u_i(\mathbf{x}_N) - \big(\mathbf{U}_{3N}\big)[g(\mathbf{x}_N)u_i(\mathbf{x}_N)] - u_i(\mathbf{y}_N)^{\text{inc}}, \quad \tilde{\text{its}} = 0$ ▷ initial residual of $\mathbf{Az} - \mathbf{b}$

  while norm$(\boldsymbol{\xi}_{3N}) > \xi$ **and** $\tilde{\text{its}} < \hat{\text{its}}$ **do** ▷ main GMRES loop
    $u_i(\mathbf{x}_N)_{\text{pre}} = \mathbf{0}_{3N}, \quad (\boldsymbol{\xi}_{3N})_{\text{pre}} = \infty, \quad \tilde{\text{its}}_{\text{pre}} = 0$ ▷ preconditioner initial values
    while norm$((\boldsymbol{\xi}_{3N})_{\text{pre}}) > \xi_{\text{pre}}$ **and** $\tilde{\text{its}}_{\text{pre}} < \hat{\text{its}}_{\text{pre}}$ **do** ▷ preconditioner
      $\big[(\mathbf{U}_{3N})_{\text{pre}}[g(\mathbf{x}_N)u_i(\mathbf{x}_N)_{\text{pre}}], (\mathbf{T}_{3N})_{\text{pre}}u_i(\mathbf{x}_N)_{\text{pre}}\big]$ = ELASTO_FMBEM$\big(k,$ $(p_l)_{\text{pre}}, u_i(\mathbf{x}_N)_{\text{pre}}, [g(\mathbf{x}_N)u_i(\mathbf{x}_N)_{\text{pre}}], \ldots\big)$
      $(\boldsymbol{\xi}_{3N})_{\text{pre}} = (\mathbf{UT})_{\text{pre}}\big[\big(\frac{1}{2}\mathbf{I}_{3N} + (\mathbf{T}_{3N})_{\text{pre}}\big)u_i(\mathbf{x}_N)_{\text{pre}} - (\mathbf{U}_{3N})_{\text{pre}}[g(\mathbf{x}_N) \times u_i(\mathbf{x}_N)_{\text{pre}}]\big] - (\mathbf{UT})_{\text{pre}}\left(\frac{(\boldsymbol{\xi}_{3N})}{\text{norm}(\boldsymbol{\xi}_{3N})}\right)$ ▷ residual of $\mathbf{A}_{\text{inv}}\mathbf{Ax} - \mathbf{A}_{\text{inv}}\mathbf{b}$ with $\mathbf{b} = \left(\frac{(\boldsymbol{\xi}_{3N})}{\text{norm}(\boldsymbol{\xi}_{3N})}\right)$ from main GMRES and $\mathbf{A}_{\text{inv}} = (\mathbf{UT})_{\text{pre}}$
      $u_i(\mathbf{x}_N)_{\text{pre}} = \text{GMRES}((\boldsymbol{\xi}_{3N})_{\text{pre}}), \quad \tilde{\text{its}}_{\text{pre}} = \tilde{\text{its}}_{\text{pre}} + 1$ ▷ update preconditioner solution using GMRES (see Ref. [152]) and update inner counter
    end while

    $\big[\big(\mathbf{U}_{3N}\big)[g(\mathbf{x}_N)u_i(\mathbf{x}_N)_{\text{pre}}], \big(\mathbf{T}_{3N}\big)u_i(\mathbf{x}_N)_{\text{pre}}\big]$ = ELASTO_FMBEM$\big(k_p, k_s, p_l,$ $u_i(\mathbf{x}_N)_{\text{pre}}, [g(\mathbf{x}_N)u_i(\mathbf{x}_N)_{\text{pre}}], \ldots\big)$ ▷ use final GMRES preconditioner solution $u_i(\mathbf{x}_N)_{\text{pre}}$ in main FMBEM
    $\boldsymbol{\xi}_{3N} = \big(\frac{1}{2}\mathbf{I}_{3N} + \big(\mathbf{T}_{3N}\big)\big)u_i(\mathbf{x}_N)_{\text{pre}} - \big(\mathbf{U}_{3N}\big)[g(\mathbf{x}_N)u_i(\mathbf{x}_N)_{\text{pre}}] - u_i(\mathbf{y}_N)^{\text{inc}}$ ▷ residual from main GMRES iteration
    $u_i(\mathbf{x}_N) = \text{fGMRES}(\boldsymbol{\xi}_{3N}) \quad \tilde{\text{its}} = \tilde{\text{its}} + 1$ ▷ update solution using fGMRES (see Ref. [152]) and update outer counter
  end while
end function

Thus applying Alg. 4.2 allows the total surface displacement $u_i(\mathbf{y}_N)$ in Eq. 4.48 to be solved using the FMBEM. The above algorithms have been presented for Eq. 4.2 assuming an impedance BC of the form $t_i(\mathbf{x}) = g(\mathbf{x})u_i(\mathbf{x})$. The algorithms can be

suitably modified for the other common BCs: if the total displacement is described by a known function $u_i(\mathbf{x}_N) = g(\mathbf{x}_N)$ on the discretised boundary surface, Eq. 4.2 becomes

$$\big(\mathbf{U}_{3N}\big)t_i(\mathbf{x}_N) = \left(\frac{1}{2}\mathbf{I}_{3N} + \mathbf{T}_{3N}\right) g(\mathbf{x}_N) - u_i^{\text{inc}}(\mathbf{y}_N) \tag{4.49}$$

in the form $\mathbf{Az} = \mathbf{b}$. Alg. 4.1 is called once to precompute $\left(\frac{1}{2}\mathbf{I}_{3N} + \mathbf{T}_{3N}\right) g(\mathbf{x}_N)$ and this is added to the known incident field $u_i^{\text{inc}}(\mathbf{y}_N)$ to construct $\mathbf{b}$ in the matrix equation. Alg. 4.2 is then used to solve Eq. 4.49 with $u_i(\mathbf{x}) = \mathbf{0}_{3N}$ (in practice the $\mathbf{T}_{3N}$ terms are not calculated at all in the iterative solution). Similarly if the surface stress is a known function on the discretised surface $t_i(\mathbf{x}_N) = g(\mathbf{x}_N)$, Eq. 4.2 can be written as a matrix equation of the form

$$\left(\frac{1}{2}\mathbf{I}_{3N} + \mathbf{T}_{3N}\right) u_i(\mathbf{x}_N) = \big(\mathbf{U}_{3N}\big)g(\mathbf{x}_N) + u_i^{\text{inc}}(\mathbf{y}_N) \tag{4.50}$$

Eq. 4.50 can be similarly solved by precomputing $\big(\mathbf{U}_{3N}\big)g(\mathbf{x}_N)$ once for the known $\mathbf{b}$ vector and then implementing Alg. 4.2 with $t_i(\mathbf{x}_N) = \mathbf{0}_{3N}$ (i.e. ignoring the $\mathbf{U}_{3N}$ terms).

4.3 Numerical Results

This section explores the performance of the elastodynamic FMBEM model in terms of both its accuracy, and the algorithmic complexity and memory requirements of the model. The elastodynamic FMBEM model has been written in MATLAB, implemented using double–precision floating point numbers and the code has not been explicitly compiled/multithreaded, however MATLAB may do this internally to parts of the code during execution. Numerical examples are presented for the exterior scattering of compressional plane waves from a spherical cavity embedded in an infinite elastic solid under a traction–free boundary condition, which are compared to the analytic solution. An 'application example' of the elastodynamic FMBEM code is also presented in the form of scattering of compressional waves from hemispherical and semi–ellipsoidal canyons.

All numerical results from the FMBEM code have been calculated on a workstation computer equipped with an i7–3930K hexacore processor running at 3.2GHz, and 32GB of RAM. It should be noted that the methods outlined in Section 3.3 for reducing the number of RCR translations that must be stored/implemented in the Helmholtz

FMBEM have been similarly implemented for the elastodynamic FMBEM. Additionally a slight modification of the implemented code compared to the elastodynamic FMBEM algorithms presented in the previous section is that not all of the sets of spherical basis functions are precomputed and stored. In total 20 sets of expansion sets are required: for each wavenumber (k_p, k_s) the original regular expansion set, three first–order partial derivative sets and six unique second–order partial derivative sets are required. As opposed to storing all 20 sets in memory, only the regular expansions for the two wavenumbers are precomputed/stored while the other sets are computed as required at the start of the upward pass and in the final summation for each of the FMM iterations. The calculation time required to build the expansions is small compared to the total time of the FMM procedure. A more stringent management of the various expansion sets constructed during the elastodynamic FMBEM has also been employed to reduce the total memory footprint of the procedure. In particular, the S expansions on each octree level may be discarded once the $S|R$ translations are applied on that level, while only the R expansions on the parent level must be stored when applying the $S|R$ translations on each level in the downward pass.

4.3.1 Compressional Plane Wave Scattering from a Spherical Cavity: On–Surface Results

This section presents numerical results from the elastodynamic FMBEM for the scattering of plane compressional waves from a spherical cavity embedded in an infinite elastic solid under a traction–free BC. The analytic solution for this problem can be found in, for example, Refs. [194] and [195]. Fig. 4.1 shows a comparison between the elastodynamic FMBEM and the analytic solution for the total radial displacement on the surface of a unit radius $a = 1$ spherical cavity impinged by a $k_s a = 29.75$ compressional plane wave travelling in the direction $[1\,0\,0]$. The elastic medium has a Poison's ratio of $\nu = 1/3$, while the shear modulus need not be defined for the traction–free BC. A comparison of the real/imaginary components of the total radial displacement as a function of angle away from the direction of the incident field (such that 0° corresponds to the back–scatter direction) is shown in Fig. 4.2.

The relative error norm between the FMBEM and analytic solution was 4.1%. For this example the boundary element mesh contained 40096 elements giving approximetaly 15 elements per shear wavelength at the specified shear wavenumber. The elasto-

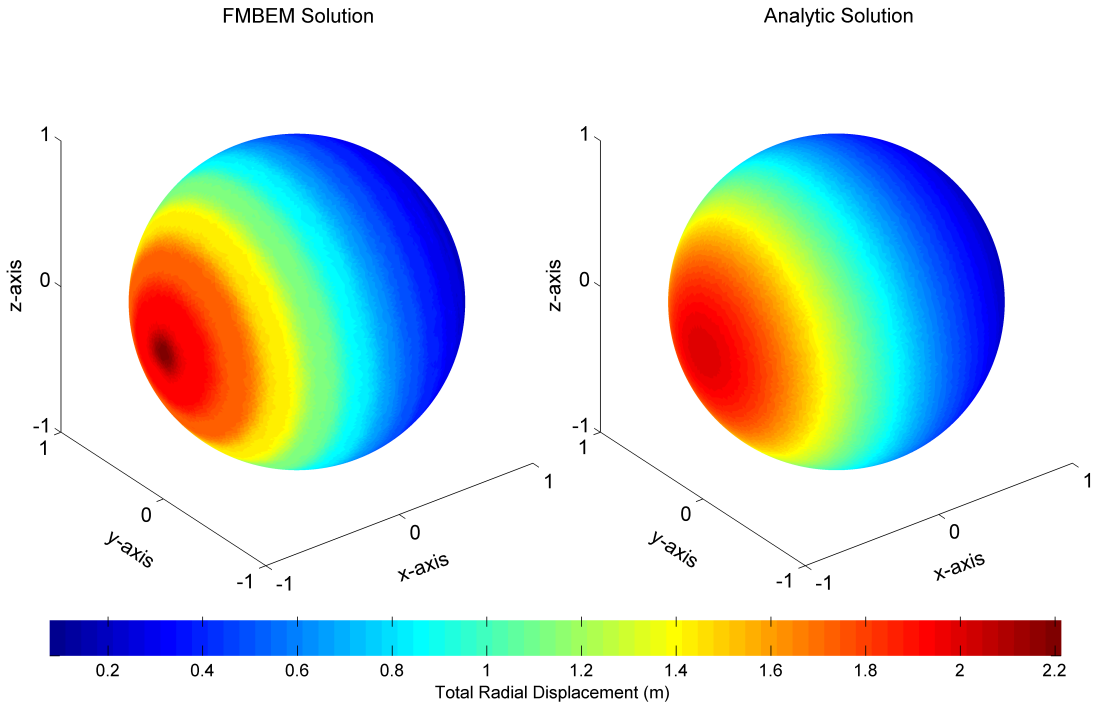

Figure 4.1: Elastodynamic FMBEM total radial displacement (left) versus the analytic solution (right) for plane compressional wave scattering from a spherical cavity at $k_s a = 29.75$ under a traction–free BC.

dynamic FMBEM took approximately 14.9 hours to set–up and solve the problem and required 2.31GB of storage space. Comparatively, the full complex 120288×120288 $\mathbf{T}_{3N}$ coefficient matrix in Eq. 4.50 would require 231.5GB of space to store. Fig. 4.3 shows analagous results for the same problem at a higher wavenumber of $k_s a = 44.5$ which corresponds to approximately 10 elements per shear wavelength. In this case the r.e. norm between the FMBEM and analytic solution was 3.3% and the solution time and memory requirements were 76.9 hours and 2.75GB respectively.

The lower wavenumber results presented here exhibit a poorer agreement with the analytic solution than the $k_s a = 44.5$ results despite having more elements per wavelength. This is because the $k_s a = 29.75$ wavenumber for the exterior problem lies close to an eigenfrequency for the adjoint interior problem and so the exterior scattered results exhibit a fictitious resonance which does not actually exist for the infinite exterior elastic solid. It is due to the presence of eigenfrequencies near the wavenumbers $k_s a = 30$ and 45 (being the same wavenumbers used in the Helmholtz FMBEM results

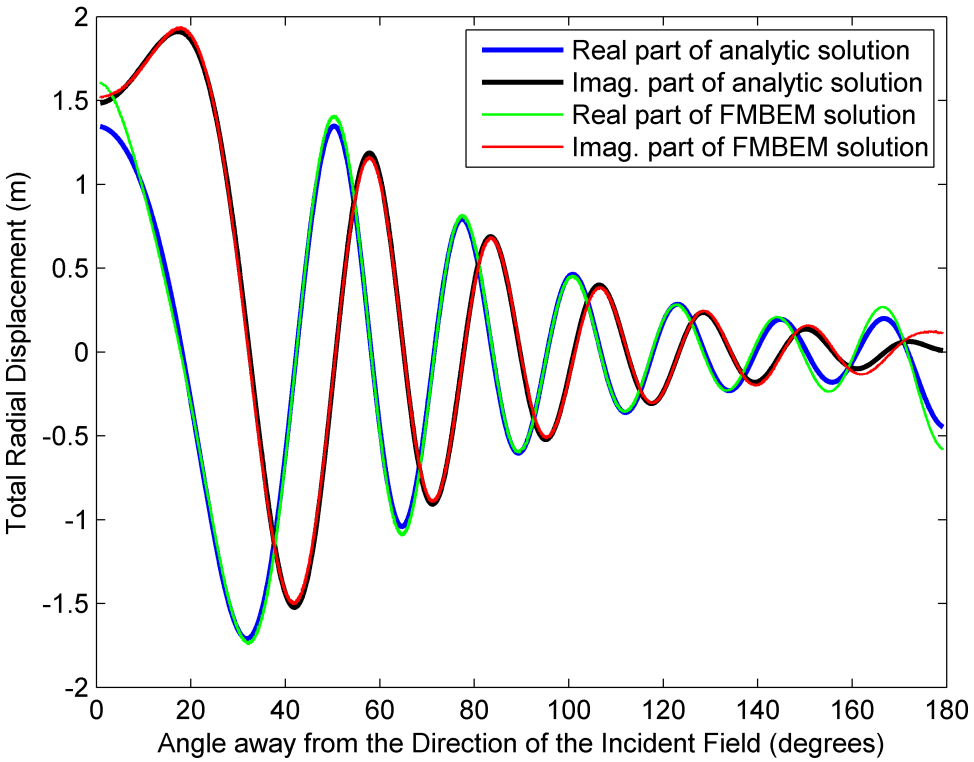

Figure 4.2: Elastodynamic FMBEM real/imaginary components of the total radial displacement versus the analytic solution for compressional plane wave scattering from a spherical cavity at $k_s a = 29.75$ under a traction–free BC.

presented in Figs. 3.8 and 3.9 in Chapter 3) that the present results were instead calculated at $k_s a = 29.75$ and 44.5 respectively. The $k_s a = 29.75$ results still lie somewhat close to an interior eigenfrequency and so a higher error is observed in those results.

Stabilisation techniques exist for the elastodynamic BIE which are analogous to the CHIEF method [196, 197] and Burton–Miller formulation [198, 199] for the Helmholtz BIE but these have not yet been implemented in the present elastodynamic FMBEM code (and, in fact, have only been implemented in one elastodynamic FMBEM code in the published literature [181] but no details are provided on the implementation). As a result, the present elastodynamic FMBEM will break down for exterior problems at certain characteristic frequencies and exhibits both poor accuracy and convergence near those frequencies. This issue is discussed further in the next subsection.

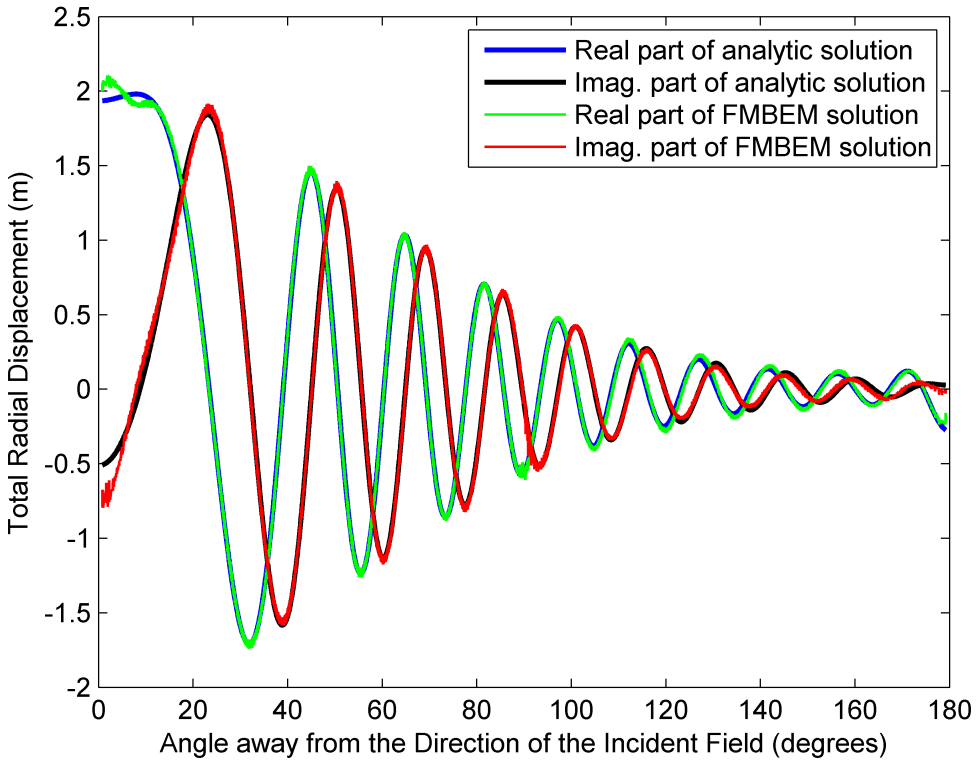

Figure 4.3: Elastodynamic FMBEM real/imaginary components of the total radial displacement versus the analytic solution for compressional plane wave scattering from a spherical cavity at $k_s a = 44.5$ under a traction–free BC.

4.3.2 Compressional Plane Wave Scattering from a Spherical Cavity: Off–Surface Results

Results are presented here for the off–surface scattering of a compressional plane wave from a spherical traction–free cavity. The off–surface displacements are calculated by first solving for the on–surface field and then integrating this displacement field over the discretised surface to evaluate the received field at the off–surface locations. For the traction–free boundary condition, Eq. 4.50 reduces to

$$u_i(\mathbf{z}_M) = -\Big(\mathbf{T}_{3M\times 3N}\Big)u_i(\mathbf{x}_N) + u_i^{\text{inc}}(\mathbf{z}_M) \tag{4.51}$$

where $\mathbf{z}_M$ is the set of M off–surface receiver locations and $\mathbf{T}_{3M\times 3N}$ is a rectangular matrix of size $3M \times 3N$. The evaluation of the off–surface integrals can similarly be accelerated using the FMM with non–coincident source/receiver sets i.e. $\mathbf{x}_N \neq \mathbf{z}_M$.

Fig. 4.4 shows the real component of the total radial displacement along radial lines emanating from the sphere surface into the exterior infinite elastic solid at angles of $\theta = 0, \pi/4, \pi/2, 3\pi/4$ away from the direction of the incident plane wave. The incident plane wave has a wavenumber of $k_p a = 4\pi$ and the elastic solid has $\nu = 1/4$. The present results are compared to digitised results from Ref. [37]. A similar number of unknowns has been used in both models: $N = 122886$ in Ref. [37] while $N = 120288$ here. The r.e. norm between the total on–surface radial displacement calculated by the elastodynamic FMBEM compared to the analytic solution was 7.58%.

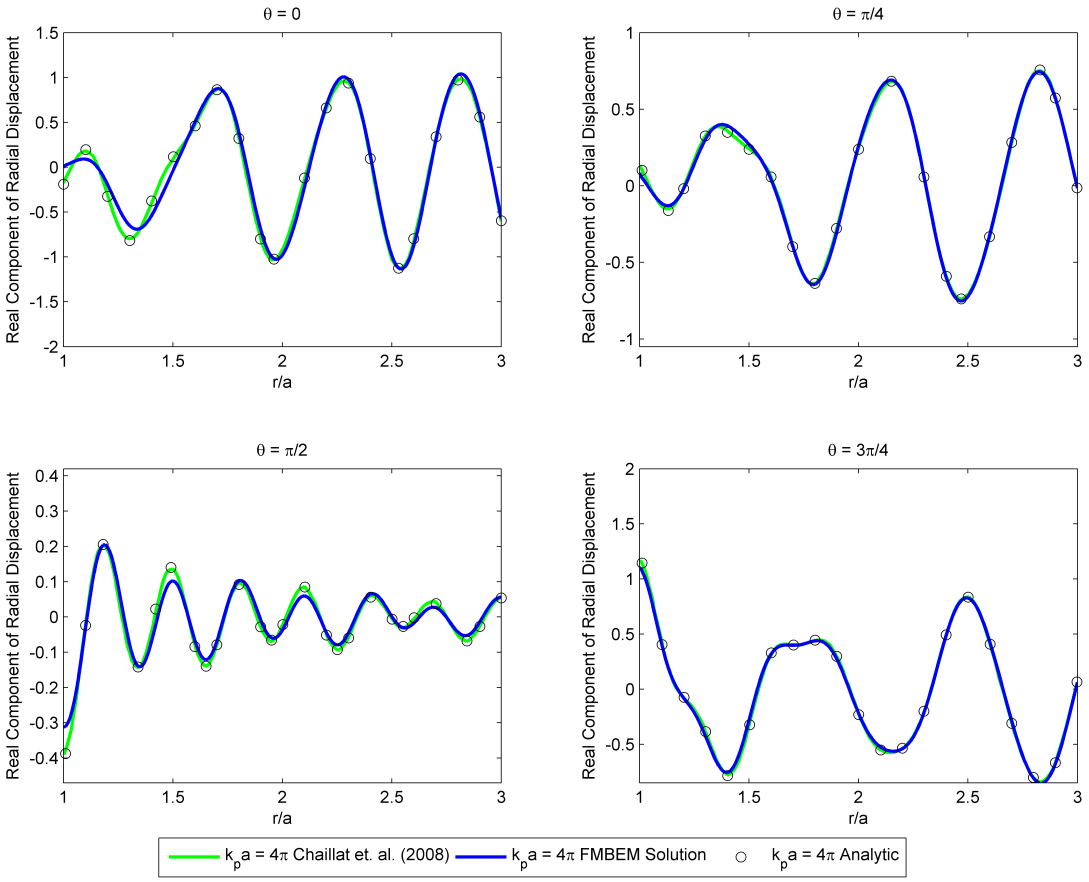

Figure 4.4: Off–surface scattering of a $k_p a = 4\pi$ compressional plane wave from a spherical traction–free cavity with Poisson's ratio $\nu = 1/4$.

A clear discrepancy can be observed in Fig. 4.4 between the present elastodynamic FMBEM results and the analytic solution, again due to the calculated wavenumber lying near to a characteristic eigenfrequency of the adjoint interior problem. To exem-

plify the issue, a plot of the r.e. norm versus frequency over the range $k_p a = 12 : 13$ for the on–surface radial displacement induced by a compressional plane wave impinging upon a spherical traction–free cavity is shown in Fig 4.5 (top) for two Poisson's ratios: $\nu = 1/4$ corresponding to the results in Fig. 4.4, and $\nu = 1/3$. Also shown in Fig 4.5 (bottom) is the sum of the total variation of the radial traction versus angle for the adjoint interior problem, defined for this example as the finite enclosed sphere made of the same elastic material as the exterior problem surrounded by an infinite vacuum, which is impinged by a similar incident plane wave (but defined as propagating *inside* the finite interior domain) under a rigid surface BC (with $\mu = 1$).

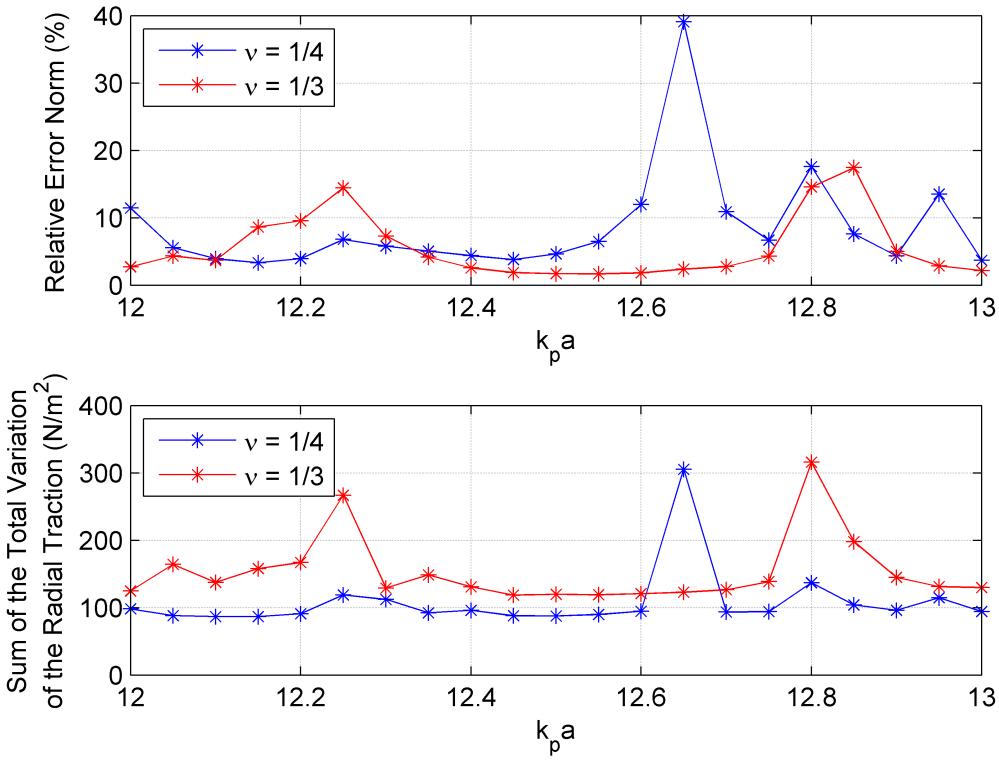

Figure 4.5: Relative error norm versus frequency for the exterior traction–free BC problem (top) and the sum of the total variation of the radial traction versus frequency for the corresponding adjoint interior rigid surface BC problem (bottom).

Fig 4.5 (top) shows that the largest errors in the total radial displacement for the exterior traction–free BC problem correspond to maxima in the total variation of the radial traction (as a function of incident angle) for the adjoint interior problem. The

total variation in the radial traction increases near the interior eigenfrequencies as significantly more oscillatory behaviour occurs in the surface field compared to similar results shifted slightly away from the eigenfrequencies. An example of this is shown in Fig. 4.6 for the $\nu = 1/4$ adjoint interior problem at two frequencies: $k_p a = 12.6$ which can be seen from Fig 4.5 (bottom) to be slightly away from a peak in the total variation of the radial traction, and $k_p a = 12.65$, which lies on the peak and corresponds to the largest r.e. norm in Fig 4.5 (top). Similar oscillatory behaviour was observed in the Helmholtz FMBEM results when setting the Burton–Miller coupling parameter to zero near an interior eigenfrequency (see Fig. 3.11 in Chapter 3).

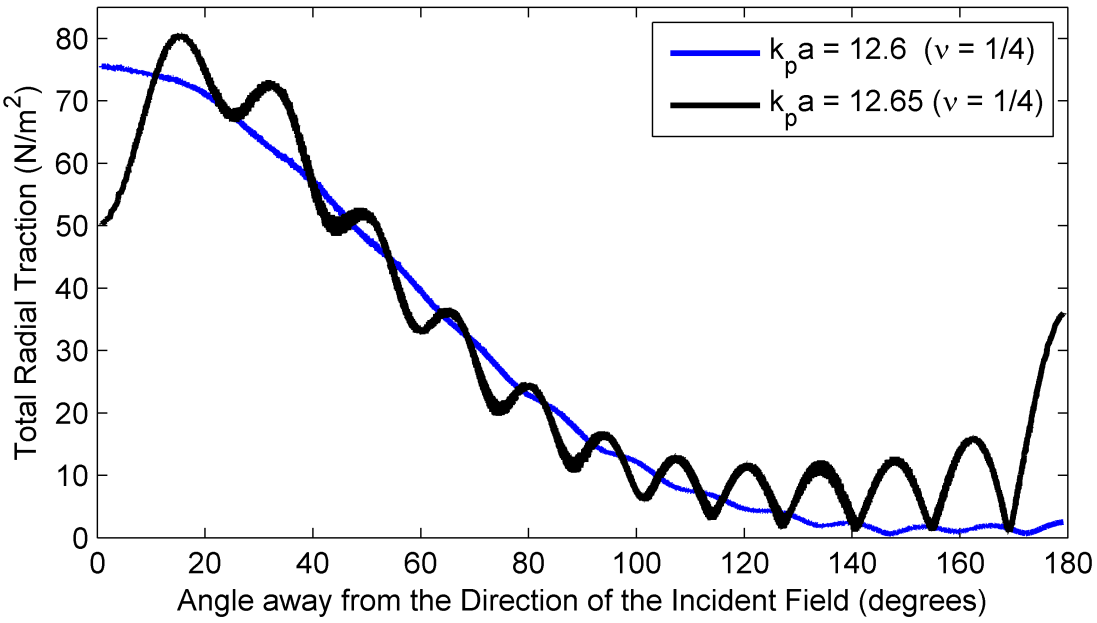

Figure 4.6: Total radial traction for the interior rigid surface BC problem with $\nu = 1/4$ and $\mu = 1$ for an incident compressional plane wave with frequencies $k_p a = 12.6$ and $k_p a = 12.65$. The $k_p a = 12.65$ frequency resides near an interior eigenfrequency.

Clearly the results presented in Fig. 4.4 suffer poor agreement with the analytic solution due to the presence of an eigenfrequency near $k_p a = 12.65$ for the elastic material with Poisson's ratio $\nu = 1/4$. The results in Fig. 4.5 indicate that no eigenfrequencies occur near $k_p a = 4\pi$ when the elastic material is specified with $\nu = 1/3$ and so the results in Fig. 4.4 are recalculated for $\nu = 1/3$ and presented in Fig. 4.7 against the analytic solution. The off–surface results now show good agreement while the on–surface r.e. norm between the FMBEM/analytic solution has reduced to 1.78%. It is curious

that the elastodynamic FMBEM results from Ref. [37] do not similarly exhibit poor agreement at $k_p a = 4\pi$ while the present elastodynamic FMBEM breaks down.

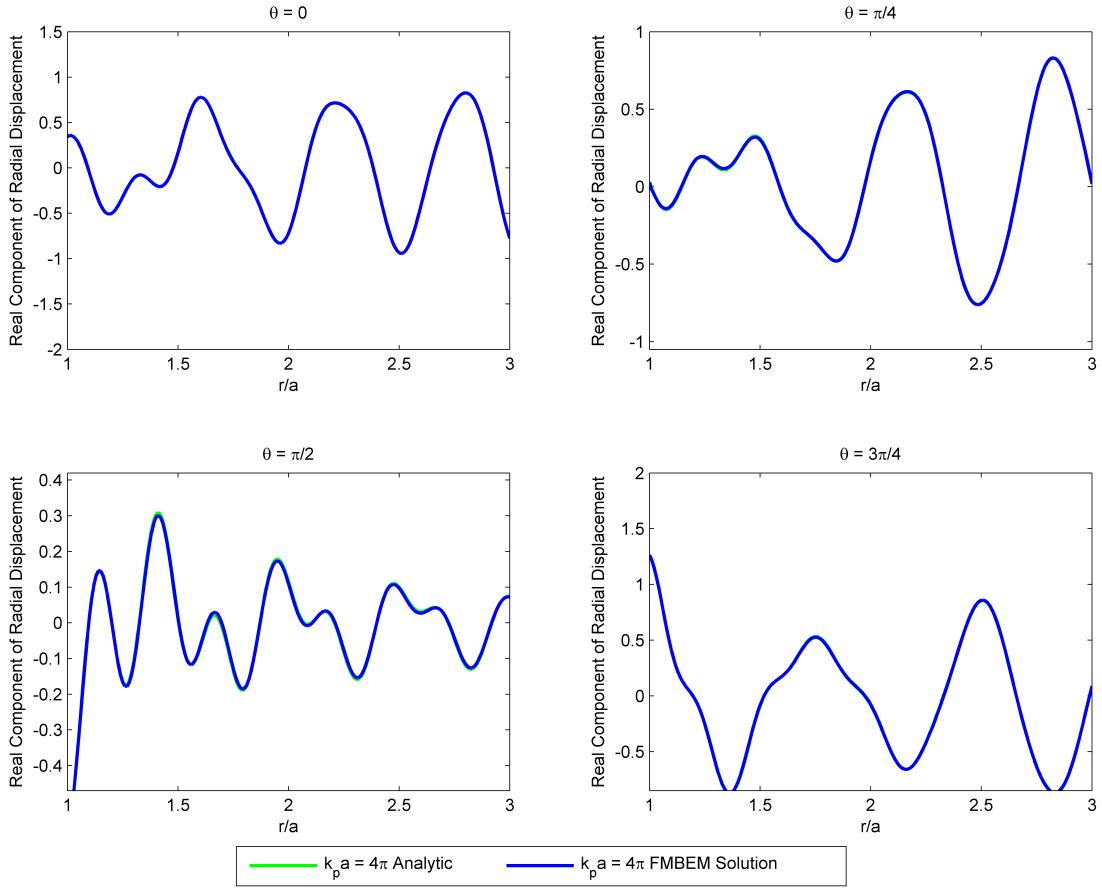

Figure 4.7: Off–surface scattering of a $k_p a = 4\pi$ compressional plane wave from a spherical traction–free cavity with Poisson's ratio $\nu = 1/3$.

Obviously the issue of break down frequencies is a problem for the elastodynamic FMBEM when modelling infinite exterior elastic domains and one of the previously cited stabilisation methods should be incorporated into the code to stabilise the BIE at all frequencies. However when using the elastodynamic FMBEM to model interior domains the BIE does not suffer from non–uniqueness as the eigenfrequencies for the finite enclosed interior space have a physical meaning. Thus the proposed dual FMBEM formulation for acoustic coupled FSI problems presented in Chapter 5 should not suffer from this kind of instability when using the elastodynamic BIE to model the interior elastic solid and the Burton–Miller formulation to model the exterior fluid domain.

4.3.3 Elastodynamic FMBEM Algorithmic Performance

This section investigates the performance of the elastodynamic FMBEM in terms of its algorithmic complexity, computational accuracy and memory requirements for the sphere scattering problem with a traction–free BC. Two scenarios are presented: the first investigates the algorithm scaling as a function of the number of unknowns with a fixed wavenumber, while the second case shows the maximum wavenumber for each mesh size as a function of the number of unknowns.

Plots of the solution time, memory usage and solution error versus the number of unknowns for an incident compressional plane wave with a fixed wavenumber of $k_s a = 13$ and $\nu = 1/3$ are shown in Figs. 4.8, 4.9 and 4.10 respectively. It can be seen from Fig. 4.8 that the least squares fit of the total solution time for the FMBEM shows a proportionality which is less than N. Comparatively, the Helmholtz FMBEM showed a slightly larger N–dependence and had an order of magnitude larger leading constant coefficient which may reflect the longer problem set–up time required by the elastodynamic FMBEM for the near field integration of the more complex fundamental solutions. The standard deviations in the least–squares data fits for the algorithmic N–scaling are again presented in the algorithmic complexity plots to indicate a rough uncertainty in the data fits. Fig. 4.8 again exhibits distinct 'steps' in the solution time, which correspond to the addition of new octree levels to the structure to accommodate the increasing mesh size. Fig. 4.9 shows that the total storage requirements in MB of the elastodynamic FMBEM is proportional to less than N. A comparison of Figs. 4.8 and 4.9 shows an inverse relation between the solution time and memory requirements of the elastodynamic FMBEM (as was the case for the Helmholtz FMBEM). Finally, the relative error norm between the analytic and FMBEM solution is shown in Fig. 4.10 for the total radial component of displacement. As expected, the error generally reduces as the number of elements per wavelength increases, while small increases $(1 - 3\%)$ in the r.e. norm occur for meshes which introduce a new level to the octree.

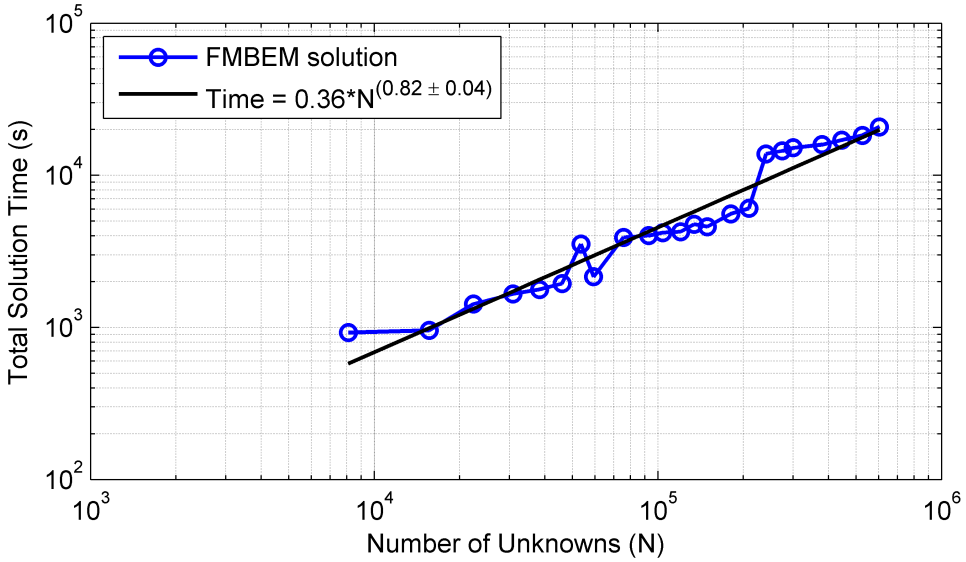

Figure 4.8: Solution time versus the number of unknowns for the elastodynamic FMBEM with a fixed wavenumber. The total solution time shows a proportionality which is less than N.

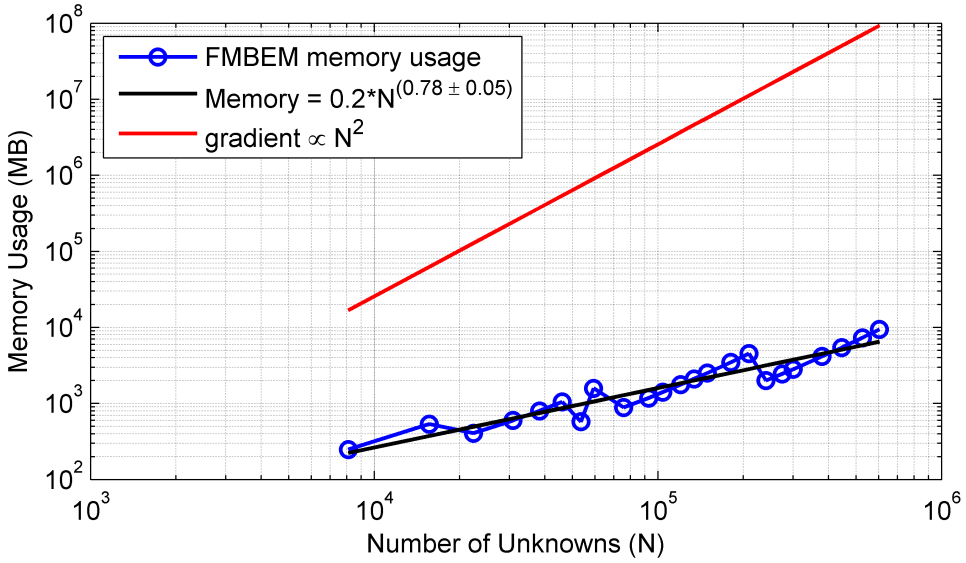

Figure 4.9: Memory usage versus the number of unknowns for the elastodynamic FMBEM with a fixed wavenumber. The storage requirements in MB of memory shows a proportionality which is less than N.

Plots of the solution time, memory usage and solution error versus the number of

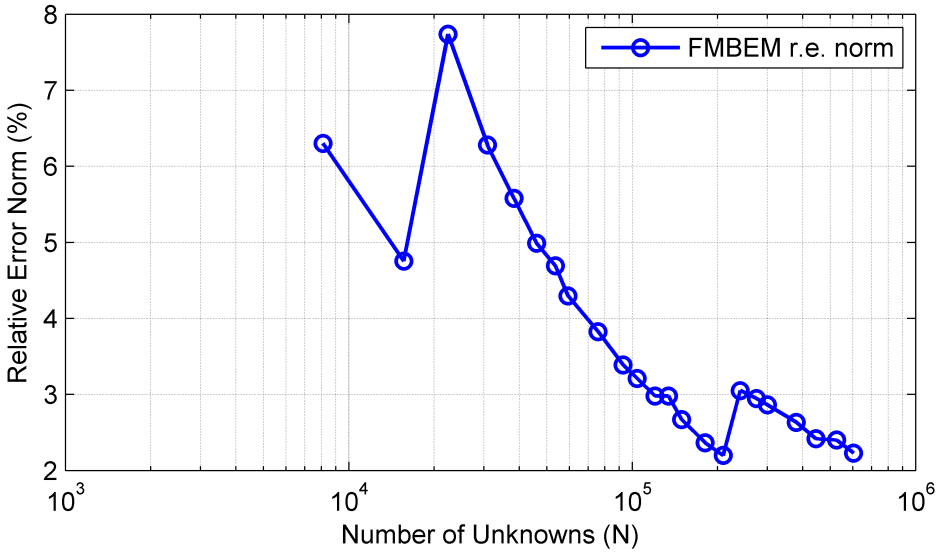

Figure 4.10: Solution error versus the number of unknowns for the elastodynamic FMBEM with a fixed wavenumber. The error generally decreases as the number of elements per wavelength increases.

unknowns for the second scenario using the maximum wavenumber for each boundary element mesh are shown in Figs. 4.11, 4.12 and 4.13 respectively. Each of the selected wavenumbers gives approximately 8–10 elements per wavelength on the corresponding mesh (measured at the equator of the sphere). It can be seen from Fig. 4.11 that the least squares fit of the total solution time for the elastodynamic FMBEM is approximately proportional to $N^{2.26}$ i.e. *greater* than the N^2 algorithmic complexity of the direct BEM method. A number of jumps in the solution time can be observed in Fig. 4.11 and a comparison of this data with the r.e. norm results presented in Fig. 4.13 indicates that the elastodynamic FMBEM models which exhibit a slow convergence correspond to those models with a poor solution accuracy. The poor performance of the elastodynamic FMBEM at certain frequencies can again be attributed to those frequencies lying near eigenfrequencies for the adjoint interior problem. Recalculating the least squares fit using the data points with the lowest r.e. norms, corresponding to the wavenumbers which lie away from the eigenfrequencies of the adjoint interior problem, gives a total solution time proportional to N^2.

Comparatively, the Helmholtz FMBEM exhibited a total solution time proportional to $N^{1.5}$ when using the maximum wavenumber for each boundary element mesh (see

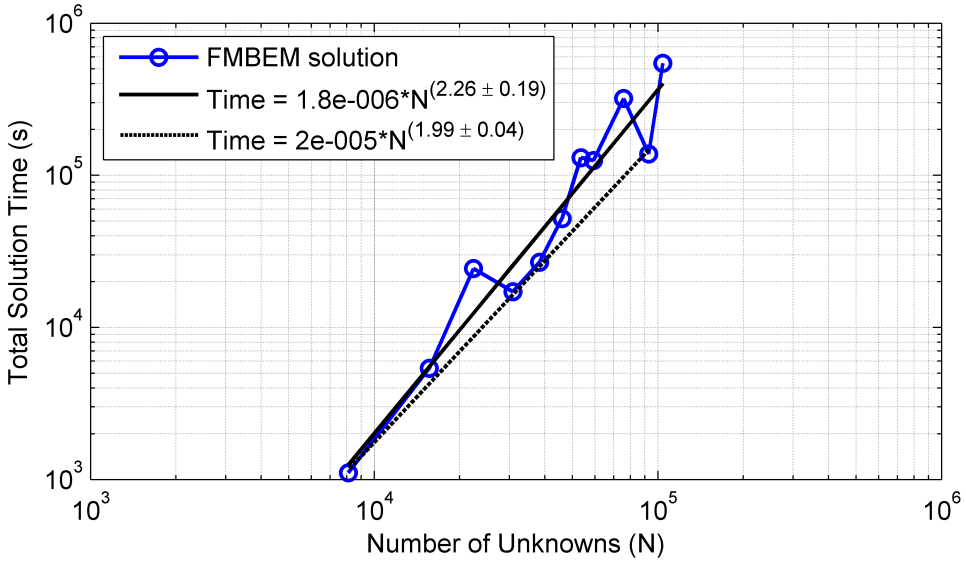

Figure 4.11: Solution time versus the number of unknowns for the elastodynamic FMBEM using the maximum allowed wavenumber on each mesh. The FMBEM total solution time is approximately proportional to $N^{2.26}$ using all data points (solid line) and proportional to N^2 using only the solution times for the frequencies which do not lie near the eigenfrequencies of the adjoint interior problem (dashed line).

Fig. 3.15 in Chapter 3). The higher algorithmic complexity of the elastodynamic FMBEM may be attributed to a number of factors. Particularly, one would expect the iterative solution of the elastodynamic FMBEM to be at least $1.\dot{6}$ times slower for the traction–free problem as the T_{ij} fundamental solution requires the propagation of five sets of expansions to solve for the Cartesian components of each unknown, while the Helmholtz FMBEM only requires the propagation of one expansion per unknown. Similarly the calculation of the nine elastodynamic near field components for the Cartesian components of each unknown should be at least three times slower than that for the Helmholtz code, although the near field computations only constitute a small portion of the total solution time — 5% or less depending on the octree settings/wavenumber — and so this scaling would have a relatively small effect on the total solution time. Most significantly the elastodynamic FMBEM generally converges more slowly than the Helmholtz FMBEM for similar sphere scattering problems, where a much larger number of low accuracy inner GMRES iterations is required by the elastodynamic FMBEM to converge to the same inner GMRES tolerance. This slower convergence may be due

simply to the fact that the elastodynamic BIE is a vector equation and involves more complicated fundamental solutions than that of the Helmholtz BIE.

It can be seen from Fig. 4.12 that the memory usage increases slightly compared to the constant wavenumber case (Fig. 4.9) as the size of the multipole expansions and RCR translation coefficients stored in memory increase proportionally to the wavenumber. Fig. 4.13 shows that the r.e. norm of the total radial displacement between the analytic and FMBEM solutions for the wavenumbers which lie away from the adjoint interior eigenfrequencies remain approximately constant at $\sim 5\%$ for roughly constant numbers of elements per wavelength, while the r.e. norms for wavenumbers near to the interior eigenfrequencies are as high as 32%. It should be noted that the elastodynamic FMBEM solves for the Cartesian components of displacement/traction and each set of xyz components is combined with the local element normal via a dot–product to give the radial components of the solution. Thus one would expect the r.e. norms of the individual displacment components to be somewhat less than 5% to yield the observed average r.e. norm in the radial displacement results. Comparatively the Helmholtz FMBEM exhibited an r.e. norm of $\sim 2\%$ in the pressures for sphere scattering problems involving similar numbers of elements per wavelength.

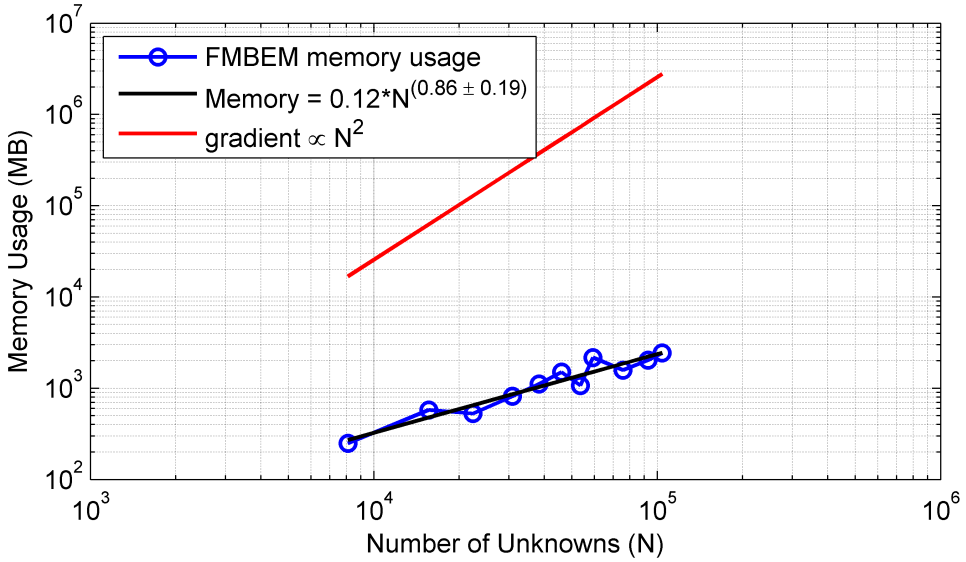

Figure 4.12: Memory usage versus the number of unknowns for the elastodynamic FMBEM using the maximum allowed wavenumber on each mesh. The storage requirements in MB of memory shows a proportionality which is less than N.

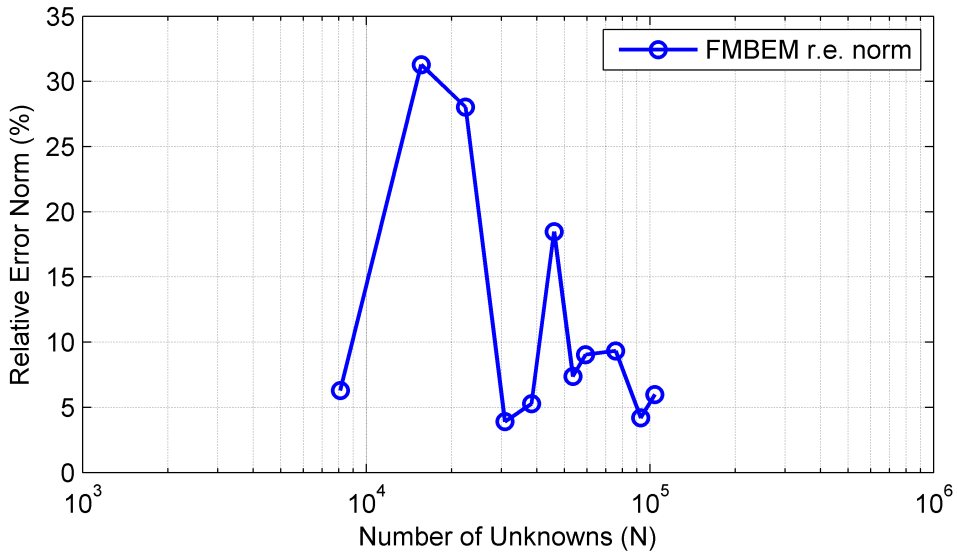

Figure 4.13: Solution error versus the number of unknowns for the elastodynamic FMBEM using the maximum allowed wavenumber on each mesh. The r.e. norm is $\sim 5\%$ for the wavenumbers which lie away from the interior eigenfrequencies.

Comparatively, Chaillat [37, 191] observed RMS errors in the range of $10^{-2} - 10^{-4}$ for the surface displacements on a pressurised spherical cavity embedded in an infinite elastic solid domain when using between 2.5–20 nodes per shear wave in their high frequency elastodynamic FMBEM (which employs continuous linear elements). Chaillat also observed RMS errors in the range of $10^{-2} - 10^{-3}$ for the off–surface displacements when using at least 10 nodes per shear wave for a similar numerical example as used here: a compressional plane wave scattering from a spherical traction–free cavity embedded in an infinite elastic solid. Grasso et al. [121] report RMS errors of $\sim 10^{-2}$ in the on–surface displacements for a similar numerical example of a compressional wave scattering from a spherical traction–free cavity when using 10 nodes per shear wavelength in their high frequency visco–elastodynamic FMBEM model (i.e. when setting the viscoelastic component to 0). Thus the present FMBEM model would appear to yield an approximately similar magnitude in the solution errors (or perhaps slightly worse due to the use of constant elements) compared to Chaillat/Grasso when using similar numbers of solution points per shear wavelength. Few other references in the elastodynamic BEM/FMBEM literature appear to provide quantifiable measures of the numerical error as a function of the element discretisation.

Finally, it should be noted that the less than N algorithmic complexity observed in the low frequency scenario would appear to scale favourably with the $O(N)$ theoretical algorithmic complexity derived by Gumerov and Duraiswami [42] for surface distributions on simple objects when using translation methods which have a greater than $O(p^2)$ algorithmic complexity. The only low frequency model for which algorithmic complexity data is available is that of Yoshida [178]. Digitisations of the numerical results appearing therein show that their low frequency elastodynamic FMBEM model (which uses $O(p^5)$ translations) approximately scales between $N^{1.3}$ and $N^{1.5}$ when increasing the number of unknowns for a fixed wavenumber, while the present model showed a less than N scaling for a similar scenario. No algorithmic scaling data has been presented for the low frequency model of Isakari [181] which uses the $O(p^3)$ RCR translations. The algorithmic scaling proportional to N^2 in the high frequency limit of the present model is larger than the expected $N^{1.5}$ scaling, as was observed in the Helmholtz FMBEM model (and was theoretically predicted by Gumerov and Duraiswami [42]). The algorithmic scaling in this case appears to be a result of the large number of GMRES iterations required for convergence. It would be interesting to see what effect stabilising the elastodynamic BIE using the equivalent CHIEF or Burton–Miller formulation would have on the iterative convergence rate, and if a further reduction in the algorithmic complexity would result from this stabilisation.

4.3.4 Scattering of Plane Elastic Waves by Canyons

As an example of the application of the elastodynamic FMBEM, total displacement results are presented for the scattering of compressional plane waves from hemispherical and semi–ellipsoidal canyons embedded into the free–surface of a homogeneous elastic half–space. Modelling of such configurations has been the focus of a number of seismological studies, which include the use of semi–analytic wave–function expansions [200, 201], elastodynamic BEMs [202, 203] and elastodynamic FMBEMs [37]. Reviews of much of the earlier work in the field, including other analytic/numerical methods not listed here, can be found in Refs. [204] and [202].

A schematic of the general problem set up is shown in Fig. 4.14. The canyon and a surrounding circular disc (with radius D) of the half–space boundary surface is discretised with boundary elements and a traction–free BC is applied to the discretised surface. The hemispherical canyon has a radius a while the semi–ellipsoidal canyon

has semi–axes a, b, a in the xyz axis directions respectively. The incident compressional plane wave is defined by the angle θ from the z–axis.

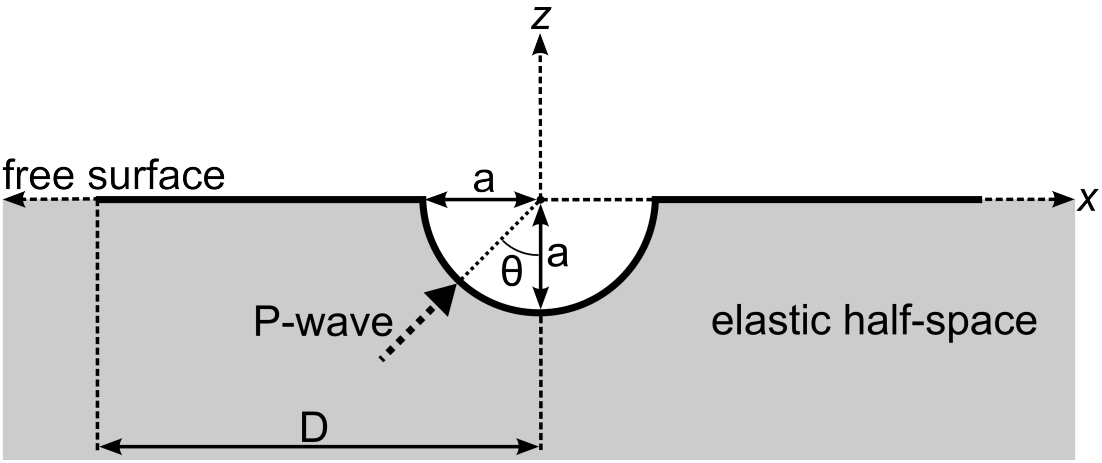

Figure 4.14: Schematic of the problem for the scattering of plane elastic waves by a canyon embedded into the free–surface of a homogeneous elastic half–space.

The numerical representation of the problem outlined in Fig. 4.14 involves the solution of an *interior* problem via the elastodynamic BIE where the half–space is the domain interior to the discretised boundary surface. This is in contrast to the other elastodynamic problems presented in this chapter which have involved infinite exterior elastic domains, where the element normals were defined as pointing outwards from the discretised boundary surface (i.e. into the exterior elastic domain). The elastodynamic BIE for an interior problem with element normals similarly defined as pointing outward from the surface (i.e. directed towards the exterior vacuum, not the interior elastic domain) is [205]

$$\frac{1}{2}u_i(\mathbf{y}) = -\int_S \Big(U_{ij}^{\mathrm{T}}(\mathbf{x},\mathbf{y})t_i(\mathbf{x}) + T_{ij}^{\mathrm{T}}(\mathbf{x},\mathbf{y})u_i(\mathbf{x})\Big)dS(\mathbf{x}) + u_i^{\mathrm{inc}}(\mathbf{y}) \tag{4.52}$$

where the integral terms have the opposite signs as that for the exterior problem (Eq. 4.2). The incident displacement field in the half–space takes the form of a 'free–field' u_i^F, a combination of the incident compressional plane wave and both the compressional and shear waves refracted from the half–space under a traction–free boundary condition. Analytical expressions for the free–field displacement from an oblique incident compressional plane wave in an elastic half–space can be found in, for example, Refs. [191] and [170]. The incident free–field also induces an incident traction or surface

stress t_i^F on the half–space boundary surface, which may be expressed in terms of the free–field displacement [202, 203]. The introduction of an irregularity to the surface of the half–space results in a scattered displacement field u_i^{sca} and so the total field is defined as $u_i = u_i^F + u_i^{\text{sca}}$. Under the traction–free BC the induced free–field traction must equal 0 on the free–surface. The corresponding scattered traction field t_i^{sca} resulting from the surface irregularity must also be 0 on the planar part of the surface while $t_i^{\text{sca}} = -t_i^F$ on the irregularity. Thus the elastodynamic BIE (Eq. 4.53) may be solved in terms of the scattered field as [191]

$$\frac{1}{2}u_i^{\text{sca}}(\mathbf{y}) - \int_S T_{ij}^{\text{T}}(\mathbf{x},\mathbf{y})u_i^{\text{sca}}(\mathbf{x})dS(\mathbf{x}) = \int_C U_{ij}^{\text{T}}(\mathbf{x},\mathbf{y})t_i^F(\mathbf{x})dS(\mathbf{x}) \tag{4.53}$$

where S denotes the complete discretised boundary surface (canyon + surrounding circular disc of the half–space) and C denotes the canyon surface. The total displacement field may then be retrieved by combining the free and scattered field components.

The first numerical example presented here involves a compressional plane wave impinging upon a hemispherical canyon of radius a at normal incidence ($\theta = 0$). The incident wavenumber is $k_p a = 0.25\pi$ and the elastic half–space has material properties $\nu = 1/4$ and $\mu = 1/3$. The canyon and a surrounding circular disc of radius $D = 3a$ of the half–space boundary surface is modelled with a 7668 element boundary mesh ($N = 23004$). Fig. 4.15 shows the total components of vertical z and horizontal x displacements along a cross section of the mesh from $x = 0 : 3a$ and $y = 0$ and compares the results from other elastodynamic BEM [202, 203] and FMBEM [37] results. Good agreement is observed between the sets of results.

The second numerical example involves a compressional plane wave impinging upon a semi–ellipsoidal canyon with a semi–axis $b = 3a$ at an oblique incidence ($\theta = 30°$). The incident wavenumber is $k_s a = 0.5\pi$ and the elastic half–space has material properties $\nu = 1/3$ and $\mu = 1$. The canyon and a surrounding circular disc of radius $D = 6a$ of the half–space boundary surface is modelled with an 8372 element boundary mesh ($N = 25116$). Fig. 4.16 shows the total components of vertical z and horizontal x displacement along a cross section of the mesh from $x = -3a : 3a$ and $y = 0$ and compares the results to those from other elastodynamic BEM [202, 203] and FMBEM [37] results, where again good agreement is observed between the sets of results.

Additionally, surface plots of the total z–components of displacement for various configurations are shown in Figs. 4.17 and 4.18 for hemispherical and semi–ellipsoidal

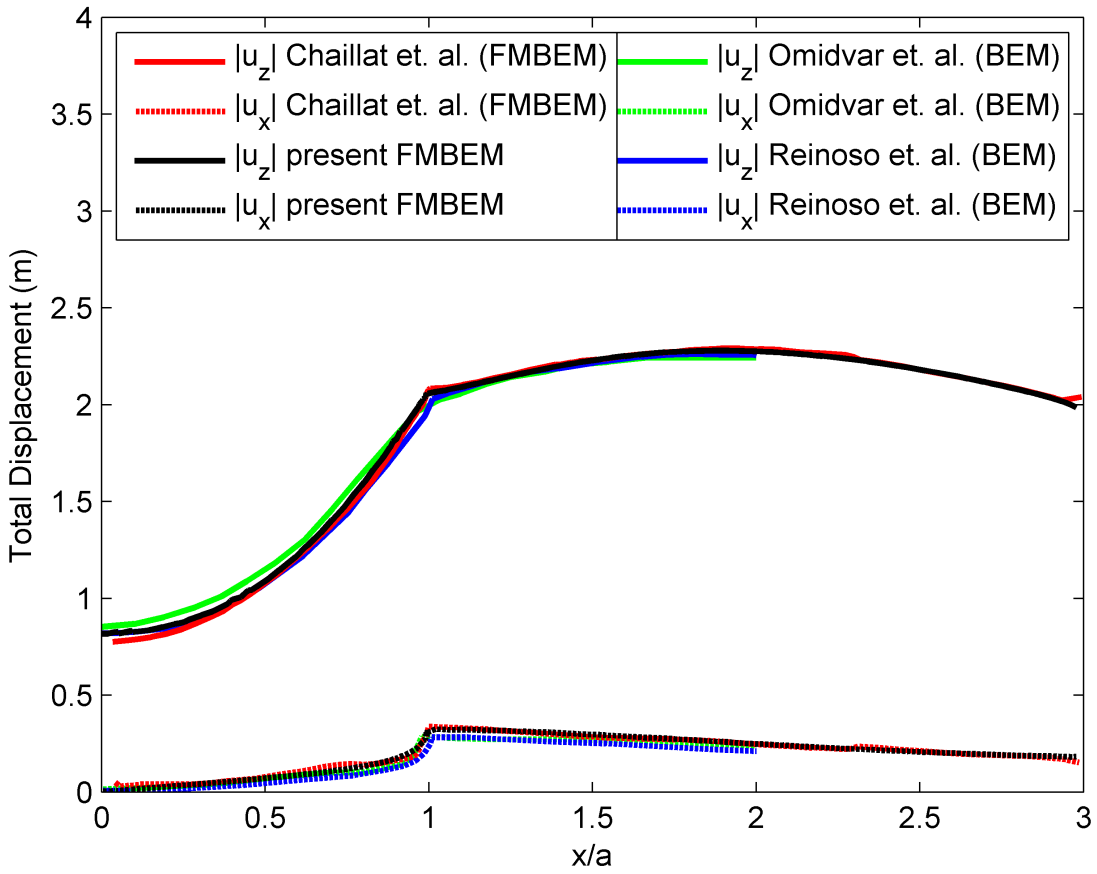

Figure 4.15: Total vertical z and horizontal x components of displacement (m) for scattering of a $k_p a = 0.25\pi$ compressional plane wave by a hemispherical canyon at vertical incidence. The total displacement components are shown along a cross section from $x = 0 : 3a$ and $y = 0$ and are compared to other numerical results [37, 202, 203].

canyons respectively. Fig. 4.17 shows the hemispherical canyon results for two frequencies: $k_p a = 0.25\pi$ (left) and $k_p a = 0.5\pi$ (right) for a compressional plane wave impinging at a normal incidence (top row) and an oblique incidence of $\theta = 30°$ (bottom row). The canyon has a radius of a and the free–surface of the elastic half–space is meshed to a radius of $D = 5a$, giving meshes with 8088 and 9416 elements for the $k_p a = 0.25\pi$ and $k_p a = 0.5\pi$ frequencies respectively. The elastic half–space for the hemispherical canyon has material properties $\nu = 1/4$ and $\mu = 1/3$. The semi–ellipsoidal canyon results presented in Fig. 4.18 are for a single frequency of $k_p a = 0.25\pi$ and a normally (left) and obliquely ($\theta = 30°$, right) incident compressional plane wave. The canyon has a semi–axis $b = 2a$ in the y–axis direction and the free–surface is meshed to a radius

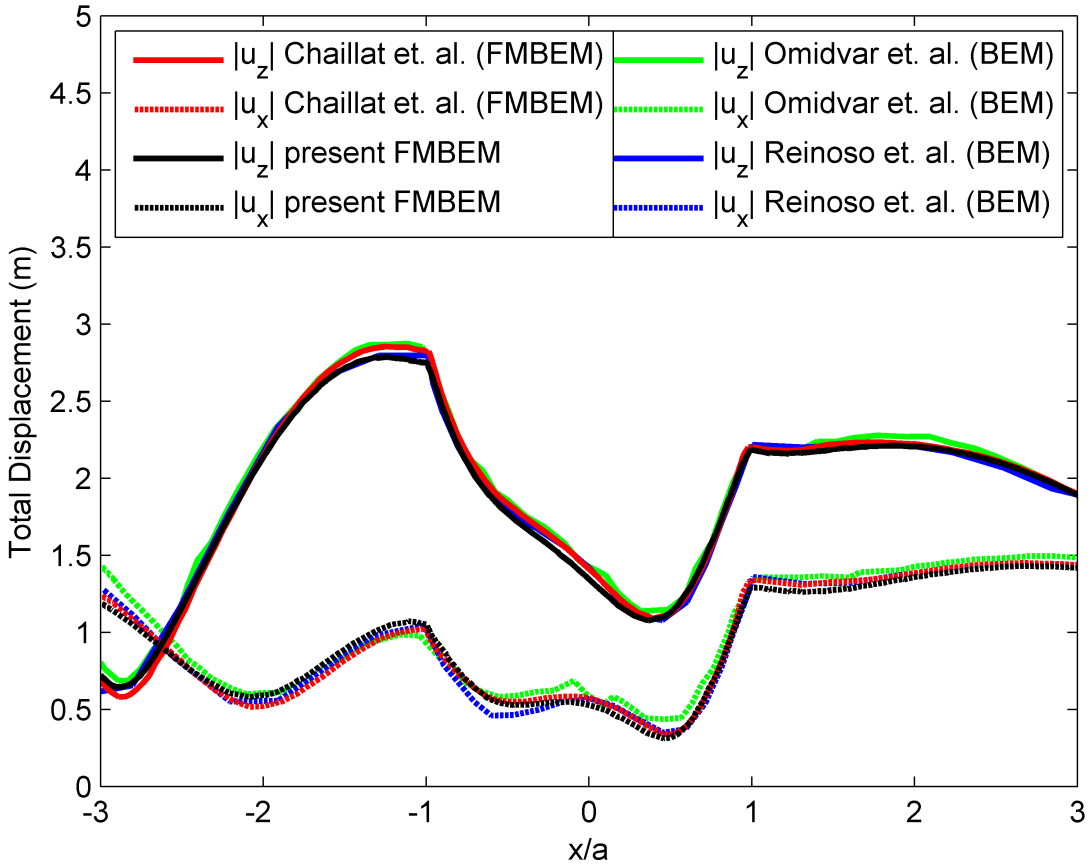

Figure 4.16: Total vertical z and horizontal x components of displacement for scattering of a $k_s a = 0.5\pi$ compressional plane wave by a semi–ellipsoidal canyon at an oblique incidence ($\theta = 30°$). The total displacement components are shown along a cross section from $x = -3a : 3a$ and $y = 0$ and are compared to other numerical results [37, 202, 203].

of $D = 8a$, giving a mesh consisting of 3266 elements. The elastic half–space for the semi–ellipsoidal canyon has material properties $\nu = 1/3$ and $\mu = 1$.

These particular problem configurations have been adopted to allow for a comparison with results presented by Chaillat which were calculated using her high–frequency elastodynamic FMBEM (cf. Figs. 5.4, 5.5, 5.8 and 5.9 in Ref. [191]). An attempt has been made to match the colour maps and colour bar axis limits of the results in Figs. 4.17 and 4.18 to that used by Chaillat. It should be noted that the z–displacement results for the normally incident $k_p a = 0.5\pi$ compressional plane wave in Fig. 5.4 of Ref. [191] does not appear to have been scaled to a minimum displacement magnitude of 0 and so the corresponding results in Fig. 4.17 have been similarly scaled for com-

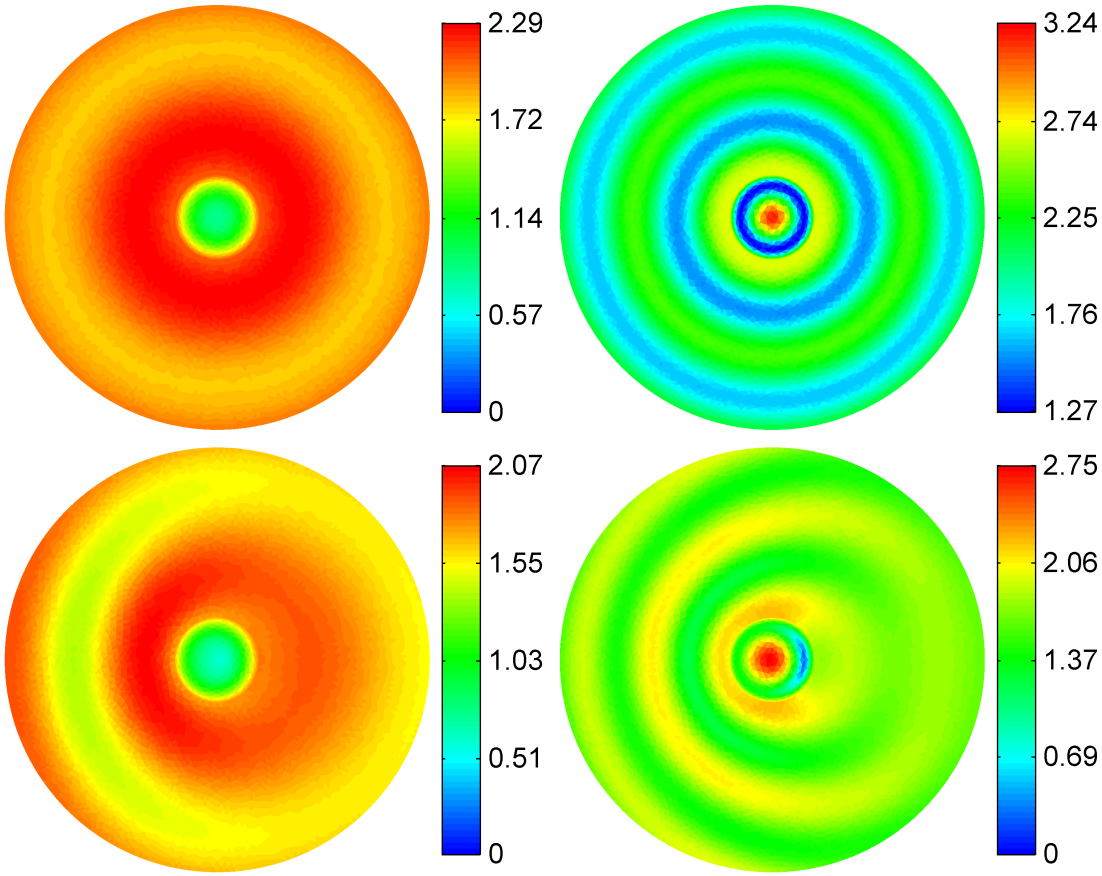

Figure 4.17: Scattering of compressional plane waves from a hemispherical canyon: total z–component of displacement (m) for incident wavenumbers $k_p a = 0.25\pi$ (left) and $k_p a = 0.5\pi$ (right) for plane waves impinging at a normal incidence (top row) and an oblique incidence of $\theta = 30°$ (bottom row).

parison. Good qualitative agreement can be observed between Chaillat's results and the present elastodynamic FMBEM results.

Finally, a large scale canyon scattering problem is treated with the elastodynamic FMBEM. The example problem involves a compressional plane wave impinging upon a semi–ellipsoidal canyon at an oblique incidence ($\theta = 30°$). The incident wavenumber is $k_s a = 2\pi$ and the elastic half–space has material properties $\nu = 1/3$ and $\mu = 1$. The canyon has a semi–axis $b = 3a$ in the y–axis direction and the free–surface is meshed to a radius of $D = 6a$, giving a mesh consisting of 119278 elements (357834 unknowns). Again, this problem configuration is chosen to allow for a comparison with the high-frequency elastodynamic FMBEM results presented by Chaillat [37, 191]. The

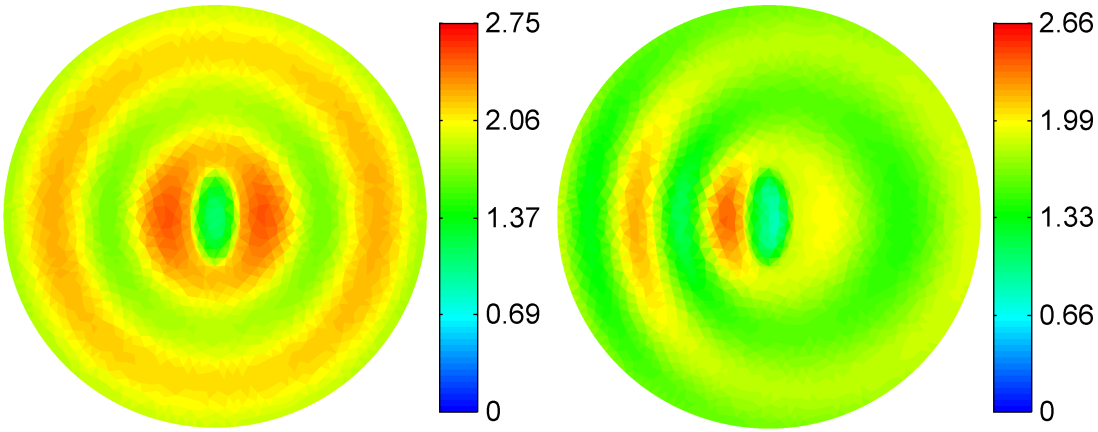

Figure 4.18: Scattering of compressional plane waves from a semi–ellipsoidal canyon: total z–component of displacement (m) for an incident wavenumber of $k_p a = 0.25\pi$ for plane waves impinging at a normal incidence (left) and an oblique incidence of $\theta = 30°$ (right).

elastodynamic FMBEM presented in this chapter solved the problem in 130 minutes, with 93 minutes of that time attributed to the GMRES solution and the remainder devoted to the problem set–up, particularly the calculation of the sparse near field matrices. The GMRES solution converged to a tolerance of 6.40×10^{-5} requiring eight outer GMRES iterations and 75 inner GMRES iterations (total). The outer GMRES iterations required 226 seconds per iteration while the inner loops required 45 seconds per iteration (including sparse matrix–vector multiplication with the SAI preconditioner). The total storage requirements of the FMBEM was 4.03GB using six octree levels (i.e. $\hat{l} = 7$), with 1.31GB required for each of the sparse near field U_{ij} and T_{ij} matrices and 342MB required for the SAI preconditioner. The remainder of the memory was used for storing the source expansions, translation coefficients and octree structure information. The equivalent BEM matrices for this problem would each require approximately 2TB to store and 1.28×10^{11} operations per matrix–vector product.

A tenuous comparison may be drawn with Chaillat's high–frequency elastodynamic FMBEM model, where a similar problem was modelled with 353232 unknowns and solved to a GMRES tolerance of $1e^{-3}$ using a maximum octree level of five. The iterative solution was stated to converge in 32 GMRES iterations requiring 143 seconds of time per iteration [37, 191], giving a total GMRES solution time of 76 minutes for Chaillat's

model compared to 93 minutes for the iterative solution in the present FMBEM model. Due to the different programming languages (MATLAB for the present elastodynamic FMBEM versus Fortran 90 for Chaillat) and utilised computer hardware, as well as the different GMRES tolerance and octree level settings used in the two models, a direct comparison between the FMBEM models is not possible.

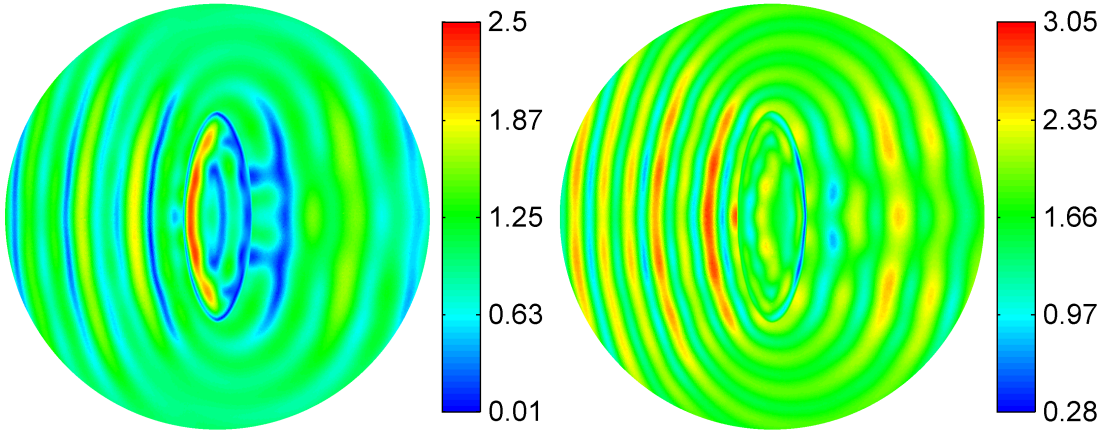

Figure 4.19: Scattering of compressional plane waves from a semi–ellipsoidal canyon: total x and z components of displacement (m) for an incident wavenumber of $k_s a = 2\pi$ at an oblique incidence of $\theta = 30°$.

4.4 Chapter Summary

This chapter has presented the elastodynamic FMBEM model developed for the coupled fluid–structure interaction model. The chapter contains a literature review of the FMM for the elastodynamic BIE, a description of the implementation of the elastodynamic FMBEM model, including pseudocode algorithms for the setup and iterative solution of the elastodynamic BIE using the FMM, and has been concluded with the presentation of numerical results which demonstrate the performance of the elastodynamic FMBEM model. The solution time of the elastodynamic FMBEM model was shown to scale between N and N^2 while the storage requirements are proportional to or less than N. As with the implemented Helmholtz FMBEM code presented in the previous chapter, the elastodynamic FMBEM model presented here exhibits the best performance in the low frequency range (where the number of unknowns is independent of the wavelength) due to the $O(p^3)$ algorithmic complexity of the RCR translation method used. The

elastodynamic FMBEM presented in this chapter constitutes the first implementation of a low frequency elastodynamic FMBEM to use both low algorithmic complexity $O(p^3)$ translation techniques and octree translation stencils.

A number of the numerical results presented in this chapter for exterior scattering problems have been observed to suffer poor accuracy and slow convergence due to the modelled frequencies being in close proximity to the eigenfrequencies of the corresponding adjoint interior problems. The breakdown of exterior problems near these frequencies is well known for the elastodynamic BIE, however no difficulty is encountered when using the elastodynamic BIE for interior problems, as the eigenfrequencies have a physical meaning related to the finite dimensions of the interior domain. The elastodynamic FMBEM presented in this chapter will be used in the acoustic coupled FSI model (presented next in Chapter 5) for the interior elastic solid part of the model while the Helmholtz FMBEM (which incorporates the stabilised Burton–Miller formulation) will be used to model the infinite exterior fluid domain.

5

Dual FMBEM for Acoustic Coupled Fluid–Structure Interactions

The dual FMBEM model for solving acoustic coupled FSI problems is presented in this chapter, constituting the principal contribution of original work in this thesis. A review of the literature relating to acoustic coupled FSI models which utilise dual BEM or FMM formulations is first presented. This is followed by a description of the developed dual FMBEM model for acoustic coupled FSI problems, including details of the coupling and preconditioning strategies used, as well as a pseudo–algorithm describing the iterative FMBEM solution for the coupled system of discretised BIEs. Numerical results for the dual FMBEM model are presented and the algorithmic and memory complexity of the model is investigated. The performance of the dual FMBEM model near eigenfrequencies is also investigated. Finally, conclusions are drawn regarding the performance of the dual FMBEM model for solving acoustic coupled fluid–structure interaction problems.

5.1 Literature Review

A number of types of numerical models have been developed for modelling acoustic coupled fluid–structure interaction problems [206, 207], with perhaps the most prevalent being the coupled FEM–BEM type models. Chen and Schweikert first developed such

a model in 1963 [63] where they used a single layer potential to represent the acoustic field and lumped masses to represent the structure. Implementations that used proper FEM representations of the solid followed in the 1970s [9, 208, 209] and now a large body of work exists in the field, with a number of reviews of the early literature available in, for example, various books [32, 169, 210] and journal papers [9, 12, 14] while the bibliographical review papers by Mackerle [211, 212] cite much of the work published throughout the 90s. A general review of coupled FEM–BEM models for acoustic coupled FSI problems would be outside the scope of this work, which is instead focused on the more relevant fields of 3D acoustic FSI models which:

1. use dual BEM (or BEM–BEM) implementations to treat both the fluid and solid domains, and

2. incorporate the FMM to accelerate the BEM in coupled FSI problems.

Dual BEM implementations for acoustic coupled FSI problems. The idea of treating acoustic coupled FSI problems with only surface integral formulations has been around for some decades. Early work along these lines was conducted by Shaw in 1973, who proposed an integral equation approach for specific geometries which treated both the fluid and elastic domains via analytically determined surface integrals [213]. The 'T–Matrix' or 'Null–field' method for acoustics [214], which represents the scattered field in the Helmholtz BIE as a series expansion and solves for the corresponding expansion coefficients by applying appropriate BCs, was applied to acoustic coupled FSI problems by several authors around 1980 [215, 216, 217]. Both the fluid and solid domains are represented by surface integrals and BCs which couple the fluid and solid at the shared boundary surface are used to solve for the expansion coefficients of the scattered field. However the T-matrix method is not considered a general purpose method as it cannot model arbitrarily shaped surfaces [32]. Tanaka and Masuda considered acoustic coupling between an interior acoustic domain and an elastic plate in 1988 [218]. The 'boundary–domain element method' used to model the plate [219] appears to require both a surface and a volume discretisation of the elastic plate and so may be considered a hybrid FEM–BEM model, while others cite the method as a dual BEM model [169].

The first numerical 3D BEM algorithms involving the Helmholtz and elastodynamic BIEs were introduced in the late 1980s by Seybert et al. [220] and Goswami et al.

[221, 222] for solid objects and shells, while 2D models were not treated until several years later [223]. The modelling of fluid–filled boreholes embedded in elastic solids with dual BEM techniques was treated by Randall [224] and Poterasu [225]. Fluid–solid interface problems involving curvatures or irregularities to the interface between the semi–infinite fluid/solid half–spaces were treated by Goswami and Rudolphi [226] and Shenoy et al. [227]. Slepyan and Sorokin [228], and Sorokin [229] used a 'two–level' boundary integral method for acoustic–structure interactions of thin composite shell structures where they used analytic forms to describe the in vacuo vibrations of each simple geometric component and then a numerically evaluated BIE to determine the coupled interaction. Chen and Liu [230] studied shell–like structures with a dual BEM formulation in 1999, while their follow–up paper in 2000 investigated efficient iterative solution techniques and preconditioning strategies for their dual BEM model [231]. The 3D elastodynamic BIE was used to model the thin–shell structures.

More recent work on dual BEM implementations for acoustic coupled FSI problems appears to be relatively sparse. In particular one can cite the work of Nolte et al. [232] (with related conference papers by Nolte and Gaul [233] and Burgschweiger et al. [234]) who treated acoustic coupled FSI problems for 3D scattering. Other recent applications have included 2D frequency–domain implementations for the scattering of acoustic waves from fluid–solid interfaces [235] and the modelling of fluid–solid interface waves [236, 237], as well as a number of papers by Soares and Mansur [238], and Soares [239, 240], which implement 2D time–domain formulations. The most recent article presenting 3D frequency domain BEM–BEM models for acoustic FSI problems appears to be by Nolte [232] in 2007, who presents BEM–BEM coupling theory but no new model results, and the work of Chen and Liu [230, 231] from around the year 2000.

Acoustic coupled FSI problems utilising FMBEM formulations The incorporation of the FMM into coupled FEM–BEM type models has been a relatively recent venture, with the first such model for acoustic coupled FSI type problems developed by Fischer and Gaul in 2004 [241, 242]. Their implementation coupled a high–frequency diagonal translation FMM for the acoustic fluid domain to a standard structural FEM model and a mortar coupling method was employed to allow coupling between non-conforming BEM and FEM meshes [243, 244]. A similar model was implemented by Schneider in 2008 [39] using a direct coupling between coincident meshes, and separate studies indicated that the direct coupling scheme is computationally superior to the

former [245, 246]. Two book chapters on the FEM–FMBEM coupling for acoustic FSI problems have been published by Gaul et al. [30, 247] and now a number of papers have been published on the application of the method to the modelling of, for example, ship–like structures [248, 249] and other partially submerged bodies [250, 251], coupling of multiple acoustic domains [252] and coupling involving acoustic FMBEM and modal-based structural models [253, 254]. Grasso has recently implemented an analogous FEM–FMBEM coupling model for elastodynamic problems [121, 255].

The review of the literature is concluded by noting that dual FMBEM implementations which treat multiple coupled fluid domains [256] or multiple coupled elastic solid domains [186] are both present in the literature. However there appears to be very little published work on dual FMBEM implementations which treat both fluid and solid domains with the FMBEM for acoustic coupled FSI problems. It appears that the only relevant publications on the subject consist of a recently published PhD thesis by Isakari [182], and a paper written in Japanese that is cited therein [257] (also written by Isakari) but was not available to the present author. Isakari presents a low frequency dual FMBEM method for acoustic coupled FSI problems, with a focus on modelling periodic structures and implementing Calderon–type preconditioners based upon Calderon's periodic boundary conditions. This contrasts with the dual FMBEM model presented in this thesis chapter, in which a low frequency dual FMBEM model for acoustic coupled FSI problems has been developed for non–periodic structures with a particular emphasis on underwater sound scattering problems. The dual FMBEM model presented here similarly uses the low algorithmic complexity RCR translation method, and additionally implements translation stencils in both the fluid and elastic solid domains to reduce the total number of required translations. Furthermore, the present implementation uses a different iterative solution strategy based upon the direct solution of the coupled system of BIEs, as well as a different preconditioning strategy, which applies a diagonal scaling and sparse approximate inverse preconditioner to the dual FMBEM in the inner GMRES loop of a nested inner–outer fGMRES solution. Finally, the present work presents numerical algorithmic complexity results for the low frequency dual FMBEM model which are shown to be in good agreement with theoretical estimates for the low frequency FMBEM [42].

5.2 The Dual FMBEM for Coupled Fluid–Structure Interaction Problems

In this section the theory and implementation of the dual FMBEM model developed for modelling acoustic coupled FSI problems is presented for problems which involve scattering of incident acoustic fields by finite elastic solid objects. The main focus of this section is on the theoretical and numerical implementation of the coupling method for simultaneously solving the Helmholtz and elastodynamic BIEs for the unknowns on the shared boundary surface between the fluid and solid domains. The FMBEM treatment of both the Helmholtz and elastodynamic BIEs remains unchanged when implemented in the coupled formulation — only the form of the various unknowns appearing in the two BIEs is altered in the coupling procedure — and so details of the FMBEMs for each of the BIEs need not be repeated here.

5.2.1 The Coupled BIE Formulation

Coupling between an exterior fluid domain and an interior solid domain in a dual BIE formulation is typically achieved by relating the unknowns appearing in the two BIEs for the respective domains on the common boundary surface shared by both media. This coupling process reduces the number of unknown terms in the BIEs and yields an exactly solvable system of integral equations relating the total pressure and total displacement on the shared boundary surface. Upon solving for these variables on the boundary surface the pressure or displacement at any point in the respective domains may then be calculated by substituting the surface solutions back into the respective BIEs to evaluate the field at the off surface locations.

The relevant BIEs for the coupling procedure are first recalled from the prior chapters for convenience. The Burton–Miller formulation of the Helmholtz BIE for exterior acoustic problems (recall Eq. 3.2 from Chapter 3) is written as

$$\begin{aligned}\frac{1}{2}\big(p(\mathbf{y})+\alpha q(\mathbf{y})\big) =&\Big(M(\mathbf{x},\mathbf{y})+\alpha M'(\mathbf{x},\mathbf{y})\Big)p(\mathbf{x}) - \Big(L(\mathbf{x},\mathbf{y})+\alpha L'(\mathbf{x},\mathbf{y})\Big)q(\mathbf{x})\\ &+\big(p^i(\mathbf{y})+\alpha q^i(\mathbf{y})\big)\end{aligned}$$

where p, p^i and q, q^i are respectively the total and incident components of the surface pressure p and normal derivative of the surface pressure q, the terms L, L', M and M'

are the various surface integrals of the Helmholtz fundamental solution and α is the Burton–Miller coupling parameter. The elastodynamic BIE for interior problems is

$$\frac{1}{2}u_i(\mathbf{y}) = \int_S \Big(T_{ij}^{\mathrm{T}}(\mathbf{x},\mathbf{y})u_i(\mathbf{x}) - U_{ij}^{\mathrm{T}}(\mathbf{x},\mathbf{y})t_i(\mathbf{x}) \Big) dS(\mathbf{x})$$

where u_i and t_i denote the i^{th} Cartesian components of the total surface displacement and total surface stress (or traction), U_{ij} and T_{ij} are the elastodynamic fundamental solutions, and the surface normal is again defined as pointing outwards to the finite enclosed boundary surface. Finally one should note the change in sign of the integral terms in the elastodynamic BIE presented here for interior problems, compared to Eq. 4.2 in Chapter 4 which was formulated for exterior problems. Furthermore, the interior elastodynamic BIE no longer contains an incident field term as the incident acoustic field is only defined in the exterior fluid domain while the interior solid domain contains no source terms.

The Helmholtz and elastodynamic BIEs involve four unknowns on the shared boundary surface: two scalar quantities in the Helmholtz equation (p, q) and two vector quantities in the elastodynamic equation (u_i, t_i). These equations may be coupled on the surface by applying boundary conditions that relate the unknowns between the two media. In particular, both the surface stresses and particle displacements must be continuous across the boundary. As the fluid cannot support shear stress, the tangential components of stress at a local point $\mathbf{x}$ on the surface must be zero, and so the stress normal to the surface must be equal and opposite to the pressure exerted on the surface by the fluid [30]. This condition may be written as

$$t_i(\mathbf{x}) = -p(\mathbf{x})n_i(\mathbf{x}) \tag{5.1}$$

Furthermore, assuming an $e^{-i\omega t}$ time–harmonic motion with angular frequency ω, the displacement and the normal derivative of pressure can be equated as

$$q(\mathbf{x}) = \rho_f \omega^2 u_i(\mathbf{x})n_i(\mathbf{x}) \tag{5.2}$$

where ρ_f denotes the fluid density and the summation over the i^{th} Cartesian components is implied. Eq. 5.1 eliminates the surface stress from the elastodynamic BIE while Eq. 5.2 eliminates the normal derivative of pressure from the Helmholtz BIE.

The resulting coupled system of equations can be written as:

$$\frac{1}{2}\big(p(\mathbf{y})+\alpha\rho_f\omega^2 u_i(\mathbf{y})n_i(\mathbf{y})\big) = \big(p^i(\mathbf{x})+\alpha q^i(\mathbf{x})\big)+\Big(M(\mathbf{x},\mathbf{y})+\alpha M'(\mathbf{x},\mathbf{y})\Big)p(\mathbf{x}) - \Big(L(\mathbf{x},\mathbf{y})+\alpha L'(\mathbf{x},\mathbf{y})\Big)\rho_f\omega^2 u_i(\mathbf{x})n_i(\mathbf{x}) \tag{5.3a}$$

$$\frac{1}{2}u_i(\mathbf{y}) = \int_S \Big(T_{ij}^{\mathrm{T}}(\mathbf{x},\mathbf{y})u_i(\mathbf{x})+U_{ij}^{\mathrm{T}}(\mathbf{x},\mathbf{y})p(\mathbf{x})n_i(\mathbf{x})\Big)dS(\mathbf{x}) \tag{5.3b}$$

which can be seen to involve only two unknowns: the scalar pressure p and vector displacement u_i on the boundary surface. The coupled system of equations may be numerically implemented and simultaneously solved for p and u_i on the surface.

5.2.2 Numerical Implementation of the Coupled System of BIEs

Eq. 5.3 constitutes an exactly solvable system of equations for determining the total pressure and displacement on the shared boundary surface S between an exterior fluid and interior solid domain. Approximating the shared boundary surface between the two domains via N plane triangular elements (i.e. using conforming meshes for both domains and applying a one–to–one fluid/solid element coupling) and using piece–wise constant unknowns at the coincident element centres/collocation points allows Eq. 5.3 to be rearranged into the form of an $\mathbf{Az}=\mathbf{b}$ matrix equation

$$\begin{bmatrix} \Big(-\mathbf{T}_{3N}+\frac{1}{2}\mathbf{I}_{3N}\Big) & \Big(-\mathbf{U}_{3N}\Big)n_i(\mathbf{x}_N) \\ \Big(\mathbf{L}_N+\alpha\frac{1}{2}\mathbf{I}_N\Big)\rho_f\omega^2 n_i(\mathbf{x}_N) & \Big(-\mathbf{M}_N+\frac{1}{2}\mathbf{I}_N\Big) \end{bmatrix} \begin{bmatrix} u_i(\mathbf{x}_N) \\ p(\mathbf{x}_N) \end{bmatrix} = \begin{bmatrix} \mathbf{0}_{3N} \\ \mathbf{p}^i \end{bmatrix} \tag{5.4}$$

where $\mathbf{p}^i = \big[p^i(\mathbf{y}_N)+\alpha q^i(\mathbf{y}_N)\big]$, $\mathbf{0}_{3N}$ denotes a $3N$ element vector of zeros and $\mathbf{L}_N$, $\mathbf{M}_N$, $\mathbf{T}_{3N}$, $\mathbf{U}_{3N}$, $\mathbf{I}_N$ and $\mathbf{I}_{3N}$ have all been previously defined. Eq. 5.4 is solved for $4N$ unknowns: $3N$ unknowns for the Cartesian components of the total surface displacement and N unknowns for the total surface pressure. The components of the discretised matrix equation can be envisioned as having the following dimensions

$$\left(\begin{array}{c|c} 3N\times 3N & 3N\times N \\ \hline N\times 3N & N\times N \end{array}\right)\times\left(\begin{array}{c} 3N\times 1 \\ \hline N\times 1 \end{array}\right)=\left(\begin{array}{c} 3N\times 1 \\ \hline N\times 1 \end{array}\right)$$

where the respective substitutions of the scalar pressures into the elastodynamic BIE, and vector displacement components into the Helmholtz BIE, yield the $3N \times N$ and $N \times 3N$ off–diagonal coupling matrices. In practice all of the implemented coefficient matrices remain square and the substitution of the unknowns for the coupling matrices either extends or contracts the unknown vectors to be the same length as the dimensions of the corresponding coefficient matrices i.e. $n_i(\mathbf{x}_N)p(\mathbf{x}_N)$ is of length $3N$ and $\rho_f\omega^2 n_i(\mathbf{x}_N)u_i(\mathbf{x}_N)$ is of length N. Of course the FMBEM only requires the sparse near field components of the full coefficient matrices to be constructed and stored.

Thus the dual FMBEM implementation of Eq. 5.4 requires the propagation of 11 sets of spherical basis functions to treat the far field parts of the discretised surface integrals: one each for $\mathbf{L}_N$ and $\mathbf{M}_N$, four for $\mathbf{U}_{3N}$ and five for $\mathbf{T}_{3N}$, while four sparse matrices must be constructed to store the near field parts of the surface integrals. Finally it is reiterated that the FMBEM treatment of Eq. 5.4 does not require any internal modification to the separate Helmholtz and elastodynamic FMBEM algorithms that were presented in previous chapters.

5.2.3 Dual FMBEM Iterative Solution and Preconditioning

The iterative solution and preconditioning methods used for solving the coupled system of equations in Eq. 5.3 are essentially the same as that used in the Helmholtz and elastodynamic FMBEM models. The fGMRES method [152, 153] is used to allow an inner–outer GMRES solution method, where a low accuracy FMBEM with a coarse convergence tolerance is iteratively solved in the inner GMRES and this solution is then used in the full accuracy outer GMRES loop. The FMM inner/outer tolerances used for truncating the expansions ($\epsilon = 10^{-4}$,$\epsilon_{\text{pre}} = 0.2$) and the analogous GMRES convergence tolerances ($\xi = 10^{-4}$,$\xi_{\text{pre}} = 0.15$) have the same settings in the coupled FMBEM as were used in the separate Helmholtz/elastodynamic FMBEM models.

A sparse approximate inverse (SAI) preconditioner [62] is similarly used to precondition the inner GMRES loop of the dual FMBEM model. The SAI matrix for the coupled coefficient matrix in Eq. 5.3 is constructed using the main diagonal coefficient matrices, yielding a 'block diagonal' SAI preconditioner [246, 258] of the form

$$\begin{bmatrix} \left(-\mathbf{T}_{3N} + \frac{1}{2}\mathbf{I}_{3N}\right)^{-1} & \mathbf{0}_{3N\times N} \\ \mathbf{0}_{N\times 3N} & \left(-\mathbf{M}_N + \frac{1}{2}\mathbf{I}_N\right)^{-1} \end{bmatrix}$$

where the approximate inverse of the block diagonal terms is constructed from the sparse near field parts of the surface integrals $\mathbf{T}_{\mathrm{nf}}$ and $\mathbf{M}_{\mathrm{nf}}$. The resulting SAI matrix is sparse and diagonally banded with a small bandwidth.

The coupled coefficient matrix in Eq. 5.4 is in general badly scaled and has a poor condition number due to the different magnitudes of the pressures and displacements expected for realistic materials (such as steel submerged in water). An attempt to solve Eq. 5.4 in its current form typically results in the larger magnitude pressures dominating the solution convergence, yielding a reasonably accurate solution for the pressure but significant errors in the displacement results. As the larger magnitude pressures still generally converge to the correct solution the specified residual of the GMRES solution is achieved despite the incorrect displacement results, which only contribute a small component to the residual due to their small magnitude relative to the pressure results. The SAI preconditioner in part alleviates the scaling issue by ensuring that the premultiplication of the SAI matrix with the coupled coefficient matrix yields an approximate identity matrix and so equalises the diagonal coefficient matrices to a degree. Faster solution convergence is achieved by also explicitly incorporating scaling factors into the coupled matrix equation to equalise the magnitudes of the four terms in the coupling matrix. Two scaling factors, Ψ and Ω, are introduced into Eq. 5.4 as follows

$$\begin{bmatrix} \frac{\Omega}{\Psi}\Big(-\mathbf{T}_{3N}+\frac{1}{2}\mathbf{I}_{3N}\Big) & \Omega\Big(-\mathbf{U}_{3N}\Big)n_i(\mathbf{x}_N) \\ \frac{1}{\Psi}\Big(\mathbf{L}_N+\alpha\frac{1}{2}\mathbf{I}_N\Big)\rho_f\omega^2 n_i(\mathbf{x}_N) & \Big(-\mathbf{M}_N+\frac{1}{2}\mathbf{I}_N\Big) \end{bmatrix} \begin{bmatrix} \Psi u_i(\mathbf{x}_N) \\ p(\mathbf{x}_N) \end{bmatrix} = \begin{bmatrix} \mathbf{0}_{3N} \\ \mathbf{p}^i \end{bmatrix} \tag{5.5}$$

where the scaling factor Ψ is used to increase the magnitude of the displacements (i.e. Ψ is large) and Ω is used to increase the magnitude of the entire elastodynamic equation relative to the Helmholtz equation (Ω is also large). Thus Eq. 5.5 solves for the displacements in the form $\Psi u_i(\mathbf{x}_N)$ and the actual displacements may be extracted by dividing by Ψ once the iterative solution converges. For the all–zero incident displacement vector the known right hand side vector $\Omega\mathbf{0}_{3N} = \mathbf{0}_{3N}$. The scaling factors are determined by the magnitudes of the main diagonal components of the sparse near field

integrals appearing in Eq. 5.4 as follows:

$$\Psi = \left|\text{mean}\left(\rho_f \omega^2 \left(\mathbf{L}_{\text{nf}} + \alpha\frac{1}{2}\right)\mathbf{I}_N\right)\right| \tag{5.6}$$

$$\frac{1}{\Omega} = \frac{1}{2}\left|\text{mean}\left(-\mathbf{U}_{\text{nf}}\mathbf{I}_{3N}\right) + \text{mean}\left(\frac{1}{\Psi}\left(-\mathbf{T}_{\text{nf}} + \frac{1}{2}\right)\mathbf{I}_{3N}\right)\right| \tag{5.7}$$

where mean( ) and | | denote the mean and the absolute value of the enclosed terms respectively. The value of Ψ is chosen to approximately normalise the coupled $\mathbf{L}_N$ coefficient matrix appearing in Eq. 5.4 to unity, while the value of Ω is chosen to be equal to the inverse of the approximate mean of the two elastodynamic BIE terms in the coupled coefficient matrix. The use of these scaling factors typically improves the condition number of the coupled coefficient matrix from 10^{26} in Eq. 5.4 to 10^3 in Eq. 5.5. The block diagonal SAI preconditioner for Eq. 5.5, $(\mathbf{TM})_{\text{pre}}$, then becomes

$$(\mathbf{TM})_{\text{pre}} = \begin{bmatrix} \left(\frac{\Omega}{\Psi}\left(-\mathbf{T}_{\text{nf}} + \frac{1}{2}\mathbf{I}_{3N}\right)\right)^{-1} & \mathbf{0}_{3N\times N} \\ \mathbf{0}_{N\times 3N} & \left(-\mathbf{M}_{\text{nf}} + \frac{1}{2}\mathbf{I}_N\right)^{-1} \end{bmatrix} \tag{5.8}$$

which gives the approximate inverse of the scaled coupled coefficient matrix in Eq. 5.5.

5.2.4 Dual FMBEM Algorithm

The section is concluded by presenting a pseudocode algorithm for the iterative solution of an acoustic coupled FSI problem using the dual FMBEM model, which involves exterior scattering by a solid elastic object submerged in an infinite fluid medium as per Eq. 5.5. Firstly the FMM 'set up' algorithms for the Helmholtz and elastodynamic FMBEMS, previously described in Sections 3.2.5 and 4.2.5 of Chapters 3 and 4 respectively, are called to construct the octrees, multipole expansions/translations and near field integrals for the Helmholtz and elastodynamic fast multipole algorithms. The only modifications required for the separate set up algorithms for their use in the dual FMBEM model is in relation to the SAI preconditioner, where only a single block diagonal SAI preconditioner (presented in Eq. 5.8) need be constructed.

The dual FMBEM similarly calls the separate Helmholtz and elastodynamic FMBEM algorithms, Algs. 3.2 and 4.1 respectively, in the iterative solution procedure. These algorithms may be directly called in the dual FMBEM iterative solution with appropriate substitutions for the surface traction and normal derivative of surface pressure

via Eqs. 5.2 and 5.1 respectively. The function calls thus take the form:

$$\begin{aligned}\big[\big(\mathbf{L}_N\big)\rho_f\omega^2 n_i(\mathbf{x}_N)u_i(\mathbf{x}_N),\big(\mathbf{M}_N\big)p(\mathbf{x}_N)\big] &= \textsc{Helm\_FMBEM}\big(k,p_l,p(\mathbf{x}_N),\\ &\quad \rho_f\omega^2 n_i(\mathbf{x}_N)u_i(\mathbf{x}_N),\alpha,A_N,R_{\hat{l}},[R_{\hat{l}}]_{\mathbf{n}(\mathbf{x}_N)},(SS)_l,(RR)_l,(SR)_l,\mathbf{L}_{\mathrm{nf}},\mathbf{M}_{\mathrm{nf}}\big)\\ \big[-\big(\mathbf{U}_{3N}\big)p(\mathbf{x}_N)n_i(\mathbf{x}_N),\big(\mathbf{T}_{3N}\big)u_i(\mathbf{x}_N)\big] &= \textsc{Elasto\_FMBEM}\big(k_p,k_s,p_l,u_i(\mathbf{x}_N),\\ &\quad -p(\mathbf{x}_N)n_i(\mathbf{x}_N),\beta,\mu,A_N,R_{\hat{l}},[R_{\hat{l}}]_i,[R_{\hat{l}}]_{ij},(SS)_l,(RR)_l,(SR)_l,\mathbf{U}_{\mathrm{nf}},\mathbf{T}_{\mathrm{nf}}\big)\end{aligned}$$

where it should be understood that the function arguments relating to the multipole expansions ($R_{\hat{l}}$, $[R_{\hat{l}}]_{\mathbf{n}(\mathbf{x}_N)}$, $[R_{\hat{l}}]_i$, $[R_{\hat{l}}]_{ij}$) and translations ($(SS)_l$, $(RR)_l$, $(SR)_l$), as well as the truncation number p_l in each algorithm are dependent upon the corresponding wavenumbers, i.e. they relate to the fluid wavenumber k in function HELM_FMBEM and the elastic solid wavenumbers k_p and k_s in function ELASTO_FMBEM. The iterative solution procedure for the dual FMBEM using the inner–outer GMRES loop and block diagonal SAI preconditioner is presented in Alg. 5.1. The main steps of the algorithm can be seen to parallel those of Algs. 3.3 and 4.2 for the iterative FMBEM solution of the Helmholtz/elastodynamic BIEs. Note that semicolons are used in the notation of Alg. 5.1 to denote vertical concatenation of column vectors, for example

$$[u_i(\mathbf{x}_N);\ p(\mathbf{x}_N)] = \begin{bmatrix} u_i(\mathbf{x}_N) \\ p(\mathbf{x}_N) \end{bmatrix}$$

denotes a column vector of length $4N$ ($3N$ terms for $u_i(\mathbf{x}_N)$ and N terms for $p(\mathbf{x}_N)$).

Algorithm 5.1 Dual FMBEM Algorithm: Iterative Solution

1: **function** IT_SOLVE($p^i(\mathbf{y}_N), q^i(\mathbf{y}_N), \alpha, u_i(\mathbf{y}_N)^{\mathrm{inc}}, \Psi, \Omega,$ HELM_FMBEM$(\ldots)$, ELASTO_FMBEM$(\ldots), (\mathbf{TM})_{\mathrm{pre}}, \xi, \xi_{\mathrm{pre}}, \hat{\mathrm{its}}, \hat{\mathrm{its}}_{\mathrm{pre}}$)

2: $[u_i(\mathbf{x}_N);\ p(\mathbf{x}_N)] = \mathbf{0}_{4N}$ ▷ set initial guess as vector of zeros

3: $\mathbf{p}^i = \big[p^i(\mathbf{y}_N) + \alpha q^i(\mathbf{y}_N)\big], \quad u_i(\mathbf{y}_N)^{\mathrm{inc}} = \mathbf{0}_{3N}$ ▷ set values for known rhs

4: $\big[-\big(\mathbf{U}_{3N}\big)p(\mathbf{x}_N)n_i(\mathbf{x}_N),\big(\mathbf{T}_{3N}\big)u_i(\mathbf{x}_N)\big] = \textsc{Elasto\_FMBEM}\big(k_p,k_s,p_l,u_i(\mathbf{x}_N), -p(\mathbf{x}_N)n_i(\mathbf{x}_N),\ldots\big)$

5: $\big[\big(\mathbf{L}_N\big)\rho_f\omega^2 n_i(\mathbf{x}_N)u_i(\mathbf{x}_N),\big(\mathbf{M}_N\big)p(\mathbf{x}_N)\big] = \textsc{Helm\_FMBEM}\big(k,p_l,p(\mathbf{x}_N), \rho_f\omega^2 n_i(\mathbf{x}_N)u_i(\mathbf{x}_N),\ldots\big)$

6: $\boldsymbol{\xi}_{4N} = \Big[\big[\frac{\Omega}{\Psi}\big(-\mathbf{T}_{3N}+\frac{1}{2}\mathbf{I}_{3N}\big)u_i(\mathbf{x}_N) - \Omega\big(\mathbf{U}_{3N}\big)[n_i(\mathbf{x}_N)p(\mathbf{x}_N)] - \Omega u_i(\mathbf{y}_N)^{\mathrm{inc}}\big];$ $\big[\frac{1}{\Psi}\big(\mathbf{L}_N+\alpha\frac{1}{2}\mathbf{I}_N\big)\rho_f\omega^2 n_i(\mathbf{x}_N)u_i(\mathbf{x}_N)+\big(-\mathbf{M}_N+\frac{1}{2}\mathbf{I}_N\big)p(\mathbf{x}_N)-\mathbf{p}^i\big]\Big], \quad \tilde{\mathrm{its}} = 0$ ▷ calculate initial residual of $\mathbf{Az}-\mathbf{b}$ and set outer loop counter

Algorithm 5.1 Dual FMBEM Algorithm: Iterative Solution (Cont.)

7: **while** $\text{norm}(\boldsymbol{\xi}_{4N}) > \xi$ **and** $\tilde{\text{its}} < \hat{\text{its}}$ **do** ▷ main GMRES loop

8: $[u_i(\mathbf{x}_N)_{\text{pre}};\ p(\mathbf{x}_N)_{\text{pre}}] = \mathbf{0}_{4N}, \quad (\boldsymbol{\xi}_{4N})_{\text{pre}} = \infty, \quad \tilde{\text{its}}_{\text{pre}} = 0$ ▷ preconditioner initial values

9:

10: **while** $\text{norm}((\boldsymbol{\xi}_{4N})_{\text{pre}}) > \xi_{\text{pre}}$ **and** $\tilde{\text{its}}_{\text{pre}} < \hat{\text{its}}_{\text{pre}}$ **do** ▷ preconditioner

11: $\big[-\big(\mathbf{U}_{3N}\big)p(\mathbf{x}_N)_{\text{pre}}n_i(\mathbf{x}_N), \big(\mathbf{T}_{3N}\big)u_i(\mathbf{x}_N)_{\text{pre}}\big] = \textsc{Elasto\_FMBEM}\big(k_p, k_s, (p_l)_{\text{pre}}, u_i(\mathbf{x}_N)_{\text{pre}}, -p(\mathbf{x}_N)_{\text{pre}}n_i(\mathbf{x}_N), \dots\big)$

12: $\big[\big(\mathbf{L}_N\big)\rho_f\omega^2 n_i(\mathbf{x}_N)u_i(\mathbf{x}_N)_{\text{pre}}, \big(\mathbf{M}_N\big)p(\mathbf{x}_N)_{\text{pre}}\big] = \textsc{Helm\_FMBEM}\big(k, (p_l)_{\text{pre}}, p(\mathbf{x}_N)_{\text{pre}}, \rho_f\omega^2 n_i(\mathbf{x}_N)u_i(\mathbf{x}_N)_{\text{pre}}, \dots\big)$

13: $(\boldsymbol{\xi}_{4N})_{\text{pre}} = (\mathbf{TM})_{\text{pre}}\Big[\big[\frac{\Omega}{\Psi}\big(-\mathbf{T}_{3N} + \frac{1}{2}\mathbf{I}_{3N}\big)u_i(\mathbf{x}_N)_{\text{pre}} - \Omega\big(\mathbf{U}_{3N}\big)[n_i(\mathbf{x}_N) \times p(\mathbf{x}_N)_{\text{pre}}]\big]; \big[\frac{1}{\Psi}\big(\mathbf{L}_N + \alpha\frac{1}{2}\mathbf{I}_N\big)\rho_f\omega^2 n_i(\mathbf{x}_N)u_i(\mathbf{x}_N)_{\text{pre}} + \big(-\mathbf{M}_N + \frac{1}{2}\mathbf{I}_N\big) \times p(\mathbf{x}_N)_{\text{pre}}\big]\Big] - (\mathbf{TM})_{\text{pre}}\left(\frac{(\boldsymbol{\xi}_{4N})}{\text{norm}(\boldsymbol{\xi}_{4N})}\right)$ ▷ residual of $\mathbf{A}_{\text{inv}}\mathbf{A}\mathbf{x} - \mathbf{A}_{\text{inv}}\mathbf{b}$ with $\mathbf{b} = \left(\frac{(\boldsymbol{\xi}_{4N})}{\text{norm}(\boldsymbol{\xi}_{4N})}\right)$ from main GMRES and $\mathbf{A}_{\text{inv}} = (\mathbf{UT})_{\text{pre}}$

14: $[u_i(\mathbf{x}_N)_{\text{pre}};\ p(\mathbf{x}_N)_{\text{pre}}] = \text{GMRES}((\boldsymbol{\xi}_{4N})_{\text{pre}}), \quad \tilde{\text{its}}_{\text{pre}} = \tilde{\text{its}}_{\text{pre}} + 1$ ▷ update preconditioner solution using GMRES (see Ref. [152]) and update inner counter

15: **end while**

16:

17: $\big[-\big(\mathbf{U}_{3N}\big)p(\mathbf{x}_N)_{\text{pre}}n_i(\mathbf{x}_N), \big(\mathbf{T}_{3N}\big)u_i(\mathbf{x}_N)_{\text{pre}}\big] = \textsc{Elasto\_FMBEM}\big(k_p, k_s, p_l, u_i(\mathbf{x}_N)_{\text{pre}}, -p(\mathbf{x}_N)_{\text{pre}}n_i(\mathbf{x}_N), \dots\big)$

18: $\big[\big(\mathbf{L}_N\big)\rho_f\omega^2 n_i(\mathbf{x}_N)u_i(\mathbf{x}_N)_{\text{pre}}, \big(\mathbf{M}_N\big)p(\mathbf{x}_N)_{\text{pre}}\big] = \textsc{Helm\_FMBEM}\big(k, p_l, p(\mathbf{x}_N)_{\text{pre}}, \rho_f\omega^2 n_i(\mathbf{x}_N)u_i(\mathbf{x}_N)_{\text{pre}}, \dots\big)$ ▷ use final GMRES preconditioner solutions $u_i(\mathbf{x}_N)_{\text{pre}}$ and $p(\mathbf{x}_N)_{\text{pre}}$ in main FMBEM

19: $\boldsymbol{\xi}_{4N} = \Big[\big[\frac{\Omega}{\Psi}\big(-\mathbf{T}_{3N} + \frac{1}{2}\mathbf{I}_{3N}\big)u_i(\mathbf{x}_N)_{\text{pre}} - \Omega\big(\mathbf{U}_{3N}\big)[n_i(\mathbf{x}_N)p(\mathbf{x}_N)_{\text{pre}}] - \Omega \times u_i(\mathbf{y}_N)^{\text{inc}}\big]; \big[\frac{1}{\Psi}\big(\mathbf{L}_N + \alpha\frac{1}{2}\mathbf{I}_N\big)\rho_f\omega^2 n_i(\mathbf{x}_N)u_i(\mathbf{x}_N)_{\text{pre}} + \big(-\mathbf{M}_N + \frac{1}{2}\mathbf{I}_N\big) \times p(\mathbf{x}_N)_{\text{pre}} - \mathbf{p}^i\big]\Big]$ ▷ residual from main GMRES iteration

20: $[u_i(\mathbf{x}_N);\ p(\mathbf{x}_N)] = \text{fGMRES}(\boldsymbol{\xi}_{4N}) \quad \tilde{\text{its}} = \tilde{\text{its}} + 1$ ▷ update solution using fGMRES (see Ref. [152]) and update outer counter

21: **end while**

22: $u_i(\mathbf{x}_N) = \frac{1}{\Psi}u_i(\mathbf{x}_N)$ ▷ Scale final displacements by Ψ

23: **end function**

Alg. 5.1 is presented for the case of the incident field being a known pressure wave in the exterior fluid domain, as described by the discretised coupled matrix equation

in Eq. 5.5. The coupled system of BIEs in Eq. 5.3 may be conversely solved in terms of a known time–harmonic displacement $u_i^{\text{inc}}(\mathbf{y})$ in the solid domain which is similarly specified on the shared boundary surface. In this case the discretised matrix equation for the coupled system of BIEs can be written as

$$\begin{bmatrix} \frac{\Omega}{\Psi}\Big(-\mathbf{T}_{3N}+\frac{1}{2}\mathbf{I}_{3N}\Big) & \Omega\Big(-\mathbf{U}_{3N}\Big)n_i(\mathbf{x}_N) \\ \frac{1}{\Psi}\Big(\mathbf{L}_N+\alpha\frac{1}{2}\mathbf{I}_N\Big)\rho_f\omega^2 n_i(\mathbf{x}_N) & \Big(-\mathbf{M}_N+\frac{1}{2}\mathbf{I}_N\Big) \end{bmatrix} \begin{bmatrix} \Psi u_i(\mathbf{x}_N) \\ p(\mathbf{x}_N) \end{bmatrix} = \begin{bmatrix} \Omega u_i^{\text{inc}}(\mathbf{y}) \\ \mathbf{0}_N \end{bmatrix} \tag{5.9}$$

where it can be seen that only the known rhs is altered in the above coupled matrix equation as compared to Eq. 5.5. In Eq. 5.9 the scaling factor Ω now also appears on the rhs as the known incident field in the elastodynamic BIE is no longer zero, while the component of the known rhs vector corresponding to the Helmholtz BIE is set to zero as there is no incident field specified in the fluid domain.

5.3 Numerical Results

This section explores the performance of the dual FMBEM model for acoustic coupled FSI problems in terms of both its accuracy and the algorithmic complexity and memory requirements of the model. The dual FMBEM model has been written in MATLAB, implemented using double–precision floating point numbers and the code has not been explicitly compiled/multithreaded, however MATLAB may do this internally to parts of the code during execution. Numerical examples are presented for the scattering of plane compressional waves from solid elastic spheres which are compared to the analytic solutions, as well as to numerical results from a commercial FEM–BEM code called PAFEC, developed by PACSYS [27]. Dual FMBEM results are also presented for compressional plane wave scattering from a solid elastic cube, again with comparisons to the PAFEC FEM–BEM model. A subsection of the results also investigates the issue of so called Jones eigenfrequencies where both the dual FMBEM and FEM–BEM models break down for certain combinations of geometry and frequency. Finally, an 'application example' of the dual FMBEM model is presented for the sound scattering from a damping plate structure which was deployed as part of an experiment conducted from the *Aurora Australis* research vessel in 2010. The damping plate structure has a complicated three dimensional shape and provides a good example of the capabilities of the dual FMBEM model in treating both large problem sizes and complex objects. It

should also be mentioned in passing that perhaps a more relevant comparative numerical model to compare to the dual FMBEM results would be one of the more recently developed FEM–FMBEM type models which treat the fluid domain via a FMBEM formulation. The differences in the numerical results would then better indicate the relative merit of the dual FMBEM model in replacing the FEM part of the model with an FMBEM formulation. However such a model was not available to the author and so the PAFEC FEM–BEM model was instead used to provide the relevant numerical comparisons.

All numerical results from the FMBEM code have been calculated on a workstation computer equipped with an i7–3930K hexacore processor running at 3.2GHz, and 32GB of RAM. Additionally, both the separate Helmholtz and elastodynamic FMBEM algorithms used in the dual FMBEM for acoustic coupled FSI results again employ the translation stencils and memory reduction techniques discussed in the prior chapters to further minimise their computational cost and memory requirements.

5.3.1 Compressional Plane Wave Scattering from a Solid Elastic Sphere

This section presents numerical results from the dual FMBEM model for the case of a plane wave scattering from a solid elastic sphere, which has a known analytic solution [259]. The material properties of the elastic solid and fluid media are chosen to represent a steel sphere submerged in seawater and are summarised in Table 5.1.

Table 5.1: Material properties for the elastic solid and fluid media used for the modelling of plane wave scattering from a solid elastic sphere.

fluid sound speed	c_f	1524 m/s
fluid density	ρ_f	1000 kg/m^3
solid density	ρ_s	7669 kg/m^3
Young's modulus	E	2.07×10^{11} Pa
Poisson's ratio	ν	0.3

Figs. 5.1 and 5.2 show a comparison of the calculated dual FMBEM results and the corresponding analytic solution for the total surface pressure and total radial dis-

placement respectively for a unit radius solid elastic sphere ($a = 1$) isonofied by a $ka = 30$ compressional plane wave travelling in the direction [1 0 0]. A comparison of the real/imaginary components of the total surface pressure and radial displacement as a function of angle away from the direction of the incident field (such that 0° corresponds to the back–scatter direction) are shown in Figs. 5.3 and 5.4 respectively.

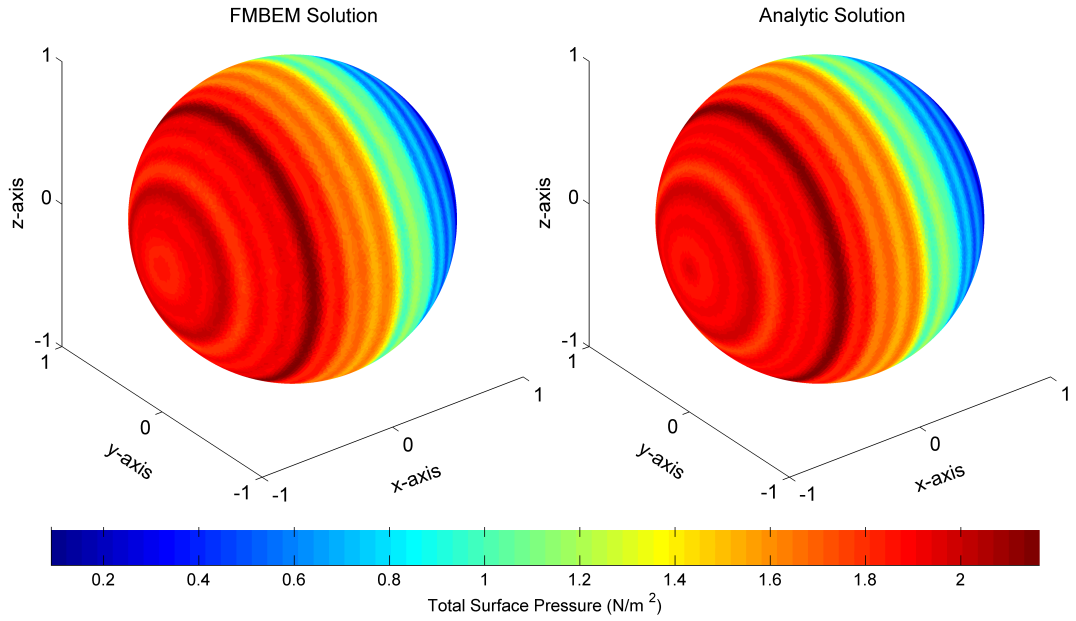

Figure 5.1: Dual FMBEM total surface pressure (left) versus the analytic solution (right) for a plane compressional wave scattering from a solid elastic sphere at $ka = 30$.

The relative error norm between the dual FMBEM and analytic solution was 1.32% for the total surface pressure and 10.60% for the total radial component of displacement. The boundary element mesh contained 40096 elements (160384 unknowns) giving approximately 15 elements per fluid wavelength, and about 30 elements per shear wavelength in the elastic solid. The dual FMBEM took approximately 5.93 hours to set–up and solve the problem and required 4.11GB of storage space. Comparatively, the full complex 160384×160384 coupled coefficient matrix in Eq. 5.5 would require 411.57GB of space to store. It can be seen from Figs. 5.3 and 5.4 that the dual FMBEM is in good agreement with the analytic solution, particularly for the total surface pressures, while the total radial component of displacement exhibits a somewhat larger error despite the higher numbers of elements per shear/compressional wavelengths in the elastic solid. Clearly the total surface fields for the acoustic coupled FSI problem have a more

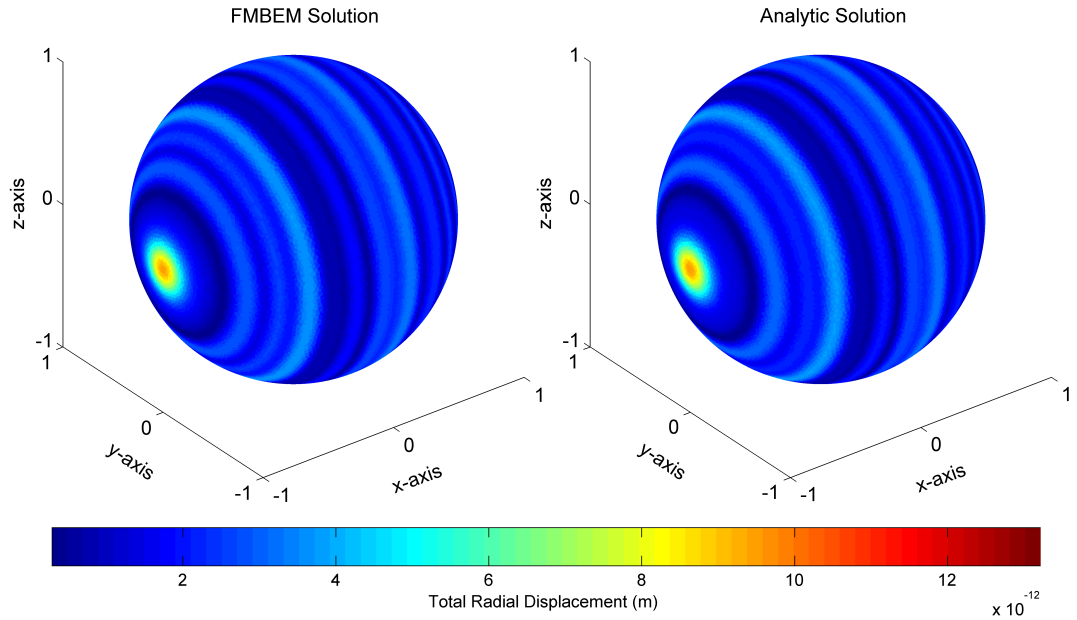

Figure 5.2: Dual FMBEM total radial displacement (left) versus the analytic solution (right) for a plane compressional wave scattering from a solid elastic sphere at $ka = 30$.

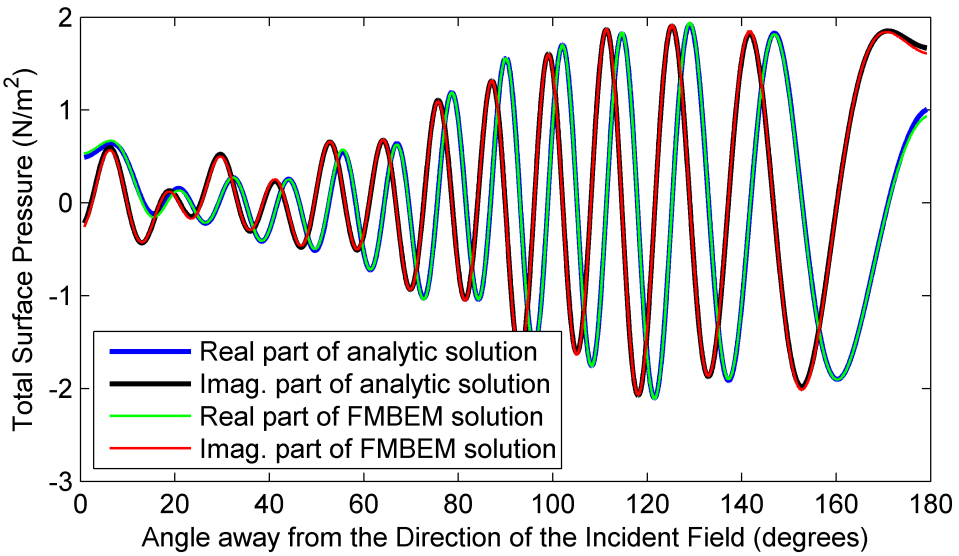

Figure 5.3: Dual FMBEM real/imaginary components of the total surface pressure versus the analytic solution for a plane compressional wave scattering from a solid elastic sphere at $ka = 30$.

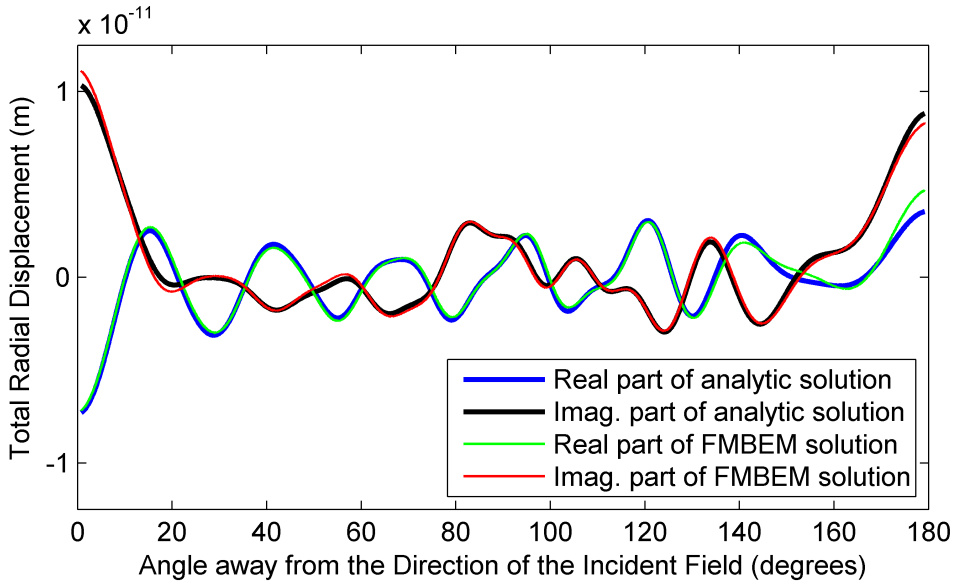

Figure 5.4: Dual FMBEM real/imaginary components of the total radial displacement versus the analytic solution for a plane compressional wave scattering from a solid elastic sphere at $ka = 30$.

complicated structure compared to similar results for the uncoupled FMBEM models presented in prior chapters (Sections 3.4.1 and 4.3.1). Comparatively the Helmholtz FMBEM pressure results presented in Section 3.4.1 exhibited an r.e. norm of 0.62%, being about half that of the present dual FMBEM pressure results. Similarly the r.e. norm for the radial displacement results of the equivalent elastodynamic FMBEM problem in Section 4.3.1 is about half that of the present displacement results, while the number of elements per shear wavelength in the present dual FMBEM results is *double* that used in the elastodynamic FMBEM results.

Analogous results to those shown in Figs. 5.3 and 5.4 are presented in Figs. 5.5 and 5.6 for the same problem at a higher wavenumber of $ka = 45$, corresponding to approximately 10 elements per wavelength in the fluid for the same 40096 element mesh. In this case the r.e. norm between the FMBEM and analytic solution was 4.8% for the total surface pressure and 32% for the total radial component of displacement, while the solution time and memory requirements increased (due to the larger truncation numbers required for the increased wavenumber) to 18.56 hours and 4.77GB respectively compared to the $ka = 30$ case. Again drawing comparisons to the separate FMBEM models presented in the previous chapters, the Helmholtz FMBEM exhibited

a similar 3–4 fold increase in the total surface pressure r.e. norm at a mesh discretisation of 10 elements per wavelength while a direct comparison with the elastodynamic FMBEM results is more difficult due to the additional errors attributed to the interior eigenfrequencies in those results. As a relative measure, both the pressure and radial displacement results from the dual FMBEM model increase by a factor of 3–4 upon reducing the relative discretisation from 15 to 10 elements per wavelength. In the case of the total pressure results an r.e. norm error of $\sim 5\%$ may be acceptable with a 10 element per wavelength discretisation, while an $\sim 30\%$ error in the radial component of displacement is likely to be too large under most circumstances. Thus a mesh discretisation of at least 15 elements per wavelength in the fluid domain would appear to be a good comprimise between the relative problem size and the solution error.

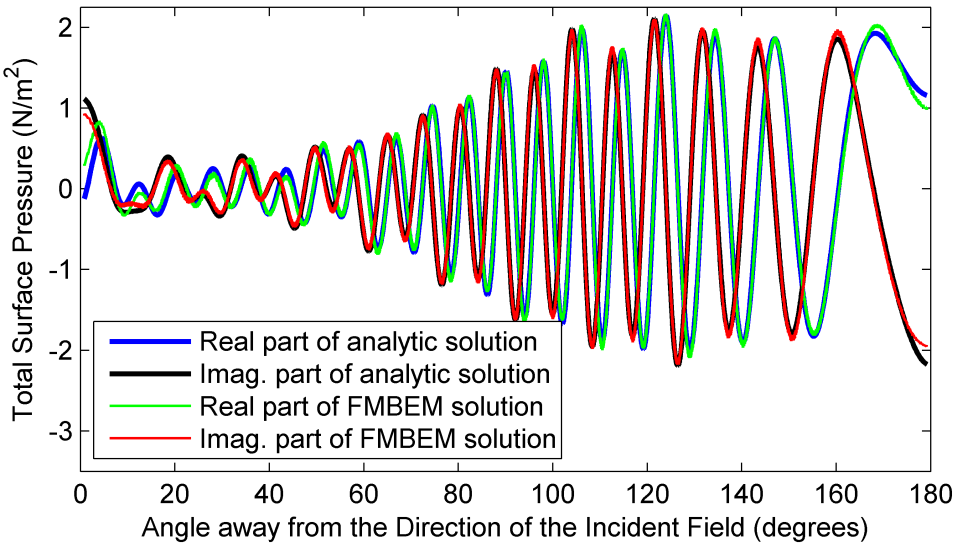

Figure 5.5: Dual FMBEM real/imaginary components of the total surface pressure versus the analytic solution for a plane compressional wave scattering from a solid elastic sphere at $ka = 45$.

Finally, a direct comparison between the numerical results from the dual FMBEM and a commercial FEM–BEM model (PAFEC) are presented for a similar problem involving plane compressional wave scattering from a solid elastic sphere. The mesh contains 5244 plane triangular boundary elements, used by both the dual FMBEM model and the BEM part of the FEM–BEM model, while the solid elastic sphere was modelled with 84567 linear tetrahedral finite elements for the FEM–BEM model. The

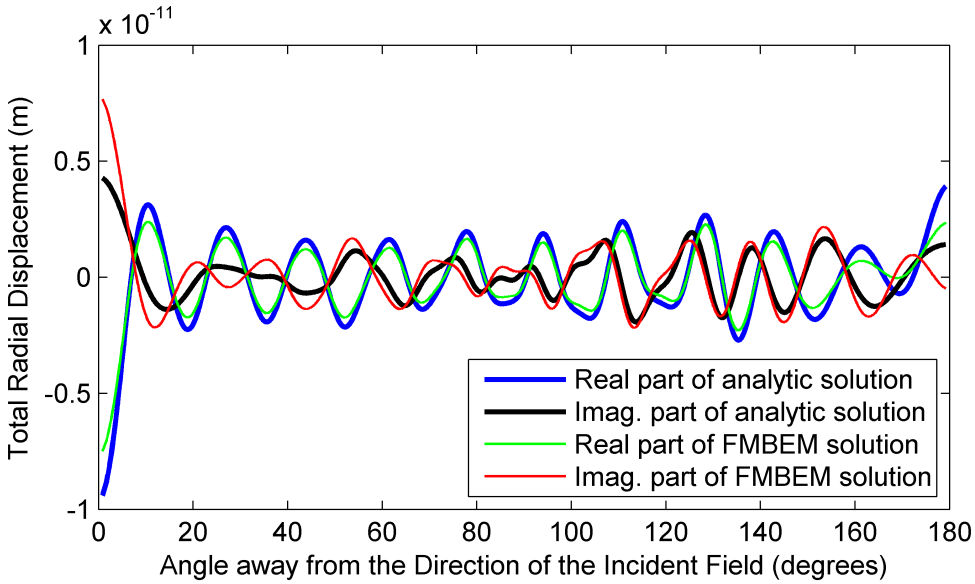

Figure 5.6: Dual FMBEM real/imaginary components of the total radial displacement versus the analytic solution for a plane compressional wave scattering from a solid elastic sphere at $ka = 45$.

material properties used for the fluid and solid domains are specified in Table 5.1 and the incident plane wave is specified in the fluid with a dimensionless wavenumber of $ka = 6.5$, corresponding to 35+ elements per wavelength in the fluid. The dual FMBEM model solved the problem in 7.16 minutes and required 905MB of storage space while the PAFEC FEM–BEM model took 11.65 hours to solve and required 8.53GB of storage space. Of course the PAFEC FEM–BEM model provides a complete solution of the interior displacement field at the finite element nodal points, while the dual FMBEM model only solves for the surface fields. The interior displacement field may be evaluated by the dual FMBEM in a post–processing step, requiring an additional calculation time proportional to the time required to set up the problem (i.e. to build the octree structure and near field integrals) and apply a single FMM–accelerated matrix–vector product, to evaluate the field at the interior points. In terms of solution accuracies, the dual FMBEM solution yielded r.e. norms of 0.39% and 1.90% for the total surface pressure and total radial displacement respectively, while the FEM–BEM model yielded r.e. norms of 0.39% and 4.40% respectively. Plots of the absolute value of the total surface pressure and radial component of total displacement for both the dual FMBEM and PAFEC FEM–BEM models are shown in Fig. 5.7,

along with the corresponding analytic solution.

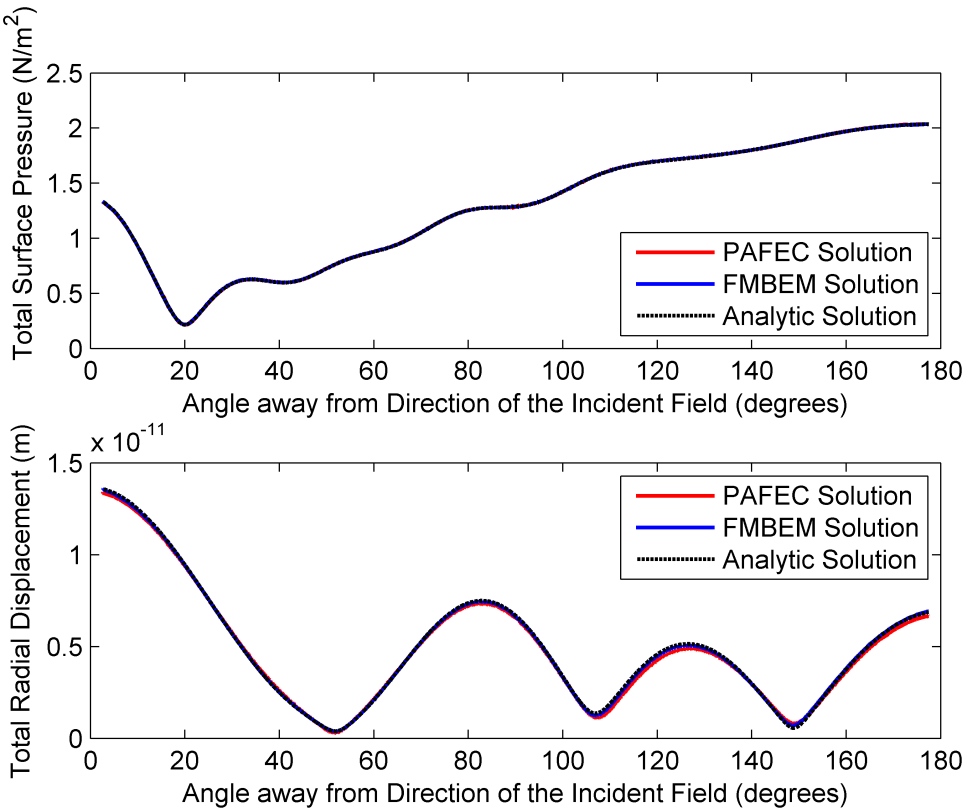

Figure 5.7: Absolute value of the total surface pressure (top) and total radial displacement (bottom) for a compressional plane wave scattering from a solid elastic sphere at $ka = 6.5$ for the dual FMBEM and PAFEC FEM–BEM models, compared to the analytic solution.

To allow for the direct comparison of the PAFEC displacement results with those of the dual FMBEM, the nodal solution values of the surface finite elements were interpolated to the centre of each corresponding boundary element, and so it is expected that some small additional error is introduced into the PAFEC displacement results from this process. Nonetheless, the dual FMBEM model is seen to yield comparable solution accuracies to the FEM–BEM model, while the total solution time and memory requirements of the dual FMBEM are substantially reduced.

5.3.2 Compressional Plane Wave Scattering from a Solid Elastic Cube

To demonstrate the dual FMBEM model for a simple non–spherical geometry, a numerical example is presented for the problem of a cube with a side length of 1m scattering a compressional plane wave specified with a shear wavenumber (in the elastic solid) of $k_s = 6$ and travelling in the direction $\frac{1}{\sqrt{3}}[1\ 1\ 1]$. The fluid and elastic solid material properties for the problem are specified in Table 5.1. The cube was modelled with 2696 plane triangular boundary elements, used by both the dual FMBEM model and the BEM part of the FEM–BEM model, while the interior elastic solid domain was modelled with 19705 linear tetrahedral finite elements for the FEM–BEM model. The corresponding fluid wavenumber calculated from the material properties is $k \approx 12.68$, yielding approximately 18–20 elements per fluid wavelength. Plots of the absolute value of the total surface pressure and total surface displacement for both the dual FMBEM and PAFEC FEM–BEM models are shown in Figs. 5.8 and 5.9 respectively.

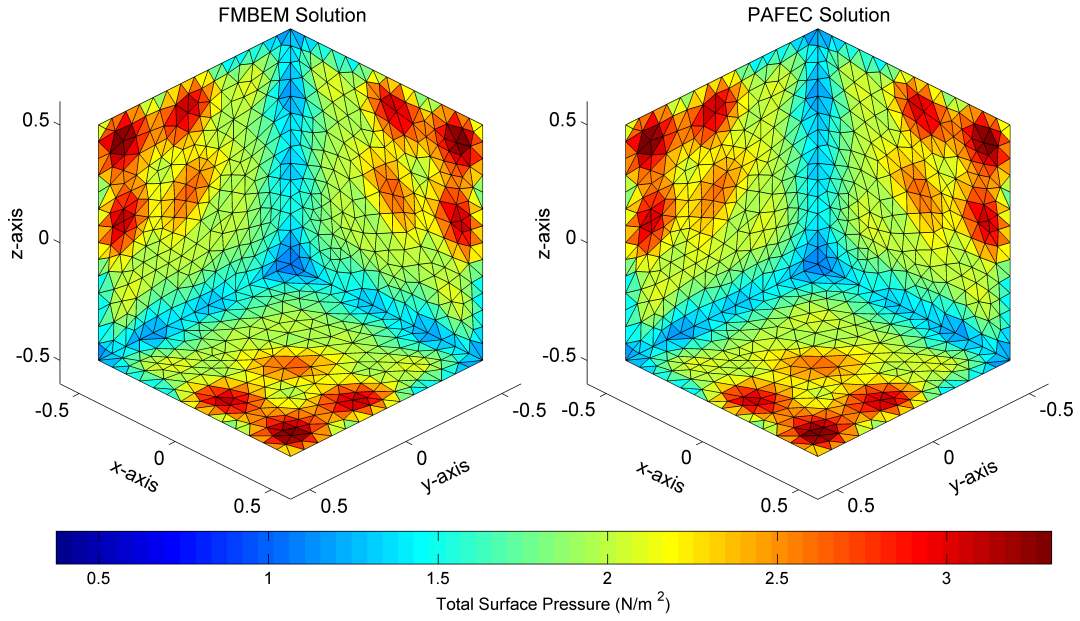

Figure 5.8: Absolute value of the total surface pressure for a compressional plane wave scattering from a solid elastic unit–length cube at $k_s = 6$ for the dual FMBEM model (left) and PAFEC FEM–BEM model (right). The cube model is shown orientated along a diagonal axis such that the incident wave is directed out of the page.

The dual FMBEM model solved the problem in 7.48 minutes and required 253MB of storage space while the PAFEC FEM–BEM model took 32.02 minutes to solve and

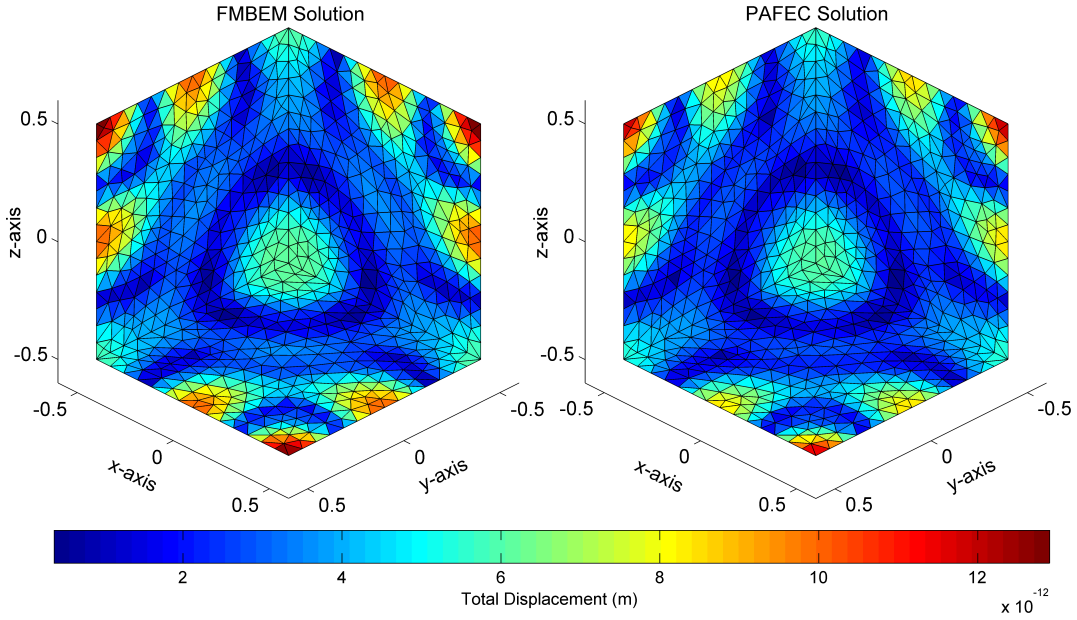

Figure 5.9: Absolute value of the total surface displacement for a compressional plane wave scattering from a solid elastic unit–length cube at $k_s = 6$ for the dual FMBEM model (left) and PAFEC FEM–BEM model (right). The cube model is shown orientated along a diagonal axis such that the incident wave is directed out of the page.

required 1.21GB of storage space. The r.e. norms between the solutions of the dual FMBEM and FEM–BEM models were 3.12% for the total surface pressure and 22.38% for the total surface displacement respectively. The dual FMBEM and commerical FEM–BEM models are in good agreement, particularly for the total surface pressures, despite the complex patterns observed in the results.

The coupling method used in all of the presented results from the PAFEC FEM–BEM model is a 'generalised fluid structure coupling' (GFSC) technique which allows coupling between the constant pressure quadratic boundary elements and the linear tetrahedral finite elements available in the PAFEC software. As the elements in the boundary meshes are flat triangular elements, and because a one–to–one coupling is used between the finite and boundary elements, the GFSC generally provides good results and is substantially faster then using a direct coupling method which requires the use of quadratic finite elements. Interestingly, the use of a direct coupling method in the FEM-BEM model for the present example yielded reduced r.e. norms in both the total surface pressure (2.77%) and total surface displacement (15.12%) compared to

the dual FMBEM results, suggesting a convergence of the FEM–BEM results towards the dual FMBEM results. Comparisons between the GFSC and direct coupling techniques for the sphere scattering problem similarly showed better agreement between the FEM–BEM results and the analytic solution when using the fully coupled model and quadratic finite elements. Of course the more accurate results yielded by the full coupling technique come at the cost of a substantially increased computational time: the same cube scattering problem presented here required 11.29 hours solution time and 5.97GB of storage space when utilising the direct coupling technique.

5.3.3 Eigenfrequencies

It was observed in the dual BEM work of Goswami et al. [222] that the typical coupling procedure between surface unknowns via Eqs. 5.1 and 5.2 is only enforced in the direction normal to the local coupling point on the surface. Thus at certain frequencies the local tangential components of the surface stress and displacement in the elastic solid may be non–zero while the corresponding normal components may still satisfy the coupling BCs with the fluid domain. Such situations are likely to occur for surfaces corresponding to general smooth bodies of revolution at frequencies corresponding to the torsional modal frequencies of the object. Hence the surface of the elastic solid domain may tangentially 'slide' relative to the coincident surface of the fluid domain. For the particular case of an elastic solid sphere the eigenfrequencies with non–unique solutions corresponding to the free–vibration torsional modes are named after Jones [260] and have been tabulated as a function of the dimensionless shear wavenumber $k_s a$ [170, 261].

Fig. 5.10 shows a plot of the solution error of the total surface pressure and total radial displacement compared to the analytic solution as a function of the shear wavenumber $k_s a$ for a plane compressional wave scattering from a solid elastic sphere, with the pertinent material properties summarised in Table 5.1. The error results are presented for both the dual FMBEM model (continuous lines) and, for certain frequency ranges of interest, the PAFEC FEM–BEM model (lines with markers). The vertical dashed lines in Fig. 5.10 denote the free–vibration torsional modes of the solid elastic sphere from 1.) the analytic solution (black), and 2.) a numerical modal analysis of the FEM mesh for the solid elastic sphere (magenta), while the in vacuo radial modes from the analytic solution are indicated by the cyan vertical dashed lines.

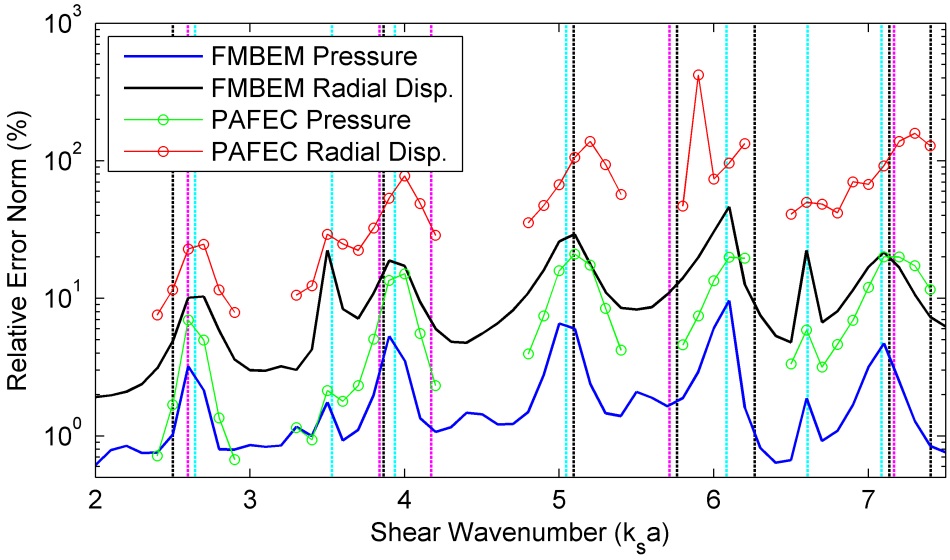

Figure 5.10: Solution error of the dual FMBEM and FEM–BEM total surface pressure and total radial displacement compared to the analytic solution as a function of shear wavenumber $k_s a$ for a plane compressional wave scattering from a solid elastic sphere. The vertical dashed lines indicate the free–vibration torsional modes from both the analytic solution (black) and a numerical modal analysis (magenta), while the cyan vertical dashed lines indicate the in vacuo radial modes from the analytic solution.

It is clear from Fig. 5.10 that both the dual FMBEM model and the conventional FEM–BEM model suffer from poorer solution accuracy near the eigenfrequencies of the torsional and/or radial modes of the solid elastic sphere. Of course for the acoustic coupled FSI results presented here the radial modes will be slightly downshifted in frequency compared to the analytic in vacuo modes, but this shift will be relatively small. Error peaks are only observed near the torsional modes which lie near radial modal frequencies, while the isolated torsional modes do not show an increase in solution error in either model. Conversely some of the smaller sharper error peaks appear to directly correspond to radial modes at wavenumbers which lie away from any torsional modes (in particular at $k_s a \approx 3.5$ and $k_s a \approx 6.5$). Numerical results from the dual FMBEM model were also calculated very close to two of the torsional modal frequencies ($k_s a \approx 2.5011$ and $k_s a \approx 6.2658$), where it was observed that the numerical error did not substantially increase compared to the results presented in Fig. 5.10 at nearby wavenumbers. This suggests that either the wavenumber must be very close to the tor-

sional modal frequencies to show an increase in error (compared to the much broader error peaks seen near the radial modal frequencies), or that the use of even a moderate element discretisation is enough to negate the sliding effect of the fluid/solid mesh surfaces at the torsional modal frequencies. Goswami et al. [222] similarly concluded that for the particular case of the solid elastic sphere, refinement of the mesh discretisation improved the numerical results near the Jones eigenfrequencies. The present analysis would appear to indicate that the eigenfrequencies for the radial modes pose more of an issue than the Jones eigenfrequencies in both the dual FMBEM and FEM–BEM models.

Finally it should be noted that the use of the elastodynamic FMBEM for modelling the interior domain in the dual FMBEM model does not appear to introduce any additional error into the numerical results near the eigenfrequencies of the problem. In all cases the dual FMBEM model is able to achieve comparable or better solution accuracies compared to the FEM–BEM model near the eigenfrequencies of the coupled problem for the similar BEM element discretisations (with the total number of elements within 5% of one another) used in both models for the $k_s a \leq 6.2$ results. The more accurate results from the dual FMBEM model thus strongly suggest that the elastodynamic FMBEM is stable at these interior frequencies, as should be the case when using the (unstabilised) BEM formulations for interior problems. This is in contrast to the very large errors observed in the numerical results obtained in Chapter 4 when the elastodynamic FMBEM was used to solve exterior problems near the eigenefrequencies of the adjoint interior problem.

5.3.4 Dual FMBEM Algorithmic Performance

This section presents results for the dual FMBEM model which indicate the performance of the model in terms of its algorithmic complexity and memory requirements. Comparisons of the algorithmic complexity, computational accuracy and memory requirements of the dual FMBEM code are presented for the problem of plane compressional wave scattering from a solid elastic sphere and are compared to the analytic solution. Two scenarios are presented: the first investigates how the algorithm scales as a function of the number of unknowns with a fixed wavenumber and the second case indicates the performance when using the maximum wavenumber for each mesh size (assuming a fixed number of elements per wavelength) as a function of the number of

unknowns. Both scenarios use the material properties summarised in Table 5.1, except for the value of Poisson's ratio, which was instead specified as $\nu = 0.45$ for the first scenario to shift the shear wavenumber away from both a torsional and radial modal frequency for the free–vibration elastic sphere that would otherwise occur near the specified wavenumber. The standard deviations in the least–squares data fits for the algorithmic power of N scaling are also shown, as was done for similar results presented in the previous chapters.

Plots of the solution time, memory usage and solution error versus the number of unknowns, N, for a fixed fluid wavenumber of $ka = 13$ are shown in Figs. 5.11, 5.12 and 5.13 respectively. Additionally, Fig. 5.14 shows the calculation time for a single matrix-vector product for the dual FMBEM as a function of the number of unknowns (for a similar fixed fluid wavenumber).

Fig. 5.11 shows that the least squares fit of the total solution time for the dual FMBEM is approximately proportional to $N^{1.1}$ for this scenario. Comparatively, both the Helmholtz and elastodynamic FMBEMs showed a total solution time proportional to or less than N for a similar problem of an increasing number of unknowns for a fixed wavenumber. The increase in the N–power of the algorithmic complexity data fit observed here for the dual FMBEM model is likely due to the influence of the large 'step' in the solution time that occurs above 2×10^5 unknowns, which corresponds to the introduction of a new octree level. Certainly the lower limit of the standard deviation in the power of N data fit would yield a proportionality closer to N. The memory requirements of the dual FMBEM are shown in Fig. 5.12 to scale with a less than N proportionality, as was the case for the separate Helmholtz and elastodynamic FMBEMs.

Fig. 5.13 shows the solution error of the dual FMBEM compared to the analytic solution for both the total surface pressure (top) and the total radial component of displacement (bottom) versus the number of unknowns. The r.e. norm results are shown here for two Poisson's ratios: $\nu = 0.3$, which for the fixed fluid wavenumber of $ka = 13$ corresponds to a shear wavenumber which lies in close proximity to both a free–vibration torsional mode (Jones eigenfrequency) and a radial mode of the elastic sphere, and $\nu = 0.45$, which for the same fluid wavenumber gives a corresponding shear wavenumber which lies away from the two modes. A general reduction in the solution error of both the total pressure and total radial displacement results is observed in the

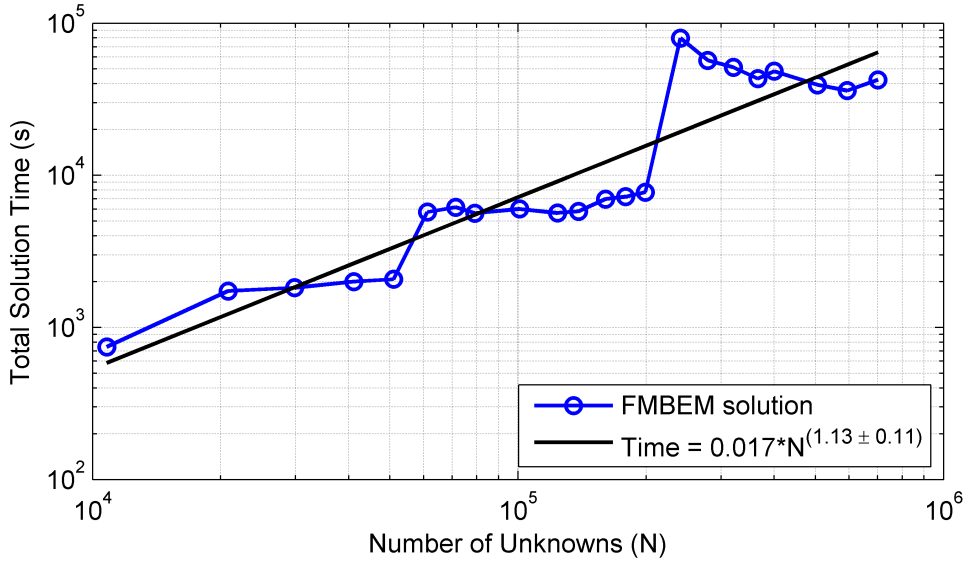

Figure 5.11: Solution time versus the number of unknowns for the dual FMBEM with a fixed wavenumber. The FMBEM total solution time is approximately proportional to $N^{1.1}$.

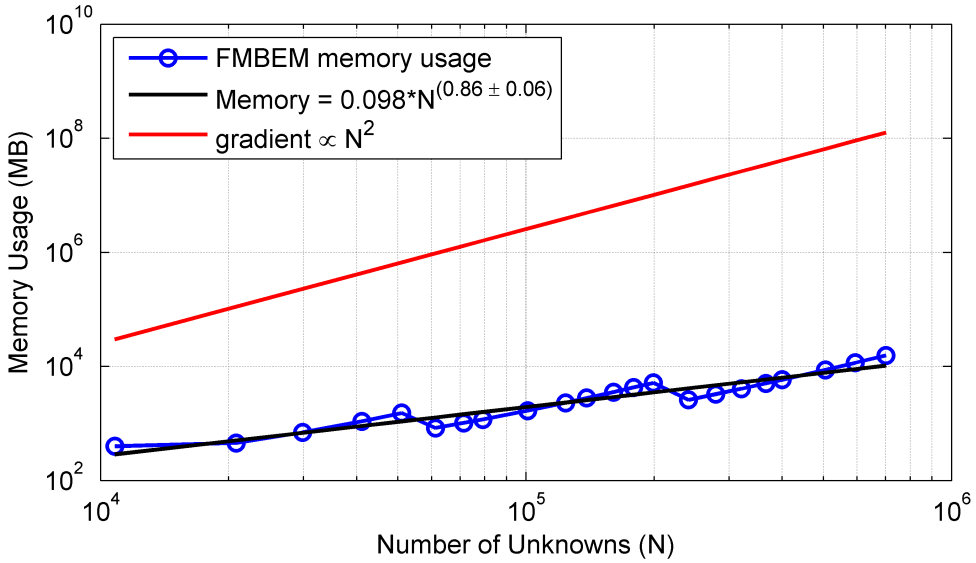

Figure 5.12: Memory usage versus the number of unknowns for the dual FMBEM with a fixed wavenumber. The memory usage (in MB) shows a less than N proportionality.

figure, again with jumps in the errors ($1-3\%$ in the pressures and $3-7\%$ in the radial displacements) for the meshes which introduce new octree levels to the structure. In

addition, the $\nu = 0.3$ results in Fig. 5.13 indicate that as the number of elements per wavelength increases the dual FMBEM solution near the modal frequencies converges. Again, due to the close proximity of both types of mode it is unclear if either or both modes contribute to the higher errors observed in the dual FMBEM solution at $\nu = 0.3$. In either case, increasing the mesh resolution provides more accurate results.

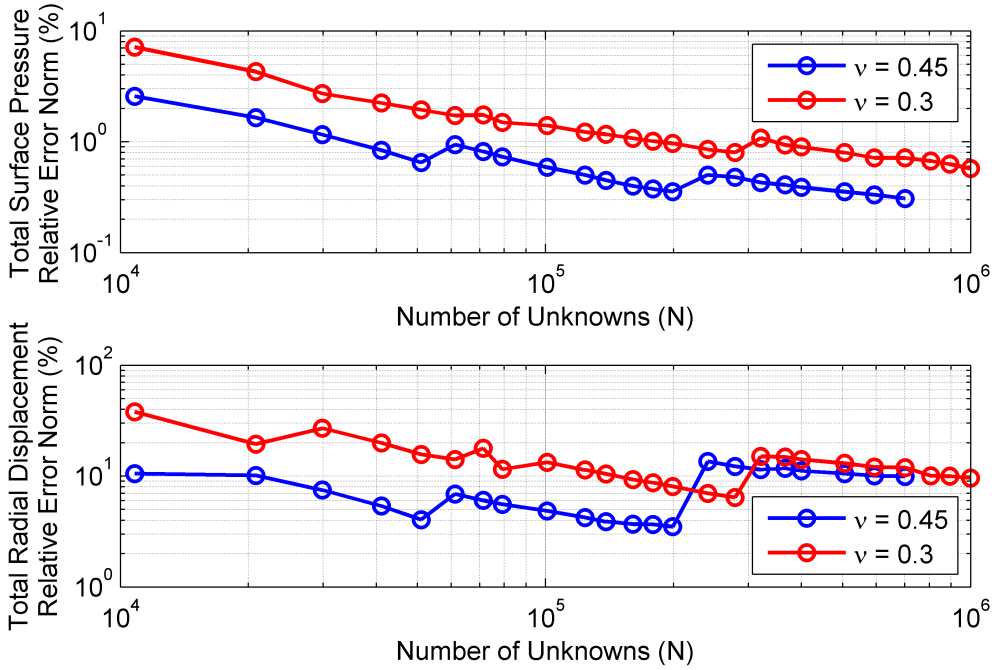

Figure 5.13: Solution error for the total surface pressure (top) and total radial displacement (bottom) versus the number of unknowns for the dual FMBEM with a fixed wavenumber for two Poisson's ratios.

Finally, Fig. 5.14 shows that the calculation time for a single matrix-vector product of the dual FMBEM has a less than N algorithmic scaling, compared to the N^2 operations that would be required for the direct matrix–vector product. The algorithmic scaling here is obviously lower than that in Fig 5.11, which indicates the algorithmic scaling of the total solution time (problem set-up, iterative solution and so on).

Analogous plots to those presented above for the second algorithmic complexity scenario involving an approximately constant number of elements per wavelength for an increasing number of unknowns are shown in Figs. 5.15, 5.16, 5.17 and 5.18. The algorithmic complexity results for this scenario are presented for three 'element per

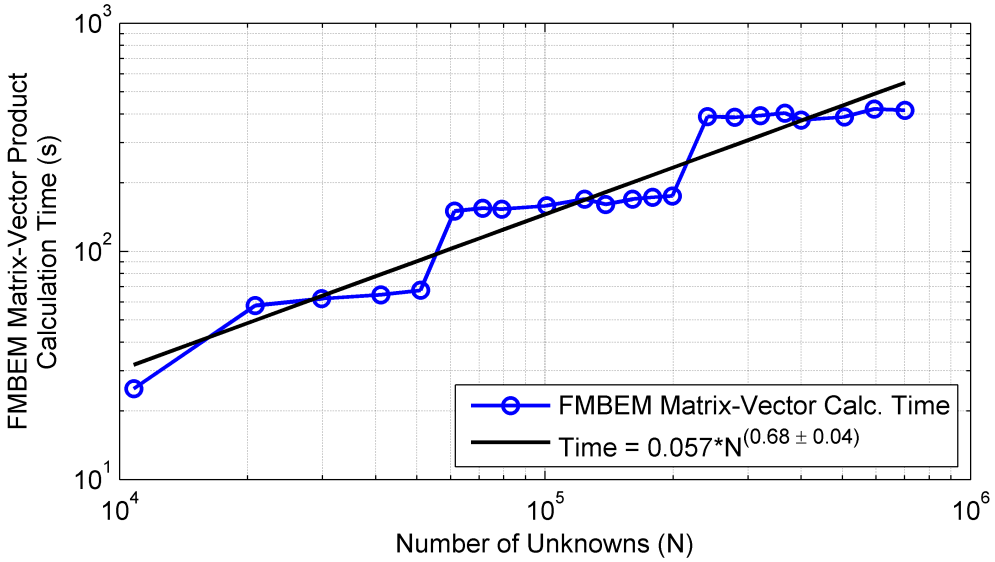

Figure 5.14: Calculation time for a single matrix-vector product for the dual FMBEM versus the number of unknowns for a fixed wavenumber.

wavelength' discretisations, corresponding to approximately 10, 15 and 20 elements per fluid wavelength (measured at the equator of the sphere) with at most a ±3 element/wavelength variation for the particular wavenumbers and element meshes available. The total solution time versus the number of unknowns for the three element discretisations shown in Fig. 5.15 indicate that the algorithmic scaling of the total solution time reduces as the number of elements per wavelength increases: scaling as approximately $N^{1.8}$, $N^{1.7}$ and $N^{1.5}$ for 10, 15 and 20 elements per fluid wavelength respectively. The inverse relationship between the power of N of the least–squares data fits and the total solution time is partly due to the reduction in the total number of inner GMRES iterations required for convergence as the number of elements per wavelength increases, and partly due to the algorithmic complexity of the FMBEM accelerated matrix–vector products being inversely related to the number of elements per wavelength (see Fig. 5.18). Comparatively, the algorithmic complexity of the dual FMBEM model for this scenario shows a similar N–proportionality when using 20 elements per fluid wavelength as compared to the 10 elements per wavelength results for the Helmholtz FMBEM, while the elastodynamic FMBEM results exhibited a much larger algorithmic complexity due to the coarser element discretisation used in those

results requiring a large number of inner GMRES iterations to converge. The memory requirements of the dual FMBEM are similarly observed in Fig. 5.16 to scale with a less than N proportionality for this scenario, as was the case for the separate Helmholtz and elastodynamic FMBEMs.

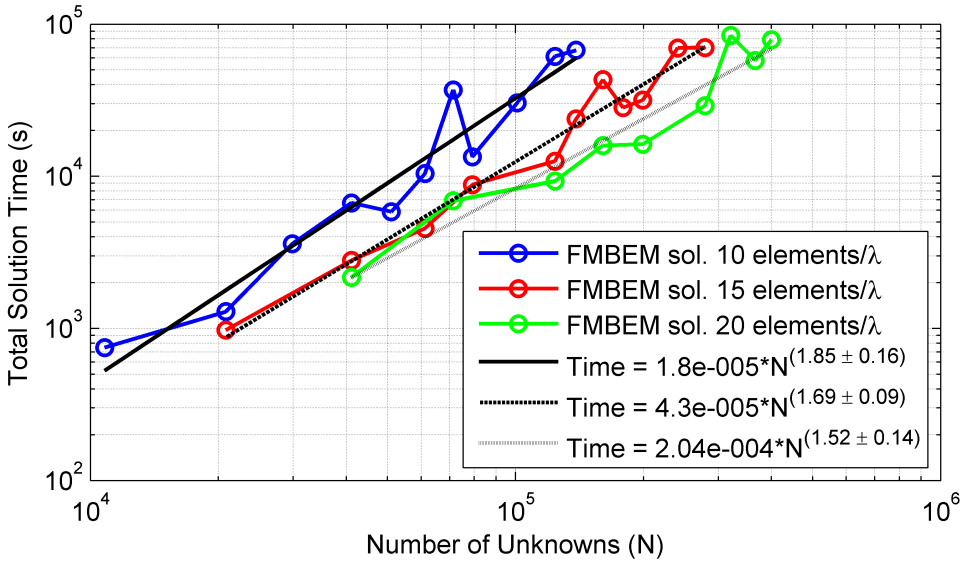

Figure 5.15: Solution time versus the number of unknowns for the dual FMBEM with a fixed number of elements per fluid wavelength. The FMBEM total solution time is approximately proportional to $N^{1.8}$, $N^{1.7}$ and $N^{1.5}$ for 10, 15 and 20 elements per fluid wavelength respectively.

The solution errors for the total surface pressure and total radial displacement under the three fixed element per wavelength discretisations are shown in Fig. 5.17. As expected the r.e. norm errors remain approximately constant for the approximately constant element per wavelength discretisations. Again there is some variation in the exact number of elements per wavelength (± 3 elements per wavelength) used in the various solutions and this is reflected in the obtained r.e. norms. Additionally the variation in the wavenumber for this scenario means that certain solutions were evaluated near the free–vibration torsional modal frequencies of the elastic sphere — particularly for the second largest wavenumber in both the 10 and 15 element per wavelength discretisations — and thus an increase in the solution error is observed near this frequency. The average errors for the 15 elements per fluid wavelength discretisation in Fig. 5.17 appear to be somewhat larger than those observed in the results presented in Figs.

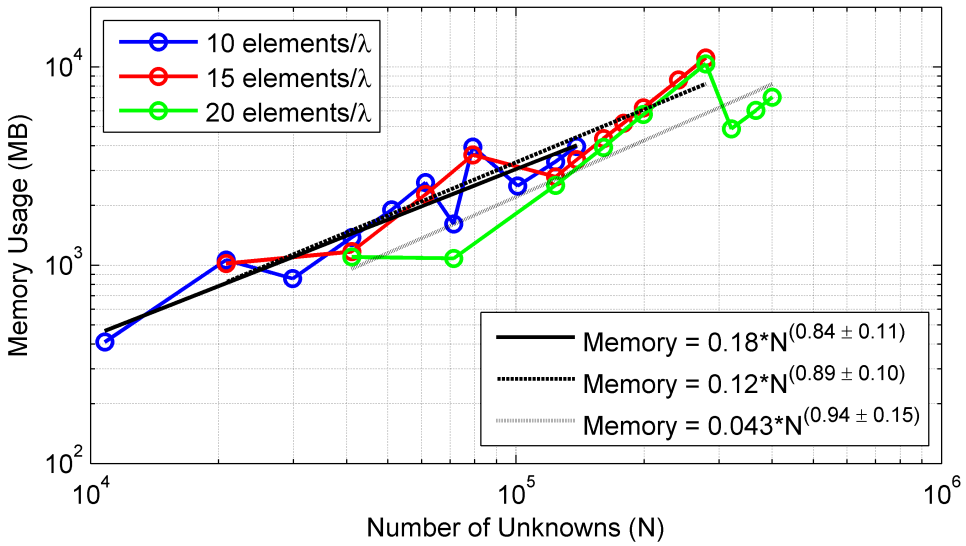

Figure 5.16: Memory usage versus the number of unknowns for the dual FMBEM with a fixed number of elements per fluid wavelength. The storage requirements in MB of memory is proportional to powers of N less than one for all three element discretisations.

5.3 and 5.4 which used an approximately similar element per wavelength discretisation, while the average errors for the 10 elements per fluid wavelength results are comparable to those observed in the results presented in Figs. 5.3 and 5.4. The r.e. norm results in Fig. 5.17 suggest that a 20 element per fluid wavelength discretisation should yield errors of $2-3\%$ in the pressures and $15-20\%$ in the radial displacements, with errors in the Cartesian displacement components being equal to or less than this.

In comparison to the other dual BEM formulations for acoustic coupled FSI problems, Seybert et al. [220] reported errors in the range of $1.5-9\%$ in the total pressures on the surface of a hollow steel sphere with a uniform internal pressure submerged in seawater when using between roughly 1 and 6 quadratic elements per fluid wavelength. No other papers on the dual BEM formulation (in particular those of Goswami et al. [221, 222] and Chen et al. [230, 231]) provide numerical results which indicate the solution error as a function of the element discretisation. Isakari [182] provides some numerical results for their dual FMBEM model for periodic structures: L^2 relative error norms of 2% in the pressures and 1.1% in the displacements are achieved for the numerical example of a plane wave scattering from a continuous slab of PMMA plastic (i.e. with an arbitrary periodicity) immersed in water, when using 20 constant elements per

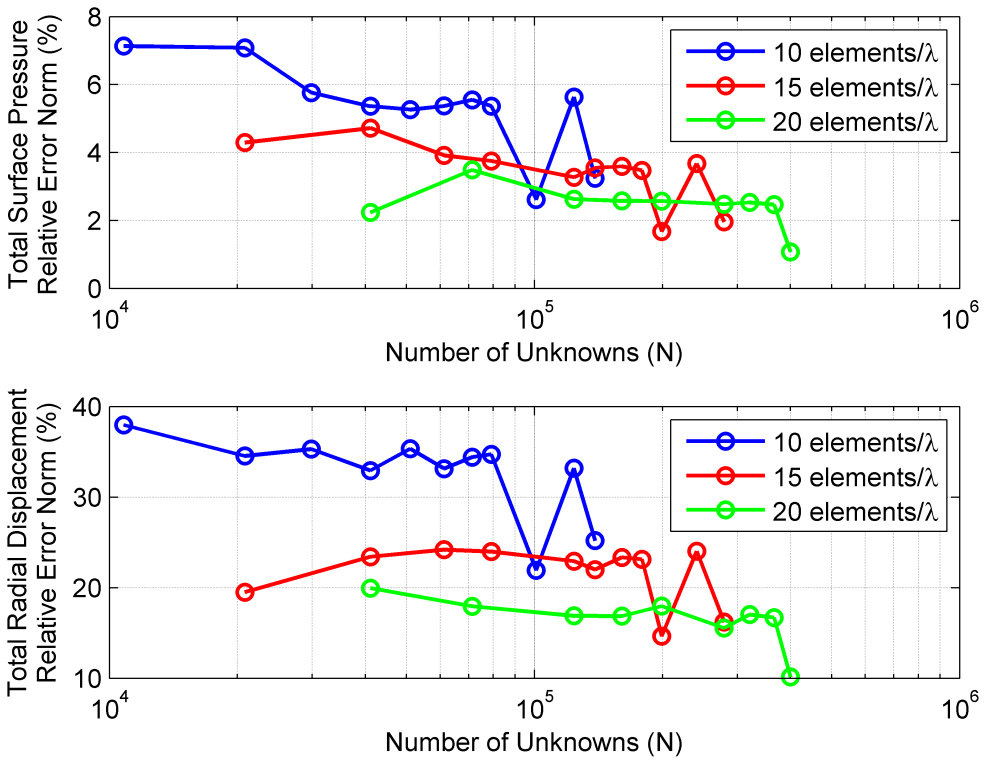

Figure 5.17: Solution error for the total surface pressure (top) and total radial displacement (bottom) versus the number of unknowns for the dual FMBEM with a fixed number of elements per fluid wavelength.

fluid wavelength. Isakari also provides numerical results for the scattering by periodic elastic spheres in water, where the maximum relative error in the sum of scattered energy to incident energy was reported as 3.8% [182]. However no data is presented on the pressure/displacement results in the later case and it is not clear as to what element per wavelength discretisation was employed. Thus the present dual FMBEM mdoel would appear to achieve a comparable solution accuracy in the pressures when using a similar number of elements per wavelength, as comapred to Isakari's dual FMBEM model for periodic structures. Conversely, the displacement results of the present dual FMBEM would appear to be an order of magnitude worse. This is likey due to the use of steel as the elastic solid material in the present results, while the material properites of the PMMA plastic used by Isakari [182] are quite similar to the exterior fluid and so displacement results which have an approximately similar errror to the pressures would

be expected. Unfortunately no other references cited herein provide any results for the coupled FSI displacements whatsoever, and so further comparison of the present dual FMBEM model to the other dual BEM formulations is not possible. To conclude, it is reiterated that the comparison between the present dual FMBEM and the FEM–BEM results presented in Section. 5.3.1 indicated that similar solution errors were achieved by the models for both the coupled pressures and displacements when using a similar element per wavelength discretisation.

Lastly Fig. 5.18 shows that the calculation time for a single matrix-vector product of the dual FMBEM scales between $N^{1.3}$ and $N^{1.0}$ for 10–20 elements per fluid wavelength, which again represents a substantially lower computational cost than the N^2 proportionality of the direct matrix–vector product. As previously mentioned, Fig. 5.18 indicates that the algorithmic complexity of the matrix-vector product of the dual FMBEM is inversely related to the number of elements per wavelength. This is due to the dominant computational cost in the FMM being the application of the multipole translations to the level–dependent truncated multipole expansions, with the translation cost being directly proportional to the truncation length. The truncation lengths of the multipole expansions are in turn directly related to the wavenumber of the problem (see Eq. 2.17). Thus if the number of elements is increased for the same mesh geometry and wavenumber, the only increase in the computational cost will be in the initial step of the upward pass when building the more numerous source expansions, and in the final summation of the downward pass when evaluating the field at the larger set of receiver points. The number of multipole translations that must be applied in the intervening steps is not altered as the individual source expansions on the lowest octree level are still combined into a single multipole expansion per occupied octree box (i.e. the number of applied translations does not change) and so the algorithmic cost per element/unknown reduces.

The algorithmic complexity of the dual FMBEM model in the low frequency regime is close to the order N theoretical algorithmic complexity estimate of Gumerov and Duraiswami [42] for their scenario of a surface distribution of sources and receivers on a 'simple surface'. The slightly higher algorithmic complexity of $N^{1.1}$ observed in the present results is likely due to the large jump in solution time observed at the larger problem sizes and corresponds to the introduction of a new octree level. A comparison of the plots of the total solution time and the calculation time for a single matrix-vector

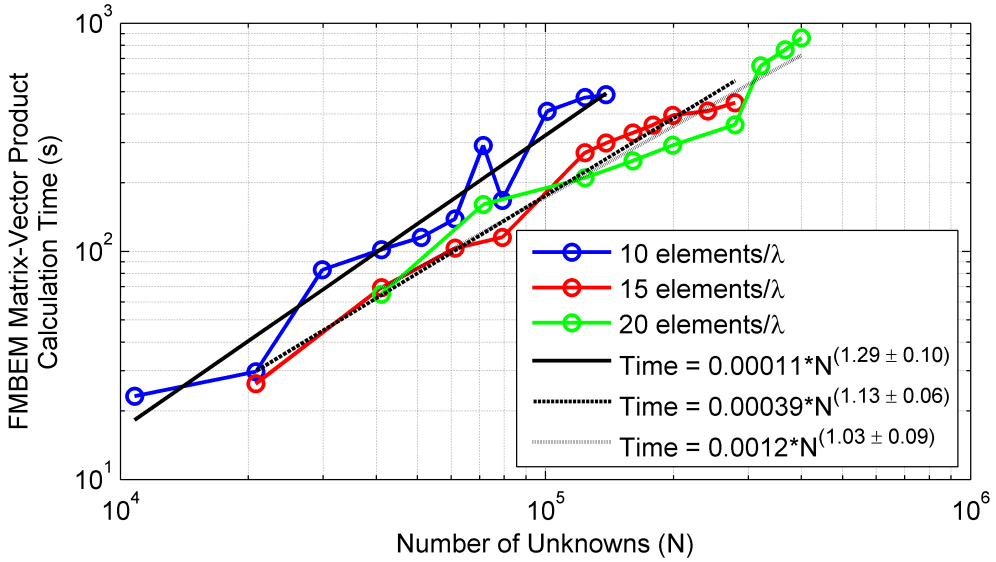

Figure 5.18: Calculation time for a single matrix-vector product for the dual FMBEM versus the number of unknowns for a fixed number of elements per fluid wavelength.

product in the low frequency scenario (shown in Figs. 5.11 and 5.14) suggests that the proportionally larger jump in solution time for the larger problem sizes is in fact due to an increased number of GMRES iterations being required for the solution, as no similar increase occurs in the calculation times for the single matrix-vector products. It was previously observed in the algorithmic complexity results presented in Chapter 4 for the elastodynamic FMBEM model that a reduction in the convergence rate had the effect of increasing the observed algorithmic complexity. Such variations in the convergence rate are not accounted for in the theoretical algorithmic complexity models.

The algorithmic complexity of the dual FMBEM model in the high frequency limit (where the mesh discretisation/number of unknowns is directly related to the wavenumber) shows a scaling proportional to $N^{1.5}$ when using a discretisation of 20 elements per fluid wavelength. This is in good agreement with Gumerov and Duraiswami's theoretical estimate for the BEM when using $O(p^3)$ translation methods [42]. Conversely the coarser element per wavelength discretisations exhibited somewhat higher algorithmic complexities, which would appear to be a result of both the increased computational cost per matrix–vector product at the lower element discretisations (see Fig. 5.18) and the increased number of iterations required for convergence. Such variations in

the algorithmic complexity of the model with the specified element per wavelength discretisation are clearly not accounted for by the theoretical model.

To conclude, the algorithmic complexity results presented in this section indicate that the dual FMBEM model performs close to the theoretical predictions in both the low frequency regime and at the upper frequency limit of the low frequency FMBEM model, while the providing reasonable solution errors when using 15–20 elements per fluid wavelength. Furthermore, comparisons between the dual FMBEM and PAFEC FEM–BEM models indicate that the dual FMBEM model is able to achieve comparable numerical errors for similar element discretisations, while the total calculation time and memory requirements are substantially reduced.

5.3.5 Acoustic Coupled FSI Scattering from a Damping Plate

As an example of the application of the dual FMBEM model for analysing acoustic coupled FSI problems, numerical results are presented for the scattering of sound from a damping plate structure, a photo of which is shown in Fig. 5.19. The structure was used as a stability and weighting platform to deploy a hydrophone (the black cylinder in Fig. 5.19) in an experiment conducted from the *Aurora Australis* research vessel in 2010 to investigate the effect of ice cover and ship noise in the communication between an autonomous underwater vehicle and its deployment vessel. FMBEM modelling was conducted as part of that work to determine the relative effect of near field sound scattering from the damping plate on the received field at the hydrophone location to provide error bounds in the experimental data [262]. Comparisons between the dual FMBEM and PAFEC FEM–BEM models for the complex three dimensional structure of the damping plate demonstrate the capabilities of the dual FMBEM model.

The damping plate structure, shown in Fig. 5.19 lying sideways on the deck of the deployment vessel, principally consists of a very thick open ended cylindrical tube with a thin circular plate attached near its 'top' end (when the structure is vertically orientated in its deployment position). A number of smaller plates are attached to the tube, including two 'L'–shaped plates attached symmetrically at the bottom of the tube and a long 'fin' plate attached along the lower half of the tube. Additionally there is a wide 'U'–shaped cut out section removed from the thin circular plate and the edge of the plate section has a lip on both the top and bottom surfaces. A list of the principal dimensions of the damping plate is provided in Table 5.2.

Figure 5.19: Photo of the damping plate structure (yellow) with hydrophone attached (black) on the deck of the *Aurora Australis* before deployment.

Table 5.2: Principal dimensions of the damping plate structure.

tube length	76.5cm
tube outer radius	4.5cm
tube inner radius	2.2cm
circular plate radius	22.0cm
circular plate thickness	0.5cm
circular plate cut out length	15.8cm
circular plate cut out width	2.5cm
circular plate height (from top of cylinder)	4.5cm

An initial comparison between the dual FMBEM and PAFEC FEM–BEM models was conducted for a simplified version of the damping plate: where the plate thickness was increased to 4cm and all of the smaller appendages ('L' and 'fin' shapes plates and the outer lip on the circular plate) were removed. These simplifications allowed a direct

comparison between the two models using the same boundary element discretisation and linear finite elements in the FEM part of the FEM–BEM model. To accurately model the circular plate in PAFEC at the smaller plate thicknesses required the use of quadratic finite elements to achieve consistent results, and this made the full FEM–BEM models prohibitively large when using tetrahedral finite elements and triangular boundary elements for direct comparison of the two models.

The simplified damping plate was modelled with a mesh consisting of 14800 boundary elements for both the fluid and elastic solid domains in the dual FMBEM model, while the FEM–BEM model used the same BEM mesh for the fluid and a finite element mesh consisting of 64710 linear tetrahedral finite elements for the elastic solid. The incident acoustic field was specified as a unit amplitude compressional plane wave travelling in the direction $\left[-\frac{\sqrt{(2)}}{2}\ 0\ \frac{\sqrt{(2)}}{2}\right]$ with respect to the global origin at the centre of the circular plate and a fluid wavenumber of $k = 35$, corresponding to 50+ elements per fluid wavelength. Plots of the absolute value of the total surface pressure and total surface displacement for both the dual FMBEM and PAFEC FEM–BEM models are shown in Figs. 5.20 and 5.21 respectively for the simplified damping plate model.

The dual FMBEM model solved the problem in 2.47 hours and required 2.4GB of storage space while the PAFEC FEM–BEM model took 19.12 hours to solve and required 22.6GB of storage space. The r.e. norms between the solutions of the dual FMBEM and FEM–BEM models were 22.44% for the total surface pressure and 29.14% for the total surface displacement. The disagreement between the two sets of results appears to be mostly due to the different predictions for the total surface pressures on the inner cylindrical surface of the hollow tube. A plot of the total surface pressure results from both models is shown in Fig. 5.22 for a cross section of the damping plate along the plane of symmetry to show the inner tube surface. It can be seen from the results presented in Fig. 5.22 that the variation in the total surface pressures over the inner cylindrical surface of the damping plate is similar for both models, but the peak pressures are predicted to be higher in the FEM–BEM model results. Interestingly, a similar comparison for the total surface displacements shows a much smaller variation in the displacement solutions between the two models along the inner tube surface. Recalculating the r.e. norms between the solutions of the dual FMBEM and FEM–BEM models for all surface elements except for those constituting the inner cylindrical

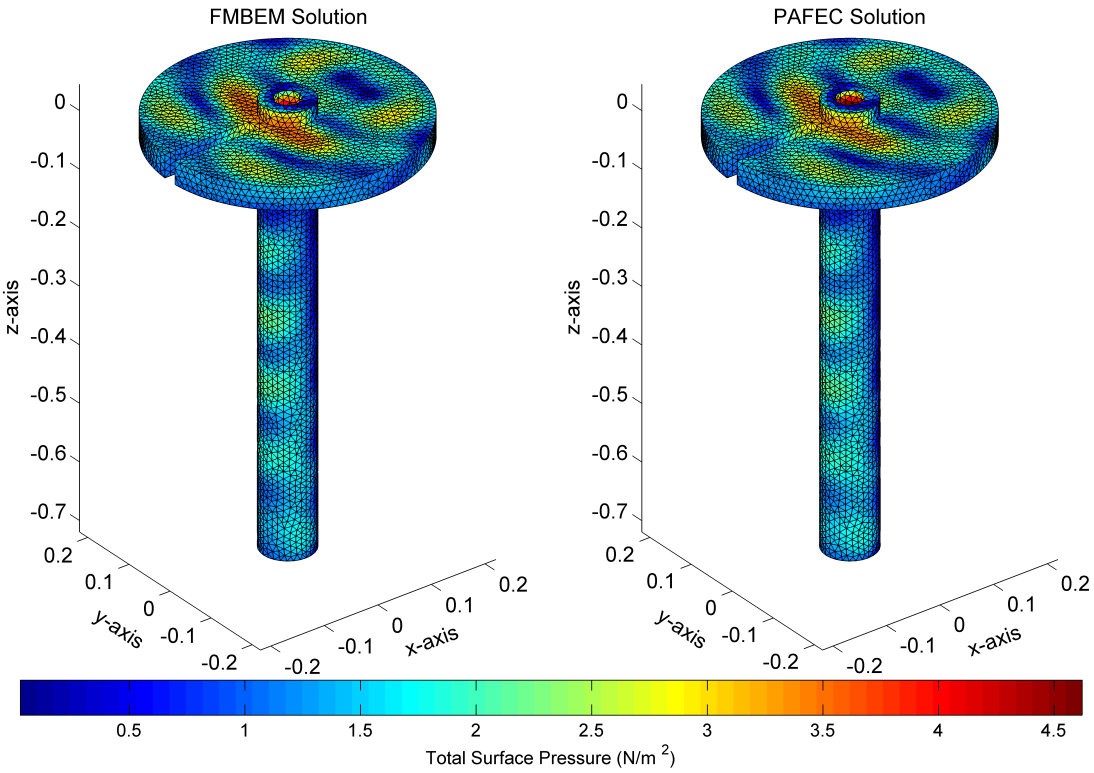

Figure 5.20: Absolute value of the total surface pressure for a compressional plane wave scattering from a simplified model of the damping plate at $k = 35$ for the dual FMBEM model (left) and PAFEC FEM–BEM model (right).

surface of the tube yields an r.e. norm of 10.02% for the total surface pressures, while that for the total surface displacements remains relatively unchanged.

The dual FMBEM model was also used to solve a coarse mesh of the full damping plate model which includes the various attachment plates. The mesh contained 8196 elements (32784 unknowns) and was impinged by a unit amplitude compressional plane wave travelling in the direction $\left[-\frac{\sqrt{(2)}}{2}\ 0\ \frac{\sqrt{(2)}}{2}\right]$ with a fluid wavenumber of $k = 17.5$. This problem involves a complicated 3D surface and so despite the large number of elements per fluid wavelength, the iterative solution was very slow to converge (requiring a large number of inner GMRES iterations) and showed instability in the results (i.e. asymmetry in the total surface fields) when a solution was attempted at higher wavenumbers or using a finer octree level. The total solution time was 3.7 hours and the problem required 3.2GB of storage space (compared to 17.2GB for the full coupled

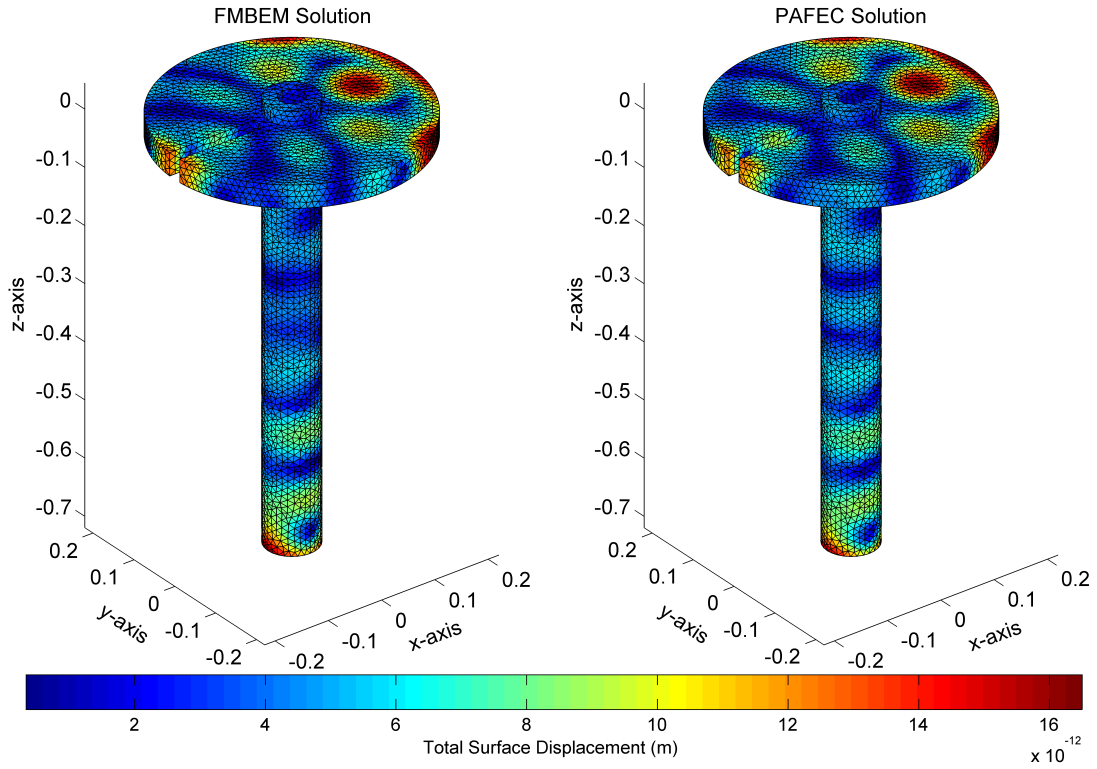

Figure 5.21: Absolute value of the total surface displacement for a compressional plane wave scattering from a simplified model of the damping plate at $k = 35$ for the dual FMBEM model (left) and PAFEC FEM–BEM model (right).

BEM matrix). Fig. 5.23 shows a plot of the total surface pressure (left) and total surface displacement (right) for the full damping plate model. It can be seen from Fig. 5.23 that the FMBEM predicts both large pressures and displacements on the two 'L' plates attached to the bottom of the cylinder. This is likely due to the fact that the 'L' plates are only attached to the main cylinder by thin connecting sections on the corners of the plates, while the lower third of each plate hangs freely from the main structure. Thus one would expect the 'L' plates to be able to vibrate with a large amplitude under the right conditions.

Due to the large amplitude pressures/displacements on the 'L' plates, little detail can be seen in Fig. 5.23 over the rest of the damping plate surface. Thus Fig. 5.24 shows similar results for a top–down view of the circular plate with the two colour bars independently rescaled to reveal more detail in the total surface pressure/displacement fields. It can be seen from Fig. 5.24 that the FMBEM solution shows good left–right

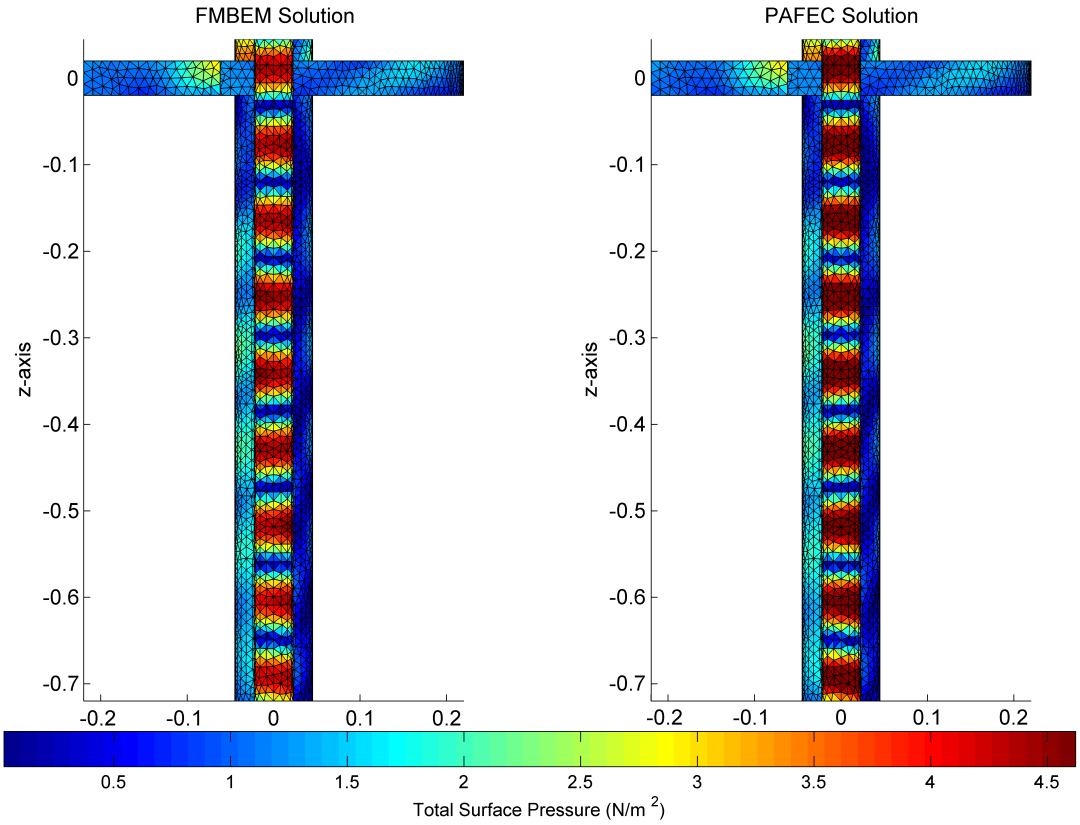

Figure 5.22: Absolute value of the total surface pressure for a compressional plane wave scattering from a simplified model of the damping plate at $k = 35$ for the dual FMBEM model (left) and PAFEC FEM–BEM model (right), shown for one half of the model along the plane of symmetry for the damping plate.

symmetry in the yz–plane of the model for both the pressures and displacements, despite the relatively low number of elements compared to the various scattering features observed in the total surface fields. Furthermore, for the coarse element discretisation used in this example, the boundary elements on each side of the circular plate have a typical side length of about 1.4cm compared to the plate thickness of 5mm and thus one might expect the Green's functions in the Helmholtz/elastodynamic BIEs to show near–singular behaviour. The proper treatment of the near–singular integrals in the dual FMBEM model allows the coarse element mesh for the thin circular plate to be solved without difficulty, although the convergence of the GMRES solution is slow.

The dual FMBEM model is able to solve much larger acoustic coupled FSI problems than the conventional FEM–BEM models. Fig. 5.25 shows the dual FMBEM total

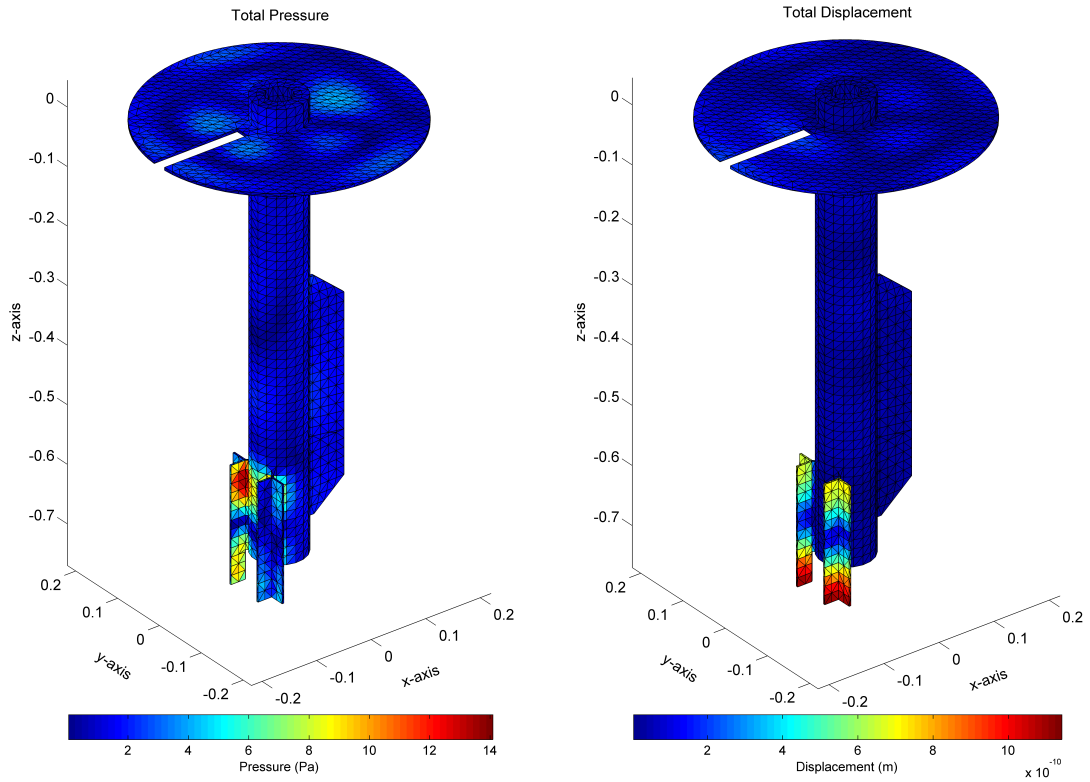

Figure 5.23: Absolute value of the total surface pressure (left) and total surface displacement (right) from the dual FMBEM model for a $k = 17.5$ compressional plane wave scattering from a low resolution model of the full damping plate structure.

surface pressure results for the simplified damping plate for a mesh containing 49200 elements (196800 unknowns) impinged by a unit amplitude compressional plane wave travelling in the direction $\left[-\frac{\sqrt{(2)}}{2}\ 0\ \frac{\sqrt{(2)}}{2}\right]$ with a fluid wavenumber of $k = 70$.

The dual FMBEM model was able to solve the above problem in 21.7hours and required 3.94GB of storage space. Comparatively, the full coupled BEM matrix would require approximately 619GB of space to store and 3.87×10^{10} operations per matrix–vector product in the iterative solution. Note that the total surface pressure results presented in Fig. 5.25 are shown from the underside of the circular plate to reveal the peak total surface pressures for this example, and are plotted without the black line edges for the triangular elements which would otherwise obscure the colour variation on the surface due to the large number of elements in the model.

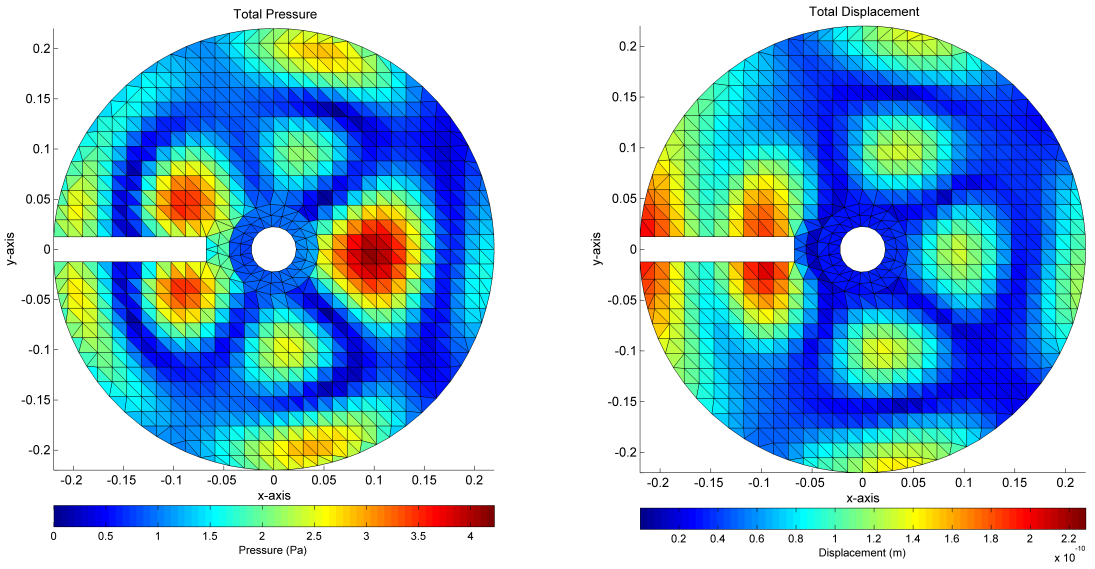

Figure 5.24: Absolute value of the total surface pressure (left) and total surface displacement (right) from the dual FMBEM model for a $k = 17.5$ compressional plane wave scattering from a low resolution model of the full damping plate structure: top–down view of the circular plate.

5.4 Chapter Summary

This chapter has presented a dual FMBEM model for acoustic coupled FSI problems, constituting the principal contribution of original work in this thesis. The chapter firstly presents literature reviews on both dual BEM and coupled FEM–FMBEM type models for acoustic FSI problems, which are both closely related to the developed dual FMBEM model. This is followed by a description of the implementation of the dual FMBEM model, including details of the procedure used to couple the unknowns on the shared surface between the fluid and elastic solid domains, as well as the preconditioning strategies employed to solve the resulting coupled system of equations. A pseudocode algorithm is then presented which details the iterative fGMRES solution procedure for solving the coupled system of BIEs using the separate Helmholtz and elastodynamic FMBEM algorithms presented in prior chapters. The chapter is concluded with the presentation of a number of numerical results which demonstrate the viability of the dual FMBEM model for solving acoustic coupled FSI problems.

Comparisons between the dual FMBEM model and a conventional FEM–BEM model for simple scattering problems with a known analytical solution indicated that

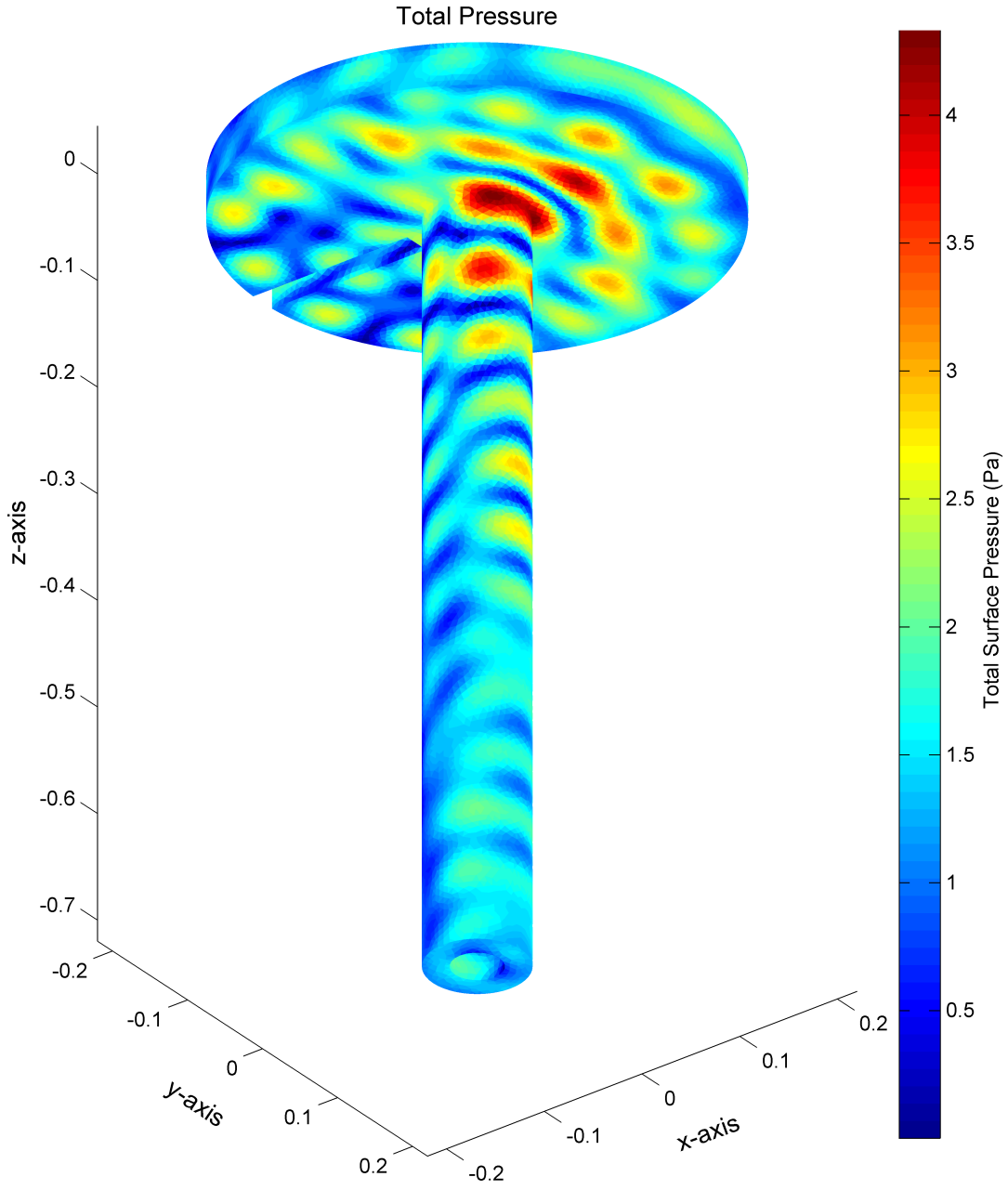

Figure 5.25: Absolute value of the total surface pressure from the dual FMBEM model for a $k = 70$ compressional plane wave scattering from a high resolution model of the simplified damping plate.

the dual FMBEM model was able to achieve comparable solution accuracies to the FEM–BEM model, while having significantly reduced total solution times and memory

requirements. The faster solutions times of the dual FMBEM model were achieved despite the model being coded in MATLAB, compared to the compiled Fortran executables used in the PAFEC FEM–BEM models. Good agreement between the dual FMBEM and FEM–BEM models was similarly observed in the numerical results for more complex geometries which have no known analytic solution. The dual FMBEM model was also shown to yield comparable or better solution accuracies than the FEM–BEM model near the free–vibration radial and torsional eigenfrequencies of the solid elastic sphere, with both models showing increased solution errors in the region of the eigenfrequencies (particularly for the radial modes). Increasing the mesh discretisation used in the dual FMBEM model was seen to reduce the solution errors of the results near the eigenfrequencies.

The total solution time of the dual FMBEM model was observed to scale proportionally to $N^{1.1}$ in the low frequency regime, where the number of unknowns/elements is independent of the wavenumber. Conversely in the high frequency regime the total solution time showed a proportionality between $N^{1.8}$ and $N^{1.5}$ when using between 10 and 20 elements per wavelength. In both cases the numerical algorithmic complexity results for the dual FMBEM model showed good agreement with the theoretical algorithmic complexity estimates. As expected, the dual FMBEM model shows substantially better performance in the low frequency regime due to the use of the low frequency $O(p^3)$ RCR translation method, which becomes increasingly expensive at higher frequencies. In all scenarios the storage requirements were proportional to N to a power less than one.

Thus the dual FMBEM model developed in this chapter is seen to provide a substantial computational benefit over the conventional modelling techniques for acoustic coupled FSI problems while providing a similar solution accuracy to those models.

6

Conclusions and Further Work

The principal focus of this thesis has been the development of a new numerical model for acoustic coupled FSI problems in which both the fluid and elastic solid domains are treated with the FMBEM. The primary advantages of this implementation are that only the shared boundary surface between the fluid and solid domains must be discretised and so the total number of unknowns is minimised, while the use of the FMM provides a significant reduction in the computational and memory requirements of the BEM calculations in both domains. Such a dual FMBEM model for acoustic coupled FSI problems has been developed in this thesis using the low frequency FMM to solve coupled problems involving a single exterior fluid domain and a single interior elastic solid domain, with both media having homogeneous isotropic properties. Chapter 2 first presented the main details of the developed low frequency FMM, based upon the multipole expansion of the Helmholtz Green's function using the spherical basis functions and the RCR translation method. The low frequency FMM was used to develop both a Helmholtz FMBEM, presented in Chapter 3, and an elastodynamic FMBEM, presented in Chapter 4. In both cases the computational requirements of the FMBEM models were further reduced via the use of translation stencils, while a nested inner–outer fGMRES iterative solution technique and an SAI preconditioner was employed to increase the convergence rate of the solution. The separate Helmholtz and elastodynamic FMBEMs were then combined in Chapter 5 to build the dual FMBEM model for acoustic coupled FSI problems, where the coupling between the fluid and elastic solid domains was applied between the unknowns on the shared boundary surface. The coupled system of discretised BIEs were solved using an inner–outer fGMRES iterative

solution, where a low accuracy FMBEM was used as a preconditioner in the inner loop and a full accuracy FMBEM used in the outer loop, while the inner FMBEM was itself preconditioned using a diagonal scaling and an SAI preconditioner. Translation stencils were again used in the FMBEM calculations for both media to further reduce the computational cost of the FMBEM calculations in the iterative solution.

The dual FMBEM model exhibited a total solution time proportional to $N^{1.1}$ in the low frequency regime (where the wavelength is independent of the number of unknowns), and $N^{1.5}$ in the high frequency regime when using 20 elements per fluid wavelength. In both cases the observed algorithmic complexities were in good agreement with the theoretical estimates for the FMBEM when using $O(p^3)$ translation methods. Comparisons of the dual FMBEM numerical results for problems with a known analytic solution indicated that a boundary discretisation of 15–20 piecewise constant plane triangular elements per fluid wavelength yielded solution accuracies which would be sufficient for most modelling applications. The r.e. norms for the total surface pressures and total radial displacements were approximately 2–4% and 15–25% respectively when using element discretisation within this range. Comparisons between the solution error of the present dual FMBEM model and other dual BEM/FMBEM models published in the literature indicated that the present model was able to achieve a comparable solution accuracy in the surface pressures when using a similar element per wavelength discretisation, while comparitive data for the coupled displacement results was somewhat lacking in the published literature. Similar comparisons between the dual FMBEM model and a commercial FEM–BEM model showed that the dual FMBEM model was able to achieve a comparable solution accuracy to the FEM–BEM model in both the coupled surface pressures and displacements when using a similar element discretisation. Near the eigenefrequencies of the coupled problem both the dual FMBEM and the conventional FEM–BEM models were shown to have increased solution errors. However the errors from the dual FMBEM model were comparable to or less than the those of the FEM–BEM models when using a similar boundary element discretisation, suggesting that the use of the elastodynamic FMBEM to model the interior elastic solid domain in lieu of the FEM poses no difficulty and is stable near the eigenfrequencies of the coupled problem. Furthermore, the accuracy of the dual FMBEM model was shown to improve with increasing element discretisation near the eigenfrequencies of the coupled problem.

The dual FMBEM model was able to solve large scale acoustic coupled FSI problems involving up to 10^5–10^6 unknowns in several hours on a desktop workstation computer. Thus the dual FMBEM model developed in this thesis provides a significant improvement over conventional FEM–BEM models for acoustic coupled FSI problems in terms of the solution time and computational resources required, while being able to achieve a similar solution accuracy to that of a conventional FEM–BEM model. The faster dual FMBEM model solution times were achieved despite the fact that the dual FMBEM model is written in MATLAB, compared to the compiled Fortran executables used in the commercial FEM–BEM model.

The dual FMBEM model presented in this thesis is well suited to solving a class of acoustic coupled FSI problems which involve a single fluid and a single elastic solid domain, such as underwater sound radiation or scattering from solid structures. The main advantages of the dual FMBEM model — the boundary only discretisation and fast multipole accelerated calculations — requires the material properties in both the fluid and elastic solid domains to have homogeneous isotropic properties. This restriction on the material properties makes the dual FMBEM method awkward to apply to objects which involve numerous different materials. In such cases an FEM model of the region may be more suitable as the FEM allows the material properties to be defined on a per element basis, while the FMBEM model would require each distinct region possessing differing material properties to be treated via a separate BIE. Additionally, the principal numerical advantage of the BEM/FMBEM is in its ability to represent the volume of an exterior or interior domain via the boundary surface that defines those domains. Thus the advantages of the dual FMBEM are most acute when modelling large volume domains via small domain surfaces. In the case of the exterior domain, the equivalent volume is infinite and so the FMBEM representation of the exterior domain presents the best numerical saving. Alternatively for the interior domains the greatest numerical savings yielded by the dual FMBEM will be for solid objects which have a large volume to surface area ratio. Thus the dual FMBEM model might be expected to perform less efficiently when modelling thin objects with a small volume to surface area ratio, compared to using a volume discretisation method, such as the FEM, to model the interior structure.

With minor modifications to the code, the dual FMBEM model for problems involving a single exterior fluid domain and a single interior elastic solid domain can be

extended to several related types or problem, including:

- The scattering of elastic waves by fluid inclusions using an exterior elastic solid domain and interior fluid domain.
- Problems involving multiple coupled domains, such as scattering from multiple elastic solid inclusions suspended in a fluid medium, where each of the finite enclosed interior domains may have different material properties.
- Scattering from fluid filled or hollow elastic objects by modelling the outer object surface as an exterior fluid/interior solid domain boundary and the inner surface as either an interior fluid/exterior solid boundary for a fluid filled object, or as an exterior solid boundary with a traction–free BC for an interior vacuum.
- Acoustic coupled FSI problems for fluid/elastic solid interfaces with the incident field defined in either the fluid medium (for modelling seabed interaction effects and/or interface waves in underwater sound modelling) or the elastic solid medium (for seismic modelling of sub sea canyons). This application in particular would seem well suited to the dual FMBEM model as both the domains are semi–infinite and so a boundary discretisation of a truncated surface represents a large volume to surface area ratio in both domains.
- Three dimensional underwater sound propagation modelling in shallow water using the dual FMBEM to model the coupled fluid–structure interaction at the seabed and a Helmholtz FMBEM with a pressure release boundary condition to model the sea surface. Again the dual FMBEM model would seem especially well suited to this type of problem compared to other numerical methods as the total number of unknowns would be minimised with a boundary–only discretisation.

Modelling any of the applications listed above via the dual FMBEM would not require any major modification to the separate Helmholtz and elastodynamic FMBEM algorithms, or to the inner–outer fGMRES solution: only the implementation of the coupling procedure of the BIEs and the SAI preconditioner would need to be modified. Coupling between multiple fluid and/or elastic solid domains could similarly be included in the dual FMBEM by incorporating appropriate boundary conditions at the fluid–fluid and solid–solid interfaces.

More substantial modifications to the dual FMBEM model could further extend its capabilities in terms of both the types of problem that could be solved, and the speed and efficiency of the numerical solution. Perhaps the most beneficial extension to the model would be the incorporation of the high frequency diagonal translation methods to make both the Helmholtz and elastodynamic FMBEM models 'broadband' algorithms which perform efficiently at all frequencies. This would allow much higher frequency problems to be treated and would also increase the speed of the dual FMBEM model at lower frequencies. As the low frequency dual FMBEM model presented in this thesis exhibited an algorithmic complexity which was in good agreement with the theoretic prediction, it is expected that a broadband dual FMBEM model will show similar agreement with the theoretical models and thus have an algorithmic complexity proportional to $O(N\log(N))$. The good agreement of the observed algorithmic complexity of the dual FMBEM model with the theoretical predictions also suggests that the values chosen for the various FMM parameters used in the dual FMBEM model, mirroring those used in the separate Helmholtz and elastodynamic FMBEM models, are near optimal choices. However a rigorous sensitivity analysis of the model's performance as a function of these parameters should be carried out to confirm the suitability of the specified model parameters.

Another way in which the implementation of the developed dual FMBEM model could be improved is with regard to the use of piecewise constant plane triangular elements in the boundary mesh discretisations of both the fluid and elastic solid domains. The choice to use this kind of element is motivated by the fact that they are both computationally quick and cheap to implement compared to higher order elements, but this comes at the cost of requiring more elements/unknowns in total to achieve a similar solution accuracy. Of course the lower algorithmic complexity of the FMBEM implementation means that the larger number of unknowns is not as critical as in the standard BEM, but one should still endeavour to minimise the total number of unknowns in a problem to achieve the desired solution accuracy. An obvious avenue for future work will be to employ higher order boundary elements (e.g. discontinuous linear/quadratic elements) in both the Helmholtz and elastodynamic FMBEMs, to allow the total number of unknowns required to represent a particular problem to be minimised. In fact some recent numerical comparisons with a conventional Helmholtz BEM Fortran code that employs discontinuous quadratic elements indicated that the

total number of unknowns can reduced by 50% or more compared to the constant element mesh, while the low frequency Helmholtz FMBEM model presented here was several times slower for high wavenumber problems. This slower solution time of the Helmholtz FMBEM is in part due to the larger number of unknowns required in the constant element FMBEM mesh, in part due to applying the low frequency Helmholtz FMBEM to high wavenumber problems (where its computational efficiency is known to degrade), and in part due to the difference in programming languages (FMBEM model in MATLAB vs. BEM model in Fortran).

Other beneficial extensions to the model include the use of a stabilised elastodynamic BIE (i.e. via the equivalent CHIEF or Burton–Miller formulations) to overcome the fictitious eigenfrequency problem when modelling exterior elastic solid domains and thus provide accurate results at all frequencies. Stabilisation of the elastodynamic BIE may also provide faster convergence for exterior problems near the wavenumbers of the adjoint interior eigenfrequencies and so reduce the observed algorithmic scaling of the developed elastodynamic FMBEM for exterior problems. A more economical method for calculating the elastodynamic singular integrals would also be of significant worth. Introducing a method to allow coupling between non–conforming fluid/solid boundary meshes would allow the total number of unknowns to be reduced by utilising a coarser elastodynamic FMBEM mesh in the general case where the sound speed in the elastic solid is faster and so larger elements may be used compared to the fluid mesh. The incorporation of a conventional structural FEM model into the dual FMBEM code would further add to the capabilities of the model, allowing fine structure in the elastic solid to be treated with the FEM and larger continuous elastic solid regions to be treated with the elastodynamic FMBEM. A number of more complex preconditioning methods are also available in the literature which would improve the solution convergence and so could feasibly reduce the algorithmic complexity of the total solution time for the dual FMBEM model, while the initial residual of the iterative solution may be substantially reduced by determining a better candidate for the initial solution, for example by using a plane wave approximation of the incident field for acoustic scattering problems.

Finally, the choice of the MATLAB programming language for the development of the dual FMBEM model was principally motivated by the relative ease of algorithm development in such a ‘high level’ language, with the execution speed of the language being of ancillary concern. Further reductions in the total solution time of the dual

FMBEM model can be achieved by rewriting the computationally intensive parts of the code as compiled Fortran or C files which can be directly called from the main MATLAB program, or by directly compiling the MATLAB code via the MATLAB compiler. MATLAB also provides direct support for a number of advanced features such as CPU multithreading and GPU computing which will allow further reductions in the solution time of the dual FMBEM model.

References

[1] O. C. Zienkiewicz and R. L. Taylor. *Finite Element Method*, **1**. Elsevier, 5th edition, 2000. 1

[2] O. C. Zienkiewicz, R. L. Taylor, P. Nithiarasu, and J. Z. Zhu. *The Finite Element Method: It's Basis and Fundamentals*. Butterworth - Hienemann, 2005. 1

[3] J. N. Reddy. *An Introduction to Nonlinear Finite Element Analysis*. Oxford University Press, New York, 2004. 2

[4] F. Ihlenburg. **Finite Element Analysis of Acoustic Scattering**. In J. E. Marsden and L. Sirovich, editors, *Applied Mathematical Sciences*, **132**. Springer-Verlag, New York, 1998. 2

[5] Z. Chen. *Finite Element Methods and Their Applications*. Springer-Verlag, Berlin, 2005. 2

[6] S. M. Kirkup. *The Boundary Element Method in Acoustics*. Integrated Sound Software, 1998. 2, 41, 48

[7] O. C. Zienkiewicz, D. W. Kelly, and P. Bettess. **The coupling of the finite element method and boundary solution procedures**. *Int. J. Num. Meth. Engng.*, **11**:355–375, 1977. 2

[8] S. Marburg. **Six boundary elements per wavelength: Is that enough?** *J. Comp. Acoust.*, **10**(1):25–51, 2002. 2, 73, 78

[9] D. T. Wilton. **Acoustic radiation and scattering from elastic structures**. *Int. J. Num. Meth Engng.*, **13**:123–138, 1978. 3, 130

[10] A. Ali, C. Rajakumar, and A. Ali. *The Boundary Element Method: Applications in Sound and Vibration*. Taylor & Francis, 2004. 3

[11] F. B. Jensen, F. A. Kuperman, M. B. Porter, and H. Schmidt. *Computational Ocean Acoustics*. AIP Series in Modern Acoustics and Signal Processing. Springer-Verlag, New York, 2000. 3, 9

[12] G. C. Everstine and F. M. Henderson. **Coupled finite element/boundary element approach for fluid-structure interaction**. *J. Acoust. Soc. Am.*, **87**(5):1938–1947, 1990. 3, 130

[13] H. Peters, S. Marburg, and N. Kessissoglou. **Structural-acoustic coupling on non-conforming meshes with quadratic shape functions**. *Int. J. Numer. Meth. Engng.*, **91**:27–38, 2012. 3

[14] I. C. Mathews. **Numerical techniques for three-dimensional steady-state fluid-structure interaction**. *J. Acoust. Soc. Am.*, **79**(5):1317–1325, May 1986. 3, 130

[15] F. Fahy and P. Gardonio. *Sound and Structural Vibration: Radiation, Transmission and Response*. Academic Press, second edition, 2007. 3

[16] R. Morgans, B. Cazzolato, A. Zander, C. Hansen, and S. Griffin. **Passive control of launch noise in rocket patload bays**. In *Ninth International Congress on Sound and Vibration, ICSV9*, Orlando, FL, USA, 2002. 3

[17] R. Citarella, L. Federico, and A. Cicatiello. **Modal acoustic transfer vector approach in a FEM-BEM vibro-acoustic analysis**. *Eng. Anal. Boundary Elem.*, **31**:248–258, 2007. 3

[18] N. A. Gumerov and R. Duraiswami. **A broadband fast multipole accelerated boundary element method for the 3D Helmholtz equation**. *J. Acoust. Soc. Am.*, **125**(1):191–205, January 2009. 4, 13, 14, 22, 25, 43, 45, 50, 56, 88

[19] C. S. Krishnamoorthy. *Finite Element Analysis: Theory and Programming*. McGraw-Hill, 2 edition, 1994. 4

[20] G.R. Liu and S. S. Quek. *The Finite Element Method: A Practical Course*. Butterworth - Hienemann, 2 edition, 2013. 4

[21] L. Greengard and V. Rokhlin. **A fast algorithm for particle simulations**. *J. Comput. Phys.*, **73**:325–348, 1987. 4, 42, 44, 45

[22] S. Amini and A. T. J. Profit. **Multi-level fast multipole solution of the scattering problem**. *Eng. Anal. Boundary Elem.*, **27**:547–564, 2003. 4

[23] R. Coifman, V. Rockhlin, and S Wandzura. **The fast multipole method for the wave equation: A pedestrian perscription**. *IEEE Antennas Propag.*, **35**:7–12, 1993. 4, 42

[24] H. Fujiwara. **A fast multipole method for solving integral equations of three-dimensional topography and basin problems**. *Geophys. J. Int.*, **140**:198–210, 2000. 4, 87

[25] V. Rokhlin. **Diagonal forms of translation operators for the Helmholtz equation in three dimensions**. Technical Report YALEU/DCS/RR-894, Department of Computer Science, Yale University, March 1992. 4, 42

[26] M. Bonnet, S. Chaillat, and J. F. Semblat. **Multi-level fast multipole BEM for 3-D elastodynamics**. In G. D. Manolis and D. Polyzos, editors, *Recent Advances in Boundary Element Methods*, pages 15–27. Springer, 2009. 4

[27] **PACSYS website**. Accessed 26/11/13. 6, 71, 141

[28] J. J. de Rego Silva. *Acoustic and Elastic Wave Scattering using Boundary Elements*, **18** of *Topics in Engineering*. Computational Mechanics Publications, 1994. 9, 47

REFERENCES

[29] T. W. Wu. **The Helmholtz integral equation**. In T. Wu, editor, *Boundary Element Acoustics: Fundamentals and Computer Codes*, Advances in Boundary Elements Series. WIT Press, Great Britain, 2000. 10, 99

[30] L. Gaul, D. Brunner, and M. Junge. **Simulation of elastic scattering with a coupled FMBE-FE approach**. In G. D. Manolis and D. Polyzos, editors, *Recent Advances in Boundary Element Methods*, pages 131–145. Springer, 2009. 10, 132, 134

[31] L. C. Wrobel. *The Boundary Element Method: Applications in Thermo-Fluids and Acoustics*, **1**. JohnWiley & Sons, England, 2002. 10, 41, 47

[32] S. Amini, P. J. Harris, and D. T. Wilton. *Coupled Boundary and Finite Element Methods for the Solution of the Dynamic Fluid-Structure Interaction Problem*. Number 77 in Lecture Notes in Engineering. Springer-Verlag, Berlin, 1992. 10, 47, 130

[33] S. Marburg and B. Nolte. **A unified approach to finite element and boundary element discretisation in linear time-harmonic acoustics**. In S. Marburg and B. Nolte, editors, *Computational acoustics of noise propagation in fluids - finite and boundary element methods*, chapter 0. Springer, Berlin, 2008. 11

[34] Y. Saad and M. H. Schultz. **GMRES: A generalized minimal residual algorithm for solving nonsymmatric linear systems**. *SIAM J. Sci. Stat. Comput.*, **7**(3):856–869, 1986. 13, 55

[35] S. Marburg and S. Schneider. **Performance of iterative solvers for acoustic problems. Part I. Solvers and effect of diagonal preconditioning**. *Eng. Anal. Boundary Elem.*, **27**:727–750, 2003. 13, 55

[36] S. Li and Q. Huang. **A fast multipole boundary element method based on the improved Burton-Miller formulation for three-dimensional acoustic problems**. *Eng. Anal. Boundary Elem.*, **35**:719–728, 2011. 13

[37] S. Chaillat, M. Bonnet, and J. F. Semblat. **A multi-level fast multipole BEM for 3-D elastodynamics in the frequency domain**. *Comp. Meth. Appl. Mech. Eng.*, **197**:4233–4249, 2008. 13, 88, 89, 97, 110, 113, 119, 120, 122, 123, 124, 125, 126

[38] Y. Liu. *Fast Multipole Boundary Element Method: Theory and Applications in Engineering*. Cambridge University Press, New York, 2009. 13, 42, 46

[39] S. Schneider. **FE/FMBE coupling to model fluid-structure interactions**. *Int. J. Numer. Meth. Engng.*, **76**:2137–2156, 2008. 13, 131

[40] E. Darve and P. Have. **Efficient fast multipole method for low-frequency scattering**. *J. Comput. Phys.*, **197**:341–363, 2004. 13, 17

[41] Y. Yasuda, T. Oshima, T. Sakuma, A. Gunawan, and T. Masumoto. **Fast multipole boundary element method for low-frequency acoustic problems based on a variety of formulations**. *J. Comp. Acoust.*, **18**(4):363–395, 2010. 13, 43, 80

[42] N. A. Gumerov and R. Duraiswami. *Fast Multipole Methods for the Helmholtz Equation in Three Dimensions*. Elsevier Series in Electromagnetism. Elsevier, 2004. 15, 16, 17, 18, 21, 24, 25, 42, 45, 46, 50, 57, 60, 71, 81, 97, 120, 132, 161, 162

[43] N. A. Gumerov and R. Duraiswami. **Recursions for the computation of multipole translation and rotation coefficients for the 3-D Helmholtz equation**. *SIAM J. Sci. Comput.*, **25**:1344–1381, 2003. 15, 16, 20, 21, 42, 43, 45, 50

[44] M. C. Junger and D. Feit. *Sound, Structure and Their Interaction*. Acoustical Society of America, 1993. 15

[45] N. A. Gumerov and R. Duraiswami. **Computation of scattering from N spheres using multipole reexpansion**. Technical report, University of Maryland, Institute for Advanced Computer Studies, Perceptual Interfaces and Reality Laboratory, 2002. 16

[46] M. A. Epton and B. Dembart. **Multipole translation theory for the three-dimensional Laplace and Helmholtz equations**. *SIAM J. Sci. Comput.*, **16**(4):865–897, 1995. 16, 19, 42

[47] N. A. Gumerov and R. Duraiswami. **Data structures, optimal choice of parameters, and complexity results for generalized multilevel fast multipole methods in d dimensions**. Technical report, UMIACS Technical Report TR 2003-28, University of Maryland, Perceptual Interfaces and Reality Laboratory, Institute for Advanced Computer Studies, College Park, MD, 2003. 17, 23, 24

[48] L. Shen and Y. J. Liu. **An adaptive fast multipole boundary element method for three-dimensional acoustic wave problems based on the Burton-Miller formulation**. *Comput. Mech.*, **40**:461–472, 2007. 19, 42

[49] M. S. Bapat, L. Shen, and Y. J. Liu. **Adaptive fast multipole boundary element method for three-dimensional half-space acoustic wave problems**. *Eng. Anal. Boundary Elem.*, **33**:1113–1123, 2009. 19

[50] W. C. Chew. **Recurrence relations for three-dimensional scalar addition theorem**. *J. Electromagn. Waves Appl.*, **6**(2):133–142, 1992. 20, 42

[51] C. A. White and M. Head-Gordon. **Derivation and efficient implementation of the fast multipole method**. *J. Chem. Phys.*, **101**:6593–6605, 1994. 20, 45

[52] C. A. White and M. Head-Gordon. **Rotating around the quartic angular momentum barrier in fast multipole method calculations**. *J. Chem. Phys.*, **105**:5061–5067, 1996. 20, 42, 45

[53] L. Greengard, J. Huang, V. Rokhlin, and S. Wandzura. **Accelerating fast multipole methods for the Helmholtz equation at low frequencies**. *IEEE Comput. Sci. Eng.*, **5**(3):32–38, 1998. 21, 43

[54] N. A. Gumerov and R. Duraiswami. **Comparison of the efficiency of translation operators used in the fast multipole method for the 3D Laplace equation**. Technical Report CS-TR-4701, University of Maryland, Department of Computer Science, 2005. 21, 42, 43

[55] S. Amini and A. Profit. **Analysis of the truncation errors in the fast multipole method for scattering problems**. *J. Comput. Appl. Math.*, **115**:23–33, 2000. 25, 46

[56] J. Rahola. **Diagonal forms of the translation operators in the fast multipole algorithm for scattering problems**. *BIT*, **36**:333–358, 1996. 25, 45

[57] E. Darve. **The fast multipole method I: Error analysis and asymptotic complexity**. *SIAM J. Numer. Anal.*, **38**:98–128, 2000. 25, 46

[58] H. G. Petersen, E. R. Smith, and D. Soelvason. **Error estimates for the fast multipole method. II. The three-dimensional case**. *Proc. R. Soc. Lond. A*, **448**:401–418, 1995. 25, 45

[59] S. Koc, J. Song, and W. C. Chew. **Error analysis for the numerical evaluation of the diagonal forms of the scalar spherical addition theorem**. *SIAM J. Numer. Anal.*, **36**:906–921, 1999. 25, 45

[60] M. Nilsson. **Stability of the fast multipole method for Helmholtz equation in three dimensions**. Technical report, Technical Report 2003-54, Department of Information Technology, Scientific Computing, Uppsala University, 2003. 25

[61] N. A. Gumerov and R. Duraiswami. **Fast multipole accelerated boundary element methods for the 3D Helmholtz equation**. Technical report, Perceptual Interfaces and Reality Laboratory, Department of Computer Science and Institute for Advanced Computer Studies, University of Maryland, December 2007. 25, 43

[62] K. Chen and P. J. Harris. **Efficient preconditioners for iterative solution of the boundary element equations for the three-dimensional Helmholtz equation**. *Appl. Numer. Math.*, **36**:475–489, 2001. 27, 56, 58, 100, 136

[63] L. H. Chen and D. G. Schweikert. **Sound radiation from an arbitrary body**. *J. Acoust. Soc. Am.*, **35**:1626–1632, 1963. 41, 130

[64] R. P. Banaugh and W. Goldsmith. **Diffraction of steady acoustic waves by surfaces of arbitrary shape**. *The Journal of the Acoustical Society of America*, **35**:1590–1601, 1963. 41

[65] M. B. Friedman and R. Shaw. **Diffraction of pulses by cylindrical obstacles of arbitrary cross section**. *J. Appl. Mech.*, **29**:40–46, 1962. 41

[66] R. D. Ciskowski and C. A. Brebbia, editors. *Boundary Element Methods in Acoustics*. Springer, 1991. 41

[67] T. Wu, editor. *Boundary Element Acoustics: Fundamentals and Computer Codes*. WIT Press, 2000. 41

[68] O. von Estorff, editor. *Boundary Elements in Acoustics: Advances & Applications*. WIT Press, 2000. 41

[69] V. Rokhlin. **Rapid solution of integral equations of classical potential theory**. *J. Comput. Phys.*, **60**:187–207, 1985. 41, 44, 45

[70] L. Greengard and V. Rokhlin. **A fast algorithm for particle simulations**. *J. Comput. Phys.*, **135**:280–292, 1997. 42

[71] V. Rokhlin. **Rapid solution of integral equations of scattering theory in two dimensions**. *J. Comput. Phys.*, **86**:414–439, 1990. 42

[72] W. C. Chew, H. Y. Chao, T. J. Cui, C. C. Lu, S. Ohnuki, Y.C. Pan, J. M. Song, S. Velamparambil, and J. S. Zhao. **Fast integral equation solvers in computational electromagnetics of complex structures**. *Eng. Anal. Boundary Elem.*, **27**:803–823, 2003. 42

[73] L. Greengard. **The rapid evaluation of potential fields in particle systems**. Research Report RR-533, Yale University Department of Computer Science, 1987. 42, 45

[74] L. Greengard and V. Rokhlin. **On the efficient Implementation of the Fast Multipole Algorithm**. Research Report RR-602, Yale University Department of Computer Science, 1988. 42

[75] N. Engheta, W. D. Murphy, V. Rokhlin, and M. S. Vassiliou. **The fast multipole method (FMM) for electromagnetic scattering problems**. *IEEE Trans. Antennas Propag.*, **40**(6):634–641, 1992. 42

[76] V. Rokhlin. **Diagonal forms of translation operators for the Helmholtz equation in three dimensions**. *Appl. Comput. Harmon. Anal.*, **1**:82–93, 1993. 42, 44

[77] B. Dembart and E. Yip. **The accuracy of fast multipole methods for Maxwell's equations**. *IEEE Comput. Sci. Eng.*, **5**(3):48–56, 1998. 42, 44, 45

[78] N. A. Gumerov and R. Duraiswami. **Fast, exact, and stable computation of multipole translation and rotation coeffiucients for the 3-D Helmholtz equation**. Technical report, University of Maryland, Institute for Advanced Computer Studies, Perceptual Interfaces and Reality Laboratory, 2001. 42, 50

[79] N. A. Gumerov and R. Duraiswami. **Computation of scattering from N spheres using multipole reexpansion**. *J. Acoust. Soc. Am.*, **112**(6):2688–2701, 2002. 42

[80] L. Greengard and V. Rokhlin. **A new version of the fast multipole method for the Laplace equation in three dimensions**. *Acta Numerica*, **6**:229–269, 1997. 43

[81] S. Koc and W. C. Chew. **Calculation of acoustical scattering from a cluster of scatters**. *J. Acoust. Soc. Am.*, **103**:721–734, 1998. 43

[82] J. Zhao and W. C. Chew. **Applying matrix rotation to the three-dimensional low-frequency fast multipole method**. *Microwave Opt. Technol. Lett.*, **26**(2):105–110, 2000. 43

[83] Z. Gimbutas and L. Greengard. **A fast stable method for rotating spherical harmonic expansions**. *J. Comput. Phys.*, **228**:5621–5627, 2009. 43

[84] T. Hrycak and V. Rokhlin. **An improved fast multipole algorithm for potential fields**. Research Report RR-1089, Yale University, Department of Computer Science, 1995. 43, 45

REFERENCES

[85] T. Hryack and V. Rokhlin. **An improved fast multipole algorithm for potential fields**. *SIAM J. Sci. Comput.*, **19**(6):1804–1826, 1998. 43

[86] H. Cheng, L. Greengard, and V. Rokhlin. **A fast adaptive multipole algorithm in three dimensions**. *J. Comput. Phys.*, **155**:468–498, 1999. 43

[87] R. Beatson and L. Greengard. **A short course on the fast multipole method**. In *Wavelets, Multilevel Methods and Elliptic PDEs*, pages 1–37. Oxford University Press, 1997. 43

[88] N. Nishimura. **Fast multipole accelerated boundary integral equation methods**. *Appl. Mech. Rev.*, **55**(4):299–324, 2002. 43, 44, 46

[89] E. Darve and P. Have. **A fast multipole method for maxwell equations stable at all frequencies**. *Phil. Trans. R. Soc. Lond. A*, **362**:603–628, 2004. 43, 45

[90] L. J. Jiang and W. C. Chew. **A mixed-form fast multipole algorithm**. *IEEE Trans. Antennas Propag.*, **53**(12):4145–4156, 2005. 43

[91] H. Cheng, W. Y. Crutchfield, Z. Gimbutas, L. F. Greengard, J. F. Ethridge, J. Huang, V. Rokhlin, N. Yarvin, and J. Zhao. **A wideband fast multipole method for the Helmholtz equation in three dimensions**. *J. Comput. Phys.*, **216**:300–325, 2006. 43

[92] M. S. Tong, W. C. Chew, and M. J. White. **Multilevel fast multipole algorithm for acoustic scattering by truncated ground with trenches**. *J. Acoust. Soc. Am.*, **123**:2513–2521, 2008. 44

[93] H. Wallen and J. Sarvas. **Translation procedures for broadband MLFMA**. *Prog. Electromagn. Res.*, **PIER 55**:47–78, 2005. 44, 45

[94] H. Wallen, S. Jarvenpaa, and P. Yla-Oijala. **Broadband multilevel fast multipole algorithm for acoustic scattering problems**. *J. Comp. Acoust.*, **14**(4):507–526, 2006. 44, 45

[95] T. Dufva and J. Sarvas. **Broadband MLFMA with plane wave expansions and optimal memory demand**. *IEEE Trans. Antennas Propag.*, **57**(3):742–753, 2009. 44, 45

[96] W. R. Wolf and S. K. Lele. **Wideband fast multipole boundary element method: Application to acoustic scattering from aerodynamic bodies**. *Int. J. Num. Meth Fluids*, **67**:2108–2129, 2011. 44

[97] C. C. Lu and W. C. Chew. **Fast algorithm for solving hybrid integral equations**. *IEEE Proc. H*, **140**(6):455–460, 1993. 44

[98] A. Brandt. **Multilevel computations of integral transforms and particle interactions with oscillatory kernals**. *Comp. Phys. Commun.*, **65**:24–38, 1991. 44

[99] C. C. Lu and C. Chew. **A multilevel algorithm for solving boundary integral equation**. Technical report, University of Illinois, Department of Electrical and Computer Engineering, 1995. 44

[100] C. C. Lu and C. Chew. **A multilevel algorithm for solving a boundary integral equation of wave scattering**. *Microw. Opt. Technol. Lett.*, **7**(10):466–470, 1994. 44

[101] B. Dembart and E. Yip. **A 3D fast multipole method for electromagnetics with multiple levels**. In *Proc. 11th Ann. Rev. Progress in Applied Computational Electromagnetics*, pages 621–628, Monterey, CA, USA, 1995. 44

[102] J. Song, C. C. Lu, and W. C. Chew. **Multilevel fast multipole algorithm for electromagnetic scattering by large complex objects**. *IEEE Trans. Antennas Propag.*, **45**(10):1488–1492, 1997. 44, 55

[103] J. M. Song and W. C. Chew. **Multilevel fast-multipole algorithm for solving combined field integral equations of electromagnetic scattering**. *Microw. Opt. Technol. Lett.*, **10**(1):14–19, 1995. 44

[104] J. M. Song and W. C. Chew. **Fast multipole method solution of three dimensional integral equation**. In *Antennas and Propagation Society International Symposium*, **3**, pages 1528–1531, 1995. 44

[105] R. L. Wagner and W. C. Chew. **A ray-propagation fast multipole algorithm**. *Microw. Opt. Technol. Lett.*, **7**(10):435–438, 1994. 44

[106] R. J. Burkholder and D. H. Kwon. **High-frequency asymptotic acceleration of the fast multipole method**. *Radio Science*, **31**(5):1199–1206, 1996. 44

[107] M. F. Gyure and M. A. Stalzer. **A prescription for the multilevel Helmholtz FMM**. *IEEE Comput. Sci. Eng.*, **5**(3):39–47, 1998. 44

[108] E. Darve. **The fast multipole method: Numerical implementation**. *J. Comput. Phys.*, **160**:195–240, 2000. 44

[109] J. Sarvas. **Performing interpolation and anterpolation entirely by fast Fourier transform in the 3-D multilevel fast multipole method**. *SIAM J. Numer. Anal.*, **41**(6):2180–2196, 2003. 45

[110] R. Jakob-Chien and B. K. Alpert. **A fast spherical filter with uniform resolution**. *J. Comput. Phys.*, **136**:580–584, 1997. 45

[111] N. Yarvin and V. Rokhlin. **An improved fast multipole algorithm for potential fields on the line**. *SIAM J. Numer. Anal.*, **36**(2):629–666, 1999. 45

[112] N. A. Gumerov and R. Duraiswami. **Computation of scattering from clusters of spheres using the fast multipole method**. *J. Acoust. Soc. Am.*, **117**(1):1744–1761, 2005. 45

[113] J. Carrier, L. Greengard, and V. Rokhlin. **A fast adaptive multipole algorithm for particle simulations**. Research Report RR-496, Yale University Department of Computer Science, 1987. 45

[114] J. Carrier, L. Greengard, and V. Rokhlin. **A fast adaptive multipole algorithm for particle simulations**. *SIAM J. Sci. Stat. Comput.*, **9**(4):669–686, 1988. 45

[115] H. G. Petersen, E. R. Smith, and D. Soelvason. **Error estimates for the fast multipole method. I. The two-dimensional case**. *Proc. R. Soc. Lond. A*, **448**:389–400, 1995. 45

[116] S. Ohnuki and W. C. Chew. **Numerical accuracy of multipole expansion for 2-D MLFMA**. *IEEE Trans. Antennas Propag.*, **51**(8):1883–1890, 2003. 46

[117] S. Ohnuki and W. C. Chew. **Truncation error analysis of multipole expansion**. *SIAM J. Sci. Comput.*, **25**(4):1293–1306, 2003. 46

[118] S. Ohnuki and W. C. Chew. **Error minimization of multipole expansion**. *SIAM J. Sci. Comput*, **26**(6):2047–2065, 2005. 46

[119] J. Song and W. C. Chew. **Error analysis for the truncation of multipole expansion of vector Green's functions**. *IEEE Micro. Wireless Components Lett.*, **11**(7):311–313, 2001. 46

[120] F. A. Cruz and L. A. Barba. **Characterization of the accuracy of the fast multipole method in particle simulations**. *Int. J. Num. Meth Engng.*, **79**:1577–1604, 2009. 46

[121] E. Grasso, S. Chaillat, M. Bonnet, and J. F. Semblat. **Application of the multi-level time-harmonic fast multipole BEM to 3-D visco-elastodynamics**. *Eng. Anal. Boundary Elem.*, **36**:744–758, 2012. 46, 88, 119, 132

[122] W. C. Chew, J. M. Jin, E. Michielssen, and J. Song, editors. *Fast and Efficient Algorithms in Computational Electromagnetics*. Artech House, Boston, 2001. 46

[123] L. Greengard. *The Rapid Evaluation of Potential Fields in Particle Systems*. MIT Press, Cambridge, 1988. 46

[124] S. Amini and S. M. Kirkup. **Solution of Helmholtz equation in the exterior domain by elementary boundary integral methods**. *J. Comput. Phys.*, **118**:208–221, 1995. 47

[125] S. Amini and D. T. Wilton. **An investigation of boundary element methods for the exterior acoustic problem**. *Comp. Meth. Appl. Mech. Eng.*, **54**:49–65, 1986. 47

[126] R. E. Kleinman and G. F. Roach. **Boundary integral equations for the three-dimensional Helmholtz equation**. *SIAM Review*, **16**(2):214–236, 1974. 47

[127] G. W. Benthien and H. A. Schenck. **Nonexistence and nonuniqueness problems associated with integral equation methods in acoustics**. Technical report, RDT&E Division, Naval Command, Control and Ocean Surveillance Center, San Diego, CA, 1997. 47

[128] S. Marburg and T-W. Wu. **Treating the phenomenom of irregular frequencies**. In S. Marburg and B. Nolte, editors, *Computational Acoustics of Noise Propagation in Fluids*, chapter 15. Springer-Verlag, Berlin, 2008. 47

[129] H. A. Schenck. **Improved integral formulation for acoustic radiation problems**. *J. Acoust. Soc. Am.*, **44**:41–58, 1968. 47

[130] A. J. Burton and G. F. Miller. **The application of integral equation methods to the numerical solution of some exterior boundary value problems**. *Proc. Roy. Soc. Lond. A.*, **323**(1553):201–210, 1971. 47, 48, 54

[131] A. F. Seybert and T. L. Rengarajan. **The use of CHIEF to obtain unique solutions for acoustic radiation using boundary integral equations**. *J. Acoust. Soc. Am.*, **81**(5):1299–1306, 1987. 48

[132] C. M. Piaszczyk and J. M. Klosner. **Acoustic radiation from vibrating surfaces at characteristic frequencies**. *J. Acoust. Soc. Am.*, **75**(2):363–375, 1984. 48

[133] S. Amini. **On the choice of the coupling parameter in boundary integral formulations of the exterior acoustic problem**. *Appl. Anal.*, **35**:75–92, 1990. 48

[134] H. T. Rathod, K. V. Nagaraja, B. Venkatesudu, and N. L. Ramesh. **Gauss Legendre quadrature over a triangle**. *J. Indian Inst. Sci.*, **84**:183–188, 2004. 54, 58, 99

[135] L. Scuderi. **On the computation of nearly singular Integrals in 3D BEM collocation**. *Int. J. Numer. Meth Engng.*, **74**:1733–1770, 2008. 54, 58, 99

[136] C. C. Chien, H. Rajiyah, and S. N. Atluri. **An effective method for solving the hypersingular integral equations in 3-D acoustics**. *J. Acoust. Soc. Am.*, **88**(2):918–937, 1990. 54

[137] Y. Liu and F. J. Rizzo. **A weakly singular form of the hypersingular boundary integral equation applied to 3-D acoustic wave problems**. *Comp. Meth. Appl. Mech. Eng.*, **96**:271–287, 1992. 54

[138] K. Chen, J. Cheng, and P. J. Harris. **A new study of the Burton and Miller method for the solution of a 3D Helmholtz problem**. *IMA J. Appl. Math.*, **74**(2):163–177, 2009. 54

[139] S. Li and Q. Huang. **An improved form of the hypersingular boundary integral equation for exterior acoustic problems**. *Eng. Anal. Boundary Elem.*, **34**:189–195, 2010. 54

[140] T. Matsumoto, C. Zheng, S. Harada, and T. Takahashi. **Explicit evaluation of hypersingular boundary integral equation for 3-D Helmholtz equation discretized with constant triangular element**. *J. Comput. Sci. Tech.*, **4**(3):194–206, 2010. 55, 58

[141] C. Zheng, T. Matsumoto, T. Takahashi, and H. Chen. **Explicit evaluation of hypersingular boundary integral equations for acoustic sensitivity analysis based on direct differentiation method**. *Eng. Anal. Boundary Elem.*, **35**:1225–1235, 2011. 55

[142] H. Wu, Y. Liu, and W. Jiang. **A low-frequency fast multipole boundary element method based on analytical integration of the hypersingular integral for 3D acoustic problems**. *Eng. Anal. Boundary Elem.*, **37**:309–318, 2013. 55

[143] M. Benzi. **Preconditioning techniques for large linear systems: A survey**. *J. Comput. Phys.*, **182**:418–477, 2002. 55

REFERENCES

[144] K. Nabors, S. Kim, and J. White. **Fast capacitance extraction of general three-dimensional structures**. *IEEE Trans. Microwave Theory Tech.*, **40**:1496–1505, 1992. 55

[145] K. Nabors, F. T. Korsmeyer, F. T. Leighton, and J. White. **Preconditioned, adaptive, multipole-accelerated iterative methods for three-dimensional first-kind integral equations of potential theory**. *SIAM J. Sci. Comput.*, **15**(3):713–735, 1994. 55

[146] K. Sertel and J. L. Volakis. **Incomplete LU preconditioner for FMM implementation**. *Microw. Opt. Technol. Lett.*, **26**(4):265–267, 2000. 55

[147] L. Gurel and O. Ergul. **Comparisons of FMM implementations employing different formulations and iterative solvers**. In *Antennas and Propagation Society International Symposium*, **1**, pages 19–22, Columbus, OH, USA, 2003. 55

[148] J. Lee, J. Zhang, and C. C. Lu. **Sparse inverse preconditioning of multilevel fast multipole algorithm for hybrid integral equations in electromagnetics**. *IEEE Trans. Antennas Propag.*, **52**(9):2277–2287, 2004. 55

[149] S. Schneider and S. Marburg. **Performance of iterative solvers for acoustic problems. Part II. Acceleration by ILU-type preconditioner**. *Eng. Anal. Boundary Elem.*, **27**:751–757, 2003. 55

[150] M. Fischer, H. Perfal, and L. Gaul. **Approximate inverse preconditioning for the fast multipole BEM in acoustics**. Technical report, Institute of Applied and Experimental Mechanics, University of Stuttgart, 2004. 55

[151] M. Fischer and L. Gaul. **Application of the fast multipole BEM for structural acoustic simulations**. *J. Comp. Acoust.*, **13**(1):87–98, 2005. 55

[152] Y. Saad. **A flexible inner-outer preconditioned GMRES algorithm**. *SIAM J. Sci. Comput*, **14**:461–469, 1993. 56, 60, 100, 104, 136, 140

[153] Y. Saad. **A flexible inner-outer preconditioned GMRES algorithm**. Research Report UMSI 91/279, Supercomputer Institute, University of Minnesota, 1200 Washington Avenue South, Minneapolis, Minnesota 55415, 1991. 56, 100, 136

[154] B. Carpentieri, I. S. Duff, L. Giraud, and G. Sylvand. **Combining fast multipole techniques and an approximate inverse preconditioner for large electromagnetic calculations**. *SIAM J. Sci. Comput*, **27**(3):774–792, 2005. 56

[155] M. Darbas, E. Darrigrand, and Y. Lafranche. **Combining analytic preconditioner and fast multipole method for the 3-D Helmholtz equation**. *J. Comput. Phys.*, **236**:289–316, 2013. 56

[156] B. Carpentieri. **Fast iterative solution methods in electromagnetic scattering**. *Prog. Electromagn. Res.*, **PIER 79**:151–178, 2008. 56

[157] N. A. Gumerov and R. Duraiswami. **Fast multipole methods on graphics processors**. *J. Comp. Phys.*, **227**:8290–8313, 2008. 62, 63, 64, 69

[158] C. W. Nell and L. E. Gilroy. **An improved BASIS model for the BeTSSi submarine**. Technical Report DRDC Atlantic TR 2003-199, Defence R&D Canada, 2003. 71, 81, 83

[159] S. Marburg and S. Schneider. **Influence of element types on numeric error for acoustic boundary elements**. *J. Comp. Acoust.*, **11**(3):363–386, 2003. 78

[160] A. V. Osetrov and M. Ochmann. **A fast and stable numerical solution for acoustic boundary element method equations combined with the Burton and Miller method for models consisting of constant elements**. *J. Comp. Acoust.*, **13**(1):1–20, 2005. 78

[161] S. N. Makarov and N. Ochmann. **An iterative solver for the Helmholtz integral equation for high-frequency acoustic scattering**. *J. Acoust. Soc. Am.*, **103**(2):742–750, 1998. 78

[162] M Fischer, U. Gauger, and L. Gaul. **A multipole galerkin boundary element method for acoustics**. *Eng. Anal. Boundary Elem.*, **28**:155–162, 2003. 80

[163] S. Schneider. **Application of fast methods for acoustic scattering and radiation problems**. *J. Comp. Acoust.*, **11**(3):387–401, 2003. 80

[164] Y. J. Liu, S. Mukherjee, N. Nishimura, M. Schanz, W. Ye, A. Sutradhar, E. Pan, N. A. Dumont, A. Frangi, and A. Saez. **Recent advances and emerging applications of the boundary element method**. *Appl. Mech. Rev.*, **64**:1–38, 2011. 87, 88

[165] T. A. Cruse and F. J. Rizzo. **A direct formulation and numerical solution of the general transient elastodynamic problem. I**. *J. Math. Anal. Appl.*, **22**:244–259, 1968. 87

[166] T A. Cruse and F. J. Rizzo. **A direct formulation and numerical solution of the general transient elastodynamic problem. II**. *J. Math. Anal. Appl.*, **22**:341–355, 1968. 87

[167] D. E. Beskos. **Boundary element methods in dynamic analysis**. *Appl. Mech. Rev.*, **40**(1):1–23, 1987. 87

[168] S. Kobayashi. **Elastodynamics**. In D. E. Beskos, editor, *Boundary element methods in mechanics*, pages 192–225. North-Holland Publishing, 1987. 87

[169] D. E. Beskos. **Boundary element methods in dynamic analysis: Part II (1986-1996)**. *Appl. Mech. Rev.*, **50**(3):149–197, 1997. 87, 130

[170] A. C. Eringen and E. S. Suhubi. *Elastodynamics*, **2**. Academic Press, New York, 1975. 87, 121, 151

[171] D. E. Beskos and G. D. Manolis. *Boundary Element Methods in Elastodynamics*. George Allen and Unwin, London, 1987. 87

[172] M. Bonnet. *Boundary Integral Equation Methods for Solids and Fluids*. John Wiley & Sons, 1995. 87, 98

[173] M. H. Aliabadi. *The Boundary Element Method: Applications in Solids and Structures*, **2**. Wiley, New York, 2002. 87

[174] D. E. Beskos. **Dynamic analysis of structures and structural systems**. In D. Beskos and G. Maier, editors, *Boundary Element Advances in Solid Mechanics*, number 440 in CISM Courses and Lectures. Springer, 2003. 87

[175] Y. H. Chen, W. C. Chew, and S. Zeroug. **Fast multipole methods as an efficient solver for 2D elastic wave surface integral equations**. *Comput. Mech.*, **20**:495–506, 1997. 87

[176] T. Fukui and K. Inoue. **Fast multipole boundary element method in 2D elastodynamics**. *J. Appl. Mech. JSCE*, **1**:373–380, 1998. 87

[177] H. Fujiwara. **The fast multipole method for integral equations of seismic scattering problems**. *Geophys. J. Int.*, **133**:773–782, 1998. 87

[178] K. Yoshida. *Applications of fast multipole method to boundary integral equation method*. PhD thesis, Dept. of Global Environment Eng., Kyoto Univ., Japan, 2001. 88, 89, 90, 91, 97, 120

[179] K. Yoshida, N. Nishimura, and S. Kobayashi. **Analysis of three dimensional scattering of elastic waves by a crack with fast multipole boundary integral equation method**. *J. Appl. Mech. JSCE*, **3**:143–150, 2000. 88

[180] K. Yoshida, N. Nishimura, and S. Kobayashi. **Applications of a diagonal form fast multipole BIEM to the analysis of three dimensional scattering of elastic waves by cracks**. *Trans. JASCOME J. BEM*, **18**:77–80, 2001. 88

[181] H. Isakari, H. Yoshikawa, and N. Nishimura. **A periodic FMM for elastodynamics in 3D and its applications to problems related to waves scattered by a doubly periodic layer of scatterers**. *J. Appl. Mech. JSCE*, **13**:169–178, 2010. 88, 89, 108, 120

[182] H. Isakari. *Periodic FMMs and Calderon's preconditioning in acoustics and elastodynamics*. PhD thesis, Graduate School of Engineering, Kyoto University, 2012. 88, 89, 132, 159, 160

[183] S. Chaillat, M. Bonnet, and J. F. Semblat. **A fast multipole formulation for 3D elastodynamics in the frequency domain**. *C. R. Mecanique*, **335**:714–719, 2007. 88, 90

[184] J. A. Sanz, M. Bonnet, and J. Dominguez. **Fast multipole method applied to 3-D frequency domain elastodynamics**. *Eng. Anal. Boundary Elem.*, **32**:787–795, 2008. 88

[185] S. Chaillat, J. F. Semblat, and M. Bonnet. **A preconditioned 3-D multi-region fast multipole solver for seismic wave propagation in complex geometries**. *Commun. Comput. Phys.*, **11**:594–609, 2012. 88

[186] S. Chaillat, M. Bonnet, and J. F. Semblat. **A new fast multi-domain BEM to model seismic wave propagation and amplification in 3-D geological structures**. *Geophys. J. Int.*, **177**:509–531, 2009. 88, 132

[187] M. S. Tong and W. C. Chew. **Multilevel fast multipole algorithm for elastic wave scattering by large three-dimensional objects**. *J. Comp. Phys.*, **228**:921–932, 2009. 88

[188] H. Isakari, K. Niino, H. Yoshikawa, and N. Nishimura. **Calderon's preconditioning for periodic fast multipole method for elastodynamics in 3D**. *Int. J. Num. Meth Engng.*, **90**:484–505, 2012. 88

[189] T. Takahashi. **A wideband fast multipole accelerated boundary integral equation method for time-harmonic elastodynamics in two dimensions**. *Int. J. Num. Meth Engng.*, **91**:531–551, 2012. 88

[190] S. Chaillat and M. Bonnet. **Recent advances on the fast multipole accelerated boundary element method for 3D time-harmonic elastodynamics**. *Wave Motion*, **50**:1090–1104, 2013. 88

[191] S. Chaillat. *Fast multipole method for 3-D elastodynamic boundary integral equations. Application to seismic wave propagation*. PhD thesis, Laboratoire de Mecanique des Solides, Ecole Polytechnique, 2008. 89, 97, 99, 119, 121, 122, 124, 125, 126

[192] Z. Tong, Y. Zhang, Z. Zhang, and H. Hua. **Dynamic behaviour and sound transmission analysis of a fluid-structure coupled system using the direct-BEM/FEM**. *J. Sound Vib.*, **299**:645–655, 2007. 89

[193] P. Dangla, J. F. Semblat, H. Xiao, and N. Delepine. **A simple and efficient regularization method for 3D BEM: Application to frequency-domain elastodynamics**. *B. Seismol. Soc. Am.*, **95**(5):1916–1927, 2005. 99

[194] C. F. Ying and R. Truell. **Scattering of a plane longitudinal wave by a spherical obstacle in an isotropically elastic solid**. *J. Appl. Phys.*, **27**(9):1086–1097, 1956. 106

[195] Y. Pao and C. C. Mow. **Scattering of plane compressional waves by a spherical obstacle**. *J. Appl. Phys.*, **34**(3):493–499, 1963. 106

[196] I. R. Gonsalves, D. J. Shippy, and F. J. Rizzo. **Overcoming nonuniqueness in the direct BIEM for three-dimensional steady-state exterior elastodynamic problems**. In B. S. Annigeri and K. Tseng, editors, *Boundary Element Methods in Engineering*, pages 317–323. Springer, 1990. 108

[197] L. Lee and T. W. Wu. **An enhanced CHIEF method for steady-state elastodynamics**. *Eng. Anal. Boundary Elem.*, **12**:75–83, 1993. 108

[198] D. S. Jones. **Boundary integrals in elastodynamics**. *IMA J. Appl. Math.*, **34**:83–97, 1985. 108

[199] Y. Liu and F. J. Rizzo. **Hypersingular boundary integral equations for radiation and scattering of elastic waves in three dimensions**. *Comp. Meth. Appl. Mech. Eng.*, **107**:131–144, 1993. 108

[200] F. J. Sanchez-Sesma. **Diffraction of elastic waves by three-dimensional surface irregularities**. *Bull. Seism. Soc. Am.*, **73**(6):1621–1636, 1983. 120

[201] H. Eshraghi and M. Dravinski. **Scattering of plane harmonic SH, SV, P and Rayleigh waves by non-axisymmetric three-dimensional canyons: a wave function expansion approach**. *Earthq. Eng. Struct. D.*, **18**:983–998, 1989. 120

[202] E. Reinoso, L. C. Wrobel, and H. Power. **Three-dimensional scattering of seismic waves from topographical structures**. *Soil Dyn. Earthquake Engng.*, **16**:41–61, 1997. 120, 122, 123, 124

[203] B. Omidvar, M. Rahimian, T. Mohammadnejad, and A. Sanaeiha. **Three-dimensional scattering of plane harmonic SH, SV, and P waves in multilayered alluvial valleys**. *AJCE (Building and Housing)*, **11**(5):605–626, 2010. 120, 122, 123, 124

[204] F. J. Sanchez-Sesma and F. Luzon. **Seismic responce of three-dimensional alluvial valleys for incident P, S, and Rayleigh Waves**. *Bull. Seism. Soc. Am.*, **85**(1):269–284, 1995. 120

[205] M. S. Tong and W. C. Chew. **Nystrom method for elastic wave scattering by three-dimensional obstacles**. *J. Comput. Phys.*, **226**:1845–1858, 2007. 121

[206] N. Atalla and R. J. Bernhard. **Review of numerical solutions for low-frequency structural-acoustic problems**. *Appl. Acoust.*, **43**:271–294, 1994. 129

[207] G. C. Everstine. **Finite element formulations of structural acoustic problems**. *Comput. Struct.*, **65**(3):307–321, 1997. 129

[208] F. M. Henderson. **A structure-fluid interaction capability for the NASA structural analysis (NASTRAN) computer program**. Technical Report 3962, Naval ship research and development center, Computation and mathematics department, Bethesda, Maryland, 1972. 130

[209] R. R. Smith, J. T. Hunt, and D. Barach. **Finite element analysis of acoustically radiating structures with applications to sonar transducers**. *J. Acoust. Soc. Am.*, **54**:1277–1288, 1973. 130

[210] L. H. Chen. **Acoustic emissions from submerged structures**. In P. K. Banerjee and R. P. Shaw, editors, *Developments in Boundary Element Methods*, **2**, chapter 9, pages 245–281. Applied Science Publishers, 1982. 130

[211] J. Mackerle. **Finite and boundary element techniques in acoustics - A bibliography (1990-1992)**. *Finite Elem. Anal. Des.*, **15**:263–272, 1994. 130

[212] J. Mackerle. **Fluid-structure interaction problems, finite element and boundary element approaches. A bibliography (1995-1998)**. *Finite Elem. Anal. Des.*, **31**:231–240, 1999. 130

[213] R. P. Shaw. **Integral equation formulation of dynamic acoustic fluid-elastic solid interaction problems**. *J. Acoust. Soc. Am.*, **53**:514–520, 1973. 130

[214] P. C. Waterman. **New formulation of acoustic scattering**. *J. Acoust. Soc. Am.*, **45**(6):1417–1429, 1969. 130

[215] A. Bostrom. **Scattering of stationary acoustic waves by an elastic obstacle immersed in a fluid**. *J. Acoust. Soc. Am.*, **67**(2):390–398, 1980. 130

[216] B. Peterson, V. V. Varadan, and V. K. Varadan. **Scattering of acoustic waves by elastic and viscoelastic obstacles immersed in a fluid**. *Wave Motion*, **2**(2):23–38, 1980. 130

[217] J. Su, V. V. Varadan, V. K. Varadan, and L. Flax. **Acoustic wave scattering by a finite elastic cylinder in water**. *J. Acoust. Soc. Am.*, **68**(2):686–691, 1980. 130

[218] M. Tanaka and Y. Masuda. **Boundary element method applied to certain structural-acoustic coupling problems**. *Comp. Meth. Appl. Mech. Eng.*, **71**:225–234, 1988. 130

[219] M. Tanaka and K. Tanaka. **On a new boundary element solution scheme for elastoplasticity**. *Ing. Arch.*, **50**:289–295, 1981. 130

[220] A. F. Seybert, T. W. Wu, and X. F. Wu. **Radiation and scattering of acoustic waves from elastic solids and shells using the boundary element method**. *J. Acoust. Soc. Am.*, **84**(5):1906–1912, 1988. 130, 159

[221] P. Goswami, F. J. Rizzo, and D. J. Shippy. **Acoustic scattering by elastic solids using the boundary element method**. In D. O. Thompson and D. E. Chimenti, editors, *Review of progress in quantitative NDE*, **7A**, pages 95–102. Plenum Press, 1987. 131, 159

[222] P. P. Goswami, T. J. Rudolphi, F. J. Rizzo, and D. J. Shippy. **A boundary element model for acoustic-elastic interaction with applications in ultrasonic NDE**. *J. Nondestruct. Eval.*, **9**(2):101–112, 1990. 131, 151, 153, 159

[223] V. Mallardo and M. H. Aliabadi. **Boundary element method for acoustic scattering in fluid-fluidlike and fluid-solid problems**. *J. Sound Vib.*, **216**(3):413–434, 1998. 131

[224] C. J. Randall. **Modes of noncircular fluid-filled boreholes in elastic formations**. *J. Acoust. Soc. Am.*, **89**(3):1002–1016, 1991. 131

[225] V. F. Poterasu. **Coupled vibrations of a cavity filled with a pulsating fluid in elastic infinite media by the boundary element method**. *Comp. Meth. Appl. Mech. Eng.*, **106**:285–296, 1993. 131

[226] P. P. Goswami and T. J. Rudolphi. **Numerical simulation of ultrasonic transmission through curved interface**. *Int. J. Num. Meth Engng.*, **36**:2369–2393, 1993. 131

[227] S. Shenoy, T. J. Rudolphi, and F. J. Rizzo. **Boundary element solutions to wave scattering by surface irregularities on a fluid-solid interface**. In C. A. Brebbia and H. Power, editors, *Boundary Elements XVII*, pages 505–512. WIT Press, 1995. 131

[228] L. I. Slepyan and S. V. Sorokin. **Analysis of structural-acoustic coupling problems by a two-level boundary integral method, part 1: A general formulation and test problems**. *J. Sound Vib.*, **184**(2):195–211, 1995. 131

[229] S. V. Sorokin. **Analysis of structural-acoustic coupling problems by a two-level boundary integral method, part 2: Vibrations of a cylindrical shell of finite length in an acoustic medium**. *J. Sound Vib.*, **184**(2):213–228, 1995. 131

[230] S. Chen and Y. Liu. **A unified boundary element method for the analysis of sound and shell-like structure interactions. I. Formulation and verification**. *J. Acoust. Soc. Am.*, **106**(3):1247–1256, 1999. 131, 159

[231] S. Chen, Y. Liu, and X. Dou. **A unified boundary element method for the analysis of sound and shell-like structure interactions. II. Efficient solution techniques**. *J. Acoust. Soc. Am.*, **108**(6):2738–2745, 2000. 131, 159

[232] B. Nolte, I. Schafer, J. Ehrlich, M. Ochmann, R. Burgschweiger, and S. Marburg. **Numerical methods for wave scattering phenomena by means of different boundary integral formulations**. *J. Comp. Acoust.*, **15**(4):495–529, 2007. 131

[233] B. Nolte and L. Gaul. **Fluid-structure-interaction with the boundary element method**. In *IMAC XVII - 17th international modal analysis conference*, pages 496–502, Kissimee, FL, USA, 1999. 131

[234] R. Burgschweiger, M. Ochmann, and B. Nolte. **Calculation of the acoustic target strength of elastic objects based on BEM-BEM-coupling**. In *Proceedings of Acoustics '08*, pages 5219–5222, Paris, France, 2008. 131

[235] A. Rodriguez-Castellanos, E. Flores, F. J. Sanchez-Sesma, C. Ortiz-Aleman, M. Nava-Flores, and R. Martin. **Indirect boundary element method applied to fluid-solid interfaces**. *Soil Dyn. Earthquake Engng.*, **31**:470–477, 2011. 131

[236] E. Flores-Mendez, M. Carbajal-Romero, N. Flores-Guzman, R. Sanchez-Martinez, and A. Rodriguez-Castellanos. **Rayleigh's, Stonley's, and Scholte's interface waves in elastic models using a boundary element method**. *J. Appl. Math.*, **2012**:15 pages, 2012. 131

[237] M. Carbajal-Romero, N. Flores-Guzman, E. Flores-Mendez, J. Nunez-Farfan, E. Olivera-Villasenor, and F. J. Sanchez-Sesma. **Scholte waves on fluid-solid interfaces by means of an integral formulation**. *Geofisica Internacional*, **52**(1):21–30, 2013. 131

[238] D. Soares Jr. and W. J. Mansur. **Dynamic analysis of fluid-soil-structure interaction problems by the boundary element method**. *J. Comp. Phys.*, **219**:498–512, 2006. 131

[239] D. Soares Jr. **Numerical moelling of acoustic-elastodynamic coupled problems by stabilized boundary element techniques**. *Comput. Mech.*, **42**:787–802, 2008. 131

[240] D. Soares Jr. **Coupled numerical methods to analyze interacting acoustic-dynamic models by multidomain decomposition techniques**. *Math. Probl. Eng.*, **2011**:28 pages, 2011. 131

[241] M. Fischer. *The fast multipole boundary element method and its application to structure-acoustic field interaction*. PhD thesis, Institute of Applied and Experimental Mechanics, University of Stuttgart, 2004. 131

[242] M. Fischer and L. Gaul. **Fast BEM-FEM mortar coupling for acoustic-structure interaction**. *Int. J. Numer. Meth. Engng.*, **62**:1677–1690, 2005. 131

[243] L. Gaul and M. Fischer. **Large-scale simulations of acoustic-structure interaction using the fast multipole BEM**. In R. Helmig, A. Mielke, and B. Wohlmuth, editors, *Multifield Problems in Solid and Fluid Mechanics*, **28** of *Lecture Notes in Applied and Computational Mechanics*. Springer, 2006. 131

[244] L. Gaul and M. Fischer. **Fast multipole boundary element method for the simulation of acoustic-structure interaction**. In S. K. Chakrabarti and C. A. Brebbia, editors, *Fluid Structure Interaction and Moving Boundary Problems IV*, **92** of *WIT Transactions on The Built Environment*, pages 313–319. WIT Press, 2007. 131

[245] D. Brunner, M. Junge, and L. Gaul. **Strong coupling of the fast multilevel multipole boundary element method with the finite element method for vibro-acoustic problems**. In *ICSV14: 14th International Congress on Sound and Vibration*, Cairns, Australia, 2007. 132

[246] D. Brunner, M. Junge, and L. Gaul. **A comparison of FE-BE coupling schemes for large-scale problems with fluid-structure interaction**. *Int. J. Num. Meth Engng.*, **77**:664–688, 2009. 132, 136

[247] L. Gaul, D. Brunner, and M. Junge. **Coupling a fast boundary element method with a finite element formulation for fluidstructure interaction**. In S. Marburg and B. Nolte, editors, *Computational acoustics of noise propagation in fluids - finite and boundary element methods*, chapter 19, pages 519–546. Springer, 2008. 132

[248] D. Brunner, M. Junge, M. Wilken, C. Cabos, and L. Gaul. **Vibro-acoustic simulations of ships by fast BE-FE approaches**. In *Proceedings of the IMAC-XXVII*, Orlando, FL, USA, 2009. 132

[249] M. Junge, D. Brunner, and L. Gaul. **Solution of FE-BE coupled eigenvalue problems for the prediction of the vibro-acoustic behaviour of ship-like structures**. *Int. J. Num. Meth Engng.*, **87**:664–676, 2011. 132

[250] D. Brunner, M. Junge, C. Cabos, and L. Gaul. **Vibroacoustic simulation of partly immersed bodies by a coupled fast BE-FE approach**. In *Proceedings of Acoustics '08*, Paris, France, 2008. 132

[251] D. Brunner, G. Of, M. Junge, O. Steinbach, and L. Gaul. **A fast BE-FE coupling scheme for partly immersed bodies**. *Int. J. Num. Meth. Engng.*, **81**:28–47, 2010. 132

[252] V. K. Ambarisha. **Coupling between multiple acoustic domains through elastic structures: Rapid solutions using fast multipole BEM**. In *inter.noise 2012*, New York, NY, USA, 2012. 132

[253] T. Masumoto, A. Gunawan, T. Oshima, Y. Yasuda, and T. Sakuma. **Coupling analysis between FMBEM-based acoustic and modal-based structural models - Convergence behaviour of iterative solutions**. In *inter.noise 2008*, New York, NY, USA, 2008. 132

[254] T. Masumoto. **Application of numerical acoustic analysis in the household appliance industry**. In *The 1st IEEE Global Conference on Consumer Electronics 2012*, pages 728–732, Tokyo, Japan, 2012. 132

[255] E. Grasso. *Modelling visco-elastic seismic wave propagation: A fast multipole boundary element method and its coupling with finite elements*. PhD thesis, Laboratoire de Mecanique des Solides, Ecole Polytechnique, 2012. 132

[256] H. Wu, Y. Liu, and W. Jiang. **A fast multipole boundary element method for 3D multi-domain acoustic scattering problems based on the Burton-Miller formulation**. *Eng. Anal. Boundary Elem.*, **36**:779–788, 2012. 132

[257] H. Isakari, H. Yoshikawa, and N. Nishimura. **A periodic FMM for Helmholtz-elastodynamics coupled problems**. *Transactions of the Japan Society for Computational Methods in Engineering,*, **11**:59–64, 2011. 132

[258] M. D. Hughes and K. Chen. **An efficient preconditioned iterative solver for solving a coupled fluid structure interaction problem**. *Int. J. Comput. Math.*, **81**(5):583–594, 2004. 136

[259] J. Faran. **Sound scattering by solid cylinders and spheres**. *J. Acoust. Soc. Am.*, **23**:405 – 418, 1951. 142

[260] D. S. Jones. **Low-frequency scattering by a body in lubricated contact**. *Quart. J. Mech. Appl. Math.*, **36**(1):111–138, 1983. 151

[261] Y. Sato and T. Usami. **Basic study on the oscillation of a homogeneous elastic sphere I. Frequency of free oscillations**. *Geophys. Mag.*, **31**:15–24, 1962. 151

[262] D. Wilkes, P. Alexander, and A. Duncan. **FMBEM analysis of sound scattering from a damping plate in the near field of a hydrophone**. In *Proceedings of Acoustics 2012*, Perth, Australia, 2012. 163